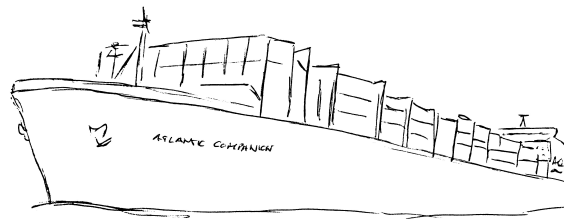


Autonomous ^{13}C measurements in the North Atlantic -
a novel approach for identifying patterns and driving
factors of the upper ocean carbon cycle



Dissertation zur Erlangung des Doktorgrades
der Mathematisch-Naturwissenschaftlichen Fakultät
der Christian-Albrechts-Universität zu Kiel
vorgelegt von

Meike Becker

Kiel, 2016

Erste/r Gutachter/in: Prof. Dr. Arne Körtzinger
Zweite/r Gutachter/in: Prof. Dr. Christa Marandino

Tag der mündlichen Prüfung: 23. Mai 2016
Zum Druck genehmigt: 06. Juli 2016

gez. Prof. Dr. Wolfgang J. Duschl, Dekan

*... the ocean is still out there, magnificent and wide.
She's got open arms to hold me, and endless space to hide,
And the only things that hold me back are things I hold inside,
The ocean is still out there, magnificent and wide.*

A-sailing I should go.

Frank Turner

Abstract

The North Atlantic Ocean plays a major role in climate change not least due to its importance in CO₂ uptake and thus natural carbon sequestration. The CO₂ concentration in its surface waters, which determines the ocean's CO₂ sink/source function, varies on seasonal and interannual timescales and is mainly driven by air-sea gas exchange and biological production/respiration. However, the quantification of these processes is still afflicted with a high degree of uncertainty. During the past 30 years substantial progress has been made in observing the CO₂ variability in the surface ocean by performing extensive underway measurements on board voluntary observing ships (VOS). Isotope measurements of dissolved inorganic carbon as a tracer for mass flows between different reservoirs can also help to improve the understanding of the controls of the surface ocean carbon system. One major limitation of using isotope data lies in the significant effort involved in their collection and the resulting scarce number of available data. Continuous wave Cavity Ringdown Spectroscopy (*cw*-CRDS), a relatively novel technology that has recently been introduced into environmental research, now provides the possibility of precise and continuous isotope ratio measurements. In combination with a classical, equilibrator based *p*CO₂ system, this technique enables underway isotope ratio measurements with a high temporal and spatial resolution. A cavity ringdown spectrometer (G2131-*i*, Picarro, USA) was installed on a VOS line that regularly sails across the subpolar North Atlantic between North America and Europe. From summer 2012 to the end of 2014, two and a half years of $\delta^{13}\text{C}(\text{CO}_2)$ underway data was obtained along with continuous measurements of temperature, salinity and *f*CO₂. Combined with a discrete sampling program (consisting of DIC, TA, nutrients, Chl *a*, POM, DOC, $\delta^{13}\text{C}(\text{POC})$ and $\delta^{15}\text{N}(\text{PON})$ samples), the dynamics of the upper North Atlantic Ocean were studied. This analysis comprises interannual variations of *f*CO₂ and $\delta^{13}\text{C}(\text{CO}_2)$, relative changes of nutrient concentration in comparison with C:N ratios of suspended particle matter, biologically and mixing driven variability in DIC and $\delta^{13}\text{C}(\text{DIC})$ and the fractionation between dissolved CO₂ and particulate matter. Based on the variations in

DIC, $f\text{CO}_2$, $\delta^{13}\text{C}(\text{DIC})$, nitrate, phosphate and silicate, the respective change rates and overall inventory changes due to air-sea gas exchange, net community production and convective mixing were calculated utilizing a box model.

Zusammenfassung

Der Nordatlantik spielt eine wichtige Rolle für den Klimawandel. In dieser Region wird anthropogenes CO_2 aus der Atmosphäre im Ozean gebunden. Das Ausmaß dieser Senke wird durch die Konzentration an CO_2 im Oberflächenwasser, die jahreszeitlichen sowie zwischenjährlichen Schwankungen unterliegt, bestimmt. Diese Veränderungen der CO_2 Konzentration werden hauptsächlich durch den Gasaustausch mit der Atmosphäre und den Auf- und Abbau von Biomasse getrieben. Die quantitative Beschreibung dieser Prozesse ist allerdings noch immer mit starken Fehlern behaftet. In den letzten 30 Jahren konnte unser Wissen über die CO_2 Variabilität des Oberflächenozeans mit Hilfe eines umfangreichen Messprogramms deutlich verbessert werden. Ein Großteil dieser Messungen wurde an Bord von, so genannten 'Voluntary Observing Ships' (VOS) durchgeführt. Neben der Analyse von Konzentrationsänderungen kann die isotopische Zusammensetzung einer Substanz Hinweise auf Transportprozesse zwischen verschiedenen Reservoiren, wie z.B. Atmosphäre und Ozean, geben. Bisher war die Verwendung dieser Isotopiemessungen allerdings häufig durch die komplizierte und zeitaufwändige Probenanalyse im Labor und die daher schlechte räumliche und zeitliche Auflösung der Daten limitiert. Cavity Ringdown Spektroskopie (CRDS) ist eine relativ neu entwickelte Technologie im Bereich der Umweltanalytik, die es uns jetzt ermöglicht, kontinuierlich die Isotopie einer Substanz aufzulösen. Kombiniert mit einem klassischen, auf einem Equilibrator basierenden $p\text{CO}_2$ -Messsystem, sind nun kontinuierliche Messungen der CO_2 Isotopie des Oberflächenozeans direkt auf See möglich. Während dieser Arbeit wurde ein CRDS (G2131-*i*, Picarro, USA) auf einem VOS, das regelmäßig zwischen Nordeuropa und Nordamerika pendelt, installiert. Zwischen Mitte 2012 und Ende 2014 konnten $\delta^{13}\text{C}(\text{CO}_2)$ Daten des oberflächennahen Nordatlantiks, sowie die dazugehörige Wassertemperatur, der Salzgehalt und die $f\text{CO}_2$, aufgenommen werden. Zusammen mit einem diskreten Probenprogramm (bestehend aus DIC, TA, Nährstoffen, Chl *a*, POM, DOC, $\delta^{13}\text{C}(\text{POC})$ und $\delta^{15}\text{N}(\text{PON})$ Proben) konnte die Dynamik des oberen Nordatlantiks untersucht werden. Diese Analyse kombiniert die Jahressgänge von $f\text{CO}_2$ und $\delta^{13}\text{C}(\text{CO}_2)$, die relativen

Veränderungen der Nährstoffkonzentrationen im Vergleich mit den C:N Verhältnissen der partikularen Biomasse, biologisch und durch Vermischung ausgelöste Veränderungen im DIC und $\delta^{13}\text{C}(\text{DIC})$, sowie die Fraktionierung zwischen gelöstem CO_2 und partikulärem Kohlenstoff. Basierend auf den Veränderungen in DIC, $f\text{CO}_2$, $\delta^{13}\text{C}(\text{DIC})$, Nitrat, Phosphat und Silikat, wurden die jeweiligen Änderungsraten und die jeweiligen Budgetänderungen durch Gasaustausch mit der Atmosphäre, Netto Kohlenstoffaufnahme der Planktongemeinschaft (NCP) und Durchmischung mit einem Box-Modell berechnet.

Contents

1	Introduction	1
2	Scientific background	7
2.1	Properties of the North Atlantic Ocean	7
2.2	Carbonate system	9
2.3	Stable isotopes of carbon and nitrogen	13
2.4	Cavity Ringdown Spectroscopy	20
3	Experimental	23
3.1	Precise measurements of $x\text{CO}_2$ and $\delta^{13}\text{C}(\text{CO}_2)$ using CRDS	23
3.2	Underway measurements and data reduction of $f\text{CO}_2$ and $\delta^{13}\text{C}(\text{CO}_2)$. .	25
3.3	Sample analysis	30
3.3.1	DIC and TA	31
3.3.2	Nutrients	31
3.3.3	Chl <i>a</i> , POM, $\delta^{13}\text{C}(\text{POC})$ and $\delta^{15}\text{N}(\text{PON})$	31
3.3.4	TOC and DOC	31
3.3.5	Seasonal cycles	32
3.4	Model description	33
4	An internally consistent dataset of $\delta^{13}\text{C}$-DIC in the North Atlantic Ocean-NAC13v1	37
5	Underway measurements on the North Atlantic of $f\text{CO}_2$ and $\delta^{13}\text{C}(\text{CO}_2)$	57
6	Modeling inventory changes of carbon and nutrients	65
6.1	Seasonal evolution and integrated inventory changes of carbon and nutrients	66
6.2	Chances and limitations in using stable carbon isotopes for flux calculations	74

7	Seasonality of the surface North Atlantic	81
7.1	Seasonal variability of SST, SSS and MLD	81
7.2	Seasonal changes in nutrient concentrations	84
7.3	Seasonal changes of the carbon system and its isotopic composition . . .	88
7.4	Seasonal variability of Chl <i>a</i> , POC and DOC and the Chl <i>a</i> / POC ratio	94
7.5	Synthesis	98
8	Stoichiometry of biomass production and upwelling of nutrients	99
8.1	C:N ratios of suspended particulate matter and the influence of calcification	100
8.2	Stoichiometry of nutrient consumption and convective mixing	103
9	Measurements of stable isotope signatures of particulate organic matter	115
9.1	Seasonality of $\delta^{13}\text{C}(\text{POC})$ and $\delta^{15}\text{N}(\text{PON})$	116
9.2	The fractionation between dissolved CO_2 and POC	119
10	Conclusions and outlook	125
11	Supplement	131

List of Figures

1.1	Atmospheric CO ₂ concentrations at Bermuda.	2
1.2	Global carbon cycle.	3
1.3	Air-to-sea CO ₂ flux.	4
2.1	Mean surface currents from 2012-2014.	8
2.2	Effects of processes on the carbon system.	12
2.3	Rayleigh fractionation process during primary production of nitrate and DIC.	16
2.4	Isotopic composition of carbon and nitrogen in selected materials.	18
2.5	Isotope fractionation inside the carbonate system.	19
2.6	Basic setup of a CRDS experiment.	21
3.1	Absorption spectrum.	24
3.2	Allan deviation.	25
3.3	Standard gas measurements.	26
3.4	Vessel tracks of M/V Atlantic Companion.	27
3.5	Setup on board M/V Atlantic Companion.	28
3.6	Salinity-Alkalinity correlation.	29
3.7	Model description.	35
5.1	Hovmoeller plots of underway $f\text{CO}_2$ and $\delta^{13}\text{C}(\text{CO}_2)$	58
5.2	Hovmoeller plots of the atmospheric disequilibrium of $f\text{CO}_2$ and $\delta^{13}\text{C}(\text{CO}_2)$	59
5.3	Hovmoeller plots of wind velocity and Mixed layer depth.	61
5.4	Variations of the NAO index.	63
6.1	Inventory changes box 1025.	67
6.2	Inventory changes box 2540.	68
6.3	Inventory changes box 4055 - sub.	69
6.4	Inventory changes box 4055 - pol.	70

6.5	Integrated inventory changes.	71
6.6	Influence of measurement uncertainties on Δ BIO, calculated from isotope measurements.	77
6.7	Schematic illustration of a flux isotope signature.	78
6.8	Seasonality of α_{ASE}	79
7.1	Seasonality of SST.	82
7.2	Seasonality of SSS.	83
7.3	Seasonal variations in MLD.	83
7.4	Seasonality of nitrate.	85
7.5	Seasonality of phosphate.	85
7.6	Seasonality of silicate.	86
7.7	Seasonality of nitrite.	87
7.8	Seasonality of $f\text{CO}_2$	89
7.9	Seasonality of $\delta f\text{CO}_2$	89
7.10	Seasonality of $\delta^{13}\text{C}(\text{CO}_2)$	90
7.11	Seasonality of TA.	91
7.12	Seasonality of DIC.	92
7.13	Seasonality of $\delta^{13}\text{C}(\text{DIC})$	92
7.14	Seasonality of Chl <i>a</i> concentration.	96
7.15	Seasonality of Chl <i>a</i> / POC.	96
7.16	Seasonality of POC concentration.	97
7.17	Seasonality of DOC concentration.	97
8.1	C:N ratio of suspended particulate matter.	101
8.2	The amount of inorganic carbon in particulate matter.	102
8.3	C:N ratios derived from changes in nutrient concentrations.	105
8.4	C:P ratios derived from changes in nutrient concentrations.	108
8.5	N:P ratios derived from changes in nutrient concentrations.	110
8.6	C:Si ratios derived from changes in nutrient concentrations.	112
8.7	N:Si ratios derived from changes in nutrient concentrations.	113
8.8	Si:P ratios derived from changes in nutrient concentrations.	114
9.1	Sampling locations of POM isotope samples.	116
9.2	Seasonality of $\delta^{13}\text{C}(\text{POC})$	117

9.3	Seasonality of $\delta^{15}\text{N}(\text{PON})$	118
9.4	Seasonality of ϵ_{p}	119
9.5	Parametrization of ϵ_{p}	120
9.6	Comparison of different ϵ_{p} parametrizations.	122
11.1	Wind speed, $f\text{CO}_{2,\text{ATM}}$ and $\delta^{13}\text{C}(\text{CO}_{2})_{\text{ATM}}$	132
11.2	Latitudinal variations in the data.	132
11.3	Average summer profiles of DIC and $\delta^{13}\text{C}(\text{DIC})$	133
11.4	Average summer profiles of nitrate, phosphate and silicate.	134

List of Tables

2.1	Fractionation factors within the marine carbon system	20
6.1	Comparison of different estimates of net community production.	72
8.1	Time range for nutrient correlation.	103
8.2	Mean C:N _{POM} and C:N _{PM}	106
8.3	Stoichiometric ratios from nutrient concentration changes.	107
8.4	Diatom abundance.	109
11.1	Overview of all crossings.	135

1 Introduction

Since the first observation of a rising carbon dioxide (CO_2) content in the atmosphere (Keeling, 1960), the Earth's carbon cycle has received particular attention. Understanding which exact processes are forcing this increase and which have the potential to weaken it has become one of the major tasks of humankind. Since the start of the industrialization in the 18th century, the carbon content in the atmosphere rose from $x\text{CO}_2 = 279$ ppmv to currently (January 2016) $x\text{CO}_2 = 402.59$ ppmv (Dlugokencky and Tans, 2016). The increase during the last decades from 355 ppmv to about 400 ppmv and the simultaneous decrease in its stable carbon isotope ratio at the atmospheric measurement site in Bermuda (32.26°N , -64.88°E) is shown in Figure 1.1. This increase is caused by the combustion of fossil fuels and emissions due to land use changes which are both mediated by the ongoing industrialization as confirmed through the isotope measurements. The annual variability of CO_2 and its stable carbon isotope ratio is mostly driven by changes in land biomass which reduces the atmospheric carbon content towards a minimum in CO_2 in late summer. The rising CO_2 in the atmosphere is only accounting for about half of the carbon that was released via fossil fuel combustion and land use changes. The other half is stored in the ocean and in vegetation and soils. The amount of carbon stored in land vegetation and soils is usually calculated as the difference between sources, remaining carbon in the atmosphere and the ocean sink (Le Quéré et al., 2015). In this approach, a better estimation of the ocean carbon sink subsequently reduces the uncertainty in the land carbon sink. Figure 1.2 shows a schematic overview of the Earth's carbon cycle. The major part of the oceanic carbon is stored in the intermediate and deep sea. The surface ocean as relative small carbon reservoir is the only connection between the deep ocean and atmosphere.

The magnitude of the ocean carbon sink, however, is highly variable and strongly depending on region, wind conditions, and the difference between atmospheric and surface ocean CO_2 partial pressure. The North Atlantic plays a major role when it comes to quantifying the oceanic carbon sink. Here, one of the highest uptake rates of CO_2 was

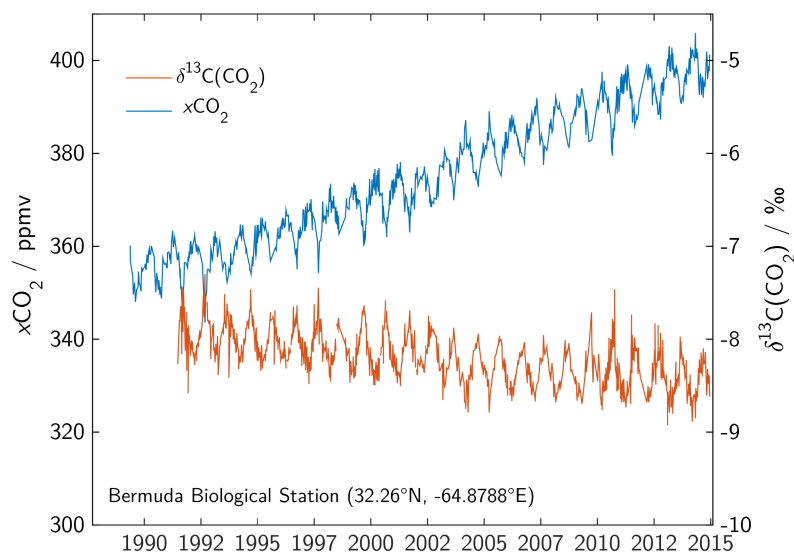


Figure 1.1: Atmospheric CO_2 concentrations and its stable carbon isotope ratio at Bermuda (data taken from "Cooperative Global Atmospheric Data Integration Project" (2015) and White et al. (2015)).

detected ($(2.2 \pm 0.7) \text{ molC m}^{-2}\text{yr}^{-1}$, (Takahashi et al., 2009; Ciais et al., 2013)). This high uptake rate is mostly driven by a large disequilibrium during the spring and summer period. For a better quantification of the North Atlantic carbon sink and a prediction of its future changes it is necessary to understand the underlying processes. When and why does the spring bloom start? How fast is biomass growing? What is supporting this growth and what slows it down? When does it run into nutrient limitation? Which role does the community structure of phytoplankton play (i.e., calcifying vs. non-calcifying phytoplankton)? How many nutrients are remineralized at which depth? Which influence has the the maximum winter depth for the nutrient budget and, consequently, the productivity of the following productive season? How does this picture change spatially, but also in response to interannual climate variability or long term processes such as climate change? Many scientists are working towards finding answers to these questions by doing field measurements, lab experiments or model studies. In addition, much effort is being made to improve the understanding of the gas exchange velocity and its relationship with the wind or an organic microlayer covering the surface ocean (Wanninkhof et al., 2009).

Another approach considers the establishment of a widespread observation system for

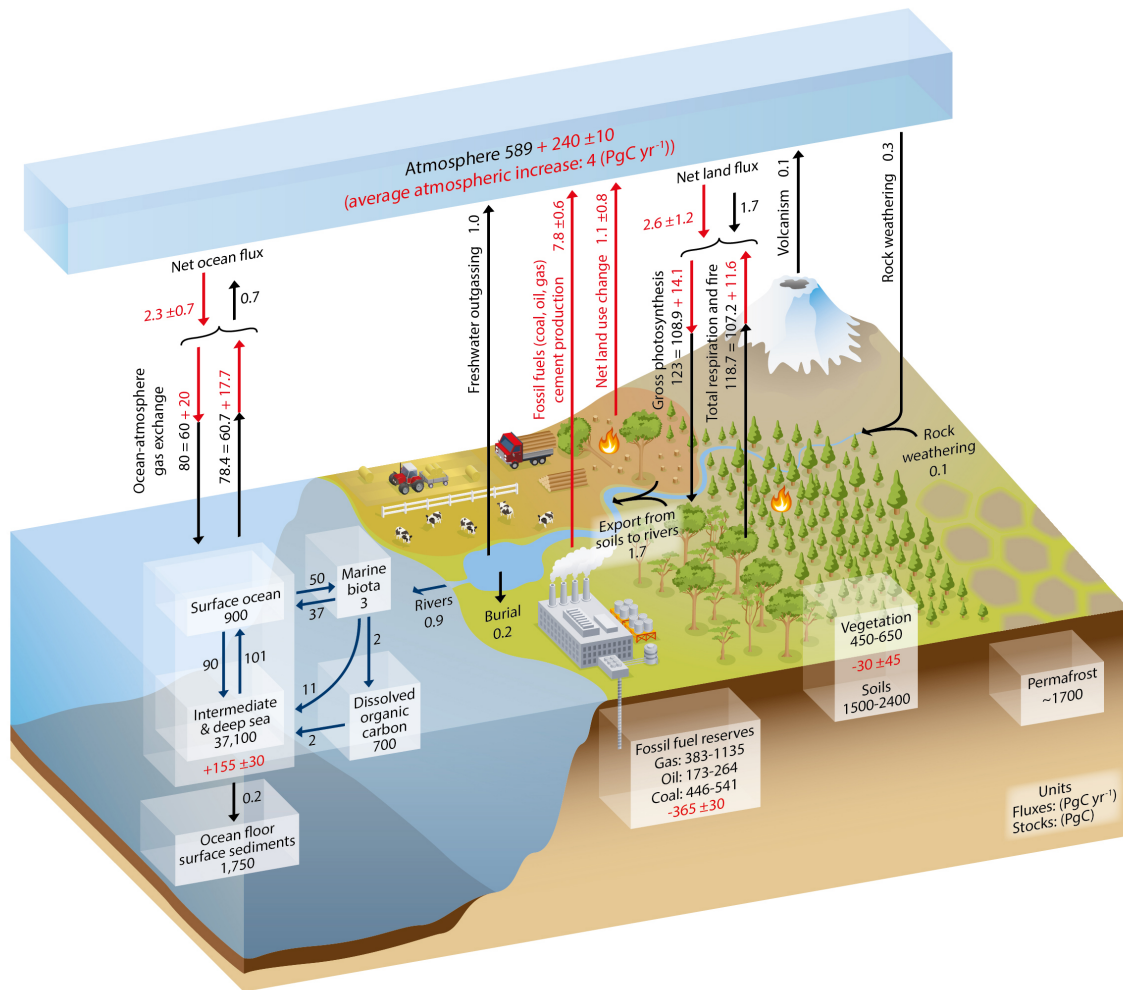


Figure 1.2: The global carbon cycle and the size of its reservoirs and annual fluxes. Black numbers denote the preindustrial conditions and red numbers account for the respective anthropogenic influences as average over the years 2000-2009. Arrows show the annual fluxes between different reservoirs (Ciais et al., 2013).

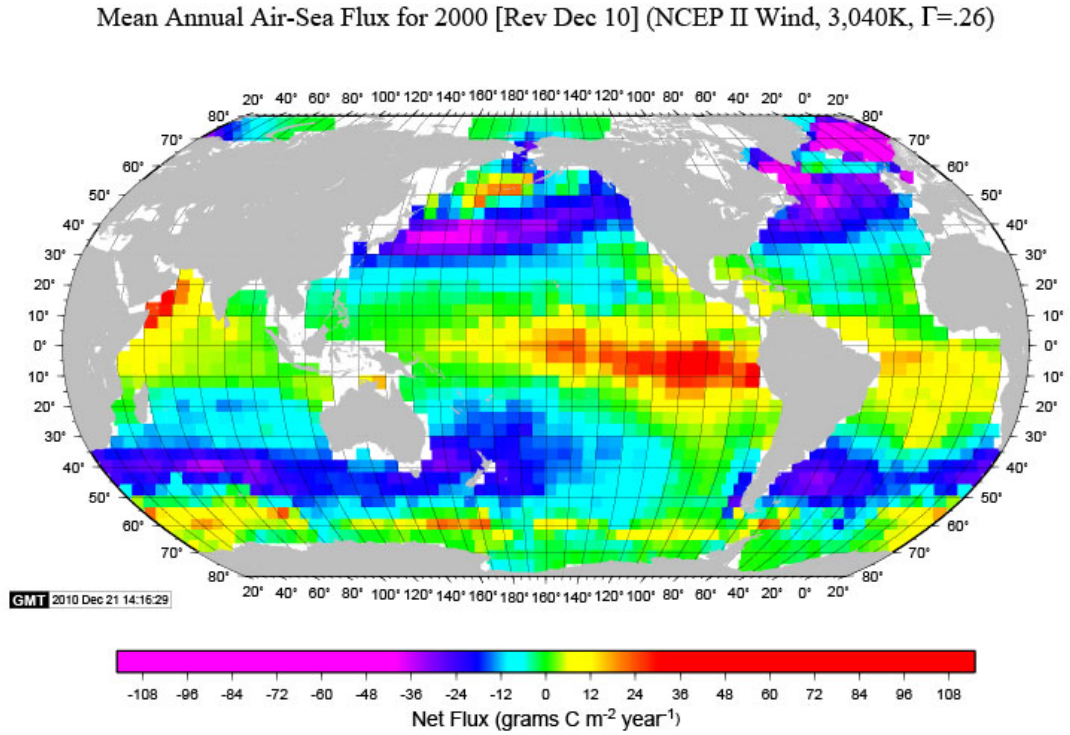


Figure 1.3: Net the air-to-sea CO₂ flux as estimated from surface ocean $p\text{CO}_2$ measurements (Takahashi et al., 2009).

CO₂ dynamics in the surface ocean. Using commercial ships for investigating ocean and atmosphere is a relatively efficient method that has already been used for meteorological measurements and monitoring changes in plankton abundances (Reid et al., 2003). Since the possibility of autonomous measurements of surface water CO₂ was developed, a network of Voluntary Observing Ships (VOS) has been established and equipped with measurement systems for CO₂ partial pressure ($p\text{CO}_2$). The data from this network has been combined, quality controlled and provided the basis for calculating a climatology of seawater $p\text{CO}_2$ and the corresponding annual air-to-sea fluxes (Takahashi et al., 2009; Watson et al., 2009). Up until now, this data compilation is continuously growing and provides the possibility to have a look on interannual variations in the air-to-sea CO₂ flux (Bakker et al., 2014; Landschützer et al., 2014).

Measuring $p\text{CO}_2$ alone, however, does not give a complete picture. Consistent datasets

have also been developed for other relevant parameters such as the total dissolved inorganic carbon (DIC), total alkalinity (TA), nutrients and the stable carbon isotope ratio of DIC $\delta^{13}\text{C}(\text{DIC})$ (Olsen et al., 2016; Becker et al., 2016). Isotope measurements can improve the understanding of complex systems since each process has a different impact on the respective isotopomers. The measurement of stable carbon isotopes in DIC, for example, has been used as tracer for net community production and anthropogenic carbon (Körtzinger et al., 2003; Quay et al., 2009). However, the applicability of this parameter was always limited due to an insufficient temporal and spatial data resolution. With the ongoing development of high resolution spectrometric methods, new measuring systems became available. Robust and sensitive cavity ringdown analyzer provide the possibility of autonomous isotope measurements directly onboard a vessel. By combining these instruments with the VOS network, the spatial and temporal resolution of isotope data can be significantly improved.

The aim of this work is to draw a full picture of surface ocean carbon and nutrient dynamics in the North Atlantic. Therefore, full annual cycles of stable carbon isotope ratio of surface water CO_2 have been measured on a VOS sailing routinely between Liverpool, UK and Halifax, Canada. The changes in the stable carbon isotope ratio were compared to continuous measurements of the fugacity of carbon dioxide ($f\text{CO}_2$) and discrete samples of inorganic and organic carbon parameter and nutrients. By setting up a small box model, the seasonal influences of air-sea gas exchange, net community production and convective mixing on the carbon and nutrient cycles in surface water have been calculated.

At first, an internally consistent dataset of the stable carbon isotope ratio of DIC in the North Atlantic Ocean is presented (Chapter 4). In Chapter 5, the obtained underway data of surface ocean $f\text{CO}_2$ and its stable carbon isotope ratio ($\delta^{13}\text{C}(\text{CO}_2)$) from 2012 to 2015 will be presented and its interannual variability will be interpreted. Chapter 6 describes the outcome of a simple box model and the magnitude of air-sea gas exchange, net community production and convective mixing across the North Atlantic. In the following, the seasonal changes in seawater $f\text{CO}_2$ and $\delta^{13}\text{C}(\text{CO}_2)$, DIC, $\delta^{13}\text{C}(\text{DIC})$, TA, chlorophyll *a*, particulate and dissolved organic matter, nitrate, phosphate, silicate and nitrite will be discussed. The stoichiometric composition of the produced particulate matter and the relative consumption of DIC, nitrate, phosphate and silicate will be addressed in Chapter 8. Eventually, some insight into the variability of stable isotopes in particulate carbon and nitrogen ($\delta^{13}\text{C}(\text{POC})$ and $\delta^{15}\text{N}(\text{PON})$) and the fractionation

between particulate organic carbon and CO₂ during carbon fixation will be given.

2 Scientific background

2.1 Properties of the North Atlantic Ocean

The study region, the North Atlantic between 40 and 60 °N, shows both, subpolar and subtropical influences. According to Longhurst (2007) the surface water can be divided into different biogeographical provinces of comparable ecology, the Gulf Stream province (GFST), the Northwest Atlantic Shelves (NWCS) and the North Atlantic Drift (NADR). The mean surface velocity and flow direction for the years 2012-2014 for this region as well as the provinces are shown in Figure 2.1.

The GFST province is located in the western part and characterized by warm and saline water masses that are transported northeastwards by the 'Gulf Stream'. The Gulf Stream forms in the Gulf of Mexico, follows north the American coast and finally turns east into the North Atlantic. The position at which it leaves the coast as well as its strength is varying slightly during the year, with the northernmost position occurring in fall and a more southward position in winter and early spring (Auer, 1987; Frankignoul et al., 2001). The water transport is highest in fall and lowest in spring (Zlotnicki, 1991; Hogg and Johns, 1995). The Gulf Stream shows a significant meandering which changes from a single branch to multiple fronts once it reaches the Grand Banks and shows a high amount of eddy activity. Here it meets the western boundary current of the subpolar gyre, the Labrador Current, which transports cold and relatively fresh water out of the Labrador Sea and forms at the front a region with high kinetic energy. At any time of the year cold, cyclonic eddies at the seaward side of the front and warm, anticyclonic eddies on the shore side can be observed. These eddies can be 1000 – 3000 m deep and 100 – 300 km wide (Frankignoul et al., 2001). The cold water side is representing the northern part of the NWCS province which covers the entire US coast between the Florida Keys and the Street of Belle Isle.

The continuation of the northward branch of the Gulf Stream which is intensified by mixing with the Labrador Current, is the North Atlantic Current (NAC). Most of it

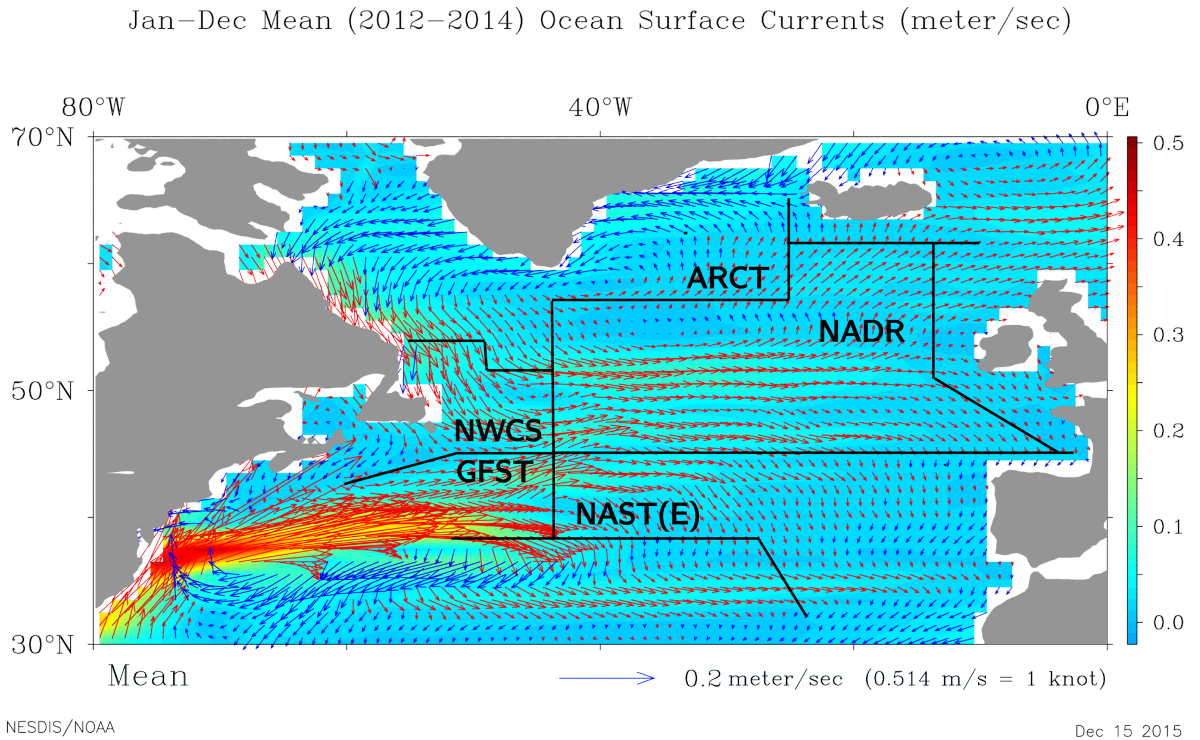


Figure 2.1: Mean surface currents from 2012-2014 and the Longhurst. The arrows indicate the velocity and the flow direction (red: eastwards, blue: westwards) (Bonjean and Lagerloef, 2002). According to Longhurst (2007) the different biogeographical provinces are shown (NWCS: Northwest Atlantic Shelf, GFST: Gulf Stream, ARCT: Atlantic Arctic, NADR: North Atlantic Drift, NAST(E): Northeast Atlantic subtropical gyre).

flows north until about 52°N , forms a loop and then turns east (Krauss et al., 1987). The other part of the NAC flows directly in northeastern direction. Around 30°W the NAC turns into the North Atlantic Drift Current (NADC) which is slowly moving northeastwards, feeding the currents of the Nordic Seas. The southern boundary of the NADC is formed by the eastwards flowing southern branch of the NAC which is the northern part of the subtropical gyre.

It could be seen that climate variations such as the North Atlantic Oscillation (NAO) can induce latitudinal variations of the Gulf Stream and can influence the timing of the spring bloom (Henson et al., 2009b) as well as the abundance of certain plankton species (Hays et al., 1993; Borkman and Smayda, 2009). The mostly wind driven NADC is also influenced by changing wind patterns, which themselves depend on the NAO (Bigg

et al., 2005).

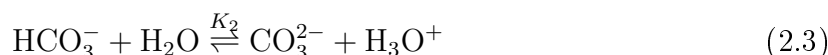
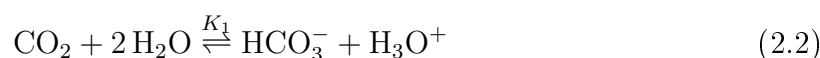
The biological seasonality of the sampling region is mainly driven by deep convection in winter time which transports nutrients to the surface and a distinct spring bloom during which the nutrients are more or less completely depleted. In the western part, where the winter convection is not as deep, eddies and turbulence at the front of Labrador Current and Gulf Stream play a significant role in nutrient supply. The onset of the spring bloom can vary by one month between the south and the north of the sampling area but has been shown to start way before a complete stratification is reached (Colebrook, 1982). For the eastern North Atlantic it was observed that first a diatom-dominated bloom is developing, which then is followed by flagellates after silicate depletion has occurred (Sieracki et al., 1993; Lochte et al., 1993). Data from Continuous Plankton Recorder (CPR) measurements indicate a southwards decreasing spring bloom intensity and increasing fall bloom intensity (Colebrook, 1979). In the frontal region of the Labrador Current and Gulf Stream the stratification develops earlier than in the surrounding water masses. Due to this fact and a continuous nutrient supply by upwelling the bloom can persist longer and intensified (Ferrari et al., 2015). In the eastern part of the North Atlantic, also a small bloom in fall can be observed. The extent to which nutrients are depleted at the end of spring bloom and deepening of the mixed layer can trigger a bloom at the end of the summer is increasing towards the south (Chiswell et al., 2015).

The composition of biomass in the ocean follows a relatively fixed stoichiometric ratio of C:N:P = 106:16:1, the so called Redfield ratio (Redfield, 1958). However, this is only a mean value and the composition of newly produced phytoplankton biomass can deviate widely from this ratio (Körtzinger et al., 2001). This can happen by processes such as nitrogen fixation and denitrification (Gruber and Deutsch, 2014), or a shift in internal lipid structure from phospholipids to other lipids under phosphate limitation (Geider and Roche, 2002). Moreover, different responses to nutrient limitation combined with species shifts as well as different measurement techniques lead to a wide range of reported element ratios for ocean biomass (Koeve, 2006).

2.2 Carbonate system

Inorganic carbon in the ocean can appear in several different forms. When atmospheric CO_2 dissolves in the ocean ($\text{CO}_{2,\text{aq}}$) it can react with water by forming true carbonic

acid (H_2CO_3), which then can dissociate to bicarbonate (HCO_3^-) and carbonate ions (CO_3^{2-}). For describing the speciation of dissolved inorganic carbon in the ocean, the entire inorganic carbon system has to be taken into account. The two electrically neutral forms of dissolved CO_2 are usually combined and here denoted by CO_2 . The following equilibria govern the marine CO_2 system.



Here, K_0 is the Henry constant for carbon dioxide in seawater and K_1 and K_2 the dissociation constants of carbonic acid in seawater. Please note, that all constants used in this thesis are related to the respective concentrations and not activities in seawater. Because of that, they depend on temperature, salinity and pressure (Mehrbach et al., 1973; Lueker et al., 2000; Millero et al., 2002).

In typical seawater at a pH around 8, bicarbonate is the dominant species ($[\text{HCO}_3^-] : [\text{CO}_3^{2-}] : [\text{CO}_2] \simeq 86.5\% : 13\% : 0.5\%$) (Zeebe and Wolf-Gladrow, 2005). The variations within the CO_2 system are usually described by four different parameters, fugacity of carbon dioxide ($f\text{CO}_2$), pH, total alkalinity (TA), and total dissolved inorganic carbon (DIC). By knowing two of these, the other two can be calculated.

Parameters describing the carbonate system

The amount of carbon dioxide in seawater is usually expressed as fugacity ($f\text{CO}_2$) or partial pressure ($p\text{CO}_2$) of carbon dioxide in a gas phase that is in equilibrium with the seawater. The fugacity considers also the non-ideal behavior of CO_2 in air and, therefore, is the more accurate parameter. It can be determined from the equation of state.

$$\ln\left(\frac{f\text{CO}_2}{p}\right) = \ln(x\text{CO}_2) - \times \frac{1}{RT} \int_0^p \left[\frac{RT}{p} - V_m(p) \right] dp \quad (2.4)$$

where p is the pressure, $x\text{CO}_2$ the mole fraction, V_m the molar volume of carbon dioxide, R the gas constant and T the absolute temperature. A good approximation for real gases is given by an empirical power series expansion, the virial equation (Eq. 2.5).

$$\frac{pV_m}{RT} = \frac{B(x, T)}{V_m} + \frac{C(x, T)}{V_m^2} + \dots \quad (2.5)$$

where B and C are called virial coefficients and both are functions of temperature. Neglecting higher order terms leads to a simple expression for the fugacity of pure CO_2 by inserting Eq. 2.5 in Eq. 2.4:

$$f_{\text{CO}_2} = x_{\text{CO}_2} \times p \exp\left(\frac{B_{\text{CO}_2}}{V_m}\right) \quad (2.6)$$

The second virial coefficient B_{CO_2} considers the interactions between two molecules of the same type. When investigating a gas mixture, the cross-virial coefficient δ_{CO_2} has to be taken into account, which considers the interactions between molecules of different type (Guggenheim, 1950).

The pH is the negative common logarithm of the H^+ -ion concentration and, therefore, represents the thermodynamic state of all acid-base-systems in the seawater. In the marine environment it is reported in three different scales (total scale, seawater scale, and free scale). They depend on different consideration of protonated species of sulphate and fluoride ions and can be converted among each other.

The alkalinity is related to the charge balance of seawater. It is defined as the number of moles of hydrogen ion equivalent to the excess of proton acceptors over proton donors in one kilogram of sample. (Dickson, 1992; Wolf-Gladrow et al., 2007)

$$\begin{aligned} \text{TA} = & [\text{HCO}_3^-] + 2[\text{CO}_3^{2-}] + [\text{B}(\text{OH})_4^-] + [\text{OH}^-] \\ & + [\text{HPO}_4^{2-}] + 2[\text{PO}_4^{3-}] + [\text{H}_3\text{SiO}_4^-] + [\text{NH}_3] + [\text{HS}^-] \\ & - [\text{H}^+]_{\text{F}} - [\text{HSO}_4^-] - [\text{HF}] - [\text{H}_3\text{PO}_4] \end{aligned} \quad (2.7)$$

with $[\text{H}^+]_{\text{F}}$ referring to the free pH-scale.

The dissolved inorganic carbon represents the mass balance of the carbon system as it is the sum of the concentrations of all dissolved inorganic carbon species.

$$[\text{DIC}] = [\text{CO}_2] + [\text{HCO}_3^-] + [\text{CO}_3^{2-}] \quad (2.8)$$

Processes driving the carbonate system

Processes influencing the oceanic carbonate system such as air-sea gas exchange of CO_2 , primary production or calcification influence these four carbon parameter in a different way. Figure 2.2 shows these different influences as a function of DIC and TA. At different depths in the ocean different processes are important. At the surface CO_2 can enter the ocean from the atmosphere, resulting in increasing the DIC concentration and decreasing the pH. The outgassing of CO_2 into the atmosphere has opposite effects.

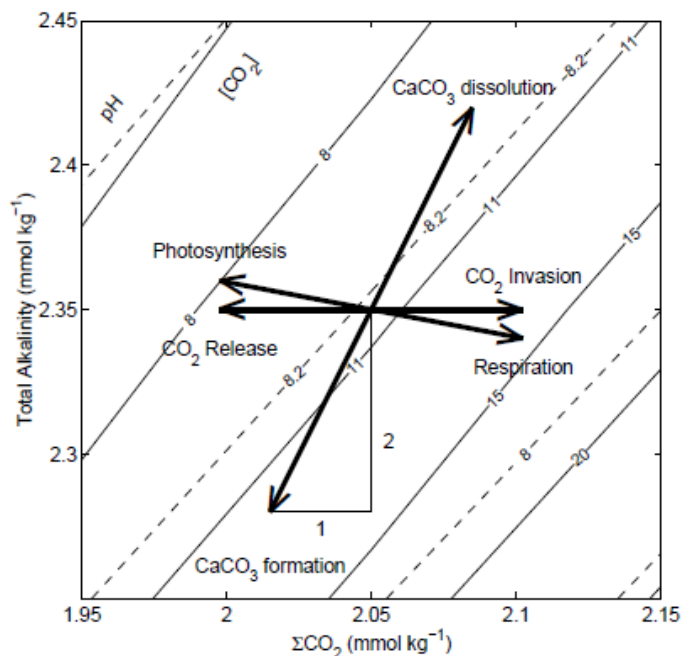


Figure 2.2: Effects of different processes (air-sea gas exchange, photosynthesis, respiration, dissolution and formation of CaCO_3) on the carbon system parameters in the ocean. The solid and dashed contours indicate different levels of CO_2 concentrations and pH as a function of DIC and TA, respectively. The arrows show the respective influence of each process on DIC, TA, $p\text{CO}_2$ and pH (Zeebe and Wolf-Gladrow, 2005).

The production of biomass leads to a decrease in DIC concentration and a small increase of TA due to the consumption of other nutrients such as nitrate and a concurrent uptake of H^+ .

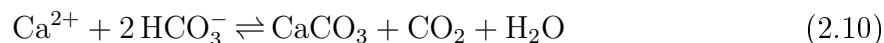
The air-sea gas exchange is driven by the fugacity difference of CO_2 between the atmosphere ($f\text{CO}_{2,\text{ATM}}$) and the ocean ($f\text{CO}_{2,\text{SEA}}$). The atmospheric $f\text{CO}_2$ undergoes only relatively small changes throughout the year since it is well mixed. In contrast to that, the oceanic $f\text{CO}_2$ can show a higher variability caused by the contribution of various physical, biological and chemical processes such as temperature changes, vertical and horizontal mixing, air-sea gas exchange or primary production. However, the actual exchange flux between ocean and atmosphere is limited by the turbulence at the

interface. The flux between atmosphere and ocean is expressed as

$$F_{\text{CO}_2} = k \times K_0 \times (f\text{CO}_{2,\text{ATM}} - f\text{CO}_{2,\text{SEA}}) \quad (2.9)$$

where K_0 is the solubility of CO_2 in seawater (Weiss, 1974) and k the gas transfer velocity. The gas transfer velocity is commonly related to wind speed (Wanninkhof, 1992; Wanninkhof et al., 2009; Nightingale et al., 2000) but is also be effected by waves, bubbles or surfactants which can lead to deviations from the wind speed relationship especially under intense bloom conditions with a high surfactant concentration.

The exchange of CO_2 between the surface ocean and deeper water masses is driven by different biologically or physically driven pumps. The 'solubility pump', or 'physical pump' transports the CO_2 by subduction of water masses and convective mixing. Biological processes are divided due to their different influences on the carbon system (see Figure 2.2) into the 'soft tissue pump' and the 'hard tissue pump'. The 'soft tissue pump' (also 'organic carbon pump') represents the production of particulate organic carbon in the productive area which partly sinks to deeper water masses where it is remineralized and released in the form of CO_2 . This process removes fixed carbon from the air-sea interface and therefore reduces the CO_2 concentration at the surface. The 'hard tissue pump' is based on the formation of particulate inorganic carbon, mainly calcium carbonate, which then sinks into the deep ocean, where it can be either buried or dissolved. In contrast to the soft tissue pump the biological production of calcium carbonate leads to an increase of CO_2 concentrations in the productive zone.



2.3 Stable isotopes of carbon and nitrogen

The different abundances of stable isotopes in chemical substances give us the possibility to distinguish between different biological and physical processes such as biological uptake, remineralization, air-sea gas exchange or fossil fuel burning.

The isotope composition of a material concerning a given element is usually described as the molar ratio of the heavier to the lighter isotope, ν_R , with ν_h being the mass number of the heavier isotope and ν_l the mass number of the lighter isotope. For the

two stable carbon isotopes this yields:

$${}^{\nu}\text{R} = \frac{{}^{\nu}\text{hC}}{{}^{\nu}\text{lC}} = \frac{{}^{13}\text{C}}{{}^{12}\text{C}} \quad (2.11)$$

The common expression to report isotopic abundances in environmental science is the δ notation. For this, the isotopic ratio of the sample substance is expressed as per mil deviation from that of a reference material.

$$\delta^{\nu} = \left(\frac{{}^{\nu}\text{R}_{\text{sample}}}{{}^{\nu}\text{R}_{\text{reference}}} - 1 \right) \times 10^3 \quad (2.12)$$

For carbon, this reference material is Pee-Dee-Belemnite (PDB) with a molar ratio of ${}^{13}\text{R}_{\text{PDB}} = 0.0112372(\pm 3)$ (Craig, 1957). This reference substance stems originally from a limestone from a marine fossil, *Belemnitella americana*, sampled at the Pee Dee formation in South Carolina, USA. However, caused by the limited availability of this today artificial standard materials such as Vienna Pee-Dee-Belimmnite (V-PDB) are used. For nitrogen, atmospheric nitrogen is used as reference material.

Most chemical reactions or phase transitions alter the isotopic ratio of a substance which is called fractionation. The fractionation between two chemical or physical states A and B can be expressed by the fractionation factor ${}^{\nu}\alpha_{(\text{A-B})}$.

$${}^{\nu}\alpha_{(\text{A-B})} = \frac{{}^{\nu}\text{R}_{\text{A}}}{{}^{\nu}\text{R}_{\text{B}}} \quad (2.13)$$

Since changes in biological isotope distribution are usually very small, the fractionation factor can also be expressed in ‰ according to the δ notation.

$${}^{\nu}\epsilon_{(\text{A-B})} = \left(\frac{{}^{\nu}\text{R}_{\text{A}}}{{}^{\nu}\text{R}_{\text{B}}} - 1 \right) \times 10^3 \quad (2.14)$$

Providing that α is close to unity, ϵ can be approximated by the difference of the $\delta^{13}\text{C}$ values of the two species:

$$\epsilon_{(\text{A-B})} = \frac{\delta_{\text{A}}^{\nu} - \delta_{\text{B}}^{\nu}}{1 + \delta_{\text{B}}^{\nu} \times 10^{-3}} \approx \delta_{\text{A}}^{\nu} - \delta_{\text{B}}^{\nu} \quad (2.15)$$

Fractionation Processes

With most changes in the chemical or physical state of a substance comes an isotopic fractionation. This is caused by the different mass of both isotopomers which induces small differences in their chemical and physical behavior. The fractionation processes can

be divided into chemical and physical kinetic fractionation which occur during incomplete transformations of transport processes and equilibrium fractionation at a chemical or physical equilibrium.

The fractionation in a thermodynamically equilibrated system, e.g. the reactions of the inorganic carbon species in the ocean or, more or less, the air-sea gas exchange, is called equilibrium fractionation. This fractionation is a consequence of different zero-point energies of both isotopomers at each side of the equilibrium. The difference between the zero-point energies of the two isotopomers is increasing with increasing zero-point energies, or, in other words, is larger the stronger this element is bound in the molecule. This leads for example to an enrichment of ^{13}C in bicarbonate and carbonate relative to carbon dioxide.

During incomplete reactions or transport processes kinetic fractionation can occur. The chemical kinetic fractionation arises from the mass dependence of reaction rates. It occurs only during incomplete reactions or when the product of the reaction is removed from the system. Basically all isotope effects during biological uptake and remineralization are kinetic. The reaction of the lighter isotopomer is usually slightly faster which comes from a smaller difference of the zero-point energies of the reactant and the transition state. The magnitude of the fractionation is determined by the ratio of the rate constants of the two isotopomers.

Physical kinetic fractionation occurs for example during diffusion processes or phase transitions. During diffusion the fractionation occurs because of the mass dependence of a molecules mobility. For two isotopomers having the same kinetic energy, the lighter molecule moves faster and, thus, has a higher diffusion coefficient. The fractionation is then given by the ratio of both diffusion coefficients.

The effect of kinetic fractionation while material is removed from the system is called Rayleigh process. This fractionation occurs, for example, during the assimilation of nutrients during phytoplankton growth. During a kinetic fractionation process the remaining reactant gets continuously enriched in the heavier isotopomer. With a constant fractionation factor this leads to a constant increase of the instantaneous isotope ratio in the product. When the reaction is complete no net fractionation between the reactant and the accumulated product remains. The isotope ratio of the residual reactant (${}^{\nu}\text{R}_{\text{res}}$) can be calculated using the fractionation factor α , the fraction f of the remaining

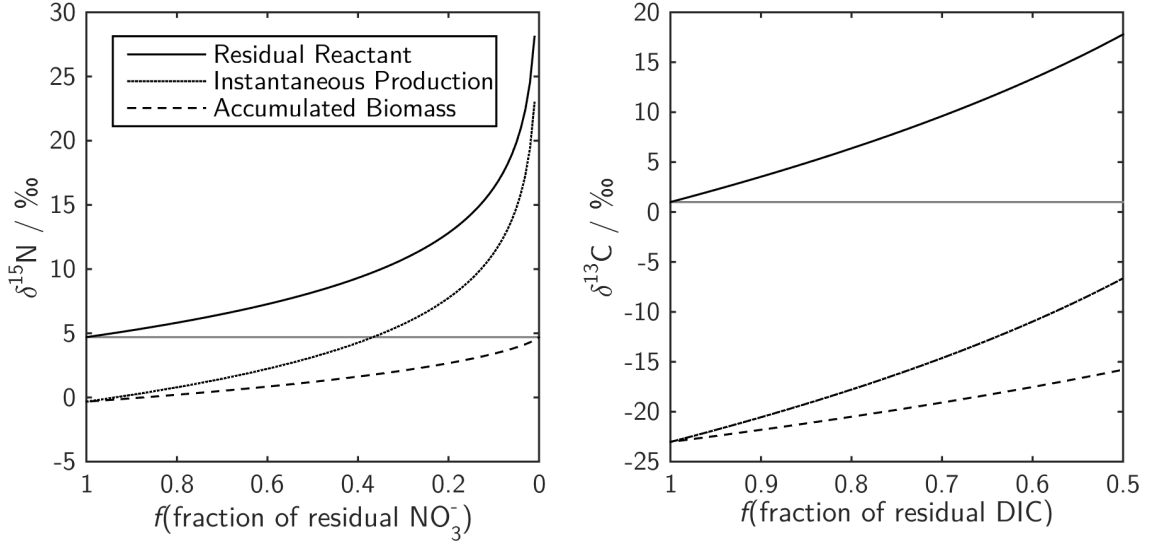


Figure 2.3: Rayleigh fractionation process during primary production from nitrate (left hand) and DIC (right hand). The change in the abundance of ^{15}N ($\delta^{15}\text{N}$) is shown for nitrate, the accumulated biomass and the instantaneous produced biomass with a fractionation between nitrate and biomass of ($\epsilon = -5 \text{‰}$). When the nitrate is consumed completely ($f=0$), the accumulated biomass has the same isotopic signature as the initial nitrate. The same is also shown for the change in ^{13}C of DIC and biomass, respectively ($\delta^{13}\text{C}$). For the fractionation between DIC and organic matter a constant value of $\epsilon = -24 \text{‰}$ was used.

reactant and the isotope ratio (${}^\nu R_0$) at $t = 0$:

$${}^\nu R_{\text{res}} = f^{(\alpha-1)} \times {}^\nu R_0 \quad (2.16)$$

From this, the instantaneous isotope ratio of the product ${}^\nu R_{\text{inst}}$ follows as:

$${}^\nu R_{\text{inst}} = \alpha \times f^{(\alpha-1)} \times {}^\nu R_0 \quad (2.17)$$

Finally, the isotope ratio of the accumulated product ${}^\nu R_{\text{acc}}$ can be calculated as:

$${}^\nu R_{\text{acc}} = \frac{f^\alpha - 1}{f - 1} \times {}^\nu R_0 \quad (2.18)$$

For the consumption of nitrate and DIC by phytoplankton the development of the different isotope ratios of ^{15}N and ^{13}C is shown in Figure 2.3. For nitrogen isotopes in the ocean this process is very important because the reservoir of inorganic nitrogen can be

completely consumed during bloom events. A sufficient change in the DIC pool to alter the isotopic composition in a significant way only occurs during very intense blooms.

Natural abundance and fractionation in the marine carbon system

The abundance of stable isotopes in the environment can vary a lot along the different components and processes. The stable carbon isotope ratio in materials that are important for the marine carbon cycle are shown in Figure 2.4. In preindustrial times, the atmosphere had a stable carbon isotope ratio of about -6.3‰ (Tagliabue and Bopp, 2008). The combustion of fossil fuels since the beginning of the industrial revolution, which reveal the relative low $\delta^{13}\text{C}$ value of their biological origin (about -23‰), leads to a continuous lightening of the atmospheric carbon along the increase of carbon dioxide in the atmosphere to values below -8‰ today (Keeling et al., 1995). This decrease was first recorded by H. Suess and is called ^{13}C Suess effect (Keeling, 1979). Caused by the equilibration processes between atmosphere and ocean, the lightening of atmospheric carbon can also be observed in the marine inorganic carbon, here known as oceanic Suess effect. The DIC is changing by about $(-0.24 \pm 0.02)\text{‰}$ per decade (Quay et al., 2003; Körtzinger et al., 2003). The typical $\delta^{13}\text{C}$ of DIC in the ocean lies between 0‰ and 2‰ (Quay et al., 2003). However, during intense bloom events these values can be clearly exceeded. This increase is a result of the fractionation that is occurring during biological carbon fixation. The isotopic composition of organic carbon in plants varies between -32‰ and -22‰ depending on the exact mechanism of carbon fixation and other effects such as the temperature dependence of fractionation. Marine carbonates such as the CaCO_3 shells of coccolithophores show an isotopic signature close to that of DIC.

The fractionation within the marine carbonate system can be described by equilibrium fractionation. Since an equilibrium reaction can be divided into reactions of ^{13}C and ^{12}C and the fractionation factor can be described using the equilibrium constants, this fractionation factor is temperature and salinity dependent. Moreover, some metal ions who are capable of building carbonate complexes in seawater, such as Mg^{2+} , can influence the fractionation factors in natural seawater compared to those determined in artificial seawater. Unfortunately, there are only a few studies available that focus on the fractionation between DIC and the different carbon species in seawater. Besides temperature and salinity, the overall fractionation between DIC and gaseous CO_2 depends also on the relative abundance of the different species inside the carbon system and,

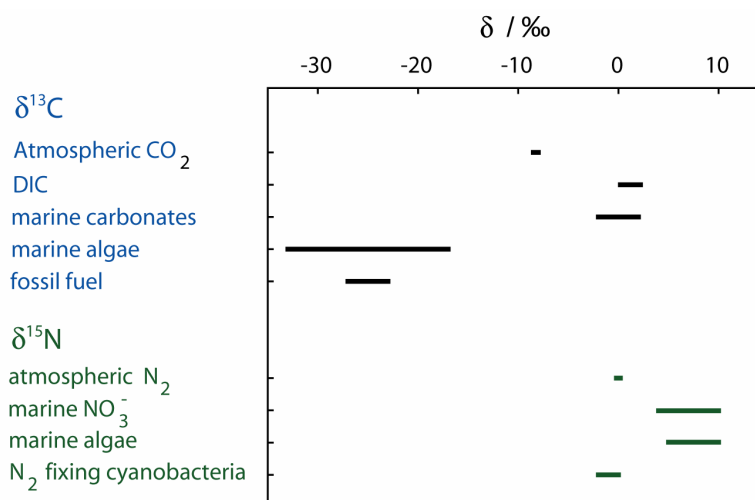


Figure 2.4: Isotopic composition of carbon and nitrogen in selected materials (redrawn after Zeebe and Wolf-Gladrow (2005); Ohkouchi et al. (2015); Sigman et al. (2009)).

thus, on the pH. The fractionation factors used in this work (Zhang et al., 1995) and the temperature dependence of the fractionation between the various inorganic carbon species are shown in Table 2.1 and Figure 2.5.

The autotrophic fixation of inorganic carbon is a non-equilibrium process causing kinetic fractionation. Besides the temperature and salinity dependence, this reaction is also dependent on the pathway over which the marine phytoplankton produces its organic matter. This 2-step process can vary with the availability of carbon dioxide and nutrients and the growth rate. Usually, the carbon dioxide diffuses through the cell membrane into the cell, where it reacts with the enzyme *RubisCO* as the first step in the formation of organic matter. The first, diffusive process is a reversible equilibrium process, whereas the enzymatic reaction is irreversible. The decreasing CO₂ concentrations in the surrounding water or a high growth rate of the cell can limit the availability of carbon dioxide inside the cell and, therefore, turn the transport into the cell to being the rate determining step. In this case, the cell can activate an active transport mechanism of bicarbonate ions into the cell. The use of bicarbonate instead of carbon dioxide leads to an increased abundance of the heavier isotope in the produced organic matter caused by the higher isotope ratio of bicarbonate compared with dissolved carbon dioxide. At which level a cell activates this active transport and to which portion bicarbonate is used, is, of course, also dependent on the species. It is shown, that the

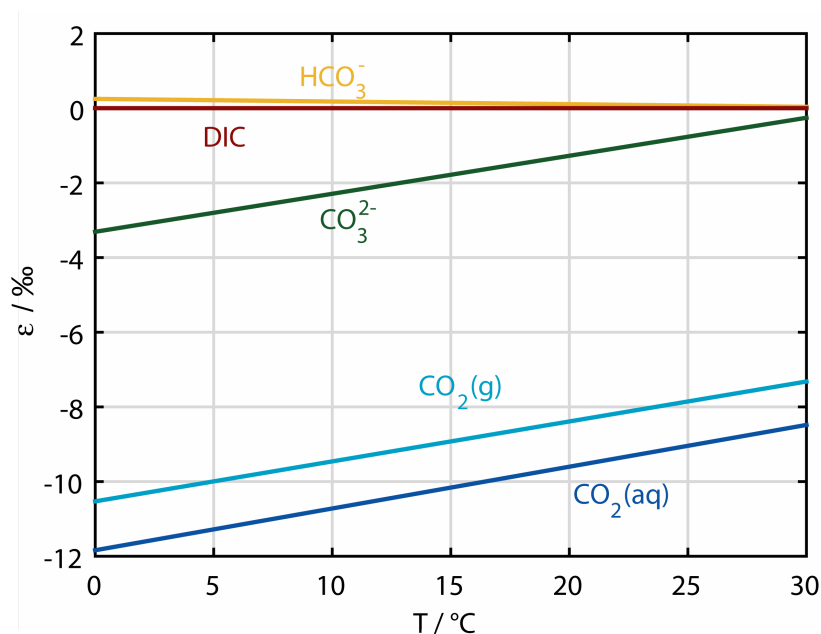


Figure 2.5: Temperature dependence of the carbon isotope fractionation between the species of the carbonate system and total dissolved inorganic carbon (DIC) (at pH=8.15) (redrawn after Zhang et al. (1995)).

fractionation of the overall carbon fixation ϵ_p correlates negatively with the growth rate, which itself is controlled by external parameters such as nutrient supply, temperature and light intensity (Takahashi et al., 1993). The more the mass transport process is the limiting process and the carboxylation happens quantitatively, the less negative the produced organic matter will be because the diffusion process induces a relatively small fractionation. The complete remineralization of organic matter is a quantitative process, leading to a release of inorganic carbon with the same isotopic signature as the organic matter.

Natural abundance and fractionation in the marine nitrogen system

Since inorganic nitrogen exists in more chemical forms in the ocean than inorganic carbon, the fractionation processes of these species among each other as well as with organic matter are more complicated. Unfortunately, the database for estimating these influences is rudimentary. Here, I will concentrate on processes that are relevant for the North Atlantic surface ocean. The abundances are shown in Figure 2.4. The dissolved N₂ is slightly enriched in ¹⁵N compared to gaseous nitrogen (Ohkouchi et al., 2015). When organic matter is produced from this nitrogen reservoir by N₂-fixation the pro-

Table 2.1: Fractionation factors within the carbon system and their temperature dependence (in °C).

Process	$\epsilon / \text{‰}$
CO ₂ invasion (ϵ_{as}) (Zhang et al., 1995)	$-0.013 \times T_C - 2.30$
CO ₂ - CO ₂ (g) (Zhang et al., 1995)	$+0.0049 \times T_C - 1.31$
HCO ₃ ⁻ - CO ₂ (g) (Zhang et al., 1995)	$-0.1141 \times T_C + 10.78$
CO ₃ ²⁻ - CO ₂ (g) (Zhang et al., 1995)	$-0.0052 \times T_C + 7.22$
DIC - CO ₂ (g) (Zhang et al., 1995)	$-0.107 \times T_C + 10.53 + 0.014 \times T_C \times f(\text{CO}_3^{2-})$
Diffusion (O’Leary, 1984; Jähne et al., 1987)	0.7 - 0.9
Carboxylation (Chikaraishi, 2014)	18 - 30

duced organic nitrogen has an isotope signature of -2 to 0‰ (Hoering and Ford, 1960; Minagawa and Wada, 1986). Nitrate has an average isotope ratio of 5‰ and is usually enriched in the photic zone due to primary production (Sigman et al., 2009). The fractionation during the nitrate assimilation of phytoplankton is about 5‰ . Since the nitrogen can be fully depleted during the spring bloom, the Rayleigh process has a large influence on the isotopic composition of nitrate and the produced organic nitrogen (see Figure 2.3). Also for nitrate, the growth rate can have a large influence on the isotopic fractionation associated with nitrate assimilation (Wada and Hattori, 1978).

2.4 Cavity Ringdown Spectroscopy

Cavity Ringdown Spectroscopy is a technique for highly accurate concentration measurements in the gas phase. The increased accuracy with respect to simple absorption techniques is based on two main factors. Using a stable optical cavity with two or more highly reflective mirrors ($R > 99.99 \%$) leads to long path-lengths of light up to several kilometers which results in an increased sensitivity of the absorption measurement. Moreover, unlike most other absorption-based methods, this technique determines the

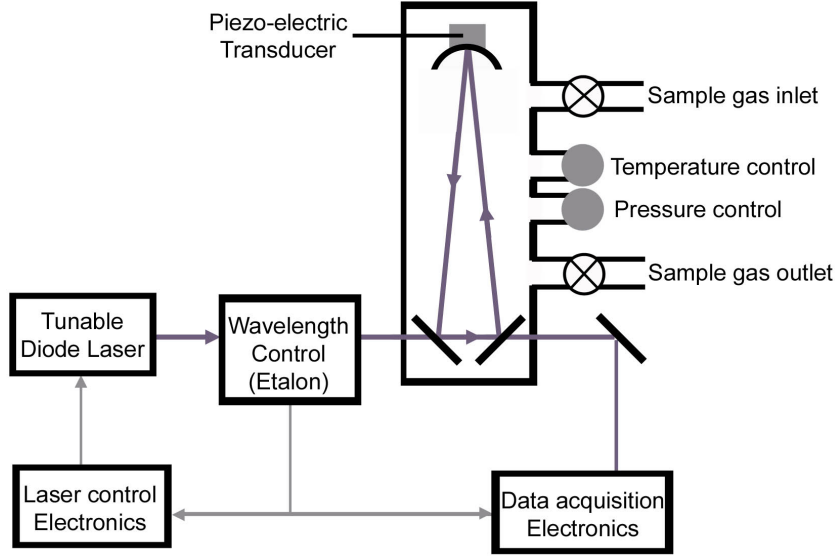


Figure 2.6: Basic setup of a CRDS experiment ("Picarro Inc.").

concentration of the target gas in the cavity by measuring the time constant of the loss of light intensity within the cavity. In the most simple setup for a CRDS experiment, a pulsed laser is coupled into a resonant optical cavity and for each laser pulse the decay time of the light intensity inside the cavity is determined by detecting the small intensity fraction leaking through the mirrors with a photodetector. This $1/e$ decay time τ is given by:

$$\tau(\nu) = \frac{t_r}{2(1 - R) + 2\alpha(\nu)L} \quad (2.19)$$

with t_r being the roundtrip time of the light within the cavity, $\alpha(\nu)$ the absorption coefficient for frequency ν , and L the cavity length. The dominant factor for the decay time of an empty cavity τ_0 is the reflectivity of the mirrors. In the presence of an absorber inside the cavity, the observed decay time of the intensity decreases. By knowing the absorption coefficient at the concrete wavelength, the concentration of the absorber can be determined from the difference between this decay time τ and τ_0 .

$$c = \frac{1}{\alpha(\nu)} \left(\frac{1}{\tau} - \frac{1}{\tau_0} \right) \quad (2.20)$$

Continuous wave CRDS (*cw*-CRDS) using a diode laser, however, requires a more complex setup (see Figure 2.6). Here, the laser beam intensity is built up in the cavity only when the laser wavelength matches the resonance frequency of a cavity mode. Mostly, this is achieved by moving one of the mirrors with a piezoelectric transducer (PZT). Once the laser is switched off the ringdown can be detected.

3 Experimental

3.1 Precise measurements of $x\text{CO}_2$ and $\delta^{13}\text{C}(\text{CO}_2)$ using CRDS

The CRDS measurements were performed using a commercial analyzer (G2131 *i*, Picarro, USA). In this instrument a tunable *cw*-diode laser with a narrow bandwidth and an emission maximum around 1600 nm is used to determine $^{12}\text{CO}_2$, $^{13}\text{CO}_2$, H_2O and CH_4 in air. The absorption spectrum of $^{12}\text{CO}_2$ and $^{13}\text{CO}_2$ which was scanned with a scan increment of 0.02 cm^{-1} is shown in Figure 3.1. The sample gas was pumped through a 3-mirror cavity by an external pump with a flow rate of about 20 mL min^{-1} . Inside the cavity, the pressure was held constant at $(140.00 \pm 0.07)\text{ torr}$, $((186.60 \pm 0.09)\text{ mbar})$, by controlling the gas flow via the inlet valve, and the temperature was locked at $(45.00 \pm 0.02)\text{ }^\circ\text{C}$. The precisions of cavity pressure and temperature were determined in the laboratory. At sea, the instrument's performance was slightly reduced, most likely due to small pressure instabilities, which were induced by the vessels vibration. The analyzer used peak heights, fitted with a Galatry line profile, instead of peak integrals to determine the sample's concentrations. This leads to a strong dependence of the measured concentration on the cavity pressure and the sample gas composition since both affect the pressure broadening of absorption lines. The analyzer was calibrated for measuring atmospheric gas and, therefore, the oxygen content was the only compound changing the gas composition. Its concentration was determined using the Galatry broadening parameter y from the analyzer's fit routine and the isotope ratio was corrected by an O_2 -calibration curve as described in Friedrichs et al. (2010) and Becker et al. (2012). The $\delta^{13}\text{C}(\text{CO}_2)$ was calculated from $x^{12}\text{CO}_2$ and $x^{13}\text{CO}_2$ which were corrected for influences of H_2O and CH_4 by internal calculation routines. An 'Allan deviation analysis' was performed for determining the precision of the analyzer and the optimal averaging time for maximal improvement of the signal to noise ratio. The Allan variance

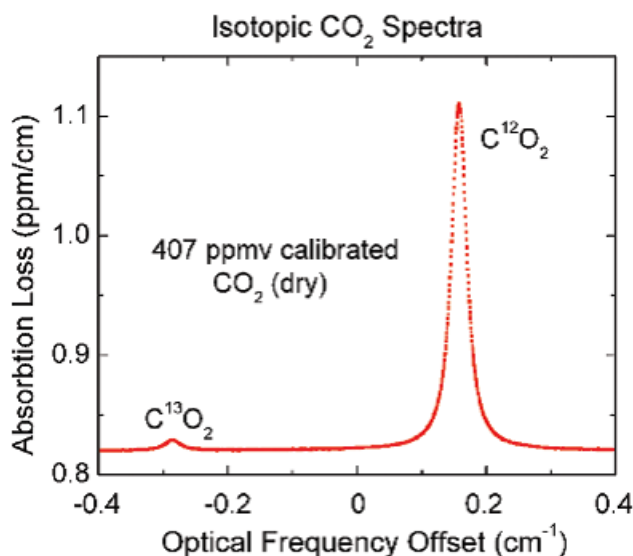


Figure 3.1: The measured absorption spectrum of $^{12}\text{CO}_2$ (6251.76 cm^{-1}) and $^{13}\text{CO}_2$ (6250.42 cm^{-1}) (van Pelt, 2008).

σ_{Allan} is defined as the average variance of two adjacent averages of a time series. In an optimal system with only statistical noise, longer averaging time would always lead to a higher precision. In reality, however, long term drifts of the instrument lead to an increase in the Allan variance. The minimum of the Allan plot (σ_{Allan} vs. averaging time τ) indicates the optimal averaging time. The result of this analysis for the $\delta^{13}\text{C}(\text{CO}_2)$ is shown in Figure 3.2. The optimal averaging time is found to be $\tau = 150\text{ min}$ yielding a precision of 0.09 ‰ , determined at $x\text{CO}_2 = 348.06\text{ ppmv}$. At higher $x\text{CO}_2$, the precision of the $\delta^{13}\text{C}(\text{CO}_2)$ measurements is improved due to a better signal-to-noise ratio.

Despite the precise temperature locking inside the cavity, the analyzer showed a strong dependence on room temperature in its measured isotope ratio as well as small influences on the measured CO_2 partial pressure. This temperature dependence is assumed to be caused by a temperature dependence of the mirror reflectivity. This effect and the dependence of the measured isotope ratio on absolute $x\text{CO}_2$ are taken care of by regular measurements of two different standard gases. The measurements were corrected towards these standard measurements by linear regression in time and $x\text{CO}_2$. As an example, the development of the standard gas measurements (at $x\text{CO}_2 = 348.06\text{ ppmv}$, $\delta^{13}\text{C}(\text{CO}_2) = -3.28\text{ ‰}$) during the westbound crossing COM 14-04 is shown in Figure 3.3. The colder room temperatures caused by colder seawater temperatures in the

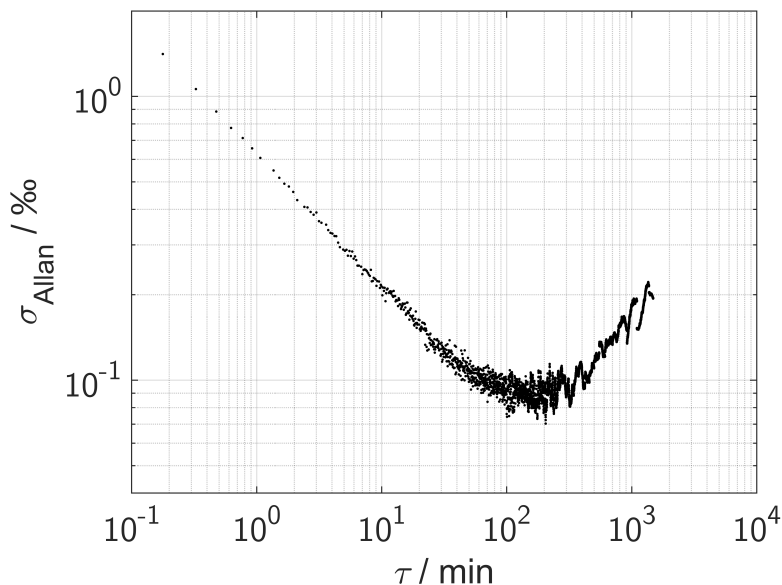


Figure 3.2: The Allan deviation of calibration gas measurements of $\delta^{13}\text{C}(\text{CO}_2)$ at $x\text{CO}_2 = 348.06$ ppmv.

last days of the crossing lead to higher isotope ratios and smaller $x\text{CO}_2$ which are corrected by linear regression between two standard measurements.

3.2 Underway measurements and data reduction of $f\text{CO}_2$ and $\delta^{13}\text{C}(\text{CO}_2)$

The data used in this study were recorded on the 'Voluntary Observing ship' (VOS) M/V Atlantic Companion (Atlantic Container Lines (ACL), New Jersey, USA), which was operating on a transatlantic route between Liverpool, UK and Halifax, Canada. The measurements used in this study were performed between January 2012 and December 2014. The extensive sampling program comprised continuous underway measurements of $f\text{CO}_2$ and $\delta^{13}\text{C}(\text{CO}_2)$ in seawater and air and discrete samples of DIC, TA, Chl *a*, POM, DOM, nitrate, phosphate, silicate, nitrite, $\delta^{13}\text{C}(\text{POC})$ and $\delta^{15}\text{N}(\text{PON})$. The tracks of the crossings and the sampling locations are shown in Figure 3.4. Whether the vessel passed Ireland on a northern or southern route was dependent on the location of the major low pressure systems, which the vessel tried to avoid, and had no seasonal pattern. In contrast to that, there was a small seasonal variation in the vessel tracks at the western

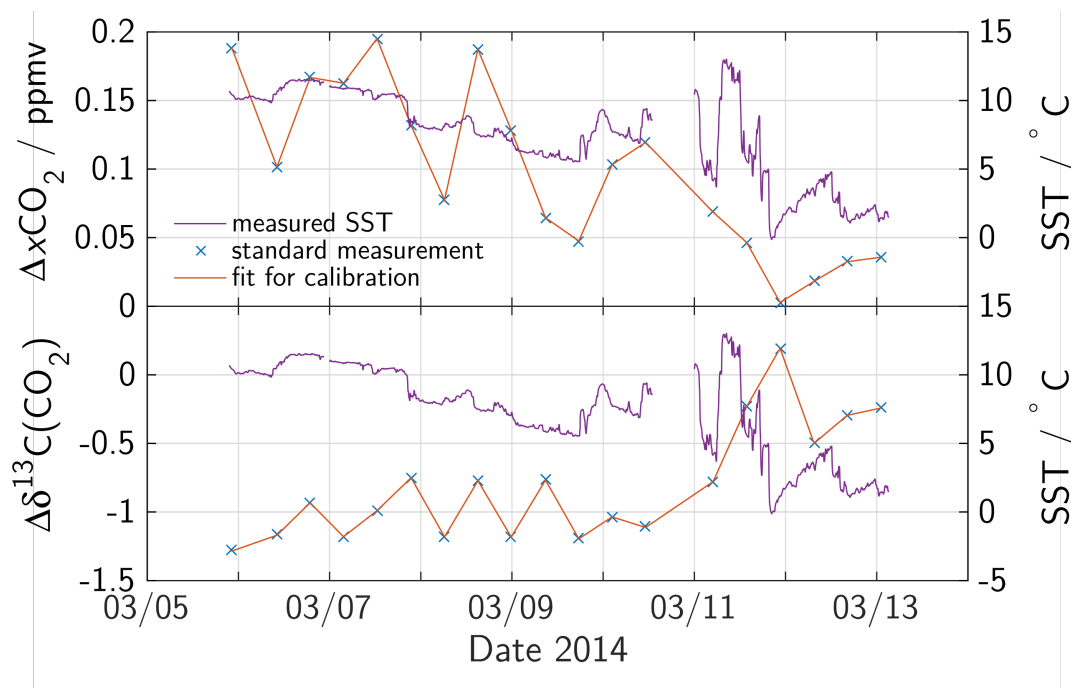


Figure 3.3: Development of standard gas measurements of $x\text{CO}_2$ (upper plot) and $\delta^{13}\text{C}(\text{CO}_2)$ (lower plot) during the westbound crossing COM 14-04 at a $x\text{CO}_2$ of 348.06 ppmv. For comparison, the measured SST is also shown.

side of the basin (west of 50°). Caused by the more southward extent of the ice border off the coast of Newfoundland in late spring and early summer, the vessel sailed more south at this time of the year, especially during 2014.

The underway unit was located in the engine room of the vessel. A schematic setup is presented in Figure 3.5. An autonomous $p\text{CO}_2$ measuring system as described in Lüger et al. (2004) and Steinhoff et al. (2010) was connected to a sea chest on port side, that was located about 250 m astern of the forecabin. On average, its water inlet was located at a depth of 9.6 m during eastbound and 10.6 m during westbound crossings as given by the vessel's draft. Directly after the water inlet the sea water temperature was measured by an external temperature sensor (SBE 38, accuracy of $\approx 0.01^\circ\text{C}$). To prevent biofouling and oxygen consumption inside the pipes, the water passed a copper electrode before it was pumped to the measuring system by a torque-flow pump. Prior to entering the $p\text{CO}_2$ measuring system, the salinity was measured by a Seabird thermosalinograph SBE 21 (accuracy: SSS: ≈ 0.1 psu, equilibrator temperature $\approx 0.01^\circ\text{C}$). The pipe length from the sea chest to the $p\text{CO}_2$ measuring system was about 4 m and the water flow rate was

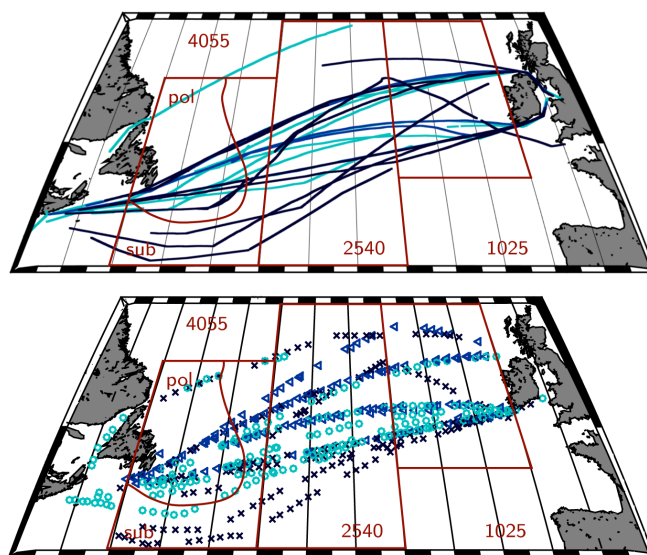


Figure 3.4: Vessel tracks of M/V Atlantic Companion and the sampling positions of underway measurements (upper panel) and discrete samples (lower panel). The location of the four boxes used in the further analysis is also illustrated. The three different years are denoted with different colors (2012: light blue/circles, 2013: mid blue/triangles, 2014: dark blue/crosses).

controlled to be at $2\text{-}3\text{ L min}^{-1}$. In the $p\text{CO}_2$ measuring system, a NDIR CO_2 analyzer (Licor 7000) was used. Downstream of the Licor, the CRDS was installed as a bypass. The gas outlet of the CRDS was redirected to the main gas flow. The CRDS pump was sealed so that its leakage was small enough to not influence the equilibration (Becker et al., 2012). The response time of the equilibrator to rapid changes in $f\text{CO}_2$ was about 2 min (Pierrot et al., 2009). The CRD analyzer was calibrated every 8 - 10 h using two standard gases with different CO_2 concentrations. Atmospheric air was also measured every 8 - 10 h. During crossings without CRDS measurements, the NDIR analyzer was calibrated every 3 h with four different standard gases as recommended by Pierrot et al. (2009). For some crossings, the SST was estimated from equilibrator temperature and water flow rate. Since the measured $f\text{CO}_2$ is very sensitive to temperature changes for these crossings only $\delta^{13}\text{C}(\text{CO}_2)$ was taken for further analysis.

The data reduction of the $f\text{CO}_2$ data was performed according to the DOE guidelines (Dickson et al., 2007) and $f\text{CO}_2$ was corrected for the temperature difference between

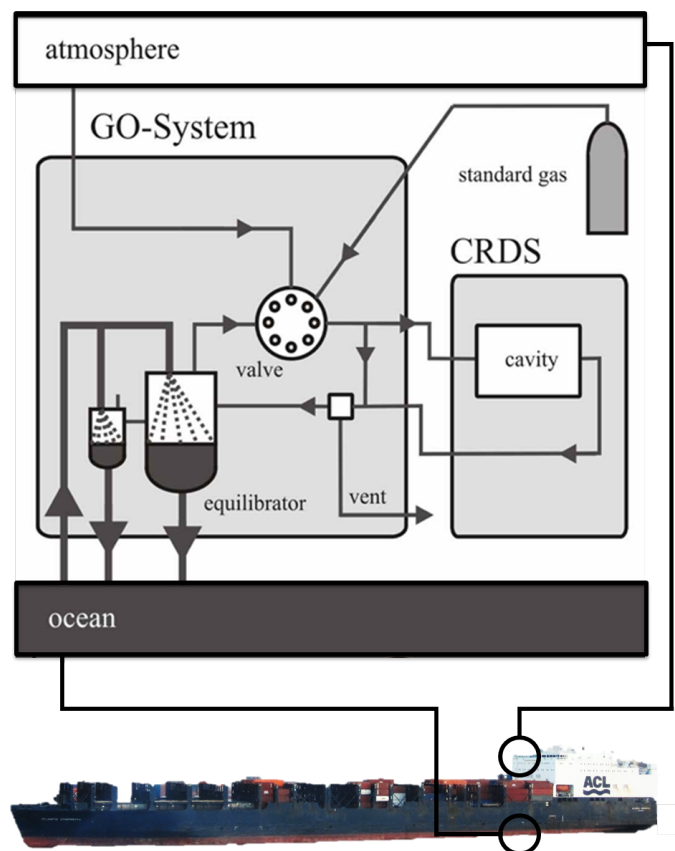


Figure 3.5: A schematic setup of the $f\text{CO}_2$ measuring system on board M/V Atlantic Companion and its location in the vessel.

equilibrator and sea water. The TA was estimated using a salinity-alkalinity-day of year correlation based on the TA-samples that were taken on crossings with discrete sampling program.

$$\text{TA}_{\text{calc}} = 738 + 43 \times \text{SSS} + 0.057 \times \text{SSS}^2 + 0.1205 \times t - 3.46 \times 10^{-4} \times t^2 \quad (3.1)$$

with TA_{calc} being the calculated alkalinity, SSS the sea surface salinity and t the day of year. The mean deviation of measured TA_{sam} and TA_{calc} is $0.17 \mu\text{mol kg}^{-1}$ with a standard deviation of $\sigma = 12 \mu\text{mol kg}^{-1}$. Figure 3.6 shows the deviation as a function of salinity and the day of year. Using this estimated alkalinity and the measured seawater $f\text{CO}_2$ values, the speciation within the carbonate system and the DIC concentration were calculated for each crossing with the inorganic carbon model CO2SYS (van Heuven et al., 2009) (CO_2 dissociation constants from Mehrbach et al. (1973), KSO_4^- dissociation constants from Dickson and Millero (1987)). The small contributions of phosphate and

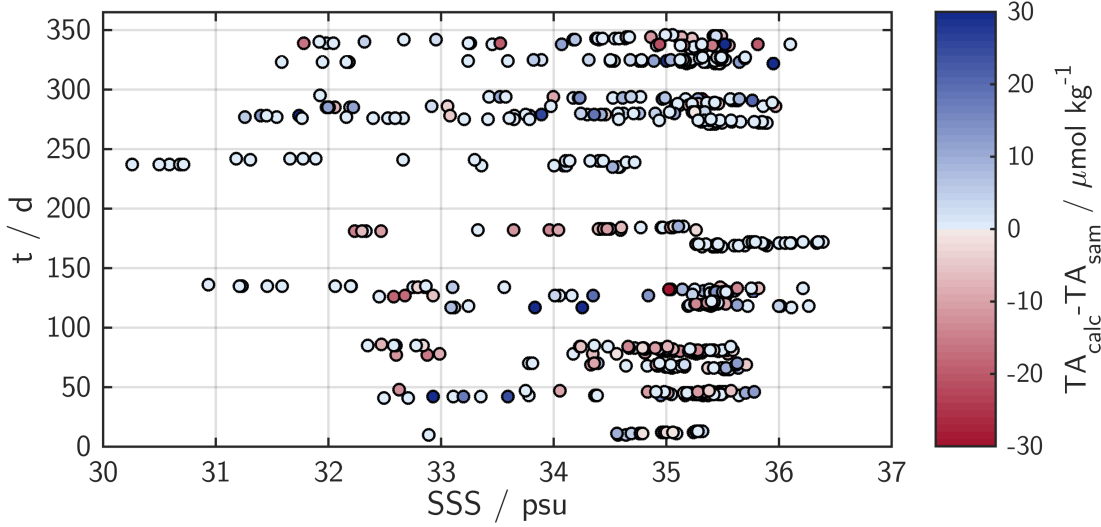


Figure 3.6: Deviation of sample alkalinity and alkalinity calculated from Equation 3.1 as a function of salinity and day of the year.

silicate to the alkalinity were neglected in this calculation because no underway measurements of these parameters were performed. Using maximum winter concentrations of phosphate ($0.8 \mu\text{mol kg}^{-1}$) and silicate ($6 \mu\text{mol kg}^{-1}$) the resulting maximum bias in TA_{calc} can be estimated to $0.93 \mu\text{mol kg}^{-1}$. By comparing the calculated DIC (DIC_{calc}) with measured DIC a good agreement of $(3 \pm 7) \mu\text{mol kg}^{-1}$ was found. For the salinity normalized DIC (nDIC) a alkalinity-salinity fit was used to determine the intercept. The salinity normalization was done using the Equation 3.2 to the mean salinity of each band, SSS_{mean} (Friis et al., 2003). If the normalization was done towards a salinity of $\text{SSS}_{\text{mean}} = 35 \text{ psu}$, the resulting DIC is denoted as nDIC_{35} .

$$\text{nDIC} = \frac{(\text{DIC} - 683) \times \text{SSS}_{\text{mean}}}{\text{SSS}} + 683 \quad (3.2)$$

The CRDS isotope ratio measurements were calibrated and corrected for varying oxygen content with an instrument-specific equation. The $\delta^{13}\text{C}(\text{CO}_2)$ was then corrected to sea surface temperature by using the temperature dependent fractionation to DIC after Zhang et al. (1995):

$$\begin{aligned} \delta^{13}\text{C}(\text{CO}_2)_{\text{SST}} = & \delta^{13}\text{C}(\text{CO}_2)_{\text{EQU}} - 0.107(T_{\text{EQU}} - T_{\text{SST}}) \\ & + \left(T_{\text{EQU}} f(\text{CO}_3^{2-})_{\text{EQU}} - T_{\text{SST}} f(\text{CO}_3^{2-})_{\text{SST}} \right) \end{aligned} \quad (3.3)$$

with T_{EQU} and T_{SST} as the equilibrator and sea surface temperature and $f(\text{CO}_3^{2-})_{\text{EQU}}$ and $f(\text{CO}_3^{2-})_{\text{SST}}$ the fraction of carbonate ions, calculated at the respective temperatures. The isotope ratio of DIC was calculated from the $\delta^{13}\text{C}(\text{CO}_2)_{\text{EQU}}$ after Zhang et al. (1995) (please see Table 2.1). At the end, a moving average filter with a length of about 15 min was applied to the isotope ratio data in order to reduce the statistical noise. The chosen average time of 15 min is a compromise between improving the instrument precision by applying longer averaging times and still capturing observed gradients and natural variations that happen on a timescale shorter than the optimal averaging time of 150 min. The optimal averaging time for field data was determined by comparing different averaging times during measurements of an intense bloom event. The chosen averaging time did improve the data precision but did not mask features that were resolved with shorter averaging times and also observed in the $f\text{CO}_2$ data.

The accuracy of the $f\text{CO}_2$ measurements is estimated to be $2 \mu\text{atm}$ for sea water. This sums up uncertainties stemming from the gas analyzer, the equilibration as well as the pressure and the temperature difference between equilibrator and surface water. For the $\delta^{13}\text{C}(\text{CO}_2)$ measurements the accuracy is in the order of 0.15‰ while the conversion $\delta^{13}\text{C}(\text{DIC})$ introduces an additional uncertainty of about 0.15‰ .

3.3 Sample analysis

Discrete samples were taken during the crossings between 10°W and 55°W from the water supply line. The handling of the different samples is described below in more detail. The sampling locations are shown in Figure 3.4. The samples were taken every 3 – 7 h. Assuming an average vessel speed of 18 kn this relates to a spatial resolution of 54 – 126 sm between two samples.

3.3.1 DIC and TA

These samples were taken following the DOE guidelines (Dickson et al., 2007). A 500 mL sample was poisoned with 100 μL saturated mercury chloride solution and then stored dark until analysis in the laboratory in Kiel. Samples were analyzed using a SOMMA system for DIC (Johnson et al., 1993, 1998) and a VINDTA system for TA (Mintrop et al., 2000). The accuracy was estimated based on repeated duplicate samples to $\Delta\text{DIC} = 2.9 \mu\text{mol kg}^{-1}$ and $\Delta\text{TA} = 5.1 \mu\text{mol kg}^{-1}$, respectively.

3.3.2 Nutrients

For the nutrient samples, 10 mL of seawater were filled into plastic bottles that were immediately frozen at -18°C . These samples were analyzed following the method of Hansen and Koroleff (1999) in Kiel. Based on repeated duplicate samples the accuracy was determined to be: nitrate $\pm 14\%$, phosphate $\pm 5.5\%$, silicate $\pm 6.0\%$, nitrite $\pm 11\%$ (in the range of $0 - 10 \mu\text{mol L}^{-1}$).

3.3.3 Chl *a*, POM, $\delta^{13}\text{C}(\text{POC})$ and $\delta^{15}\text{N}(\text{PON})$

The samples for Chl *a*, POM (including POC and PON) and stable isotope ratios of POM ($\delta^{13}\text{C}(\text{POC})$ and $\delta^{15}\text{N}(\text{PON})$) were taken in clean polyethylene bottles, filtrated using precombusted GF/F filter (Whatman, 25 mm in diameter, pore size $0.45 \mu\text{m}$) and then stored at -18°C . Depending on the filtration time of the previous sample and, thus, the amount of particulate matter in the water, the filtered volume was varying between 0.5 L and 2 L. The Chl *a* filters were ground in a cell mill, dissolved in acetone and measured in a Turner fluorometer against a blank with an estimated accuracy of 3%. The POM filters were acidified over night with fuming hydrochloric acid to remove the particulate inorganic carbon, dried and measured in a CN analyzer (EuroEA, HEKAtech GmbH). The stable isotope samples were measured in an isotope ratio mass spectrometer described in Hansen et al. (2009). The instruments precision is reported to be $\pm 0.47\%$ for ^{15}N and $\pm 0.12\%$ for ^{13}C .

3.3.4 TOC and DOC

For measurements of total organic carbon concentration (TOC), 10 mL of seawater were sampled into precombusted glass bottles and was directly frozen -18°C . In the lab-

oratory, the TOC concentration was measured with a TOC-VCSN instrument (Shimadzu, Japan) and the DOC concentration was calculated as the difference between TOC and POC. The accuracy was estimated based on repeated duplicate samples to $\Delta\text{TOC} = 13 \mu\text{mol kg}^{-1}$

3.3.5 Seasonal cycles

For studying the seasonal variations of all measured parameter, the study area was divided into three boxes of equal longitude, box 1025 (10 °W-25 °W), box 2540 (25 °W-40 °W) and box 4055 (40 °W-55 °W). The western box was then further divided into two boxes according to its sea surface salinity and temperature, one representing polar water from the Labrador Current and the other subtropical water from the Gulf Stream. Please note, that the box 4055 - pol shows strong subtropical characteristics, despite its SSS/SST signature of the Labrador Current. The location of these four boxes (1025, 2540, 4055 - pol, 4055 - sub) can be found in Figure 3.4. For the continuous measurements, the box mean of each crossing was calculated. For each parameter a harmonic function was applied according to Zeng et al. (2002),

$$\chi = c_0 + c_1 \sin\left(\frac{2\pi t}{365}\right) + c_2 \cos\left(\frac{2\pi t}{365}\right) + c_3 \sin\left(\frac{4\pi t}{365}\right) + c_4 \cos\left(\frac{4\pi t}{365}\right) \quad (3.4)$$

$$\chi = c_0 + c_1 \sin\left(\frac{2\pi t}{365}\right) + c_2 \cos\left(\frac{2\pi t}{365}\right) + c_3 \sin\left(\frac{4\pi t}{365}\right) + c_4 \cos\left(\frac{6\pi t}{365}\right) \quad (3.5)$$

where t is the day of year. Most parameters were fitted using equation 3.4. Equation 3.5 was used for fitting surface ocean $f\text{CO}_2$ and its disequilibrium with the atmosphere ($\Delta f\text{CO}_2$) in the polar and subtropical box (4055 - sub and 4055 - pol) as well as nitrite. In order to describe the nutrient dynamics (nitrate, phosphate and silicate) during summer, when nutrient concentrations were on a constant level close to zero, this season was excluded from the fit and negative fit values were set to zero (nitrate, nitrite) or the mean summer value (phosphate, silicate). The fit of the MLD was also set to a constant value of 20 m during summer. Since the sea water intake was located at a depth of 9.6 - 10.6 m, we assume that the surface ocean is mixed due to the vessels movement to a depth of up to 20 m and shallower mixed layers could not be sampled.

3.4 Model description

A box model was set up to calculate the fluxes of different processes that drive the surface ocean carbon cycle of the North Atlantic. The structure of this box model is shown in Figure 3.7. As input the harmonic fits described in the previous Section were used.

The atmospheric $f\text{CO}_2$ ($f\text{CO}_{2,\text{ATM}}$) and $\delta^{13}\text{C}(\text{CO}_2)_{\text{ATM}}$ were calculated for the longitudinal boxes 1025, 2540 and 4055 based on time series flask measurements from atmosphere monitoring stations at Mace Head/Ireland (53.33 °N, -9.90 °E), Bermuda/United Kingdom (32.26 °N, -64.88 °E), Vestmannaeyjar/Iceland (63.40 °N, 20.29 °E) and the Azores/Portugal (38.75 °N, -27.08 °E) between January 2012 and December 2014 ("Co-operative Global Atmospheric Data Integration Project", 2015; White et al., 2015). Since the atmospheric CO_2 content shows a strong latitudinal dependence, this dependence was used to calculate the atmospheric $x\text{CO}_2$ over the ocean as a function of latitude and date. For each point in a 0.5° latitude by 1096 days grid, $x\text{CO}_{2,\text{ATM}}$ and $\delta^{13}\text{C}(\text{CO}_2)_{\text{ATM}}$ were calculated by linear interpolation in space and time. For each box, all grid points of the respective latitude were averaged for each day. At the end, the three years were averaged to one mean seasonal cycle per box. The $f\text{CO}_{2,\text{ATM}}$ was calculated from the $x\text{CO}_{2,\text{ATM}}$ using the fitted SST, SSS and air pressure. The wind data was taken from the Modern Era Retrospective-analysis for Research and Applications (MERRA) which uses the Goddard Earth Observing System Data Assimilation System Version 5 (GEOS-5). The spatial resolution of the 1 h mean wind speed data is 1/2° latitude and 2/3° longitude. The air pressure obtained from this reanalysis was in good agreement with our measurements on board (not shown). Since the gas exchange is not linearly correlated to the wind speed, the gas transfer velocity k_{600} was calculated according to Nightingale et al. (2000) for the entire wind field. The gas transfer velocity was then averaged into one vector per each of the three longitudinal boxes (1025, 2540, 4055). At the end, a daily mean for each box was calculated from the three years and a 6 day moving average was applied. The actual k at the respective temperatures was calculated using the Schmidt number dependence after Wanninkhof (1992) and the solubility coefficient K_0 according to Weiss (1974). The seasonal variations of $f\text{CO}_{2,\text{ATM}}$ and $\delta^{13}\text{C}(\text{CO}_2)_{\text{ATM}}$ can be found in the Supplement.

The mixed layer depth (MLD) from January 2012 until December 2014 was taken from the Mercator Project (www.mercator-ocean.fr). The operational numerical system

(PSY2G3R3-PGN), which is a combination of a model configuration and a real time assimilation system, provides daily mixed layer depth on a $1/4^\circ$ by $1/4^\circ$ grid. For estimating the mixed layer depth, a temperature difference criterion of 0.2°C was used. The mixed layer depth was spatially averaged in the four boxes with respect to its location. The three years were averaged to a mean seasonal cycle of mixed layer depth for each box and then fitted using Equation 3.4. Due to the depth of the water intake and the water mixing that was induced by the movement of the vessel, MLD shallower than 20 m were set to 20 m as we expect the upper part of the water column to be always mixed to this depth.

For the concentration changes due to convective mixing an average end-of-summer-profile (data from July and August) was calculated based on quality-controlled data from the datasets GLODAP v2 (Olsen et al., 2016) and NAC13v1 (Becker et al., 2016). For DIC and nutrient concentrations only samples taken during the time period 1992-2012 were included. Unfortunately, there is no more recent data available in the data products. The isotope data was sampled between 1982 and 2012. The DIC and $\delta^{13}\text{C}(\text{DIC})$ profiles were corrected to the respective anthropogenic changes in the atmosphere since only the upper 100 – 400 m of the profiles were used which are in yearly contact with the atmosphere. A mean of all profiles that fall into the respective boxes was calculated. For $\delta^{13}\text{C}(\text{DIC})$ the data coverage in the polar box was too poor so that a mean profile from the southern end of the Labrador sea was used. A comparison of the DIC data from the respective area with the DIC profile in the polar box showed no major differences. All used profiles are presented in the Supplement.

For estimating the uncertainty of the reported annual and seasonal fluxes, a Monte Carlo approach was used. Each harmonic fit and also the average depth profiles were assigned with their standard deviation. For the uncertainty of the rate of DIC and nutrient change, the standard deviation was related to the amplitude of the fit. For the mean mixed layer depth, an uncertainty of 20 % was assumed, conservatively. The model was run several times and for each model run all variables were offset by a term randomly chosen from a normal distribution with the standard deviation of the respective uncertainty. The reported flux uncertainties represent the standard deviation of all these model runs.

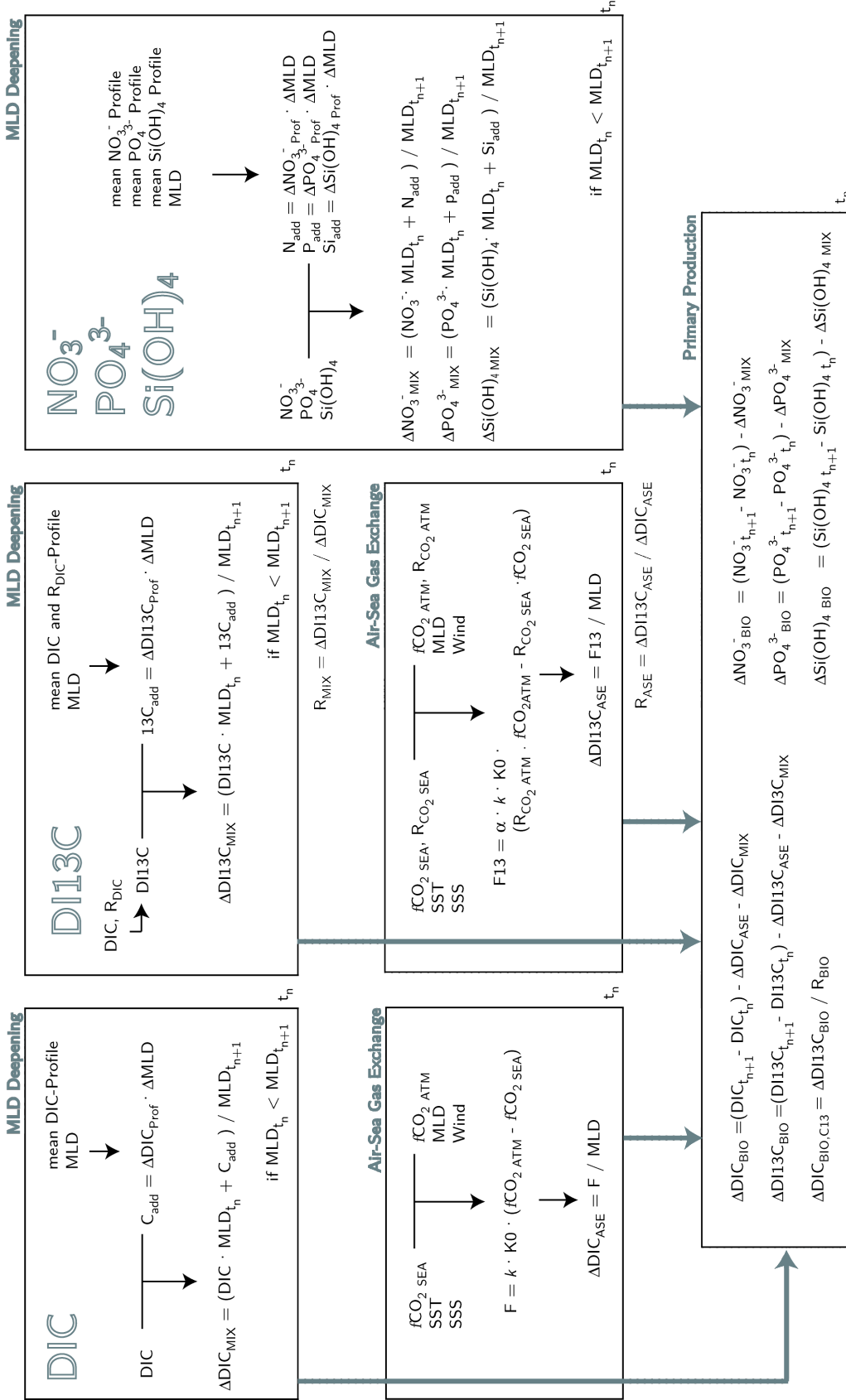


Figure 3.7: Structure of the box model and the included equations.

4 An internally consistent dataset of $\delta^{13}\text{C}$ -DIC in the North Atlantic Ocean-NAC13v1

M. Becker^{1,2}, N. Andersen³, H. Erlenkeuser³, M.P. Humphreys⁴, T. Tanhua¹, and A. Körtzinger^{1,2}

Earth System Science Data Discussions, 1-18, doi:10.5194/essd-2016-7, 2016.

¹ GEOMAR, Helmholtz Center for Ocean Research, Kiel, Germany

² Christian Albrechts University Kiel, Kiel, Germany

³ Leibniz-Laboratory for Radiometric Dating and Isotope Research, Christian Albrechts University, Kiel, Germany

⁴ Ocean and Earth Science, University of Southampton, Southampton, UK

My contribution:

- Collecting and examining the publicly available data.
- Examining the data and metadata from the cruises 06MT19941012, 06MT19970515, 06MT19970707, 06MT19970815, 06MT19990711, 06MT19990813, 06MT20010507, 06MT20030723 and 06MT20040311, performing a first quality control to spot outliers and submitting the cruise data to CDIAC.
- Performing the crossover study.
- Preparing the data set NAC13v1 and publishing it at http://cdiac.ornl.gov/oceans/ndp_096/NAC13v1.html, DOI: 10.3334/CDIAC/OTG.NAC13v1.
- Writing the paper.

An Internally Consistent Dataset of $\delta^{13}\text{C}$ -DIC in the North Atlantic Ocean - NAC13v1

Meike Becker^{1,2}, Nils Andersen³, Helmut Erlenkeuser³, Matthew.P. Humphreys⁴,
Toste Tanhua¹, and Arne Körtzinger^{1,2}

¹GEOMAR, Helmholtz Center for Ocean Research, Kiel, Germany

²Christian Albrechts University Kiel, Kiel, Germany

³Leibniz-Laboratory for Radiometric Dating and Isotope Research, Christian Albrecht University, Kiel, Germany

⁴Ocean and Earth Science, University of Southampton, Southampton, UK

Correspondence to: Meike Becker (mbecker@geomar.de)

Abstract.

The stable carbon isotope composition of dissolved inorganic carbon ($\delta^{13}\text{C}$ -DIC) can be used to quantify fluxes within the carbon system. For example, knowing the $\delta^{13}\text{C}$ signature of the inorganic carbon pool can help to describe the exchange between ocean and atmosphere as well as the amount of anthropogenic carbon in the water column. The measurements can also be used for evaluating modeled carbon fluxes, for making basin wide estimates, studying seasonal and interannual variability or decadal trends in interior ocean biogeochemistry. For all these purposes, it is not only important to have a sufficient amount of data, but these data must also be internally consistent and of high quality.

In this study, we present a $\delta^{13}\text{C}$ -DIC dataset for the North Atlantic, which has undergone secondary quality control. The data originate from oceanographic research cruises between 1981 and 2012. During a primary quality control step based on simple range tests obviously bad data were flagged. In a second quality control step, biases between measurements from different cruises were quantified through a crossover analysis using nearby data of the respective cruises and absolute values of biased cruises were adjusted in the data product. the crossover analysis was possible for 22 of the 29 cruises in our dataset and adjustments were applied to 10 of these. The internal accuracy of this dataset is 0.017‰.

The dataset is available via CDIAC at http://cdiac.ornl.gov/oceans/ndp_096/NAC13v1.html, doi:10.3334/CDIAC/OTG.NAC13v1.

20 1 Introduction

Stable carbon isotope ratios are utilized as a tracer in several applications in marine carbon research. Particularly the stable carbon isotope ratio of dissolved inorganic carbon ($\delta^{13}\text{C}$ -DIC) can be used to enhance the understanding of carbon related processes ranging widely from the estimation of

glacial circulation changes (Curry and Oppo, 2005) to testing the performance of ecosystem models
25 (Schmittner et al., 2013). By observing the temporal development of the lightening of the inorganic
carbon pool due to the uptake of CO₂ originating from the burning of ¹³C-depleted fossil fuel carbon,
a phenomenon also known as oceanic ¹³C Suess effect, an estimation of the anthropogenic carbon
fraction of DIC is possible (Gruber et al., 2002; Körtzinger et al., 2003; Olsen et al., 2006, 2010;
Quay et al., 2007; Racapé et al., 2013). Furthermore, δ¹³C can provide information concerning the
30 quantification of biological processes such as net community production (Quay et al., 2009). Using
the stable carbon isotope signature facilitates the distinction between anthropogenic, biological and
physical drivers of the carbon system.

A sample's stable carbon isotope ratio, δ¹³C-DIC, is expressed as per mil deviation from that of
the commonly used standard material Vienna Pee-Dee Belemnite (V-PDB)(Coplen, 1995).

$$35 \quad \delta^{13}\text{C} = \left(\frac{{}^{13}R}{{}^{13}R_{\text{PDB}}} - 1 \right) \cdot 10^3 \quad (1)$$

with ¹³R being the ratio of the two stable carbon isotopes ¹³C and ¹²C in the sample.

For basin-wide carbon flux estimates, studies of seasonal variations, or interannual trends it is im-
portant to have a dataset of sufficiently high coverage both in space and time. Moreover, the dataset
should be free of systematic differences between measurements carried out by different laborato-
40 ries and on different cruises. However, both criteria are not easily met. Since Isotope Ratio Mass
Spectroscopy (IRMS), the common method to analyze δ¹³C-DIC data, is a very time consuming
and expensive technique that cannot be performed at sea, data coverage has remained relatively
poor. Therefore, several efforts have been made to assemble a dataset containing as many cruises as
possible.

45 For oceanic δ¹³C-DIC data this has been done first by Kroopnick (1985) who provided an analysis
of the distribution of δ¹³C-DIC in the world's oceans. Over the years more data was accumulated
and different data collections emerged (Gruber et al., 1999; Quay et al., 2003, 2007; Schmittner
et al., 2013). During recent years, databases like GLODAP (Global Ocean Data Analysis Project)
and CARINA (Carbon dioxide in the Atlantic Ocean) were created for carbon-related parameters
50 (Olsen et al., 2016). These projects did not only assemble the data but also conducted a secondary
quality control so that systematic biases between individual cruises could be identified and adjusted
for (Tanhua et al., 2009; Velo et al., 2009; Tanhua et al., 2010a; Pierrot et al., 2010). Relative to
other parameters such as total alkalinity or DIC, however, the dataset for δ¹³C-DIC is still small and
disorganized. Therefore, no secondary quality control in which deep water samples from different
55 cruises at the nearby locations, so called crossovers, are compared to each other could be carried out
within these collections. Several new cruises have become available for the North Atlantic so that
now the present crossover study could be performed for this area. This crossover analysis features

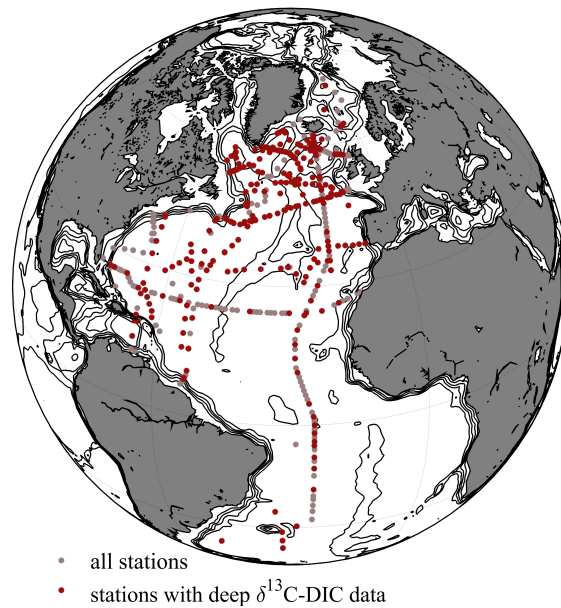


Figure 1. Map of all stations with $\delta^{13}\text{C-DIC}$ data used in this dataset. Data from deeper than 1500 m was available only for the stations in dark red, so only these stations were used for the crossover analysis.

29 cruises of which 22 could be compared quantitatively. Cruises without a quantitatively evaluable crossover were qualitatively related to the corrected dataset.

60 Please note, that for applying the crossover inversion routine we assume that the deep water masses (below 1500 m) are only to a negligible amount influenced by changes due to an increasing amount of anthropogenic carbon. Since the detected differences between some cruises were not consistent with a slowly increasing amount of anthropogenic carbon we think that this consistent dataset is a important step for improving the study of carbon isotope dynamics in the upper 1500 m. In regions
 65 for which also the deeper water masses have been shown to contain a high amount of anthropogenic carbon, were neglected crossovers with cruises that took place long before or long after the respective cruise. We believe that no temporal trends have been removed, or created by the 2nd QC procedures employed here. However, care should be exercised for calculating C_{ant} accumulation in water below 1500 m.

70

Table 1. Information about sample handling and measurements for those cruises where the $\delta^{13}\text{C}$ data have not been published elsewhere.

Cruise ID	Expocode	Laboratory	Analysis period	Sample handling	PI
1	06MT19941012	¹	9/2002 - 12/2002	200 μL $\text{HgCl}_{2\text{sat}}$ / 100 mL sample	A. Körtzinger / H. Erlenkeuser
2	06MT1997-M39	¹	1/1998 - 2/2000	200 μL $\text{HgCl}_{2\text{sat}}$ / 100 mL sample	A. Körtzinger / H. Erlenkeuser
3	06MT1999-M45	¹	7/2000 - 6/2002	50 μL $\text{HgCl}_{2\text{sat}}$ / 100 mL sample	A. Körtzinger / H. Erlenkeuser
4	06MT20010507	¹	12/2001 - 9/2002	50 μL $\text{HgCl}_{2\text{sat}}$ / 100 mL sample	A. Körtzinger / H. Erlenkeuser
5	06MT20030723	¹	3/2004 - 10/2004	100 μL $\text{HgCl}_{2\text{sat}}$ / 100 mL sample	A. Körtzinger / H. Erlenkeuser
6	06MT20040311	¹	1/2005 - 10/2005	200 μL $\text{HgCl}_{2\text{sat}}$ / 100 mL sample	D.W.R. Wallace / H. Erlenkeuser

¹ Leibniz Laboratory for Radiometric Dating and Isotope Research, Kiel, Germany

2 Data Provenance and Structure

75 This dataset comprises data and metadata from 29 research cruises/campaigns from several international research groups, in total 6068 samples. Some of these consist of multiple cruises and one is a time series. For the crossover analysis, some consecutive cruises whose data were analyzed together were treated as one cruise. While the focus is on the North Atlantic, four cruises were included that also have stations in the Nordic Seas, and one cruise extends into the South Atlantic. Thereby, consistency with extended quality controlled datasets for these regions is ensured. Since only deep (> 80 1500 m) samples of each cruise are compared in this study, only cruises with at least one deep station could be included in this analysis.

Figure 1 shows the locations of all stations with $\delta^{13}\text{C}$ -DIC data that are part of this compilation. For cruises that have not been published elsewhere, Table 1 shows a summary of the respective sample handling, the periods during which the samples were analyzed and the responsible PI. Some 85 cruises had $\delta^{13}\text{C}$ -DIC measurements over the entire depth range at every station, whereas others just had one or two stations with deep $\delta^{13}\text{C}$ -DIC data. Most of the cruises were conducted in the subpolar North Atlantic, while the tropical region has relative poor coverage. The temporal and latitudinal distributions of the data are displayed in Figure 2. The data was collected in the North 90 Atlantic between 1981 and 2012, with the majority falling between 1990 and 2005. Considering the

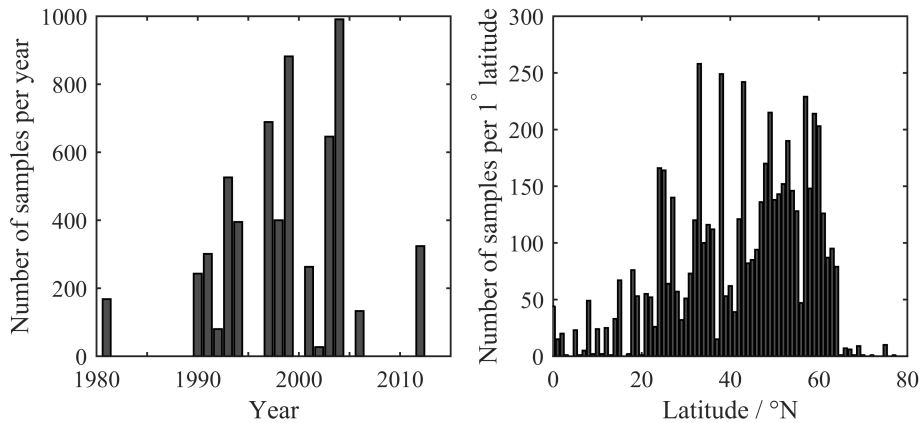


Figure 2. The temporal distribution of the presented dataset ordered by year (left panel) and the sum of all samples at each latitudinal degree (right panel).

seasonal distribution of the data, a bias towards summer time exists, especially towards late summer. The only two cruises which took place between January and March were located south of 42°N. The uncertainty of the $\delta^{13}\text{C}$ -DIC samples analyzed by IRMS is usually reported to be between $\pm 0.12\%$ (Gruber et al., 1999) and $\pm 0.03\%$ (Quay et al., 2003).

95 The presented dataset consists of 20 columns of which the first 17 are cruise number, station, sampling number, day, month, year, latitude, longitude, maximal depth, maximal sampling depth, bottle number, cast number, temperature, salinity, depth, ctd salinity and pressure. Column 18 contains the adjusted $\delta^{13}\text{C}$ -DIC data, column 19 a quality flag (C13f) and column 20 the QC-flag (C13qc, see Table 2). For bad data the quality flag was set to 'not measured' and therefore column 19 has only
 100 two entries (2: good, 9: not measured). Cruises that could be quantitatively compared to each other by the 2nd QC have a '1' in the QC-flag. All others are flagged with '0'.

Additional parameters to most of the cruises can be found in either GLODAPv2 or CARINA. Only the most recent cruises 35TH20060521 and 74DI20120731 are not included in these datasets, but the individual cruise files can be found on CDIAC. The OMEX1NA data are only part of Carina.

105 The respective cruise numbers in GLODAPv2 and CARINA of the cruises shown in the NAC13v1-dataset can be found in the documentation.

Table 2. NAC13v1 data set parameter list, column names used in the data product and the respective units.

parameter	data product parameter name	data product flag name	unit
NAC13v1 cruise number	cruiseno		
Station	station		
Sample number	nosamp		
Day	day		
Month	month		
Year	year		
Latitude	latitude		°N
Longitude	longitude		°E
Bottom depth	maxdepth		m
Pressure of the deepest sample	maxsampdepth		dbar
Bottle number	bottle		
Cast number	cast		
Temperature	temperature		°C
Salinity	salinity		
Depth	depth		m
CTD salinity	ctdsal		
Pressure	pressure		dbar
$\delta^{13}\text{C-DIC}$	C13	C13f, C13qc	‰

110 3 Computational Analysis

In order to derive an internally consistent set of $\delta^{13}\text{C-DIC}$ data in the North Atlantic all publicly available data in this area were assembled and quality controlled (QC) in two steps. At first, a primary QC was performed in order to identify obviously erroneous data, such as wrong positions, time stamps and depths. Also outliers were identified and then flagged by comparing the profiles of each cruise internally. After that, the secondary QC procedure was conducted employing a crossover analysis as described by Tanhua et al. (2010b). This MATLAB based software package compares two cruises at a time, searches for nearby stations, so-called 'crossovers', and calculates differences between all crossovers of the two cruises as additive offsets with the unit ‰. As criterion for identifying crossovers a maximum of 180 nm (3° of latitude) distance between stations was used. From these crossovers, the $\delta^{13}\text{C-DIC}$ data collected deeper than 1500 m was compared on equal potential density. Based on the resulting offsets and standard deviations determined for each of these crossovers a suggestion for a possible adjustment was made. This suggestion was obtained by an

inversion routine using a Weighted Least-Square (WLSQ) and a Weighted Damped Least Square (WDLSQ) model as described by Johnson et al. (2001). The cruise 33MW19930704-1 covers a long distance and is assumed to have high quality data. Therefore this cruise was selected as core cruise and weighted higher than the other cruises. Unfortunately this was the only cruise meeting these two criteria. Several cruises from different years were in good agreement with the core cruise while the other cruises were adjusted towards it. Choosing the appropriate distance criterion for crossover locations is always a compromise between including as many statistically relevant crossovers as possible by selecting a large enough radius on the one hand and trying to have only crossovers between stations that share similar oceanographic characteristics on the other hand. However, reducing the crossover distance to 120 nm reduced the amount of crossovers and the number of cruises that could be quantitatively compared to each other but did not significantly change the suggested magnitude of adjustments of the remaining cruises. Therefore, the 3°x3° criterion was used instead. For some crossovers in highly variable regions with deep water formation, such as the Labrador Sea and the Nordic Seas, the standard deviation was decreased significantly by restricting the comparison depths to >2000 m. Generally, offsets from crossovers in these highly variable regions, from cruises with a relatively poor data precision or with just a few deep samples were considered in the model with less influence, by weighting the offsets with their uncertainty. In Figure 3 all crossovers between the cruises 06MT20030723 and 33MW19930704-1 are shown as an example, both for the uncorrected as well as for the corrected dataset. All crossovers from the adjusted and the unadjusted dataset can be found at: http://cdiac.ornl.gov/oceans/ndp_096/NAC13v1.html.

Whether an adjustment was applied to the data was decided somewhat subjectively in each case based on a combination of the shape and distribution of individual crossover differences and the suggestions given by the inversion routine with knowledge about the sampling region. After applying the adjustments, the inversion was conducted again and it was checked whether or not the adjustment improved the overall consistency within the entire dataset. Temporal changes of the deep water masses were only considered in this step of the routine when comparing the suggested corrections and the corresponding crossover offsets between cruises in areas where also the deep water $\delta^{13}\text{C}$ -DIC was expected to change over time. In order to get a quantitative description of the internal consistency of the final dataset, a weighted mean using the respective offsets of all crossovers and their standard deviation was calculated (Tanhua et al., 2010a).

$$\text{WM} = \frac{\sum_{i=1}^L D(i)/(\sigma(i))^2}{\sum_{i=1}^L 1/(\sigma(i))^2} \quad (2)$$

L refers to the total number of crossover, D to the respective offset of all crossover and σ is their standard deviation.

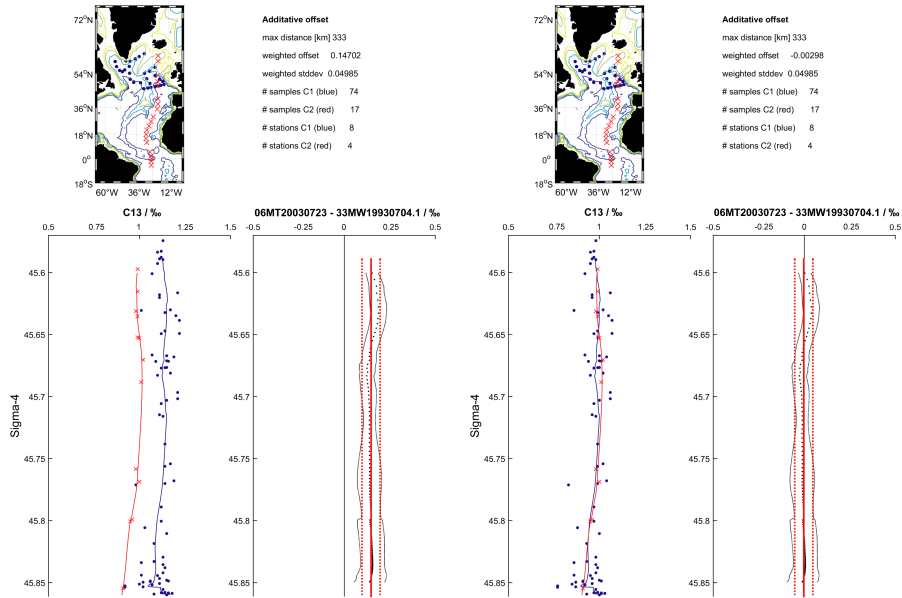


Figure 3. Crossovers between the cruises 06MT20030723 and the core cruise 33MW19930704-1. The left hand plot shows the original and the right hand plot the adjusted data. In both cases the distribution of the $\delta^{13}\text{C-DIC}$ on equal density surfaces (left hand side) as well as the mean offset between both cruises (right hand side) is shown. The cruise 06MT20030723 was adjusted by -0.20‰ .

4 Adjustments

The data of all cruises as well as locations are shown in Figure 4. The offsets, as well as the corrections suggested by the WDL SQ inversion routine, and the final adjustments are listed in Table 3. In Figure 5 the results of the WDL SQ inversion are shown before and after the adjustments were applied. Some cruises show quite big deviations from the core cruise. However, we do not know the reason for these biases. Besides the actual sample analysis in the laboratory, also different sampling routines on board the ship, insufficient poisoning and the sample storage time can cause these biases.

A detailed overview of the offset of each crossover in the original as well as the adjusted dataset is given in Table 4 in the supplementary information. Moreover, the evidence for our decision will be presented for each cruise.

4.1 06MT19941012, cruise #1

This cruise on the German R/V Meteor is also known as M30-2 (Körtzinger et al., 1998). The inversion suggested a correction of -0.07‰ . The mean offset of all crossovers is 0.11‰ too high. Based on the crossover with the core cruise an adjustment of -0.07‰ was applied.

Table 3. Overview of all cruises in this dataset. The data of some cruises were combined for the analysis. For more information, please see the detailed description in the 'Adjustments' section. Both, the mean offsets and the corrections suggested by the WDLSQ inversion are shown for the original and the adjusted dataset. In the last column the applied adjustments are displayed. NC indicates that these cruises were not considered in the inversion since they had no statistically significant crossover and the core cruise is marked with C. Cruises with insufficient quality data are denoted 'poor' and not included in the further analysis.

cruise ID	Expocode	Calculated offset		Suggested adjustments		Final adjustments
		not adjusted ‰	adjusted ‰	WDLSQ ‰	WDLSQ (adj) ‰	
1	06MT19941012	0.11	-0.02	-0.07(±0.10)	-0.01(±0.02)	-0.07
2	06MT1997-M39	-0.02	0.02	0.01(±0.14)	0.00(±0.01)	0
3	06MT1999-M45	0.16	-0.01	-0.14(±0.09)	0.00(±0.01)	-0.15
4	06MT20010507	0.16	0.00	-0.24(±0.10)	0.00(±0.01)	-0.30
5	06MT20030723	0.14	0.03	-0.15(±0.09)	0.00(±0.01)	-0.20
6	06MT20040311	-0.14	-0.02	0.10(±0.09)	0.01(±0.01)	0.10
7	316N19970717	0.17	0.02	-0.06(±0.17)	-0.01(±0.01)	-0.05
8	316N19970815					NC
9	316N20030922					NC
10	316N20031023					NC
11	33RO19980123					NC
12	33MW19910711	-0.02	-0.02	0.00(±0.01)	0.00(±0.01)	0
13	33MW19930704-1	-0.05	0.01	0.00(±0.01)	0.00(±0.01)	C
14	35TH20020611					NC
15	35TH20060521	-0.39	-0.02	0.24(±0.21)	-0.03(±0.05)	0.25
16	58JH19920712					NC
17	58JH19940723					NC
18	64TR19900417					poor
19	74DI20120731	-0.33	-0.13	0.13(±0.28)	0.12(±0.12)	0
20	OMEX1NA	-0.14	-0.03	0.03(±0.13)	0.02(±0.02)	0
21	316N19810401	-0.06	0.03	-0.03(±0.10)	-0.01(±0.03)	0

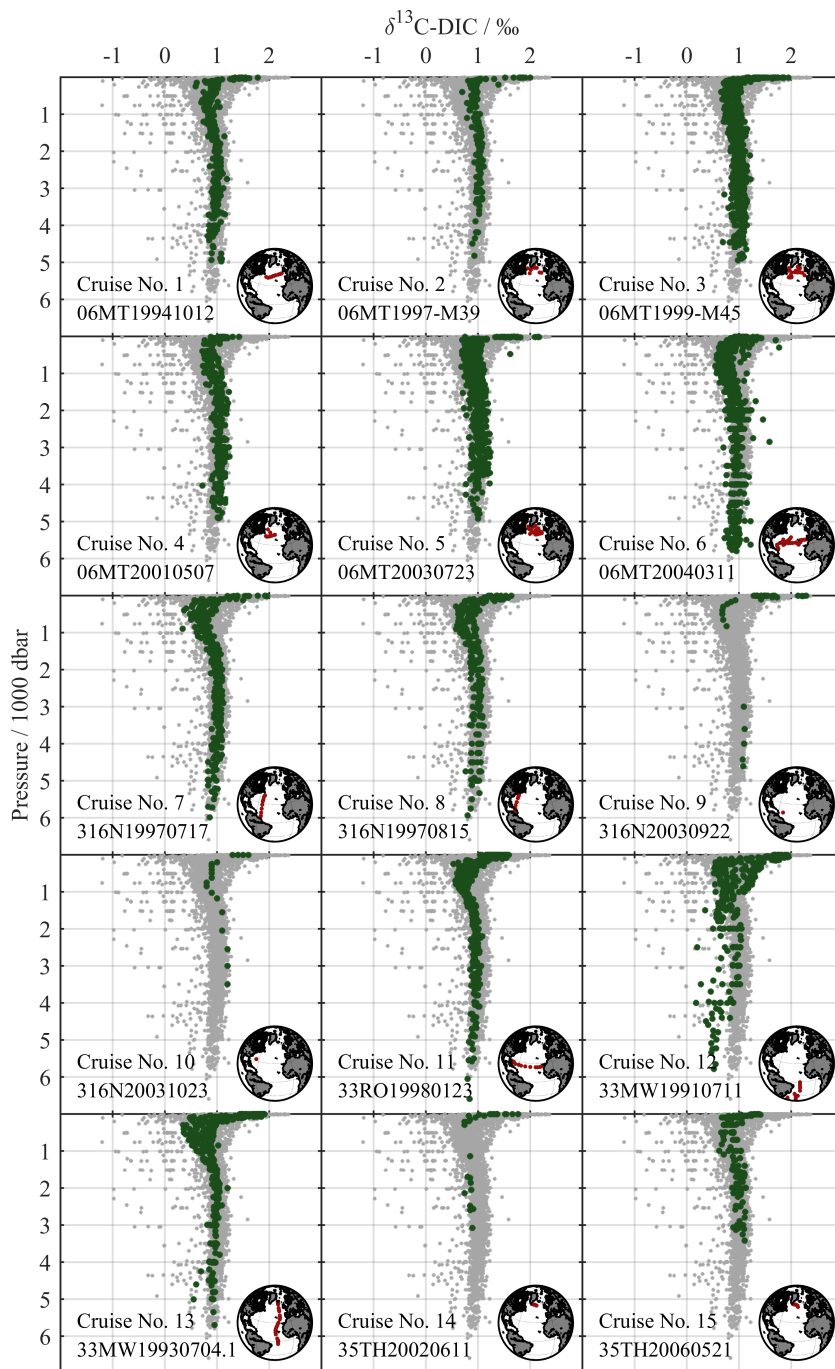


Figure 4. Adjusted $\delta^{13}\text{C-DIC}$ profiles and locations of each cruise. The green profiles represent the data of the specific cruise whereas the gray dots show all profiles in the dataset. *continued on next page*

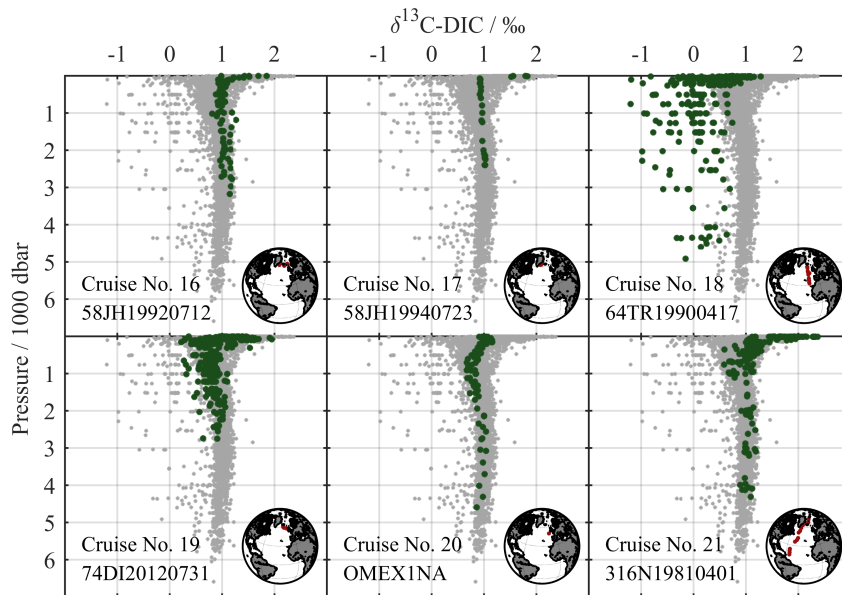


Figure 4. *continued from previous page.*
 Adjusted $\delta^{13}\text{C-DIC}$ profiles and locations of each cruise. The green profiles represent the data of the specific cruise whereas the gray dots show all profiles in the dataset.

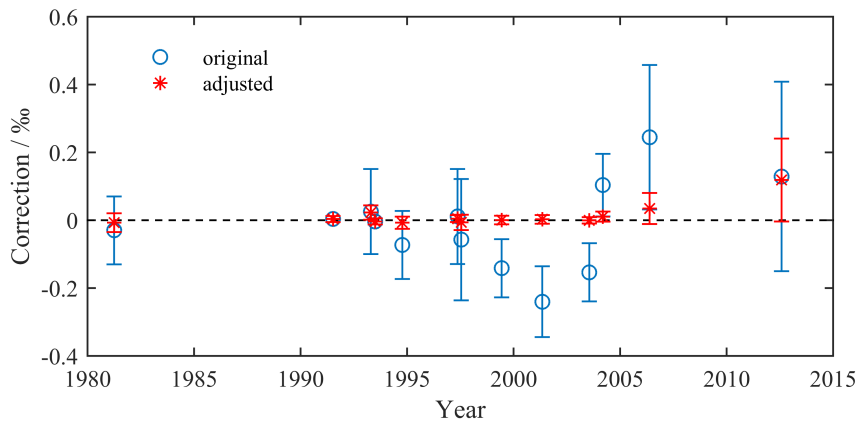


Figure 5. The results of the WDLSSQ based inversion routine for the original (blue circles) and the adjusted dataset (red stars). The cruises are plotted at the time the data was collected vs. the suggested correction.

170 **4.2 06MT19970515, 06MT19970707 and 6MT19970815, here referred to as 06MT1997-M39, cruise #2**

These cruises are also known as M39 cruises with three legs of $\delta^{13}\text{C-DIC}$ sampling (M39-2, M39-4, M39-5) (Körtzinger et al., 1999; Thomas and Ittekkot, 2001). Since each leg of this cruise had only

a few stations with $\delta^{13}\text{C}$ -DIC samples, and all these samples were analyzed together, these cruises
175 were summarized for the crossover study. Both, the inversion routine and the single crossover with
the adjusted cruises show no evidence for an offset.

4.3 06MT19990711 and 06MT19990813, here referred to as 06MT1999-M45, cruise #3

These cruises are also known as M45-2 and M45-3 (Friis et al., 2005). Since both were analyzed
together, they were summarized for this crossover study. The inversion suggested a correction of -
180 0.15 ‰ and the mean offset of all crossovers was 0.16 ‰ too high. After applying this adjustment and
comparing this cruise to the adjusted dataset, the inversion routine still suggested a small correction.
Therefore, an adjustment of -0.20 ‰ was applied.

4.4 06MT20010507, cruise #4

This cruise is also known as M50-1 (Friis et al., 2007). The inversion routine suggested a correction
185 of -0.24 ‰, whereas the mean offset was 0.16 ‰ too high. Based on the southern crossover with
cruise 06MT20040311 and 316N19970717 an adjustment of -0.30 ‰ was applied.

4.5 06MT20030723, cruise #5

This cruise is also known as M59-2 (Friis et al., 2007). The correction suggested by the inversion
routine is -0.15 ‰ which matches with the positive offsets of the crossovers, except of those with
190 33TH20060521. Based on the crossover with the core cruise, an adjustment of -0.15 ‰ was applied.

4.6 06MT20040311, cruise #6

This cruise is also known as M60-5 (Tanhua et al., 2007). The inversion routine indicates that the
 $\delta^{13}\text{C}$ -DIC data of this cruise is 0.10 ‰ too low. Additionally, the mean offset shows that this data is
too low. An adjustment of +0.10 ‰ was applied.

195 4.7 316N19970717, cruise #7 and 316N19970815, cruise #8

These cruises followed the WOCE/GO-Ship standard lines A20 and A22 (Johnson et al., 2003). The
inversion suggests a correction of -0.06 ‰ for 316N19970717. It shows one crossover with cruise
06MT20040311 in which a significant positive offset is still visible after cruise 06MT20040311 was
corrected. Therefore, an adjustment of -0.05 ‰ was applied for cruise 316N19970717. The cruise
200 316N19970815 does not show a statistically significant crossover.

4.8 316N20030922, cruise #9, and 316N20031023, cruise #10

These cruises, that took place in the tropical western Atlantic, following the A20 and A22 lines, have
only one deep station each (Feely et al., 2008). The crossovers of these stations with both, the ad-

justed data of cruise 06MT20040311 and cruise 316N19970717 show a good agreement, suggesting
205 that no adjustment should be applied.

4.9 33RO19980123, cruise #11

This cruise (Lee et al., 2003) has one statistically insignificant crossover with the cruise 06MT20040311 and one with cruise 33MW19930704-1. Both seem to be in good agreement, suggesting that no adjustment should be applied.

210 4.10 33MW19910711, cruise #12, and 33MW19930704-1, cruise #13

The cruise 33MW19930704-1 was considered as core cruise in the present analysis (Forde et al., 1996). The cruise 33MW19910711 extends into the south Atlantic and its crossover with cruise 13 shows no need for an adjustment.

4.11 35TH20020611, cruise #14, and 35TH20060521, cruise #15

215 The latter of these two cruises has a few quantitative crossovers, that show a high offset of -0.39‰ . Furthermore, the inversion suggests a correction of 0.24‰ . The high variability of the sampling area south of Iceland, as well as an increasing lightning of the deep water carbon pool over time don't give an adequate explanation for this large deviation and, therefore, an adjustment of -0.25‰ was applied. The cruise 35TH20020611 shows just a few qualitatively analyzable crossovers, that show
220 a lighter carbon pool compared to earlier cruises and a heavier one compared to the original data of cruise 35TH20060521 (Racapé et al., 2013). After adjusting this cruise, both cruises, which were analyzed in the same laboratory, are not in good agreement anymore which suggests that the earlier cruise also has too low isotope values. However, in the absence of a statistically significant crossover no adjustment was applied to this cruise.

225 4.12 58JH19920712, cruise #16, and 58JH19940723, cruise #17

These two cruises took place in a highly variable area (Gislefoss et al., 1995). No statistically relevant crossover exists but the data are in good agreement with the core cruise and the other adjusted cruises in that area.

4.13 64TR19900417, cruise #18

230 This cruise shows extreme scatter compared to all other cruises and, therefore, was not included into the adjusted product (Rommetts et al., 1991). When comparing crossover stations this cruise shows a mean offset to other cruises of about -1.2‰ .

4.14 74DI20120731, cruise #19

Both the inversion and the offset mean of the crossover suggest a correction of +0.13 ‰ for the cruise
235 (Humphreys et al., 2015). This most recent cruise took place near the Scotland-Iceland ridge where
the deep water masses cannot be assumed to be constant over time. All crossovers indicate a lower
 $\delta^{13}\text{C-DIC}$ of this cruise when comparing it with the others which is consistent with an increased
amount of anthropogenic carbon. Therefore, no adjustment was applied.

4.15 OMEX1NA, cruise #20

240 During the OMEX1 project in the North Atlantic $\delta^{13}\text{C-DIC}$ samples were taken in January 1994
(Wollast and Chou, 2001). The data is in good agreement with the other cruises in this area and no
adjustment was applied.

4.16 316N19810401, cruise #21

The cruises 316N19810401, 316N19810416, 316N19810516, 316N19810619, 316N19810721,
245 316N19810821 and 316N19810923 are combined and usually named Transient Tracers in the Oceans
North Atlantic Study (TTO-NAS) (Brewer et al., 1986). The inversion does not suggest any correc-
tion for this dataset.

5 Conclusions

The finalized, quality controlled dataset of $\delta^{13}\text{C-DIC}$ presented here consists of 22 cruises (some of
250 which consists of multiple legs) that have been quantitatively compared to each other and form an
internally consistent dataset. Seven cruises could not be quantitatively compared to the other cruises
due to a lack of crossovers and / or deep $\delta^{13}\text{C-DIC}$ data. The internal consistency of the adjusted
dataset was calculated to be 0.017‰ based on Equation 2.

The database is available at CDIAC via http://cdiac.ornl.gov/oceans/ndp_096/NAC13v1.html,
255 doi:10.3334/CDIAC/OTG.NAC13v1.

6 Acknowledgment

We would like to thank all the people, both researchers as well as captains and crews, who spend time
at sea and in the lab collecting and measuring the samples and preparing the data that is presented
here and the PIs for sharing it. The measurements of the majority of previously not public $\delta^{13}\text{C}$ data
260 was supported by the Deutsche Forschungsgemeinschaft (DFG) through SFB460 and this work was
funded by the Future Ocean Excellence Cluster Project CP1140. We also thank Aley Kozyr from
CDIAC for preparing the NAC13v1-website on CDIAC.

1	06MT19941012	●	0.18 (±0.07)	0.31 (±0.06)	0.06 (±0.06)	∧	06MT20040311	∧	0.17 (±0.05)	∨	0.13 (±0.08)	∨	33MW19930704-1	∨	33MW19910711	∨	33MW19930704-1	∨	35TH20020611	∨	35TH20060521	∨	35TH20060521	∨	58HT19920712	∨	58HT19940423	∨	74DI20120731	∨	OMEX1NA	∨	316N19810401	∨
2	06MT1997-M39	●	0.21 (±0.07)	0.15 (±0.06)	0.15 (±0.06)	∨	06MT1999-M45	∨	0.21 (±0.07)	∨	0.15 (±0.06)	∨	06MT20030723	∨	06MT19970717	∨	316N19970815	∨	316N19970717	∨	06MT20040311	∨	06MT20030723	∨	06MT20010507	∨	06MT1999-M45	∨	06MT1997-M39	∨	06MT19941012	∨	06MT19941012	∨
3	06MT1999-M45	●	-0.01 (±0.07)	0.10 (±0.07)	0.01 (±0.06)	∨	06MT1999-M45	∨	0.01 (±0.07)	∨	0.10 (±0.07)	∨	06MT20030723	∨	06MT1999-M45	∨	06MT20010507	∨	06MT1999-M45	∨	06MT20040311	∨	06MT20030723	∨	06MT20010507	∨	06MT1999-M45	∨	06MT1997-M39	∨	06MT19941012	∨	06MT19941012	∨
4	06MT20010507	●	-0.08 (±0.06)	0.02 (±0.06)	-0.08 (±0.06)	∨	06MT1999-M45	∨	-0.08 (±0.06)	∨	0.02 (±0.06)	∨	06MT20030723	∨	06MT1999-M45	∨	06MT20010507	∨	06MT1999-M45	∨	06MT20040311	∨	06MT20030723	∨	06MT20010507	∨	06MT1999-M45	∨	06MT1997-M39	∨	06MT19941012	∨	06MT19941012	∨
5	06MT20030723	●	0.00 (±0.06)	-0.07 (±0.06)	-0.07 (±0.06)	∨	06MT1999-M45	∨	0.00 (±0.06)	∨	-0.07 (±0.06)	∨	06MT20030723	∨	06MT1999-M45	∨	06MT20010507	∨	06MT1999-M45	∨	06MT20040311	∨	06MT20030723	∨	06MT20010507	∨	06MT1999-M45	∨	06MT1997-M39	∨	06MT19941012	∨	06MT19941012	∨
6	06MT20040311	●	0.02 (±0.06)	-0.06 (±0.06)	-0.06 (±0.06)	∨	06MT1999-M45	∨	0.02 (±0.06)	∨	-0.06 (±0.06)	∨	06MT20030723	∨	06MT1999-M45	∨	06MT20010507	∨	06MT1999-M45	∨	06MT20040311	∨	06MT20030723	∨	06MT20010507	∨	06MT1999-M45	∨	06MT1997-M39	∨	06MT19941012	∨	06MT19941012	∨
7	316N19970717	●	0.00 (±0.05)	-0.02 (±0.05)	-0.02 (±0.05)	∨	06MT20040311	∨	0.00 (±0.05)	∨	-0.02 (±0.05)	∨	06MT20030723	∨	06MT19970717	∨	316N19970815	∨	316N19970717	∨	06MT20040311	∨	06MT20030723	∨	06MT20010507	∨	06MT1999-M45	∨	06MT1997-M39	∨	06MT19941012	∨	06MT19941012	∨
8	316N19970815	●	0.00 (±0.05)	-0.02 (±0.05)	-0.02 (±0.05)	∨	06MT20040311	∨	0.00 (±0.05)	∨	-0.02 (±0.05)	∨	06MT20030723	∨	06MT19970717	∨	316N19970815	∨	316N19970717	∨	06MT20040311	∨	06MT20030723	∨	06MT20010507	∨	06MT1999-M45	∨	06MT1997-M39	∨	06MT19941012	∨	06MT19941012	∨
9	316N20030922	●	0.00 (±0.05)	-0.02 (±0.05)	-0.02 (±0.05)	∨	06MT20040311	∨	0.00 (±0.05)	∨	-0.02 (±0.05)	∨	06MT20030723	∨	06MT19970717	∨	316N19970815	∨	316N19970717	∨	06MT20040311	∨	06MT20030723	∨	06MT20010507	∨	06MT1999-M45	∨	06MT1997-M39	∨	06MT19941012	∨	06MT19941012	∨
10	316N20031023	●	0.00 (±0.05)	-0.02 (±0.05)	-0.02 (±0.05)	∨	06MT20040311	∨	0.00 (±0.05)	∨	-0.02 (±0.05)	∨	06MT20030723	∨	06MT19970717	∨	316N19970815	∨	316N19970717	∨	06MT20040311	∨	06MT20030723	∨	06MT20010507	∨	06MT1999-M45	∨	06MT1997-M39	∨	06MT19941012	∨	06MT19941012	∨
11	33RO19980123	●	0.00 (±0.05)	-0.02 (±0.05)	-0.02 (±0.05)	∨	06MT20040311	∨	0.00 (±0.05)	∨	-0.02 (±0.05)	∨	06MT20030723	∨	06MT19970717	∨	316N19970815	∨	316N19970717	∨	06MT20040311	∨	06MT20030723	∨	06MT20010507	∨	06MT1999-M45	∨	06MT1997-M39	∨	06MT19941012	∨	06MT19941012	∨
12	33MW19910711	●	0.00 (±0.05)	-0.02 (±0.05)	-0.02 (±0.05)	∨	06MT20040311	∨	0.00 (±0.05)	∨	-0.02 (±0.05)	∨	06MT20030723	∨	06MT19970717	∨	316N19970815	∨	316N19970717	∨	06MT20040311	∨	06MT20030723	∨	06MT20010507	∨	06MT1999-M45	∨	06MT1997-M39	∨	06MT19941012	∨	06MT19941012	∨
13	33MW19930704-1	●	0.00 (±0.05)	-0.02 (±0.05)	-0.02 (±0.05)	∨	06MT20040311	∨	0.00 (±0.05)	∨	-0.02 (±0.05)	∨	06MT20030723	∨	06MT19970717	∨	316N19970815	∨	316N19970717	∨	06MT20040311	∨	06MT20030723	∨	06MT20010507	∨	06MT1999-M45	∨	06MT1997-M39	∨	06MT19941012	∨	06MT19941012	∨
14	35TH20020611	●	0.00 (±0.05)	-0.02 (±0.05)	-0.02 (±0.05)	∨	06MT20040311	∨	0.00 (±0.05)	∨	-0.02 (±0.05)	∨	06MT20030723	∨	06MT19970717	∨	316N19970815	∨	316N19970717	∨	06MT20040311	∨	06MT20030723	∨	06MT20010507	∨	06MT1999-M45	∨	06MT1997-M39	∨	06MT19941012	∨	06MT19941012	∨
15	35TH20060521	●	0.32 (±0.06)	0.16 (±0.10)	0.33 (±0.09)	∨	06MT1999-M45	∨	0.32 (±0.06)	∨	0.16 (±0.10)	∨	06MT20030723	∨	06MT1999-M45	∨	06MT20010507	∨	06MT1999-M45	∨	06MT20040311	∨	06MT20030723	∨	06MT20010507	∨	06MT1999-M45	∨	06MT1997-M39	∨	06MT19941012	∨	06MT19941012	∨
16	58HT19920712	●	0.00 (±0.05)	-0.02 (±0.05)	-0.02 (±0.05)	∨	06MT20040311	∨	0.00 (±0.05)	∨	-0.02 (±0.05)	∨	06MT20030723	∨	06MT19970717	∨	316N19970815	∨	316N19970717	∨	06MT20040311	∨	06MT20030723	∨	06MT20010507	∨	06MT1999-M45	∨	06MT1997-M39	∨	06MT19941012	∨	06MT19941012	∨
17	58HT19940423	●	0.00 (±0.05)	-0.02 (±0.05)	-0.02 (±0.05)	∨	06MT20040311	∨	0.00 (±0.05)	∨	-0.02 (±0.05)	∨	06MT20030723	∨	06MT19970717	∨	316N19970815	∨	316N19970717	∨	06MT20040311	∨	06MT20030723	∨	06MT20010507	∨	06MT1999-M45	∨	06MT1997-M39	∨	06MT19941012	∨	06MT19941012	∨
19	74DI20120731	●	0.13 (±0.15)	0.02 (±0.10)	0.13 (±0.08)	∨	06MT20040311	∨	0.13 (±0.15)	∨	0.02 (±0.10)	∨	06MT20030723	∨	06MT19970717	∨	316N19970815	∨	316N19970717	∨	06MT20040311	∨	06MT20030723	∨	06MT20010507	∨	06MT1999-M45	∨	06MT1997-M39	∨	06MT19941012	∨	06MT19941012	∨
20	OMEX1NA	●	0.03 (±0.03)	0.02 (±0.02)	0.02 (±0.02)	∨	06MT20040311	∨	0.03 (±0.03)	∨	0.02 (±0.02)	∨	06MT20030723	∨	06MT19970717	∨	316N19970815	∨	316N19970717	∨	06MT20040311	∨	06MT20030723	∨	06MT20010507	∨	06MT1999-M45	∨	06MT1997-M39	∨	06MT19941012	∨	06MT19941012	∨
21	316N19810401	●	-0.11 (±0.06)	-0.11 (±0.06)	-0.11 (±0.06)	∨	06MT20040311	∨	-0.11 (±0.06)	∨	-0.11 (±0.06)	∨	06MT20030723	∨	06MT19970717	∨	316N19970815	∨	316N19970717	∨	06MT20040311	∨	06MT20030723	∨	06MT20010507	∨	06MT1999-M45	∨	06MT1997-M39	∨	06MT19941012	∨	06MT19941012	∨

Table 4. This table shows an overview of all crossovers. The symbol ● in each row divides the table into a triangle in the upper right and one in the lower left of the table. In the upper right corner for each crossover the offsets of the original dataset are listed. In the lower left corner the remaining offsets in the adjusted dataset are shown. Not statistically relevant crossovers are displayed with > , < and = indicating the tendency of not significant crossover. Please note that the offsets shown in the table result from $\delta^{13}\text{C}_{\text{column}} - \delta^{13}\text{C}_{\text{row}}$. All offsets are given in ‰.

References

- 265 Brewer, P., Takahashi, T., and Williams, R.: Transient tracers in the oceans (TTO)-Hydrographic data and carbon dioxide systems with revised carbon chemistry data, Tech. rep., Oak Ridge National Lab., TN (United States), 1986.
- Coplen, T.: Reporting of stable hydrogen, carbon, and oxygen isotopic abundances, *Geothermics*, 24, 707 – 712, doi:http://dx.doi.org/10.1016/0375-6505(95)00024-0, 1995.
- 270 Curry, W. B. and Oppo, D. W.: Glacial water mass geometry and the distribution of $\delta^{13}\text{C}$ of ΣCO_2 in the western Atlantic Ocean, *Paleoceanography*, 20, doi:10.1029/2004PA001021, 2005.
- Feely, R. A., Sabine, C. L., Hernandez-Ayon, J. M., Ianson, D., and Hales, B.: Evidence for upwelling of corrosive" acidified" water onto the continental shelf, *Science*, 320, 1490–1492, doi:10.1126/science.1155676, 2008.
- 275 Forde, E. B., Hendee, J. C., and Wanninkhof, R. H.: Hydrographic, Carbon Dioxide, Nutrient, and Productivity measurements from the South Atlantic during July and August of 1991, Tech. rep., NOAA/Atlantic Oceanographic and Meteorological Laboratories Miami, Florida 33149, 1996.
- Friis, K., Körtzinger, A., Pätsch, J., and Wallace, D. W.: On the temporal increase of anthropogenic CO_2 in the subpolar North Atlantic, *Deep-Sea Res. Pt I*, 52, 681–698, doi:10.1016/j.dsr.2004.11.017, 2005.
- 280 Friis, K., Najjar, R., Follows, M., Dutkiewicz, S., Körtzinger, A., and Johnson, K.: Dissolution of calcium carbonate: observations and model results in the subpolar North Atlantic, *Biogeosciences*, 4, 205–213, doi:10.5194/bg-4-205-2007, 2007.
- Gislefoss, J., Nydal, R., Skjelvan, I., Nes, A., Østerhus, S., Holmén, K., Jull, T., and Sonninen, E.: Carbon profiles in the Nordic Seas, Tech. rep., Radiological Dating Laboratory, Trondheim-NTH, 1995.
- 285 Gruber, N., Keeling, C. D., Bacastow, R. B., Guenther, P. R., Lueker, T. J., Wahlen, M., Meijer, H. A. J., Mook, W. G., and Stocker, T. F.: Spatiotemporal patterns of carbon-13 in the global surface oceans and the oceanic suess effect, *Global Biogeochem. Cycles*, 13, 307–335, doi:10.1029/1999GB900019, 1999.
- Gruber, N., Keeling, C. D., and Bates, N. R.: Interannual Variability in the North Atlantic Ocean Carbon Sink, *Science*, 298, 2374–2378, doi:10.1126/science.1077077, 2002.
- 290 Humphreys, M. P., Achterberg, E. P., Griffiths, A. M., McDonald, A., and Boyce, A. J.: Measurements of the stable carbon isotope composition of dissolved inorganic carbon in the northeastern Atlantic and Nordic Seas during summer 2012, *Earth Sys. Sci. Data*, 7, 127–135, doi:10.5194/essd-7-127-2015, 2015.
- Johnson, G. C., Robbins, P. E., and Hufford, G. E.: Systematic Adjustments of Hydrographic Sections for Internal Consistency, *J. Atmos. Ocean. Tech.*, 18, 1234–1244, doi:10.1175/1520-0426(2001)018<1234:SAOHSF>2.0.CO;2, 2001.
- 295 Johnson, K., Key, R., Millero, F., Sabine, C., Wallace, D., Winn, C., Arlen, L., Erickson, K., Friis, K., Galanter, M., Goen, J., Rotter, R., Thomas, C., Wilke, R., Takahashi, T., and Sutherland, S.: Carbon Dioxide, Hydrographic, and Chemical Data Obtained During the R/V Knorr Cruises in the North Atlantic Ocean on WOCE Sections AR24 (November 2 - December 5, 1996) and A24, A20, and A22 (May 30 - September 3, 1997), Carbon Dioxide Information Analysis Center, Oak Ridge National Laboratory, U.S. Department of Energy, 300 Oak Ridge, Tennessee, doi:10.3334/CDIAC/otg.ndp082, 2003.
- Körtzinger, A., Mintrop, L., and Duinker, J. C.: On the penetration of anthropogenic CO_2 into the North Atlantic Ocean, *J. Geophys. Res.*, 103, 18 681–18 689, doi:10.1029/98JC01737, 1998.

- Körtzinger, A., Rhein, M., and Mintrop, L.: Anthropogenic CO₂ and CFCs in the North Atlantic Ocean-A comparison of man-made tracers, *Geophysical Research Letters*, 26, 2065–2068, doi:10.1029/1999GL900432, 1999.
- 305
- Körtzinger, A., Quay, P. D., and Sonnerup, R. E.: Relationship between anthropogenic CO₂ and the ¹³C Suess effect in the North Atlantic Ocean, *Global Biogeochemical Cycles*, 17, 5–1–5–20, doi:10.1029/2001GB001427, 1005, 2003.
- Kroopnick, P. M.: The distribution of ¹³C of Σ CO₂ in the world oceans, *Deep-Sea Res.*, 32, 57 – 84, doi:10.1016/0198-0149(85)90017-2, 1985.
- 310
- Lee, K., Choi, S.-D., Park, G.-H., Wanninkhof, R., Peng, T.-H., Key, R., Sabine, C., Feely, R., Bullister, J., Millero, F., et al.: An updated anthropogenic CO₂ inventory in the Atlantic Ocean, *Global Biogeochem. Cycles*, 17, doi:10.1029/2003GB002067, 2003.
- Olsen, A., Omar, A. M., Bellerby, R. G., Johannessen, T., Ninnemann, U., Brown, K. R., Olsson, K. A., Olafsson, J., Nondal, G., Kivimäe, C., et al.: Magnitude and origin of the anthropogenic CO₂ increase and ¹³C Suess effect in the Nordic seas since 1981, *Global Biogeochem. Cycles*, 20, doi:10.1029/2005GB002669, 2006.
- 315
- Olsen, A., Omar, A. M., Jeansson, E., Anderson, L. G., and Bellerby, R. G. J.: Nordic seas transit time distributions and anthropogenic CO₂, *J. Geophys. Res. Oceans*, 115, doi:10.1029/2009JC005488, c05005, 2010.
- 320
- Olsen, A., Key, R. M., van Heuven, S., Lauvset, S. K., Velo, A., Lin, X., Schirnick, C., Kozyr, A., Tanhua, T., Hoppema, M., Jutterström, S., Steinfeldt, R., Jeansson, E., Ishii, M., Pérez, F. F., and Suzuki, T.: An internally consistent data product for the world ocean: the Global Ocean Data Analysis Project, version 2 (GLODAPv2), *Earth System Science Data Discussions*, 2016, 1–78, doi:10.5194/essd-2015-42, 2016.
- Pierrot, D., Brown, P., Van Heuven, S., Tanhua, T., Schuster, U., Wanninkhof, R., and Key, R. M.: CARINA TCO₂ data in the Atlantic Ocean, *Earth Syst. Sci. Data*, 2, 177–187, doi:10.5194/essd-2-177-2010, 2010.
- 325
- Quay, P. D., Sonnerup, R., Westby, T., Stutsman, J., and McNichol, A.: Changes in the ¹³C/¹²C of dissolved inorganic carbon in the ocean as a tracer of anthropogenic CO₂ uptake, *Global Biogeochem. Cycles*, 17, 1–20, doi:10.1029/2001GB001817, 2003.
- Quay, P. D., Sonnerup, R., Stutsman, J., Maurer, J., Körtzinger, A., Padin, X. A., and Robinson, C.: Anthropogenic CO₂ accumulation rates in the North Atlantic Ocean from changes in the ¹³C/¹²C of dissolved inorganic carbon, *Global Biogeochem. Cycles*, 21, 1–15, doi:10.1029/2006GB002761, 2007.
- 330
- Quay, P. D., Stutsman, J., Feely, R. A., and Juranek, L. W.: Net community production rates across the subtropical and equatorial Pacific Ocean estimated from air-sea δ¹³C disequilibrium, *Global Biogeochem. Cycles*, 23, 1–15, doi:10.1029/2008GB003193, 2009.
- 335
- Racapé, V., Pierre, C., Metzl, N., Monaco, C. L., Reverdin, G., Olsen, A., Morin, P., Vázquez-Rodríguez, M., Ríos, A. F., and Pérez, F. F.: Anthropogenic carbon changes in the Irminger Basin (1981–2006): Coupling δ¹³C DIC and DIC observations, *J. Marine Syst.*, 126, 24–32, doi:10.1016/j.jmarsys.2012.12.005, 2013.
- Rommets, J., Dapper, R., and Fransz, H.: JGOFS North Atlantic Pilot Project - R.V.Tyro Leg 3, Upper Ocean Processes, NIOZ Data Rpt 1991-3, 1991.
- 340
- Schmittner, A., Gruber, N., Mix, A., Key, R., Tagliabue, A., and Westberry, T.: Biology and air–sea gas exchange controls on the distribution of carbon isotope ratios (δ¹³C) in the ocean, *Biogeosciences*, 10, 5793–5816, doi:10.5194/bg-10-5793-2013, 2013.

- Tanhua, T., Körtzinger, A., Friis, K., Waugh, D. W., and Wallace, D. W.: An estimate of anthropogenic CO₂ inventory from decadal changes in oceanic carbon content, *P. Natl. Acad. Sci.*, 104, 3037–3042, doi:10.1073/pnas.0606574104, 2007.
- 345
- Tanhua, T., Brown, P. J., and Key, R. M.: CARINA: nutrient data in the Atlantic Ocean, *Earth Syst. Sci. Data*, 1, 7–24, doi:10.5194/essd-1-7-2009, 2009.
- Tanhua, T., Steinfeldt, R., Key, R. M., Brown, P., Gruber, N., Wanninkhof, R., Perez, F., Körtzinger, A., Velo, A., Schuster, U., van Heuven, S., Bullister, J. L., Stendardo, I., Hoppema, M., Olsen, A., Kozyr, A., Pierrot, D., Schirnick, C., and Wallace, D. W. R.: Atlantic Ocean CARINA data: overview and salinity adjustments, *Earth Syst. Sci. Data*, 2, 17–34, doi:10.5194/essd-2-17-2010, 2010a.
- 350
- Tanhua, T., van Heuven, S., Key, R. M., Velo, A., Olsen, A., and Schirnick, C.: Quality control procedures and methods of the CARINA database, *Earth Syst. Sci. Data*, 2, 35–49, doi:10.5194/essd-2-35-2010, 2010b.
- Thomas, H. and Ittekkot, V.: Determination of anthropogenic CO₂ in the North Atlantic Ocean using water mass ages and CO₂ equilibrium chemistry, *J. Marine Syst.*, 27, 325–336, 2001.
- 355
- Velo, A., Perez, F. F., Brown, P., Tanhua, T., Schuster, U., and Key, R. M.: CARINA alkalinity data in the Atlantic Ocean, *Earth Syst. Sci. Data*, 1, 45–61, doi:10.5194/essd-1-45-2009, 2009.
- Wollast, R. and Chou, L.: The carbon cycle at the ocean margin in the northern Gulf of Biscay, *Deep-Sea Res. Pt II*, 48, 3265 – 3293, doi:10.1016/S0967-0645(01)00040-6, 2001.

5 Underway measurements on the North Atlantic of $f\text{CO}_2$ and $\delta^{13}\text{C}(\text{CO}_2)$

First, all measured CRDS- $f\text{CO}_2$ and $\delta^{13}\text{C}(\text{CO}_2)$ data as well as the related air-sea disequilibrium between ocean and atmosphere will be presented as a time-line. The vessel tracks and the study area are shown in Figure 3.4. The CRDS data was obtained between May 2012 and December 2014, Licor data between March 2012 and December 2014. Please note, that there is an inherent latitudinal shift from 45°N in the west (Halifax, CA) to $50 - 55^\circ\text{N}$ at the eastern boundary of the sampling region. East of about 45°W , the sampling region is mostly influenced by the eastward flowing North Atlantic Drift Current (NADC), leading to relatively uniform water mass properties. Here, the latitudinal variation of the vessel track ($45 - 60^\circ\text{N}$) had only small influences on the measurements, mainly in form of a slightly retarded bloom onset in regions further north and therefore a delay in nutrient draw-down compared to southern regions (Henson et al., 2009b). However, the vessel track did not show a significant seasonal pattern in this area. In fact, the decision whether the vessel sailed a northward or southward route is made each time based on the position of the major low pressure systems in the North Atlantic region. This picture changes when looking at the data west of 45°W . Here, the comparability throughout the year and between the separate trips is limited by the respective influence of the two different water masses mixing in this area (Gulf Stream (GFST) and Labrador Current (LC)). Moreover, the vessel track in this area was influenced by the ice limit which has its most southward extension in late spring. In order to avoid ice bergs, the vessel was sailing further south during this time of year, resulting in an increased signature of the salinity rich GFST water from March to July. This southward shift was exceptionally distinct in 2014.

Figure 5.1 shows a Hovmoeller plot of the underway $f\text{CO}_2$ and $\delta^{13}\text{C}(\text{CO}_2)$ data. Please

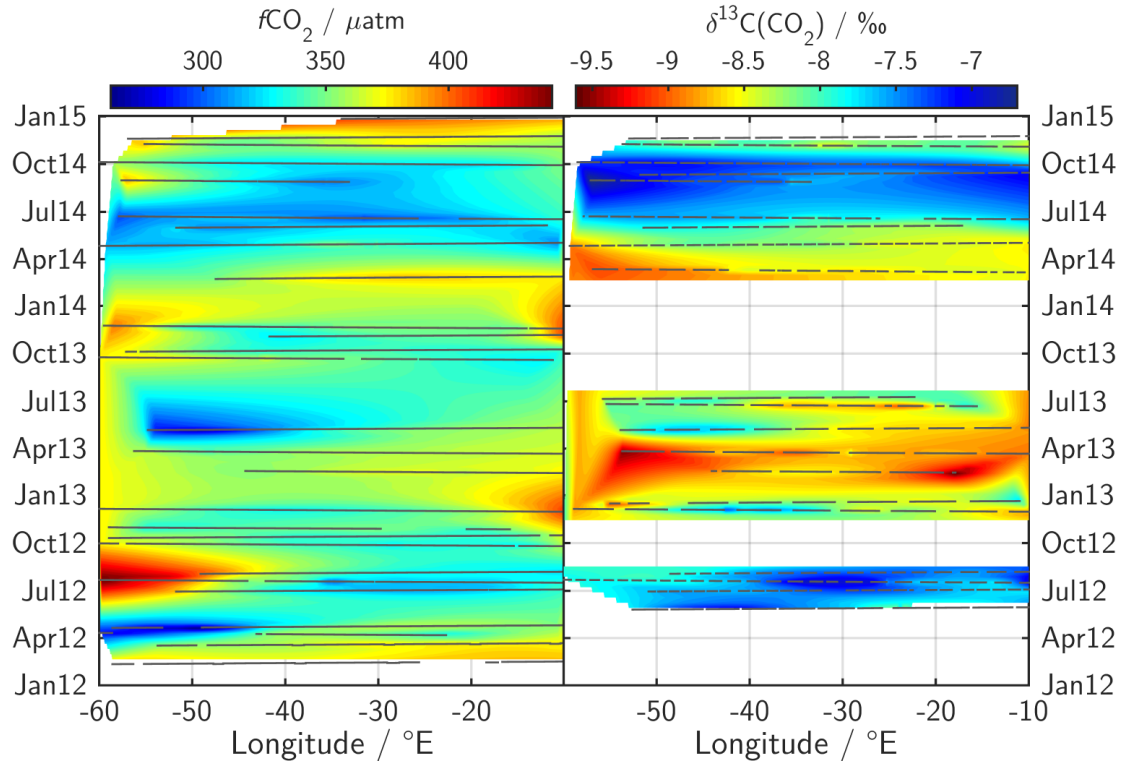


Figure 5.1: Hovmoeller plots of underway $f\text{CO}_2$ (left panel) and $\delta^{13}\text{C}(\text{CO}_2)$ (right panel).

note, that the color coding is inverted for the $\delta^{13}\text{C}(\text{CO}_2)$ so that the anti correlated behavior of both parameter shows the same color pattern. Unfortunately, problems with the CRDS analyzer resulted in two gaps of the isotope data in fall 2012 and fall/winter 2013. For the $f\text{CO}_2$ data these gaps were filled by using the NDIR data. For some trips, the SST data had to be reconstructed from the equilibrator temperature and the water flow rate. Since the $f\text{CO}_2$ has a high sensitivity towards temperature changes, only isotope data is presented for these trips.

Both parameters are influenced by a superposition of the effects of temperature variability, biological production and respiration and changing water masses. The $f\text{CO}_2$ shows some reoccurring seasonal pattern, even though the spatial extension and the intensity can vary from year to year. Generally, one can observe the development of the $f\text{CO}_2$ decrease caused by the spring bloom from west towards east. During the summer season this decrease is opposing the temperature effect, which causes an increase of the $f\text{CO}_2$ through warming. Temperature variations throughout the year are in the order of 15°C in the west to 5°C in the east and thus can easily change the $f\text{CO}_2$ about 20–50% (Takahashi et al., 1993). In the west (-50 to -60°E), this influence is visible every year

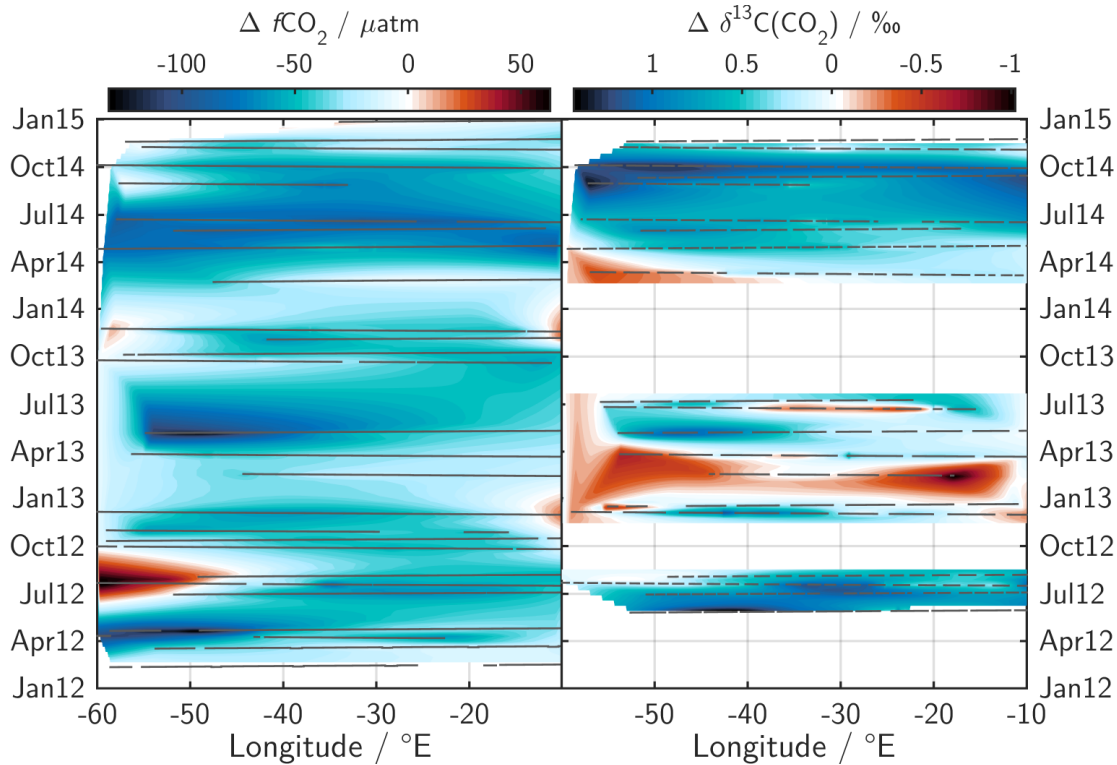


Figure 5.2: Hovmoeller plots of the atmospheric disequilibrium of underway $f\text{CO}_2$ (left panel) and $\delta^{13}\text{C}(\text{CO}_2)$ (right panel). Blue colors indicate undersaturation of $f\text{CO}_2$ and a heavier CO_2 pool than in the atmosphere, red colors indicate supersaturated water with a lighter carbon dioxide pool.

as very high $f\text{CO}_2$ between July and October. This pattern also doesn't show the same intensity every year. Other areas with high $f\text{CO}_2$ were found at the eastern side of the basin between October and March. Since the temperature varies much less in this area, this increase is most likely caused by convective mixing of water with a high carbon load by the deepening of the mixed layer in winter or respiration processes on the shelf nearby. Very low CO_2 fugacities (on average $250 - 300 \mu\text{atm}$ and $150 \mu\text{atm}$ in small scale bloom patches) were observed at the front of LW and GFST waters in April/May 2012 and 2013. In 2014, the vessel tracks were shifted more southwards, so that the front region was not sampled. In many regions, a small second $f\text{CO}_2$ minimum in October is discernible, which is more distinct in the western part. The $\delta^{13}\text{C}(\text{CO}_2)$ is less sensitive to temperature variability. The temperature dependence of $\delta^{13}\text{C}(\text{CO}_2)$ is caused by the temperature dependent fractionation to DIC. Additionally, the influence of warming is in the same direction as that of primary production. This leads to an additional increase

during summer, producing a heavy isotope signature in this season, and a light CO_2 pool during winter by summing up the effects of cooling and the addition of respirational, light carbon by convective mixing. However, many biology-related patterns that were observed for $f\text{CO}_2$ can also be seen in the $\delta^{13}\text{C}(\text{CO}_2)$, albeit with opposite sign, such as the propagation of the bloom onset from east to west and the intense front bloom in April/May.

The air-sea disequilibrium is shown for both, $f\text{CO}_2$ and $\delta^{13}\text{C}(\text{CO}_2)$, in Figure 5.2. For both parameters, the sign of the disequilibrium is color-coded. Blue colors indicate undersaturation of $f\text{CO}_2$ and a heavier CO_2 pool than in the atmosphere, red colors indicate supersaturated water with a lighter CO_2 pool. The basic patterns described above are also visible in this depiction. The North Atlantic is mostly undersaturated in $f\text{CO}_2$ and almost reaches equilibrium in late winter, prior to the onset of spring bloom. Supersaturated conditions can only be observed for the regions and time windows with very high $f\text{CO}_2$. The supersaturation in the western part is caused by a dominance of the thermal effect over the effects of primary production.

Takahashi et al. (2009) found different shapes of the $p\text{CO}_2$ seasonalities for tropical and subpolar water in the North Atlantic with a supersaturation related $p\text{CO}_2$ maximum in August for subtropical areas, while the more polar water is undersaturated during the entire year with a minimum in June and a maximum during winter. The western part of our sampling area is a transition region between these two regimes, and, therefore, showing characteristics of both, while the eastern part shows clear subpolar characteristics in this point.

The $\delta^{13}\text{C}(\text{CO}_2)$ disequilibrium changes from lighter CO_2 than the atmosphere in winter time to heavier CO_2 at the end of summer. Since both main drivers of $\delta^{13}\text{C}(\text{CO}_2)$, temperature and primary production, have a similar shape, the pattern of the atmospheric $\delta^{13}\text{C}(\text{CO}_2)$ disequilibrium is more uniform than that of $\Delta f\text{CO}_2$.

Though three years are not enough for getting a clear picture of interannual variability, the summer $f\text{CO}_2$ minimum is more pronounced during the year 2014 whereas the winter maximum $f\text{CO}_2$ is reduced during the winter 2012/2013. This pattern in the CO_2 fugacity can be seen as opposing behavior in the isotope ratio data, although the interpretation is clearly limited by the data gaps during fall and winter 2013. The interannual variations can be explained by considering wind velocity and mixed layer depth (MLD) during these years. Figure 5.3 shows monthly means of MLD and wind velocity along 50°N from January 2012 to December 2014. Both, the deepening of the mixed layer

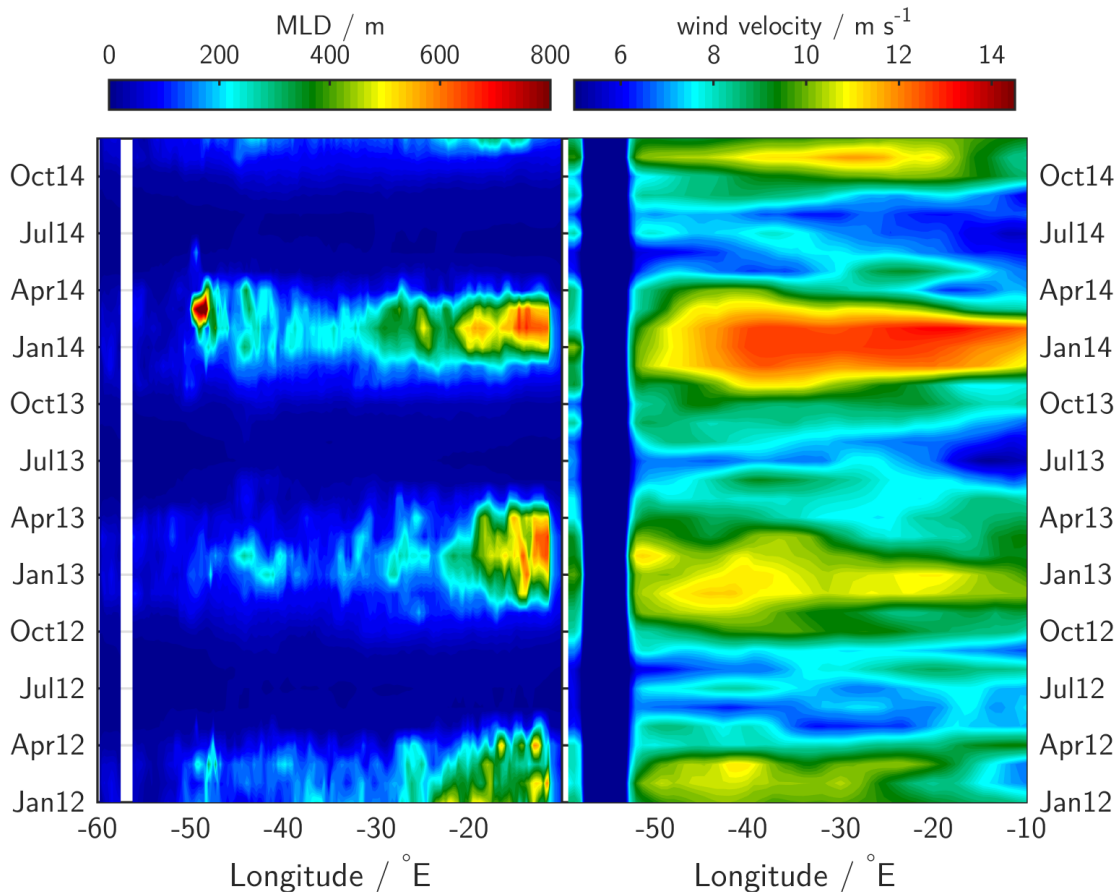


Figure 5.3: Monthly means of mixed layer depth (left panel) and wind velocity (right panel) at 50°N from January 2012 to December 2014.

as well as the wind velocity are clearly enhanced during winter 2013/2014 compared to winter 2012/2013. The deeper winter mixed layer leads to an enhanced entrainment of nutrients into the surface water. This causes the high $f\text{CO}_2$ /low $\delta^{13}\text{C}(\text{CO}_2)$ conditions in winter and provides the basis for an amplified spring bloom.

The main driver for interannual variability of the climate and ocean system of the North Atlantic is the North Atlantic Oscillation (NAO). An overview of monthly means of the NAO index from 2002 to 2016, as well as the year to year variation in winter time NAO can be found in Figure 5.4. The NAO can influence surface $f\text{CO}_2$ and $\delta^{13}\text{C}(\text{CO}_2)$ through many different paths, such as changes in temperature, salinity, wind, heat flux, biological fluxes, vertical mixing, lateral transport or freshwater input. Some of these factors take full effect directly (e.g. wind changes and corresponding changes of wind

driven surface currents in the subtropical gyre), whereas others show a delay of a few years (e.g. changes in the deep convection of the Labrador sea) (Thomas et al., 2008). The interpretation of NAO- $f\text{CO}_2$ correlations is even further complicated by the fact that the different influences can have the opposite direction, overlap each other and are not independent from each other. The increase in wind velocity and deep convection can be attributed to a positive winter mean NAO index (DJFM) during winter 2013/2014, while the winter 2012/2013 has a negative winter mean NAO index. This is in good agreement with the work of Henson et al. (2009a), who found that positive NAO years are correlated with deep winter mixed layers. These deep mixed layers cause a delayed spring bloom onset in the polar North Atlantic (light limited regime) resulting in a reduced bloom intensity and an increased bloom in subtropical water (nutrient limited regime) due to the enhanced nutrient supply. Most of our measurements were conducted in the transition zone between clearly subtropical and subpolar water masses. On the one hand, they show subpolar $\Delta f\text{CO}_2$ characteristics but on the other hand, they show summer oligotrophy (see seasonal cycles of nutrients in Chapter 7). Depleted nutrients and a fall bloom triggered by nutrient re-supply is a subtropical signature. Henson et al. (2009a) also stated that the bloom timing in this transition zone can vary tremendously between that of subtropical water (November) and polar water (April) as a response of a changing winter mean NAO index. Unfortunately, the poor data coverage during spring and summer 2013, the sampling interval of 2-3 weeks, in the best case, and the varying latitude during the crossings obstruct the possibility to detect a difference in bloom onset between both years.

For getting a better understanding of how interannual variations of the NAO or maybe other processes such as Great Salinity Anomalies (GSA) affect the marine carbon cycle and, thus, the $\Delta f\text{CO}_2$ and $\Delta\delta^{13}\text{C}(\text{CO}_2)$ in the North Atlantic more measurements in this area are necessary. The three years presented here are not enough for getting the general picture of forcing and response cycles. Moreover, the variability of $f\text{CO}_2$ cannot be explained without getting a better understanding of the interaction of physical forcing, nutrient cycling, triggering, supporting and limiting factors of phytoplankton and zooplankton growth. Besides measuring the seasonal and interannual variability of additional parameter, such as plankton community structure or growth rates of phytoplankton, changes in isotope signatures are a useful tool for monitoring e.g. the impact of N_2 fixation on the bioavailable nitrogen pool. A good leverage point for getting the bigger picture could be the combination of the here presented variations in CO_2 and other

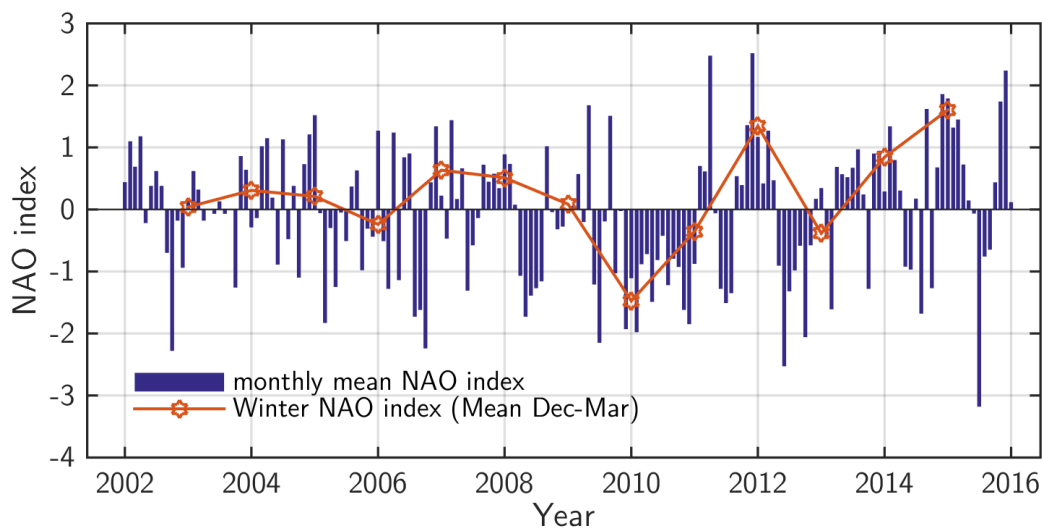


Figure 5.4: Variations of the NAO index (blue bars) and its winter mean values (red stars, December to March average) during the period 2002-2016.

nutrients with data from the CPR program (Continuous Plankton Recorder) where relative changes in the phytoplankton production are tracked since 1948 from commercial vessels.

6 Modeling inventory changes of carbon and nutrients

This Chapter deals with the impact of air-sea gas exchange, net community production and convective mixing on the surface ocean carbon and nutrient concentrations. A box model was set up to calculate the quantitative contribution of each process and the seasonal variation of each flux. First, the seasonal changes due to convective mixing (MIX), air-sea gas exchange (ASE) and net community production (NCP, referred to as BIO in the following Figures and Equations) will be presented for four boxes across the North Atlantic (1025, 2540, 4055 - sub, 4055 - pol). After that, the respective yearly surface ocean inventory changes due to ASE, MIX and the net community production during spring and fall bloom (BIO,S and BIO,F) will be discussed. For carbon, the net community production flux was calculated based not only on the DIC concentration and $f\text{CO}_2$ (BIO), but also based independently on their stable carbon isotope ratios (BIOC13). At the end of this Chapter, additional benefits and their practical limitations of the usage of stable carbon isotopes for separating carbon fluxes in the surface ocean stemming from primary production and mixing will be addressed.

The division of the data into four regional boxes, the setup of the box model itself and the calculation procedure of the input variables is described in Sections 3.3.5 and 3.4. The harmonic fits of all input variables and their seasonality is discussed in Chapter 7. In order to exclude DIC variations caused by evaporation and precipitation, a salinity normalized DIC was used in the calculation.

6.1 Seasonal evolution and integrated inventory changes of carbon and nutrients

The inventory changes in DIC, nitrate, phosphate and silicate due to net community production as the balance between autotrophic primary production and autotrophic and heterotrophic respiration are calculated from the measured concentration changes corrected for fluxes due to MIX and ASE. The seasonality of these inventory changes in each box is shown in Figures 6.1 to 6.4. Please note, that all fluxes are shown with respect to the respective surface ocean reservoirs. Fluxes increasing the species' inventory of the surface ocean are positive and those removing are negative. Especially for the air-sea gas exchange this has to be kept in mind because this parameter is normally expressed from an atmospheric perspective, resulting in opposite signs. All in all, the inventory changes for carbon and nutrients give a consistent picture. The parameters in all boxes show an alternation of a negative flux due to net community production in spring which is declining towards the summer and then increasing again in fall, and positive fluxes due to convective mixing during the winter period. The carbon flux due to air-sea gas exchange was positive for all calculations and relatively small in comparison to the fluxes mediated by other processes. The difference between net community production calculated from DIC only, and the combination of DIC and $\delta^{13}\text{C}(\text{DIC})$ is not significant. The timing of the flux caused by convective mixing as calculated by the box model starts very early for all parameters and, thus, does not capture the observed concentration changes during this period. This is caused by inaccuracies of the harmonic fit of the mixed layer depth which has its maximum earlier than the mean maximal mixed layer of the box, especially in the western boxes. This inaccuracy in the onset of the mixing flux is increasing towards the west, and, as a consequence, the positive flux of net community production prior to the spring bloom onset is increasing. Another source of uncertainty to the mixing flux is the different spatial and temporal resolution of MLD data, mean summer profiles and the underway measurements. By comparing the four boxes, it can be stated that the box 4055 - sub generally shows the highest rates of net primary production ($-0.16 \text{ mol C m}^{-2}\text{d}^{-1}$, $-32 \text{ mmol N m}^{-2}\text{d}^{-1}$, $-1.0 \text{ mmol P m}^{-2}\text{d}^{-1}$) while the polar box has the lowest ($-0.045 \text{ mol C m}^{-2}\text{d}^{-1}$, $-5.0 \text{ mmol N m}^{-2}\text{d}^{-1}$, $-0.2 \text{ mmol P m}^{-2}\text{d}^{-1}$). For silicate, box 2540 is showing the highest consumption rate and also in box 1025 the rate of silicate inventory changes due to NCP is high in relation to the rate for DIC.

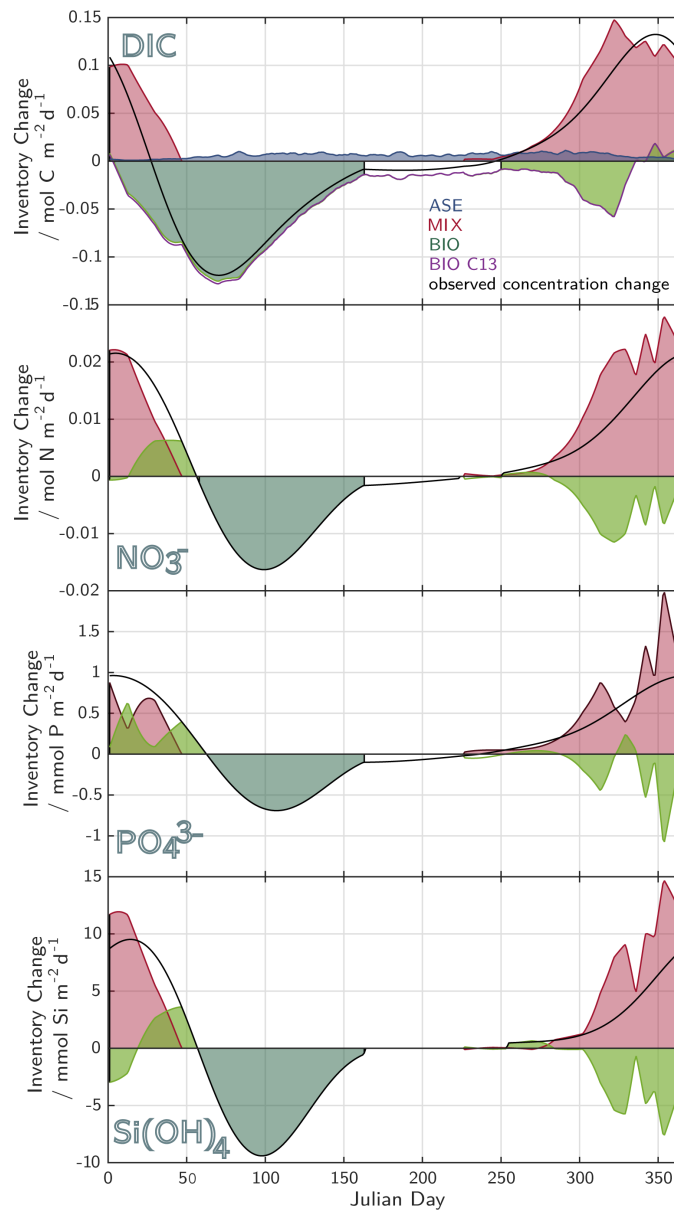


Figure 6.1: The inventory changes of inorganic carbon, nitrate, phosphate and silicate for box 1025.

Fluxes due to air-sea gas exchange are displayed in blue, convective mixing in red and net community production in green (dark green: spring bloom, light green: fall/winter bloom). The net community production of carbon calculated from isotope measurements is shown in purple. The time period used for the integrated values in the next Section is shown as colored area (BIO-C13 was integrated over the same period as BIO). The black lines represents the rate of concentration changes based on the harmonic fits.

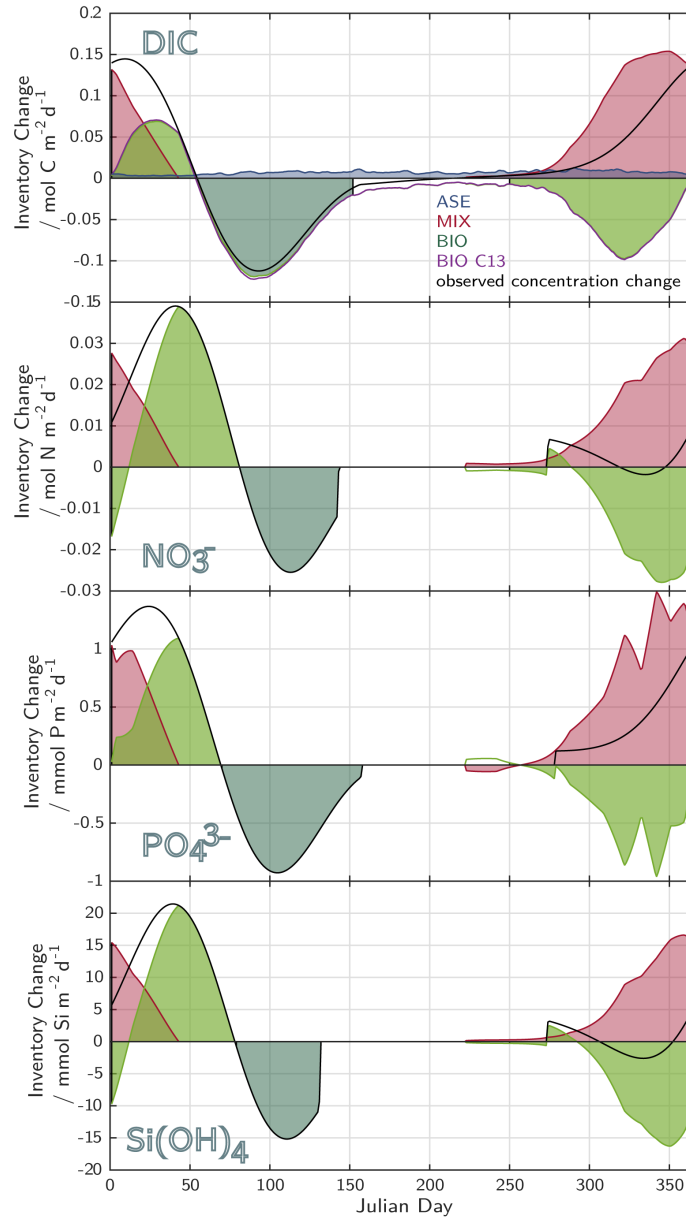


Figure 6.2: The inventory changes of inorganic carbon, nitrate, phosphate and silicate for box 2540. Fluxes due to air-sea gas exchange are displayed in blue, convective mixing in red and net community production in green (dark green: spring bloom, light green: fall/winter bloom). The net community production of carbon calculated from isotope measurements is shown in purple. The time period used for the integrated values in the next Section is shown as colored area (BIO-C13 was integrated over the same period as BIO). The black lines represents the rate of concentration changes based on the harmonic fits.

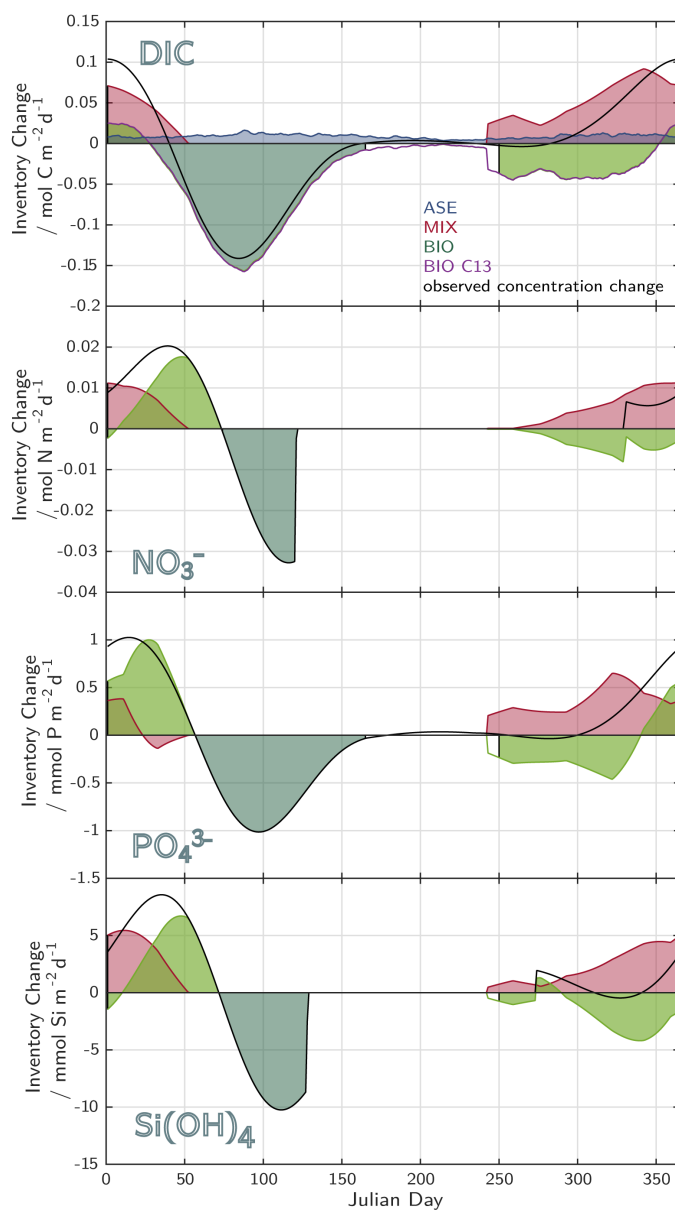


Figure 6.3: The inventory changes of inorganic carbon, nitrate, phosphate and silicate for box 4055 - sub. Fluxes due to air-sea gas exchange are displayed in blue, convective mixing in red and net community production in green (dark green: spring bloom, light green: fall/winter bloom). The net community production of carbon calculated from isotope measurements is shown in purple. The time period used for the integrated values in the next Section is shown as colored area (BIO-C13 was integrated over the same period as BIO). The black lines represents the rate of concentration changes based on the harmonic fits.

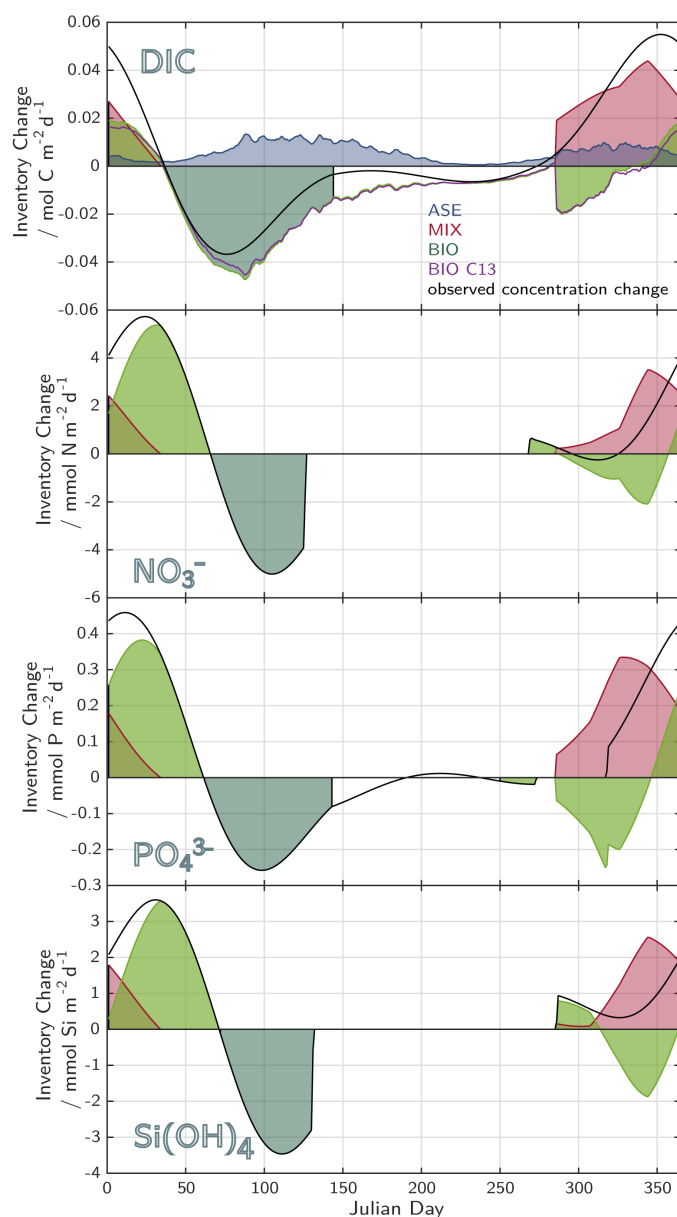


Figure 6.4: The inventory changes of inorganic carbon, nitrate, phosphate and silicate for box 4050 - pol. Fluxes due to air-sea gas exchange are displayed in blue, convective mixing in red and net community production in green (dark green: spring bloom, light green: fall/winter bloom). The net community production of carbon calculated from isotope measurements is shown in purple. The time period used for the integrated values in the next Section is shown as colored area (BIO-C13 was integrated over the same period as BIO). The black lines represents the rate of concentration changes based on the harmonic fits.

<p style="text-align: center;">4055 - pol</p> $\Delta C_{\text{BIO,S}} = (-3.23 \pm 0.43) \text{ molC m}^{-2} \text{ yr}^{-1}$ $\Delta C_{\text{BIO,S,C13}} = (-3.09 \pm 0.43) \text{ molC m}^{-2} \text{ yr}^{-1}$ $\Delta C_{\text{BIO,F}} = (-0.18 \pm 0.81) \text{ molC m}^{-2} \text{ yr}^{-1}$ $\Delta C_{\text{BIO,F,C13}} = (-0.04 \pm 0.81) \text{ molC m}^{-2} \text{ yr}^{-1}$ $\Delta C_{\text{MIX}} = (3.03 \pm 0.82) \text{ molC m}^{-2} \text{ yr}^{-1}$ $\Delta C_{\text{ASE}} = (2.11 \pm 1.05) \text{ molC m}^{-2} \text{ yr}^{-1}$		
$\Delta N_{\text{BIO,S}} = (-0.224 \pm 0.026) \text{ molN m}^{-2} \text{ yr}^{-1}$ $\Delta N_{\text{BIO,F}} = (0.179 \pm 0.051) \text{ molN m}^{-2} \text{ yr}^{-1}$ $\Delta N_{\text{MIX}} = (0.169 \pm 0.071) \text{ molN m}^{-2} \text{ yr}^{-1}$	<p style="text-align: center;">2540</p> $\Delta C_{\text{BIO,S}} = (-7.3 \pm 1.1) \text{ molC m}^{-2} \text{ yr}^{-1}$ $\Delta C_{\text{BIO,S,C13}} = (-7.5 \pm 1.1) \text{ molC m}^{-2} \text{ yr}^{-1}$ $\Delta C_{\text{BIO,F}} = (-2.9 \pm 1.4) \text{ molC m}^{-2} \text{ yr}^{-1}$ $\Delta C_{\text{BIO,F,C13}} = (-2.9 \pm 1.4) \text{ molC m}^{-2} \text{ yr}^{-1}$ $\Delta C_{\text{MIX}} = (125 \pm 2.0) \text{ molC m}^{-2} \text{ yr}^{-1}$ $\Delta C_{\text{ASE}} = (2.54 \pm 0.54) \text{ molC m}^{-2} \text{ yr}^{-1}$	<p style="text-align: center;">1025</p> $\Delta C_{\text{BIO,S}} = (-11.3 \pm 1.9) \text{ molC m}^{-2} \text{ yr}^{-1}$ $\Delta C_{\text{BIO,S,C13}} = (-11.6 \pm 2.0) \text{ molC m}^{-2} \text{ yr}^{-1}$ $\Delta C_{\text{BIO,F}} = (-1.8 \pm 2.2) \text{ molC m}^{-2} \text{ yr}^{-1}$ $\Delta C_{\text{BIO,F,C13}} = (-1.9 \pm 2.3) \text{ molC m}^{-2} \text{ yr}^{-1}$ $\Delta C_{\text{MIX}} = (12.0 \pm 4.0) \text{ molC m}^{-2} \text{ yr}^{-1}$ $\Delta C_{\text{ASE}} = (2.22 \pm 0.47) \text{ molC m}^{-2} \text{ yr}^{-1}$
<p style="text-align: center;">4055 - sub</p> $\Delta C_{\text{BIO,S}} = (-10.7 \pm 1.2) \text{ molC m}^{-2} \text{ yr}^{-1}$ $\Delta C_{\text{BIO,S,C13}} = (-10.7 \pm 1.2) \text{ molC m}^{-2} \text{ yr}^{-1}$ $\Delta C_{\text{BIO,F}} = (-2.9 \pm 1.5) \text{ molC m}^{-2} \text{ yr}^{-1}$ $\Delta C_{\text{BIO,F,C13}} = (-2.9 \pm 1.5) \text{ molC m}^{-2} \text{ yr}^{-1}$ $\Delta C_{\text{MIX}} = (8.8 \pm 2.1) \text{ molC m}^{-2} \text{ yr}^{-1}$ $\Delta C_{\text{ASE}} = (3.20 \pm 0.54) \text{ molC m}^{-2} \text{ yr}^{-1}$	$\Delta N_{\text{BIO,S}} = (-1.13 \pm 0.11) \text{ molN m}^{-2} \text{ yr}^{-1}$ $\Delta N_{\text{BIO,F}} = (0.15 \pm 0.23) \text{ molN m}^{-2} \text{ yr}^{-1}$ $\Delta N_{\text{MIX}} = (2.20 \pm 0.32) \text{ molN m}^{-2} \text{ yr}^{-1}$	$\Delta N_{\text{BIO,S}} = (-1.06 \pm 0.14) \text{ molN m}^{-2} \text{ yr}^{-1}$ $\Delta N_{\text{BIO,F}} = (-0.29 \pm 0.41) \text{ molN m}^{-2} \text{ yr}^{-1}$ $\Delta N_{\text{MIX}} = (2.09 \pm 0.59) \text{ molN m}^{-2} \text{ yr}^{-1}$
$\Delta P_{\text{BIO,S}} = (-62 \pm 75) \text{ mmolP m}^{-2} \text{ yr}^{-1}$ $\Delta P_{\text{BIO,F}} = (19 \pm 16) \text{ mmolP m}^{-2} \text{ yr}^{-1}$ $\Delta P_{\text{MIX}} = (50 \pm 160) \text{ mmolP m}^{-2} \text{ yr}^{-1}$	$\Delta P_{\text{BIO,S}} = (-50.3 \pm 7.2) \text{ mmolP m}^{-2} \text{ yr}^{-1}$ $\Delta P_{\text{BIO,F}} = (0 \pm 18) \text{ mmolP m}^{-2} \text{ yr}^{-1}$ $\Delta P_{\text{MIX}} = (100 \pm 19) \text{ mmolP m}^{-2} \text{ yr}^{-1}$	$\Delta P_{\text{BIO,S}} = (-44 \pm 5.6) \text{ mmolP m}^{-2} \text{ yr}^{-1}$ $\Delta P_{\text{BIO,F}} = (0 \pm 23) \text{ mmolP m}^{-2} \text{ yr}^{-1}$ $\Delta P_{\text{MIX}} = (92 \pm 32) \text{ mmolP m}^{-2} \text{ yr}^{-1}$
$\Delta \text{Si}_{\text{BIO,S}} = (-0.418 \pm 0.052) \text{ molSi m}^{-2} \text{ yr}^{-1}$ $\Delta \text{Si}_{\text{BIO,F}} = (0.03 \pm 0.11) \text{ molSi m}^{-2} \text{ yr}^{-1}$ $\Delta \text{Si}_{\text{MIX}} = (0.47 \pm 0.16) \text{ molSi m}^{-2} \text{ yr}^{-1}$	$\Delta \text{Si}_{\text{BIO,S}} = (-0.602 \pm 0.048) \text{ molSi m}^{-2} \text{ yr}^{-1}$ $\Delta \text{Si}_{\text{BIO,F}} = (0.05 \pm 0.15) \text{ molSi m}^{-2} \text{ yr}^{-1}$ $\Delta \text{Si}_{\text{MIX}} = (1.08 \pm 0.15) \text{ molSi m}^{-2} \text{ yr}^{-1}$	$\Delta \text{Si}_{\text{BIO,S}} = (-0.576 \pm 0.073) \text{ molSi m}^{-2} \text{ yr}^{-1}$ $\Delta \text{Si}_{\text{BIO,F}} = (-0.19 \pm 0.25) \text{ molSi m}^{-2} \text{ yr}^{-1}$ $\Delta \text{Si}_{\text{MIX}} = (0.89 \pm 0.32) \text{ molSi m}^{-2} \text{ yr}^{-1}$

Figure 6.5: Integrated inventory changes of inorganic carbon, nitrate, phosphate and silicate for each box. The time periods used for the integrals are shown as shaded areas in Figures 6.1 to 6.4.

Table 6.1: Comparison of different estimates on net community production.

Source	Location	Time period	Rate/Integral	Method
Chipman et al. (1993)	NABE (47°N, 20°W)	25-Apr-8.May 1990	$(84 \pm 18) \text{mmol C m}^{-2} \text{d}^{-1}$	^{14}C incubation method
Körtzinger et al. (2008)	NABE (47°N, 20°W)	25-Apr-8.May 1990	$(82 \pm 17) \text{mmol C m}^{-2} \text{d}^{-1}$	DIC drawdown
	PAP (49°N, 16.5°W)	Mar-Aug 2004	$(-6.4 \pm 1.1) \text{mol C m}^{-2}$	DIC drawdown
Quay et al. (2012)	PAP (49°N, 16.5°W)	Aug-Nov 2004	$(2.6 \pm 1.1) \text{mol C m}^{-2}$	DIC drawdown
	Basin wide (same as this study)	Winter	$(8 \pm 7) \text{mmol C m}^{-2} \text{d}^{-1}$	O ₂ budget
Alkire et al. (2012)	61°N, 26°W	May 2008	$(62 \pm 9) \text{mmol C m}^{-2} \text{d}^{-1}$	O ₂ +Ar budgets
	61°N, 26°W	23-27.Apr 2008	0.3mol C m^{-2}	O ₂ +Ar budgets
	61°N, 26°W	13.-16.May 2008	$(66 \text{mmol C m}^{-2} \text{d}^{-1})$ 0.8mol C m^{-2} $(115 \text{mmol C m}^{-2} \text{d}^{-1})$	O ₂ +Ar budgets
Alkire et al. (2014)	61°N, 26°W	13.-16.May 2008	$(-16 \pm 10) \text{mmol N m}^{-2} \text{d}^{-1}$ (bloom)	NO ₃ ⁻ drawdown
	61°N, 26°W	Apr to Jun 2008	$(3 \pm 8) \text{mmol N m}^{-2} \text{d}^{-1}$ (post bloom)	O ₂ +POC budgets
Ostle et al. (2015)	61°N, 26°W	3.-26.Jun 2008	2.1mol C m^{-2} $(25 \text{mmol C m}^{-2} \text{d}^{-1})$	O ₂ +POC budgets
	48-50°N, 10-30°W	Apr 2012-Feb 2013	1.0mol C m^{-2} $(32 \text{mmol C m}^{-2} \text{d}^{-1})$	DIC drawdown
	40-48°N, 40-50°W	Apr 2012-Feb 2013	$0.32 \text{mmol C m}^{-3} \text{d}^{-1}$ $(\approx 15 \text{mmol C m}^{-2} \text{d}^{-1})$ $0.36 \text{mmol C m}^{-3} \text{d}^{-1}$ $(\approx 11 \text{mmol C m}^{-2} \text{d}^{-1})$	DIC drawdown

In Figure 6.5 the integrated inventory changes are displayed. The annual flux due to air-sea gas exchange is increasing from east to west, which is in agreement with the climatology of Takahashi et al. (2009). The magnitude of the flux, and the fact that it is increasing towards the western subtropical part of our sampling region is also in agreement with earlier studies (west: $3.5 \text{ mol C m}^{-2}\text{yr}^{-1}$, east: $3.24 \text{ mol C m}^{-2}\text{yr}^{-1}$ (2002/2003, Lüger et al. (2006)), $2.4\text{-}3.0 \text{ mol C m}^{-2}\text{yr}^{-1}$ (2000, Takahashi et al. (2009)), west: $2.7 \text{ mol C m}^{-2}\text{yr}^{-1}$, east: $2.4 \text{ mol C m}^{-2}\text{yr}^{-1}$ (2006/2007, Steinhoff (2010))). Also the long-term mean for this region of $2\text{-}3 \text{ mol C m}^{-2}\text{yr}^{-1}$ fits well with our calculations (Landschützer et al., 2014). The use of different wind products as well as different parametrizations of k can, of course, cause changes in the calculated ASE flux and the inclusion of the uncertainty of k increases directly the overall uncertainty.

The integrated flux due to convection is decreasing from east to west for all parameters caused by the reduced maximal mixed layer depth. However, this flux introduces the largest uncertainty since the actual true conditions underneath the mixed layer can differ significantly from the mean depth profile at the end of the spring bloom period that was used in the calculation. The integration of the mixing flux until the maximal winter concentration reduces the error in the timing that is visible in Figures 6.1 to 6.4. The model seems to overestimate the entrainment fluxes of carbon and nutrients in the eastern boxes.

Generally, the fluxes of phosphate are small in comparison to nitrate and carbon, especially in the eastern and central box. N:P and C:P ratios of NCP during the spring bloom have values of N:P = 24 and C:P = 260 (box 1025), which is much higher than those that would be expected for a formation of biomass close to the Redfield ratio (Anderson and Sarmiento, 1994) and those estimated from the relative nutrient drawdowns. Only box 4055 - sub shows a C:P ratio that is in the order of those calculated in Chapter 8 (170). However, the C:N ratios during spring bloom of 12.8 (box 1025), 6.6 (box 2540), 10.5 (box 4055 - sub) and 14.4 (box 4055 - pol) are in good agreement with earlier studies which also found a production of carbon rich biomass (Körtzinger et al., 2008; Sambrotto et al., 1993). One process that causes an elevated fraction of consumed DIC in relation to consumed nitrate is the production of particulate inorganic carbon (PIC) by coccolithophores. N_2 fixation can also be a reason for an elevated C:N ratio in NCPs determined from concentration drawdowns. Especially in the subtropical box, this could be a reason. However, indication for N_2 fixing biomass was derived for all boxes except for box 4055 - pol (see Chapter 9).

Another interesting pattern is the bloom in fall. Such a bloom is known for subtropical regions that experience summer oligotrophy (Lipschultz, 2001). The deepening of the mixed layer in fall returns nutrients to the surface. Since all regions run into nutrient depletion, a nutrient-triggered bloom in fall/winter can be expected to occur across the entire sampling area. However, the flux calculated for NCP of carbon in fall is only significant in boxes 2540 and 4055 - sub, and for the nutrients only in the box 4055 - sub. Its magnitude in relation to the spring bloom varies between 27% (4055 - sub) and 40% (2540). The respective C:N ratio during the fall bloom is 19 (2540) and 9.3 (4055 - sub).

The problem of comparing the annual or semiseasonal fluxes shown in Figure 6.5 to other studies is that most studies report a daily flux for the observed period, which is mostly a relative short time period (see Table 6.1). However, this rate can vary extremely throughout the year (see Figures 6.1 - 6.4). The flux for the spring bloom reported by Körtzinger et al. (2008) of $(-6.4 \pm 1.1) \text{ mol C m}^{-2}$ is slightly lower than our estimate in the same region (box 1025), but fits well with the spring integral of the neighbor box 2540. The finding that a significant fraction of the NCP occurs prior to the onset of summer stratification could be confirmed. Rates of inventory changes during the spring that are reported in the literature also fit well with the daily inventory changes in the Figures above at the respective time of year (Chipman et al., 1993; Quay et al., 2012; Alkire et al., 2012, 2014). The rate of nitrate uptake observed in this work is also in good agreement with values reported by Alkire et al. (2012).

6.2 Chances and limitations in using stable carbon isotopes for flux calculations

The use of stable isotopes can principally improve flux calculations by adding an equation to the system of equations that needs to be solved. It runs into limitation, however, when this additional equation comes with more unknown variables or when the uncertainties involved become too high. For our application, the isotopic signatures of the respective fluxes need to be known. For each isotopomer, an individual budget can be formed. For the surface ocean carbon cycle, the budget fluxes for the overall DIC and for the ^{13}C fraction of DIC can be calculated as follows.

$$\Delta\text{DIC} = \Delta\text{ASE} + \Delta\text{MIX} + \Delta\text{PP} + \Delta\text{RES} + \Delta\text{LAT} + \Delta\text{DIF} \quad (6.1)$$

$$\begin{aligned} \Delta(\alpha_{\text{DIC}}) \times \text{DIC} = & \Delta(\alpha_{\text{ASE}} \times \text{ASE}) + \Delta(\alpha_{\text{MIX}} \times \text{MIX}) + \Delta(\alpha_{\text{PP}} \times \text{PP}) \\ & + \Delta(\alpha_{\text{RES}} \times \text{RES}) + \Delta(\alpha_{\text{LAT}} \times \text{LAT}) + \Delta(\alpha_{\text{DIF}} \times \text{DIF}) \end{aligned} \quad (6.2)$$

with ΔDIC being the change in DIC concentration, ΔASE the flux caused by air-sea gas exchange, ΔMIX that stemming from convective mixing, ΔPP carbon fixation by primary production, ΔRES respiration, ΔLAT a flux caused by lateral transport, ΔDIF vertical diffusion between mixed layer and underlying waters and α the respective isotopic signatures of the fluxes.

In the box model discussed above, both equations were simplified by combining primary production and respiration to net community production (BIO). Assuming that the net flux through lateral transport is small in comparison with the biological flux and that vertical diffusion can only cause significant changes in the DIC concentration when the mixed layer is shallow, and therefore does not have a large influence on the annual budget, these two fluxes can be neglected. Now, all variables are known and the equations can be solved for BIO.

$$\Delta\text{BIO} = \Delta\text{DIC} - \Delta\text{ASE} - \Delta\text{MIX} \quad (6.3)$$

$$\Delta\text{BIO} = \frac{\Delta(\alpha_{\text{DIC}} \times \text{DIC}) - \Delta(\alpha_{\text{ASE}} \times \text{ASE}) - \Delta(\alpha_{\text{MIX}} \times \text{MIX})}{\alpha_{\text{BIO}}} \quad (6.4)$$

As discussed above, both estimates differ, but not significantly. Equation 6.4 is much more sensitive towards changes in overall inorganic carbon concentrations than towards changes in the isotopic signature. In this application, the additional knowledge of $\delta^{13}\text{C}(\text{DIC})$ does, therefore, not provide significant benefit.

Another approach is to just neglect either LAT or DIF and to combine the two arising Equations 6.5 and 6.6. Now, either LAT or DIF can be calculated by estimating the respective α_{LAT} or α_{DIF} (Equations 6.7 and 6.8).

$$\Delta\text{DIC} = \Delta\text{ASE} + \Delta\text{MIX} + \Delta\text{BIO} + \Delta\text{LAT} \quad (6.5)$$

$$\Delta(\alpha_{\text{DIC}}) \times \text{DIC} = \Delta(\alpha_{\text{ASE}} \times \text{ASE}) + \Delta(\alpha_{\text{MIX}} \times \text{MIX}) + \Delta(\alpha_{\text{BIO}} \times \text{BIO}) + \Delta(\alpha_{\text{LAT}} \times \text{LAT}) \quad (6.6)$$

$$\Delta\text{BIO} = \frac{(\alpha_{\text{DIC}} - \alpha_{\text{LAT}}) \times \Delta\text{DIC} - (\alpha_{\text{ASE}} - \alpha_{\text{LAT}}) \times \Delta\text{ASE} - (\alpha_{\text{MIX}} - \alpha_{\text{LAT}}) \times \Delta\text{MIX}}{(\alpha_{\text{BIO}} - \alpha_{\text{LAT}})} \quad (6.7)$$

$$\Delta\text{LAT} = \Delta\text{DIC} - \Delta\text{ASE} - \Delta\text{MIX} - \text{BIO} \quad (6.8)$$

The clear limitation of this Equation is that it is undefined for $\alpha_{\text{LAT}} = \alpha_{\text{BIO}}$. This causes the problem that the equation becomes more sensitive towards measurement and estimation errors, especially those of α_{LAT} and α_{BIO} , the smaller the difference between α_{LAT} and α_{BIO} becomes. Figure 6.6 shows the mean annual influence of errors associated with the respective isotope signatures of all fluxes as a function of the isotope composition of the LAT flux, α_{LAT} (or in δ notation $\delta^{13}(\text{LAT})$), for the eastern box (1025) by assuming a constant $\delta^{13}\text{C}(\text{BIO})$ of -24‰ . A mean isotope ratio of the carbon flux through lateral transport of $\delta_{\text{LAT}} = -30\text{‰}$ based on the mean difference to the neighbor box was calculated for box 1025. With an α_{LAT} that close to α_{BIO} , the uncertainties of the input variables are too large for the outcome to be useful. The isotope signatures of lateral transport and primary production are so close to each other because the water masses in this area are relative similar and vary mainly in their biological history.

Another cause of problems is that the isotope signature of a flux is calculated from the difference in DIC and the ^{13}C fraction of both reservoirs, the current surface water and the water reservoir that is mixed in by lateral transport,

$$\alpha_{\text{LAT}} = \frac{\Delta\text{DIC}^{13}_{\text{LAT}}}{\Delta\text{DIC}_{\text{LAT}}} = \frac{\alpha_{\text{DIC}} \times \Delta\text{DIC} - \alpha_{\text{LAT_RES}} \times \Delta\text{LAT_RES}}{\Delta\text{DIC} - \Delta\text{LAT_RES}} \quad (6.9)$$

where the respective fluxes in DIC and ^{13}C are denoted as $\Delta\text{DIC}_{\text{LAT}}$ and $\Delta\text{DIC}^{13}_{\text{LAT}}$ and the label LAT_RES stands for the characteristics of the reservoir that is mixed in. Equation 6.9 shows that α_{LAT} is not independent of DIC and α_{DIC} and can vary extremely. When the DIC difference between both water masses is decreasing, the isotope signature of the flux reaches maximal values with an infinite α_{LAT} for $\Delta\text{DIC}_{\text{LAT}} \rightarrow 0$. A schematic illustration of how the isotope signature of a flux can vary with the absolute size of this flux is shown in Figure 6.7. The isotope signature of the flux cannot be intuitively estimated from the isotope ratios of the two mixing reservoirs. As an example of how variable such a flux between two reservoirs can be, the seasonality of α_{ASE} is shown in δ notation for the boxes 1025 and 4055-pol in Figure 6.8. While the isotope

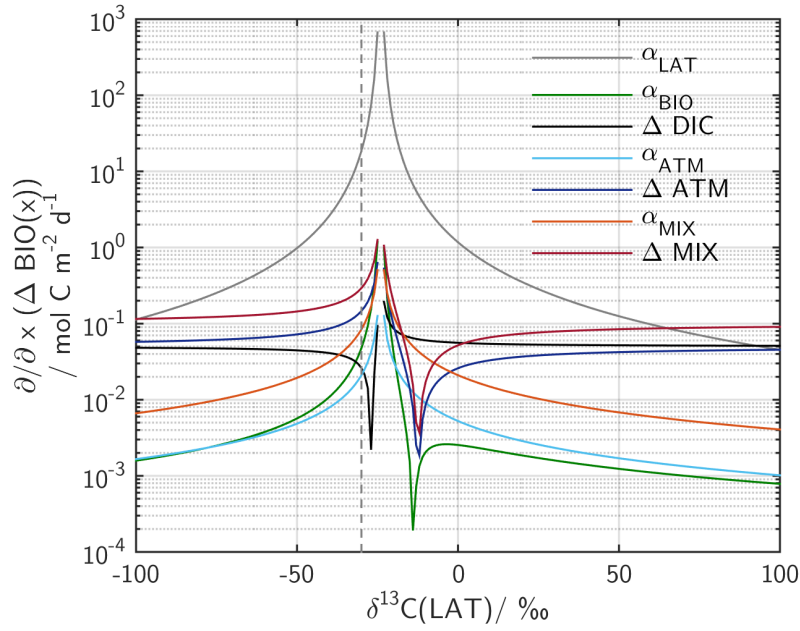


Figure 6.6: Influence of uncertainties of the input variables on ΔBIO , calculated after Equation 6.7 dependent on the isotope signature of the flux LAT. Equation 6.7 was differentiated with respect to all variables and then multiplied with the respective standard deviation of the harmonic fits. Since the influence of the respective parameter on uncertainty of ΔBIO is varying throughout the year the annual mean is shown. As a gray line the calculated isotope signature of lateral transport for the box 1025 is displayed.

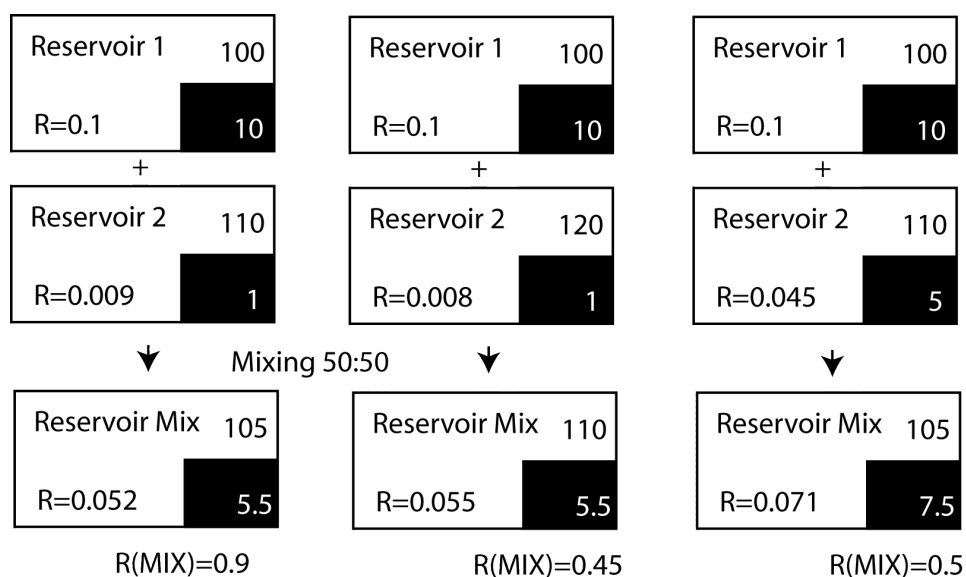


Figure 6.7: Schematic illustration of how the isotope signature of a flux is influenced by the magnitude of entire concentration fluxes and the isotope ratio of both reservoirs. Two reservoirs with different isotope ratios (black and white) are mixed 50:50. In the three different examples, different gradients in both isotopomers are displayed. Small relative changes in the bulk concentration causes high changes in the isotopic composition of the flux between both reservoirs ($R(\text{MIX})$).

signature of the ASE flux is relative constant in box 1025, the higher variability in the air-sea disequilibrium of both, $f\text{CO}_2$ and $\delta^{13}\text{C}(\text{CO}_2)$ in box 4055-pol heavily increases the variability in the isotope signature of the ASE flux.

In summary, it can be said that at the current state of the knowledge, the approach of Equation 6.7 and 6.8 is very limited if not unfeasible. Besides a reduced spatial scattering of the data and a better measurement precision of the respective parameter, our knowledge of isotope fluxes by lateral transport and diffusion needs to be improved.

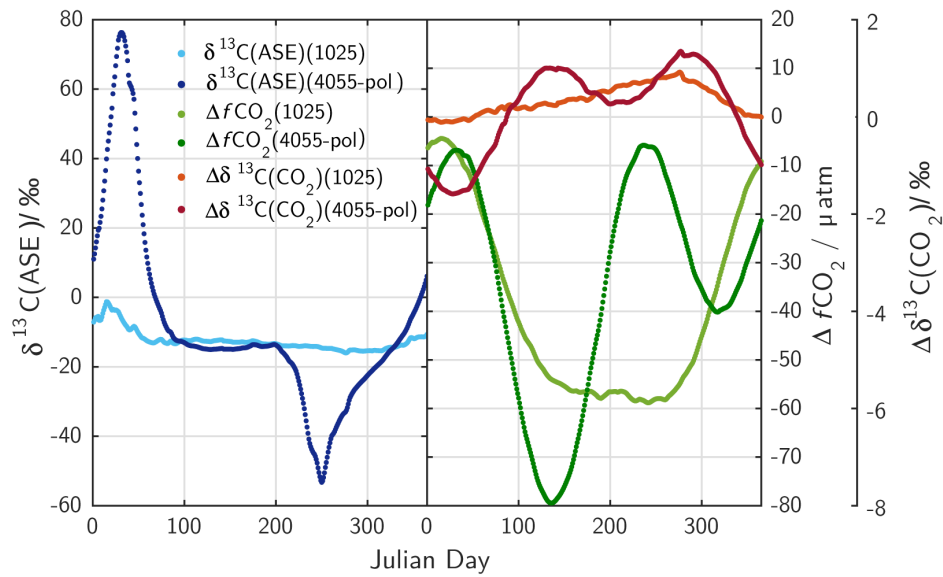


Figure 6.8: Seasonal variation of the isotope signature of the air-sea gas exchange for boxes 1025 (light colored lines) and 4055 - pol (light colored lines) (left panel). The respective air-sea disequilibria of $f\text{CO}_2$, $\Delta f\text{CO}_2$, (green lines) and $\delta^{13}\text{C}(\text{CO}_2)$, $\Delta\delta^{13}\text{C}(\text{CO}_2)$ (red lines) are shown in the right panel.

7 Seasonality of the surface North Atlantic

In this section, the mean seasonal variations of relevant carbon system parameter will be addressed. Besides the seasonality of basic parameters such as SST, SSS, and mixed layer depth, the seasonality of carbon dioxide fugacity ($f\text{CO}_2$), the related disequilibrium with the atmosphere ($\Delta f\text{CO}_2$), dissolved inorganic carbon (DIC), total alkalinity (TA) and the stable carbon isotope signature of CO_2 ($\delta^{13}\text{C}(\text{CO}_2)$) and DIC ($\delta^{13}\text{C}(\text{DIC})$) will be discussed. Furthermore, the temporal variations of nitrate, nitrite, phosphate and silicate throughout the year will be discussed. At the end, the seasonal variations of Chl *a* concentration, dissolved (DOC) and particulate organic carbon (POC) will be presented. The seasonal variability of the relative abundances of carbon and nitrogen in the produced organic matter will be discussed in Chapter 8.

All data were divided into four boxes of comparable water properties (1025, 2540, 4055-sub, 4055-pol) as described in Section 3.3.5. A description of the sample handling and measuring techniques can be found in Section 3.3. Each crossing's continuous measurements were averaged for the respective box and the standard deviations are shown as gray bars in the plots. The fits describing the mean seasonal evolution of each parameter were performed using a harmonic function (see Section 3.3.5). The ship tracks and sampling locations can be found in Figure 3.4 and the latitudinal distribution of the data in each box is shown in the Supplement.

7.1 Seasonal variability of SST, SSS and MLD

Generally, the variability of most parameters is increasing towards the west due to the mixing of two water masses with very differing characteristics (Labrador Current water and Gulf Stream water, see Section 2.1). The variability between data from different crossings at the same time of the year, can either be caused by interannual variability

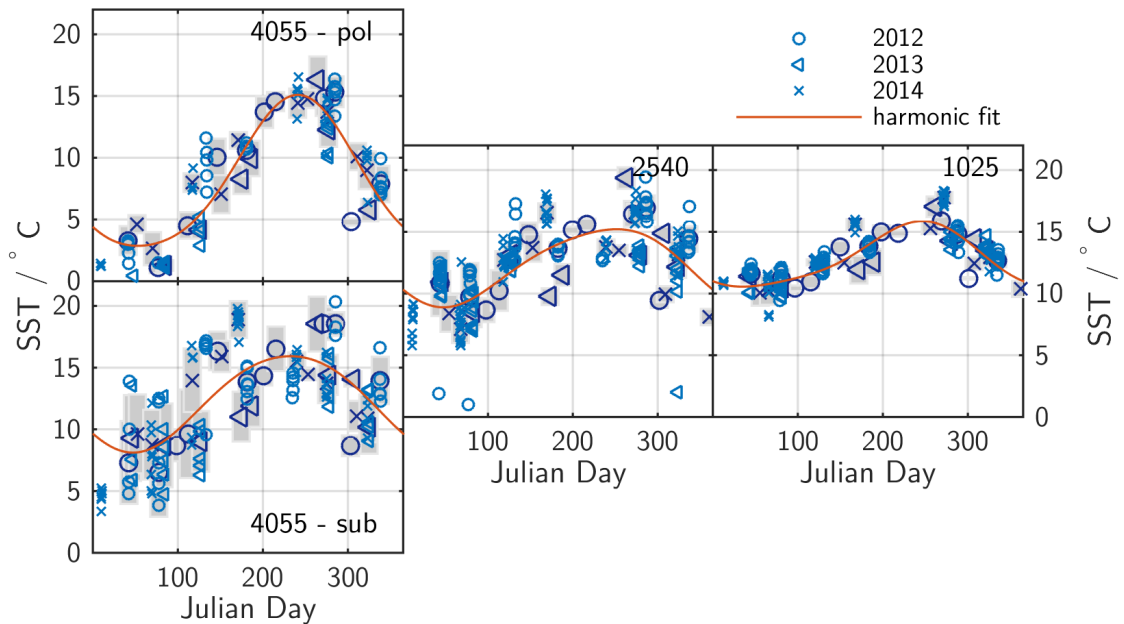


Figure 7.1: Seasonal variations of the sea surface temperature (SST) across the North Atlantic (2012: circle, 2013: triangle, 2014: cross; dark blue: box means of underway data, gray bar: box mean \pm standard deviation of underway data, light blue: SST at sampling position, red line: harmonic fit).

or latitudinal shifts of the ship track. A systematic southward shift in the western part due to the ice limit caused a high temperature, high salinity shift in the subtropical box during April and May (Figures 7.1 and 7.2). Apart from this, the salinity shows only small variations throughout the year with lower salinities in fall and high salinities during spring. The smallest amplitude in the annual cycle of the sea surface temperature can be found in the east (5°C) and is increasing towards the west with the polar water having the largest amplitude (15°C) (Figure 7.1). The variability in temperature is also higher in the western part of the basin due to the front between Labrador Current and Gulf Stream. For the boxes 2540 and 4055, data from the crossings in August 2012 and January 2014 have to be handled with care because the ship was sailing north of Newfoundland through the Strait of Belle Isle, which is further north than the normal ship tracks.

The mixed layer depth was taken from the operational numerical system output (PSY2G3R3-PGN) provided by the Mercator Project (www.mercator-ocean.fr). The

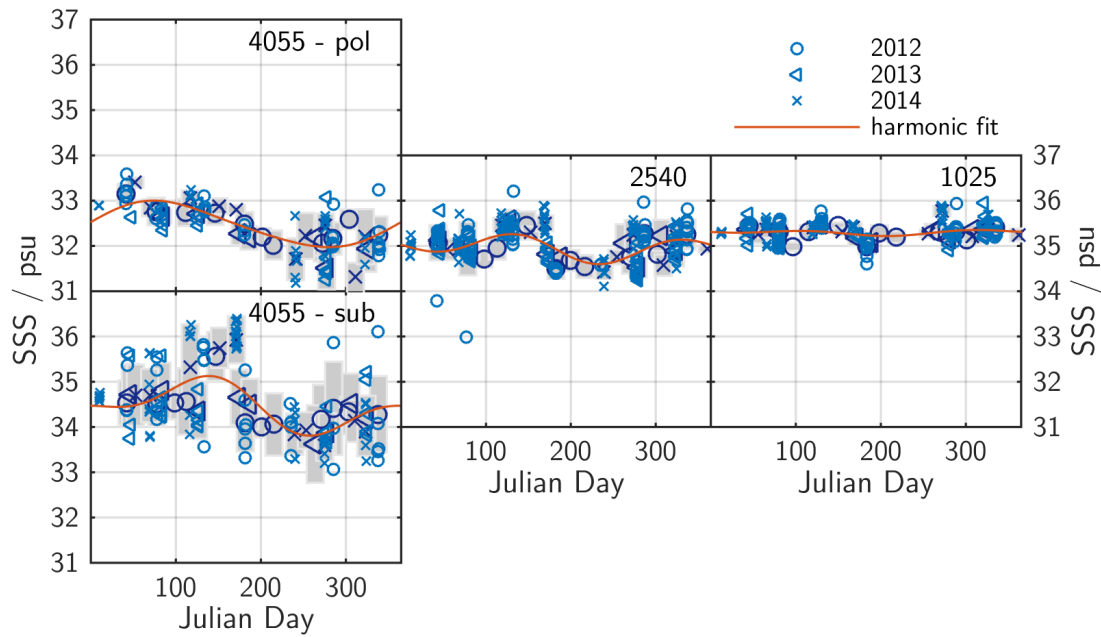


Figure 7.2: Seasonal variations of sea surface salinity across the North Atlantic (for an explanation of the different markers, please see caption of Figure 7.1).

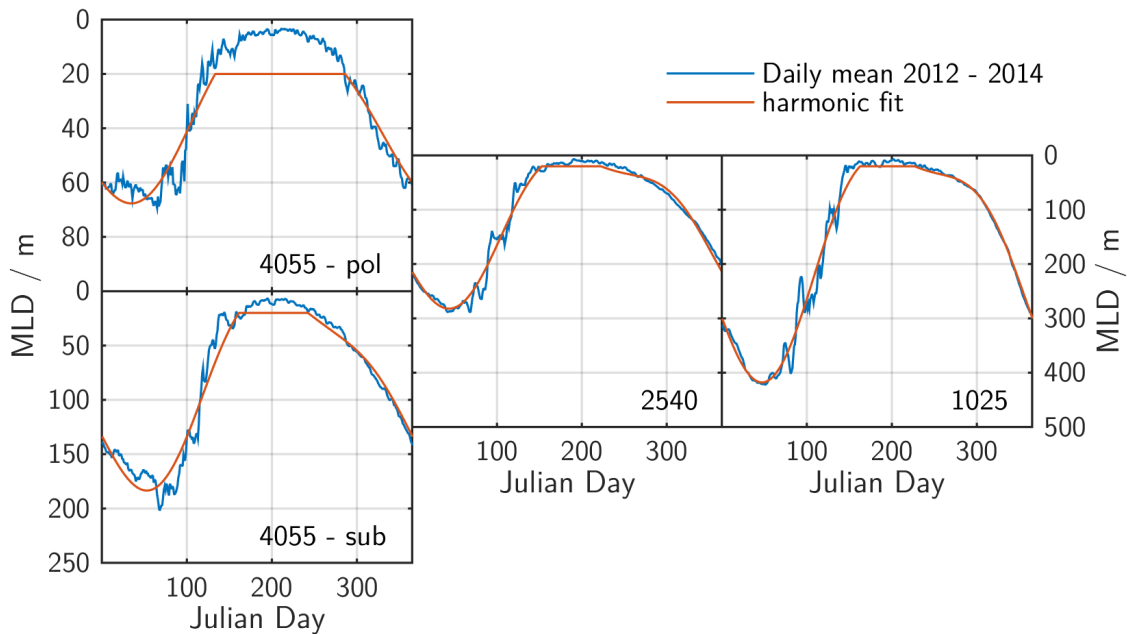


Figure 7.3: Mean seasonal variations of mixed layer depth across the North Atlantic (blue line) and the fit used for the box model (red line).

mean seasonal variation in each box from 2012 to 2014 is shown in Figure 7.3. Please note the different y-axis ranges in the east and west. The maximal mixed layer depth in all boxes occurs between Julian day 50 and 80, while the maximal winter mixed layer depth is much deeper in the east (420 m) than in the western boxes (200 m in 4055 - sub and 70 m in 4055 - pol). The harmonic fit tends to flatten the jump-like formation of summer stratification and shows a too early maximal MLD, especially in the west. Since the water intake is located at a water depth of 8-9 m and about 250 m astern of the fore-castle we assume that we don't measure undisturbed mixed layer depths shallower than 20 m and, therefore, the fit was set to 20 m for periods with a MLD shallower than 20 m. Summer stratification forms slightly earlier in the west than in the east and is shallower in the western boxes. The mixed layer deepening starts at the same time in each box but proceeds fastest in the east.

7.2 Seasonal changes in nutrient concentrations

The seasonality of nitrate, phosphate and silicate concentrations is driven by the interaction of nutrient consumption during primary production and entrainment of nutrient rich waters due to convective mixing (Figures 7.4 to 7.6). The amplitude is highest in the central box and lowest in the box 4055 - pol, while the duration of summer oligotrophy is increasing from west to east. The scatter of the data for each crossing, as well as between different crossings at the same time of year is mainly caused by latitudinal differences, especially during the spring bloom. The latitudinal difference between Halifax in the west (44°N) and Ireland in the east (51°N or 55°N) and, thus, the more subtropical characteristics in the west lead to a slightly earlier spring bloom onset at the western side of each box. Moreover, the box 1025 can be influenced by an earlier bloom onset at the shelf edge of the Celtic Sea. The maximal mixed layer depth can change within each box, as well, so that the sampled water can have experienced different entrainment fluxes.

The average nitrate concentration in late winter varies between $10 \mu\text{mol kg}^{-1}$ (2540) and $5 \mu\text{mol kg}^{-1}$ (4055 - pol). In the west, nitrate is completely depleted by May while in box 1025 there is still some nitrate left until Julian day 200. This long period of nitrate below the detection limit is well known for subtropical regions and decreasing with increasing polar influences (Lipschultz, 2001; Takahashi et al., 1993). The concentration increase due to entrainment starts earlier in the east while the slope of the nitrate

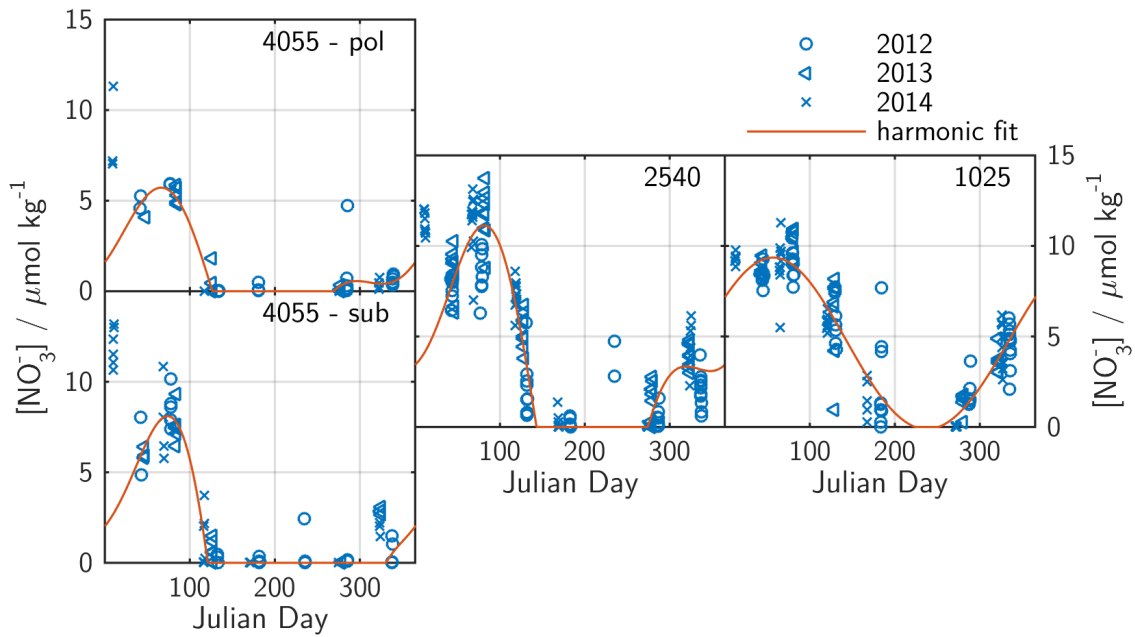


Figure 7.4: Seasonal variation of nitrate concentration in the four regional domains (2012: circle, 2013: triangle, 2014: cross, harmonic fit: red line).

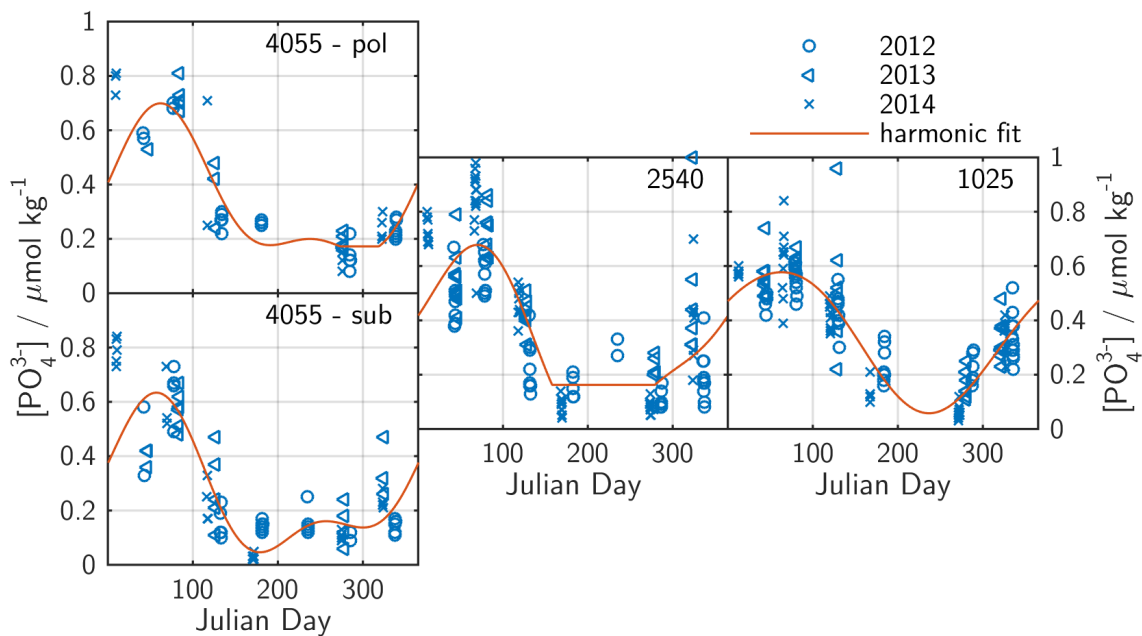


Figure 7.5: Seasonal variation of phosphate concentration in the four regional domains (2012: circle, 2013: triangle, 2014: cross, harmonic fit: red line).

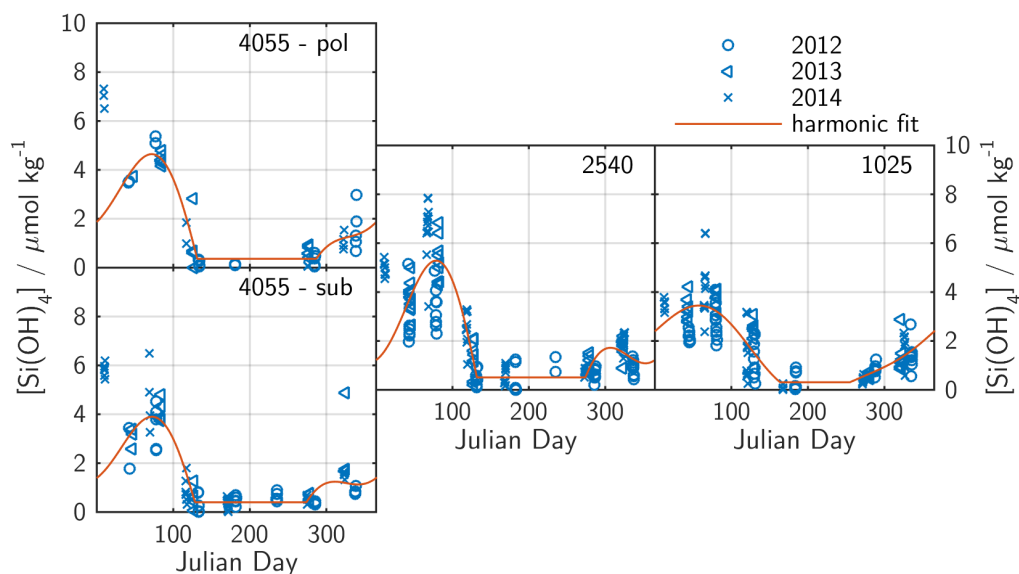


Figure 7.6: Seasonal variation of silicate concentration in the four regional domains (2012: circle, 2013: triangle, 2014: cross, harmonic fit: red line).

drawdown is much steeper in the central and western boxes than in the eastern box. The slope and the timing of a net entrainment flux is determined by the start and magnitude of convective mixing and the size of a possible fall bloom. This fall bloom can be triggered by the availability of nutrients after summer oligotrophy and is reported for subtropical waters, with decreasing intensity towards the north. Of course, it can only develop when the surface water is depleted in at least one nutrient, which here is for all regions the case.

The phosphate concentration varies in all boxes between maximal concentrations in late winter of $0.6 - 0.7 \mu\text{mol kg}^{-1}$ and a summer minimum of $0.1 - 0.2 \mu\text{mol kg}^{-1}$. The lowest summer concentration was observed in the subtropical box, but all boxes always showed a residual phosphate above the detection limit during summer. The lowest summer phosphate values in the subtropical box are most likely caused by nitrogen fixation, which is more pronounced there and consumes the residual phosphate after the onset of nitrate depletion. This longitudinal difference in the relative abundances of nitrate and phosphate can also be seen when comparing the maximal winter concentrations. The ratio of winter nitrate to phosphate concentrations is decreasing from 16.2 in box 1025 to 7.8 in box 4055 - pol.

Silicate depletion in the east occurs earlier than the minimum in nitrate and phosphate

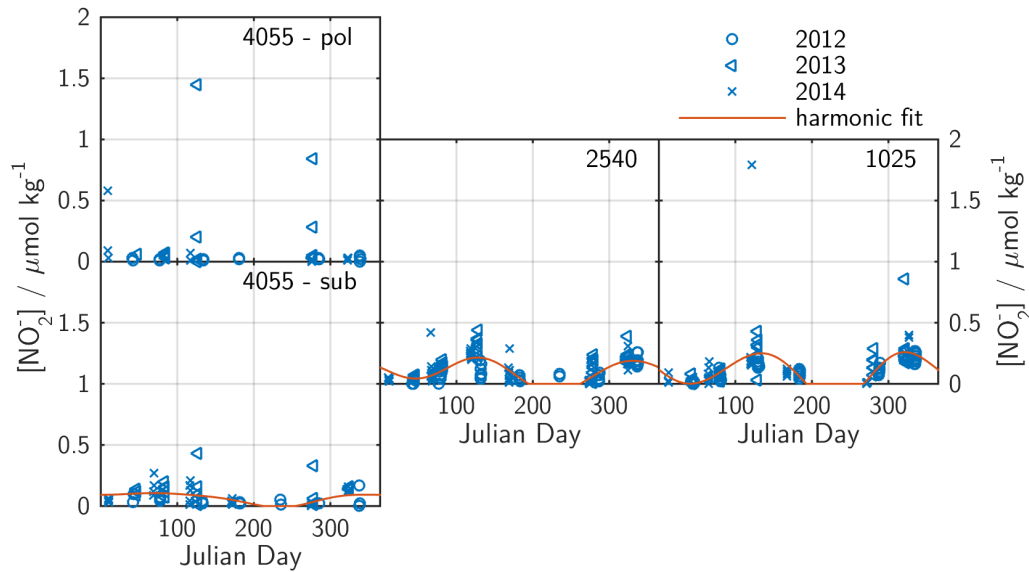


Figure 7.7: Seasonal variation of nitrite concentration in the four regional domains (2012: circle, 2013: triangle, 2014: cross, harmonic fit: red line).

concentrations. In the western part, however, the depletion of nitrate, phosphate and silicate occurs at the same time of year. This indicates that a diatom dominated bloom in the east develops first, but cannot consume all available nitrate. After a species shift away from diatoms, the bloom continues until late summer. In relation to the maximal winter nitrate concentration, the late winter silicate concentration peaks higher in the west than in the east of the study area. This can be caused by a silicate triggered fall bloom in the east that shows a relative high fraction of diatom biomass accumulation. In box 1025, nitrate just reaches depletion at the end of summer, while silicate is depleted for about 100 days.

The nitrite concentration shows a bimodal seasonality in the eastern and central boxes with maxima during spring bloom and fall bloom / convective mixing. In the western boxes the data are much more scattered and barely show significant seasonal changes. In principle, nitrite can be produced as an intermediate during the reduction of nitrate during primary production and the oxidation of organic nitrogen during respiration (Zehr and Ward, 2002). Typically, elevated nitrite concentrations are observed for areas with intense primary production and respiration. In the water column, a nitrite maximum occurs beneath the euphotic zone. This nitrite is transported to the surface during convection and can be responsible for the fall peak. The smaller amplitude in nitrite in

the west can be due to a stronger limitation in nitrogen and shallower maximal mixed layer depths. A very early onset of spring bloom even in fall, as it known for the subtropics (Henson et al., 2009b), can also be a reason why we cannot observe a winter minimum here. The upwelled nitrite would be directly consumed by the developing bloom. During winter, the growth rates are decreased and the dilution effect caused by a deeper mixed layer can prevent the nitrite concentration from building up significantly.

7.3 Seasonal changes of the carbon system and its isotopic composition

The observed seasonal variability within the inorganic carbon system is varying significantly between the eastern and western part of the study area. While the eastern regions show more subpolar patterns, the western boxes show clear subtropical influences. The shape of the $f\text{CO}_2$ seasonality and the respective air sea disequilibrium are in agreement with previous studies of Lüger et al. (2004) and Takahashi et al. (2009) (Figure 7.8 and Figure 7.9). In the eastern and central box, the $f\text{CO}_2$ is close to equilibrium with the atmosphere during winter time and shows an undersaturation of about $50 \mu\text{atm}$ from April to November. This undersaturation is caused by carbon fixation during the spring bloom. The increase in inorganic carbon due to convective mixing in fall and winter brings the $f\text{CO}_2$ close to the atmospheric $f\text{CO}_2$. The picture looks different in the two western boxes. Here, the seasonal cycles of $f\text{CO}_2$ and $\Delta f\text{CO}_2$ have a bimodal pattern. The $f\text{CO}_2$ maximum in summer is a feature known for subtropical water masses (Lüger et al., 2006). An air sea disequilibrium during winter is observed, which is caused by a combination of cooling and an early onset of the spring bloom, possibly even in fall. The spring bloom in this region can easily reduce the $f\text{CO}_2$ to $250 \mu\text{atm}$ or less in April/May. These waters influenced by an elevated primary production can be very patchy and are mostly located at the front of Labrador Current and Gulf Stream or at the shelf edge of the Grand Banks. After this bloom event and after the nutrients being depleted, the influence of primary production on the $f\text{CO}_2$ declines and warming starts to be the major driver of $f\text{CO}_2$ changes. The seasonal change in SST is two to three times larger in the western boxes than in the eastern ones. The warming brings the $f\text{CO}_2$ close to atmospheric equilibrium or can even lead to supersaturation (4055 - pol).

The stable carbon isotope ratio of CO_2 , $\delta^{13}\text{C}(\text{CO}_2)$ (see Figure 7.10), is driven by

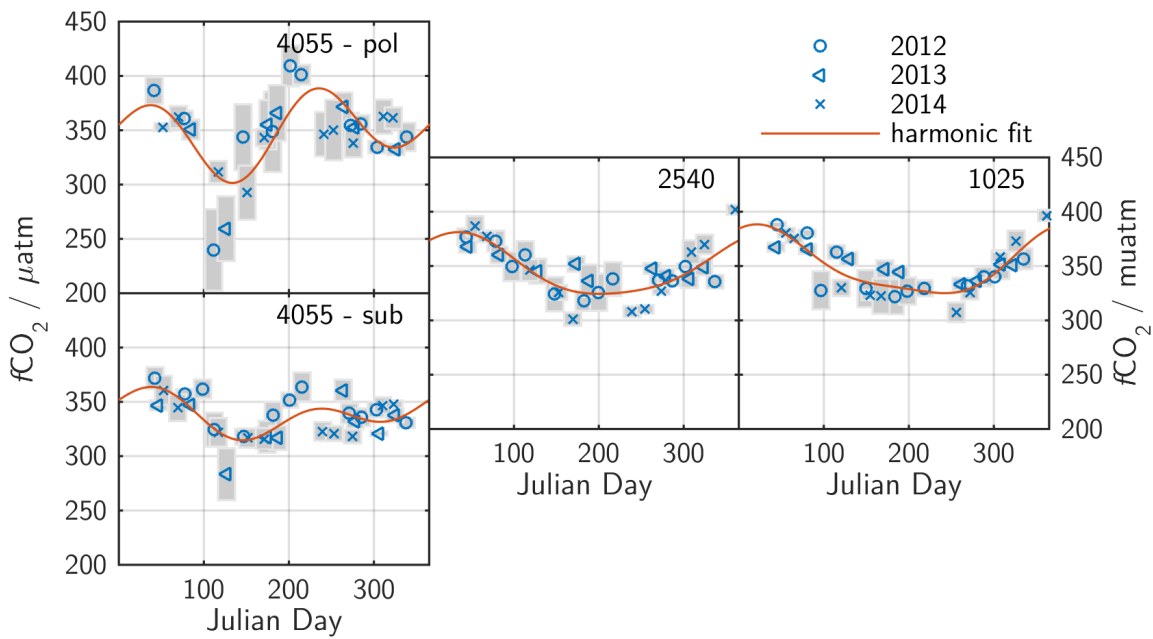


Figure 7.8: Seasonal variation of $f\text{CO}_2$ in the four regional domains. Data from different years are denoted with different symbols (2012: circle, 2013: triangle, 2014: cross) and the respective standard deviation is shown as gray bars.

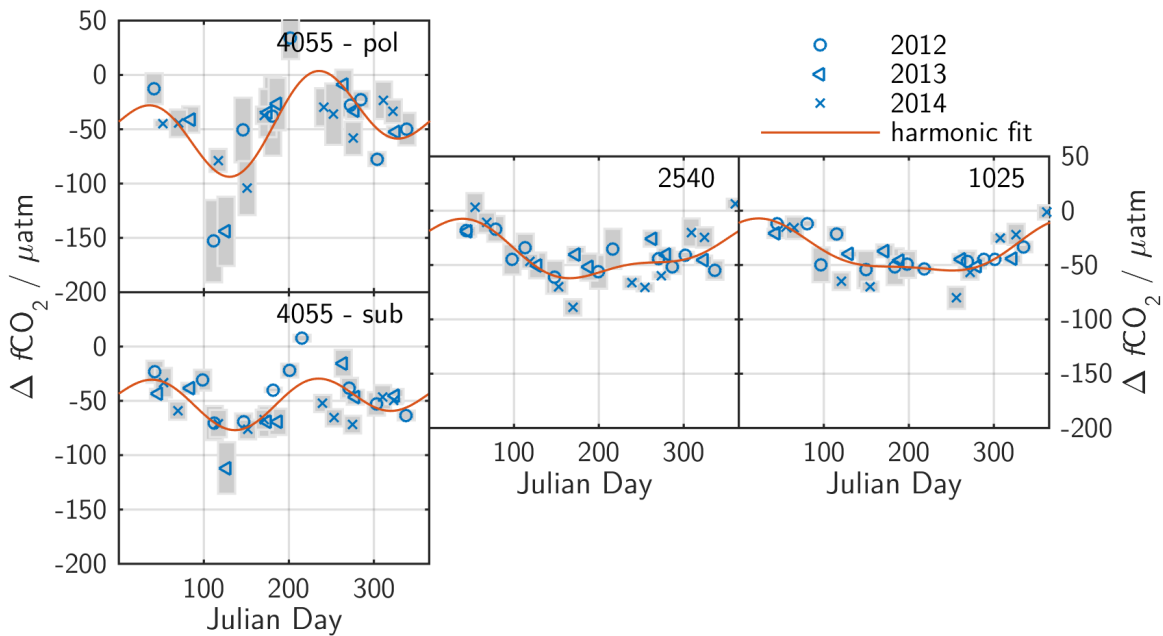


Figure 7.9: Seasonality of $\Delta f\text{CO}_2$ in the four regional domains (for an explanation of the different markers, please see caption of Figure 7.8).

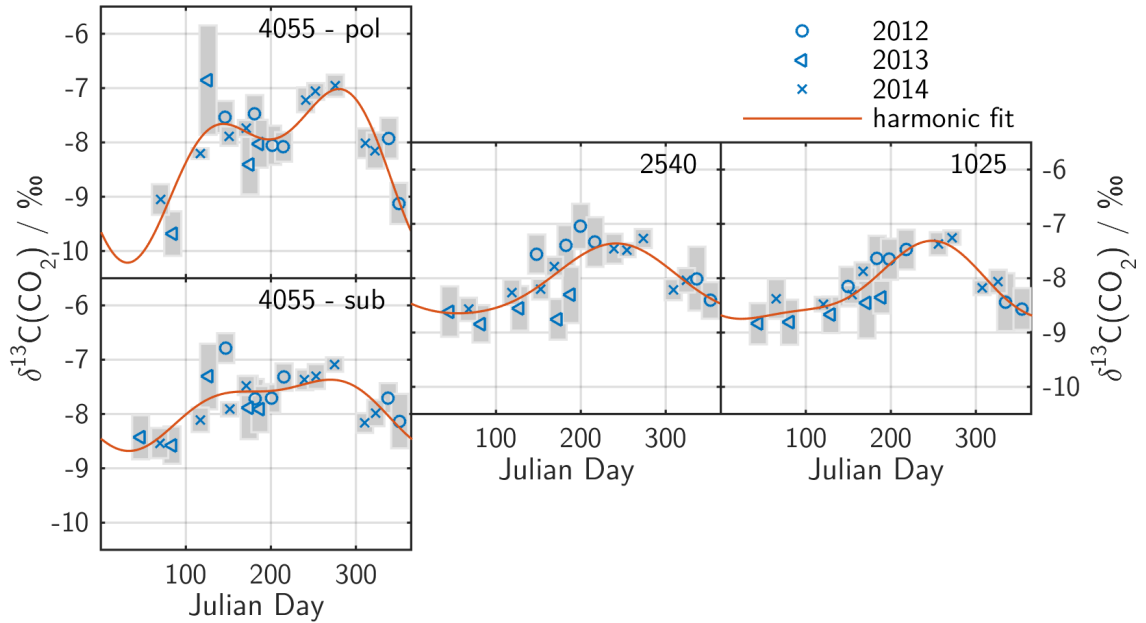


Figure 7.10: Seasonal variation of $\delta^{13}\text{C}(\text{CO}_2)$ in the four regional domains (for an explanation of the different markers, please see caption of Figure 7.8).

a combination of temperature changes and biological effects. In contrast to $f\text{CO}_2$, the impacts of these two drivers are in phase resulting in a heavier CO_2 pool during summer. The $\delta^{13}\text{C}(\text{CO}_2)$ amplitude is increasing from east to west. About half of the amplitude in $\delta^{13}\text{C}(\text{CO}_2)$ can be attributed to the temperature dependent fractionation between CO_2 and the entire DIC (about 2‰ per 10 °C (Zhang et al., 1995)). With increasing temperature, the CO_2 fraction of the DIC pool in the surface ocean becomes heavier. Carbon fixation by phytoplankton gives the lighter isotopomer an advantage due to kinetic fractionation so that the remaining carbon pool in the surface ocean gets enriched in the heavier isotopomer. During respiration, the effect is in the opposite direction, so that the $\delta^{13}\text{C}(\text{CO}_2)$ decreases again when remineralized nutrients are mixed to the surface during convective mixing. Gas exchange with the atmosphere usually lightens the surface ocean CO_2 pool. When the CO_2 reservoir gets very light by winter cooling and the ocean is still undersaturated, the isotope ratio of the flux can turn positive, and, thus, lightens the pool of inorganic carbon in the surface ocean. The isotope ratio of the flux changes sign when the $\Delta f\text{CO}_2$ changes its sign while the $\Delta\delta^{13}\text{C}(\text{CO}_2)$ doesn't, and vice versa (for more explanation, see Chapter 6, Equation 6.9). The changes in

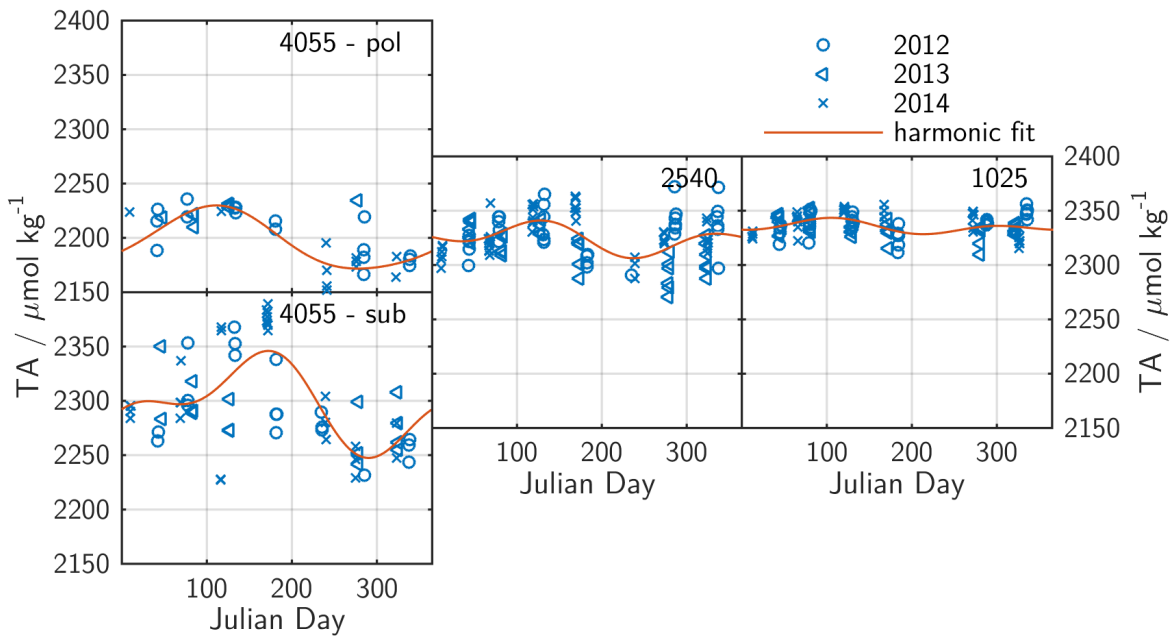


Figure 7.11: Seasonal variation of TA in the four regional domains. Data from different years are denoted with different symbols (2012: circle, 2013: triangle, 2014: cross, harmonic fit: red line).

$\delta^{13}\text{C}(\text{CO}_2)$ directly drive the influence of air-sea gas exchange on the isotopic signature of the inorganic carbon pool as well as the $\delta^{13}\text{C}$ of the produced organic matter.

The seasonal variations in alkalinity are mainly following the SSS (Figure 7.11). The influences of primary production, which increases the alkalinity by removing nitrate, or calcification, which would result in an alkalinity decrease, cannot be observed. First, these two processes have a relative small effect on alkalinity and second, the blooms can be very patchy and this can be a reason for the scatter within the data.

Figure 7.12 and Figure 7.13 show the seasonality of DIC concentration and its stable carbon isotope ratio, $\delta^{13}\text{C}(\text{DIC})$. The amplitude in DIC concentration is increasing from east to west with maximal DIC concentrations in late winter caused by entrainment of high DIC subsurface waters and decreases towards a summer minimum as soon as the removal of DIC by primary production exceeds the entrainment flux. The amplitude and the absolute $\delta^{13}\text{C}(\text{DIC})$ are also increasing from east to west. In the two eastern boxes it is clearly anti correlated to the changes in DIC concentration. The increase of about 1‰ is reflecting a biologically driven DIC drawdown of about $80 \mu\text{mol kg}^{-1}$ (assuming a mean

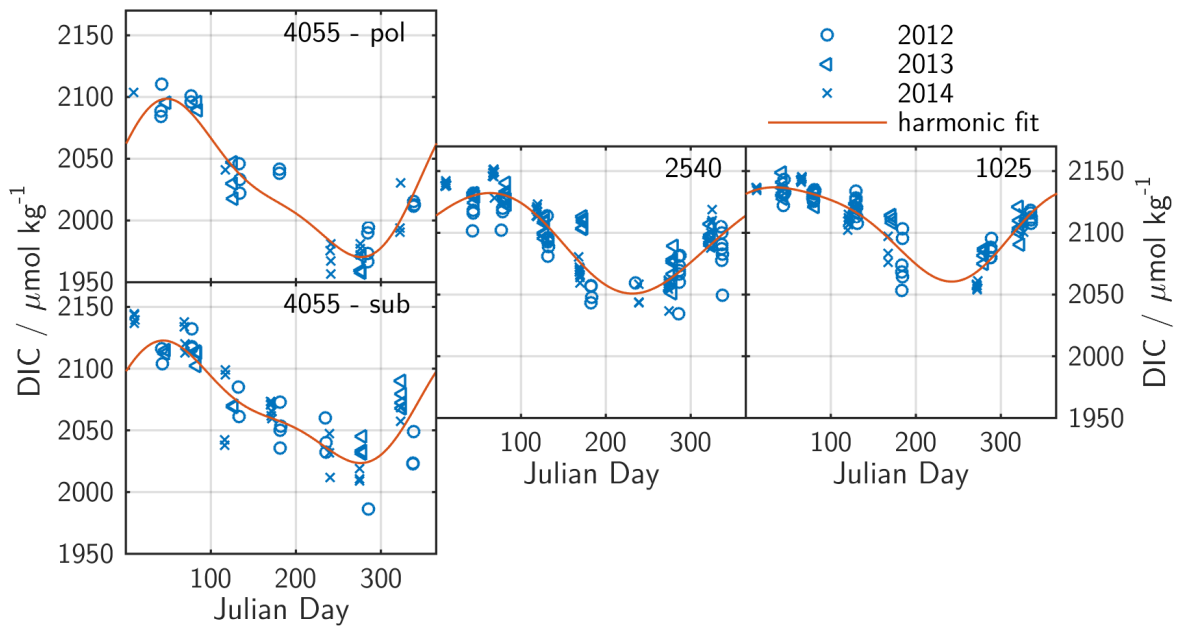


Figure 7.12: Seasonal variation of DIC in the four regional domains. Data from different years are denoted with different symbols (2012: circle, 2013: triangle, 2014: cross, harmonic fit: red line).

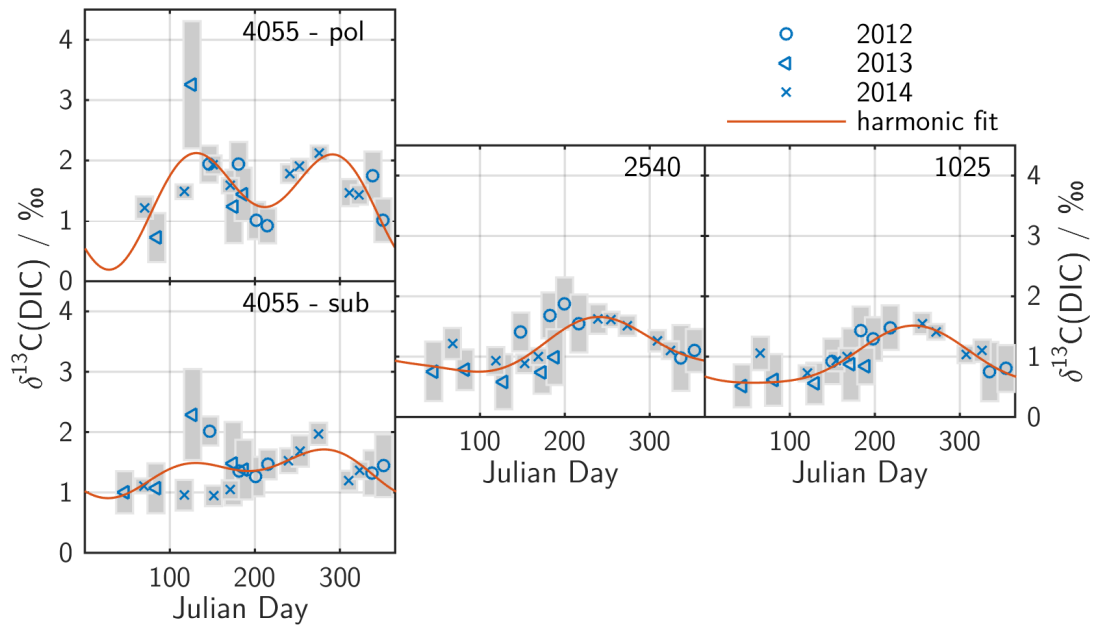


Figure 7.13: Seasonal variation of $\delta^{13}\text{C}(\text{CO}_2)$ in the four regional domains (for an explanation of the different markers, please see caption of Figure 7.8).

$\delta^{13}\text{C}(\text{POC})$ of about 24 ‰) and the decrease in fall can be related to the net entrainment of the same amount of respiratory DIC. So both, the DIC and $\delta^{13}\text{C}(\text{DIC})$ changes are fully biologically driven. This fits with other studies in the subpolar North Atlantic (Racapé et al., 2014; Gruber et al., 1999). However, the picture in the western boxes is more complicated. In agreement with the nutrient drawdowns, the decrease in DIC starts earlier and is steeper in the western boxes. The later onset of a net entrainment flux that has been observed for the nutrients can also be found in the DIC seasonality in the west. However, a remarkable difference between nutrients and DIC concentration is their behavior during summer. The DIC concentration in the western boxes decreases to about half of its amplitude and then the decline flattens. This is the time when nutrients start to become depleted. In the second half of the year, the DIC continues to decrease even though the nutrients are depleted (boxes 4055 - pol and 4055 - sub). One reason for a continued DIC drawdown during nitrate depletion could be nitrogen fixation. However, the phosphate concentrations are too low to support a DIC decrease by N_2 fixation in the order observed here. This DIC decrease is rather correlated with a decreasing salinity and, thus, the salinity normalized DIC (nDIC) stays constant until it is increasing again at the end of the year. A reason for this decrease in both, DIC and SSS, could be the entrainment of low salinity water, possibly more polar water masses that were influenced by ice melting during summer. The understanding of this further DIC decrease improves by taking the $\delta^{13}\text{C}(\text{DIC})$ into account. The $\delta^{13}\text{C}(\text{DIC})$ shows here a bimodal seasonality. During spring bloom, the DIC pool becomes enriched in the heavier isotopomer. At the frontal region of Labrador Current and Gulf Stream, this enrichment can lead to $\delta^{13}\text{C}(\text{DIC})$ values up to 5 ‰ that are usually not observed in the open ocean, correlated to the extraordinary low $f\text{CO}_2$ observed in that area. When the surface water has reached oligotrophic conditions, the $\delta^{13}\text{C}(\text{DIC})$ starts to decrease and subsequently starts to increase again as the DIC concentration is further diminished. The lightening after the end of spring bloom could be caused by air-sea gas exchange which can have a large influence on surface layer $\delta^{13}\text{C}(\text{DIC})$ during shallow mixed layer conditions. The increase in the second half of the year is also showing a biological signature (about 0.5 ‰ per $40 \mu\text{mol kg}^{-1}$ decrease in DIC). However, since the decrease in DIC stems from a lower salinity, this signature must be caused by mixing with lower salinity water that comes with a different isotopic signature. The coincident increase in $\delta^{13}\text{C}(\text{DIC})$ indicates that this entrainment water has experienced a DIC decrease caused by a phytoplankton bloom but had most likely a lower winter DIC concentration

compared to the two observed western boxes. The decrease in salinity is a seasonal signature that occurs simultaneously with the onset of convective mixing. Since the MLD in this region is very shallow during summer (5-10 m, see Figure 7.3), evaporation could increase the salinity in the surface layer, so that mixed layer deepening can cause a decrease in salinity. After the cessation of the spring bloom there can be a significant amount of primary production occurring underneath the very shallow mixed layer where the nutrient concentration is not yet depleted. Mixing with this shallow subsurface water mass that is not influenced by air sea gas exchange could give a persistent primary production signal in the $\delta^{13}\text{C}(\text{DIC})$. Subsurface blooms in mid summer with a deep chlorophyll maximum are reported for subtropical regions and consume nutrients below the shallow summer mixed layer. This scenario is consistent with the delay of a net entrainment flux of nutrients relative to the onset of MLD deepening and can explain the observed pattern. Another process that could possibly cause such a signature would be a fall bloom that produces the biological isotope signature and coincides with lateral mixing of lower salinity waters that were influenced by ice melting in summer. However, the distinction between these two is not possible which represents a clear limitation of underway data limited to surface measurements. For this purpose, a research cruise with CTD data or at least a float measuring biogeochemical parameter would have been necessary. Another approach could be to study the relative abundance of ^{18}O in water molecules, that could give a suggestion of the relative influences of melt water and precipitation on the salinity decrease (Newton et al., 2013).

7.4 Seasonal variability of Chl *a*, POC and DOC and the Chl *a* / POC ratio

The Chl *a* concentration is often used as an indicator of primary production. The seasonal variation of Chl *a* concentration in this study shows a bimodal shape in all boxes, with the peak in fall increasing with respect to the spring peak when going from east to west (Figure 7.14). The concentration at the summer minimum decreases towards the west while the minimal winter concentration is increasing. This can be explained with a spring bloom onset in fall in the western part while the bloom in the eastern boxes, which extend more northwards, starts in spring. The summer minimum in the west is caused by the limitation of primary production due to nutrient depletion and increased

grazing pressure. Another parameter for studying the primary productivity of suspended biomass is the relative amount of Chl *a* and particulate organic carbon, the Chl *a* / POC (Figure 7.15) ratio. Dependent on the species, this ratio can change remarkably during a bloom and was found to be linearly correlated to nutrient limited growth rate (Cullen, 1982). Besides a reduced growth rate, a higher amount of zooplankton can be another reason for declining Chl *a* / POC ratios. The Chl *a* / POC ratio peaks in every box in late winter. Two processes can be the cause of this early peak. The shorter days and the deeper mixing trigger the phytoplankton to include a higher amount of Chl *a* due reduced light availability. Moreover, at this time of the year the fraction of primary producers in the surface water is relative high while the abundance of herbivores and carnivores increases with increasing food supply during spring. The decrease in the Chl *a* / POC ratio around Julian day 100 - 200 is most likely caused by a combination of decreasing growth rate due to reduced nutrient availability, a reduced fraction of Chl *a* within the primary producers due a an increase in light intensity as well as an increase in zooplankton biomass. When comparing this to the nutrient cycles, the slightly earlier decrease in Chl *a* / POC in the western part is correlated with the earlier onset of summer oligotrophy in this region.

The concentration of suspended particulate matter shows a clear seasonality with minimum concentrations in winter and higher concentrations during the summer period (Figure 7.16). The higher the measured concentrations, the higher was also the scatter within one crossing. In the subtropical box, the maximal POC concentration is found at the time when the bloom starts to become nutrient limited (around Julian day 120) while the summer POC peaks later and higher in the eastern boxes. The decrease towards the winter minimum starts in October/November. The seasonality of dissolved inorganic carbon shows relatively constant concentrations during spring bloom that are slightly higher in the western part of the basin, which is in agreement with studies that showed higher concentrations in subtropical compared to subpolar regions (Carlson et al., 2010) (see Figure 7.17). With the onset of nutrient depletion, the DOC concentration is increasing and reaches values up to $120 \mu\text{mol kg}^{-1}$. With increasing entrainment flux in fall, the DOC concentration turns back to its winter/spring value. The increase at the onset of nutrient depletion is supposed to be caused by a release of small, carbon rich molecules such as sugars. However, the DOC presented here has only scarce data coverage compared to most other parameters, especially during summer. This clearly limits its interpretability.

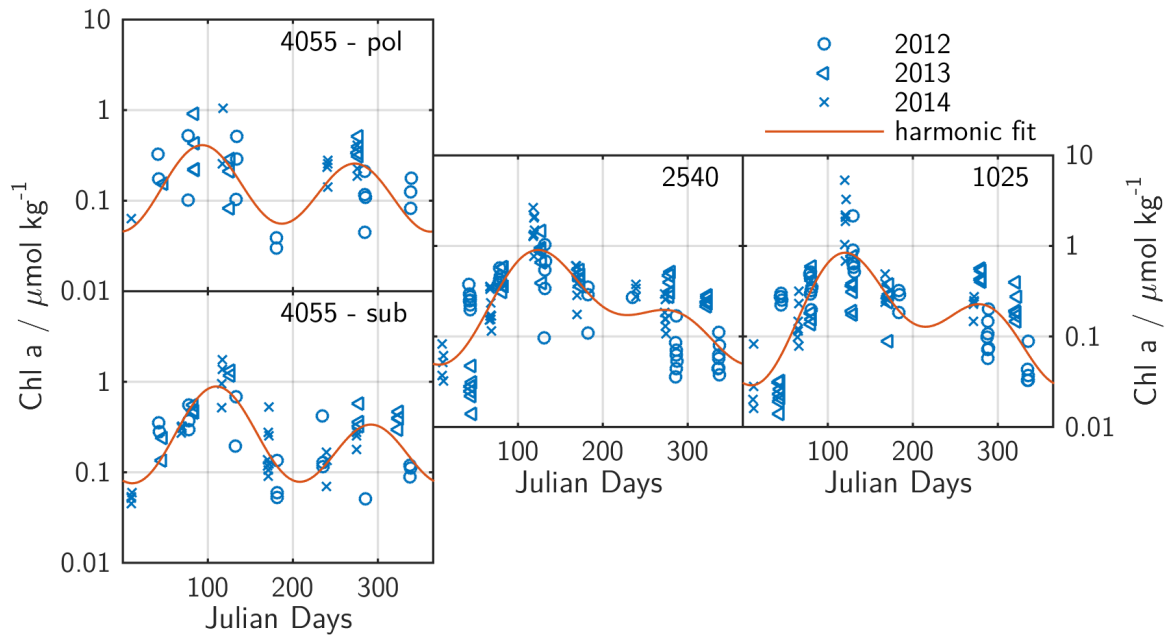


Figure 7.14: Seasonal variations of Chl *a* concentration in the four regional domains (2012: circle, 2013: triangle, 2014: cross, harmonic fit: red line).

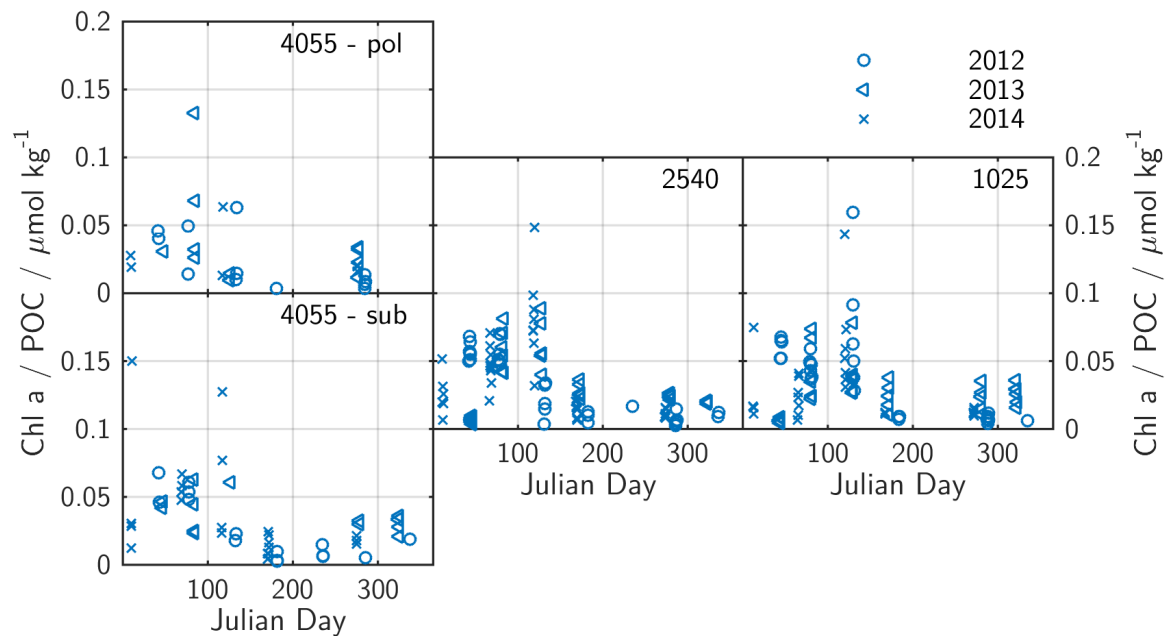


Figure 7.15: Seasonal variation of Chl *a* / OIC in the four regional domains (2012: circle, 2013: triangle, 2014: cross)

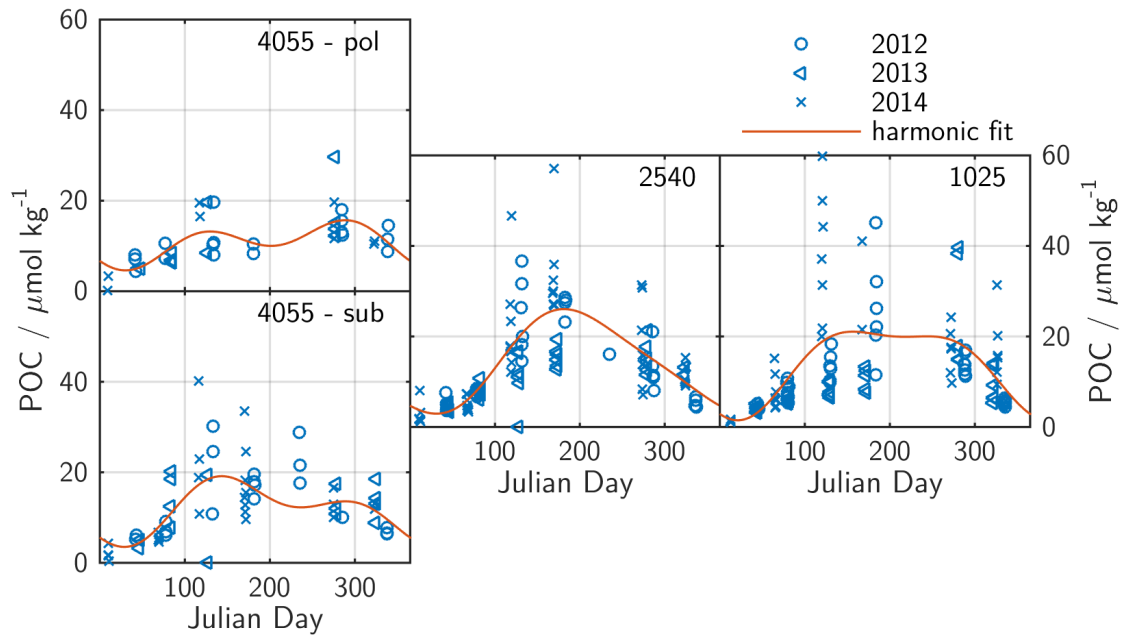


Figure 7.16: Seasonal variation of POC in the four regional domains (2012: circle, 2013: triangle, 2014: cross, harmonic fit: red line).

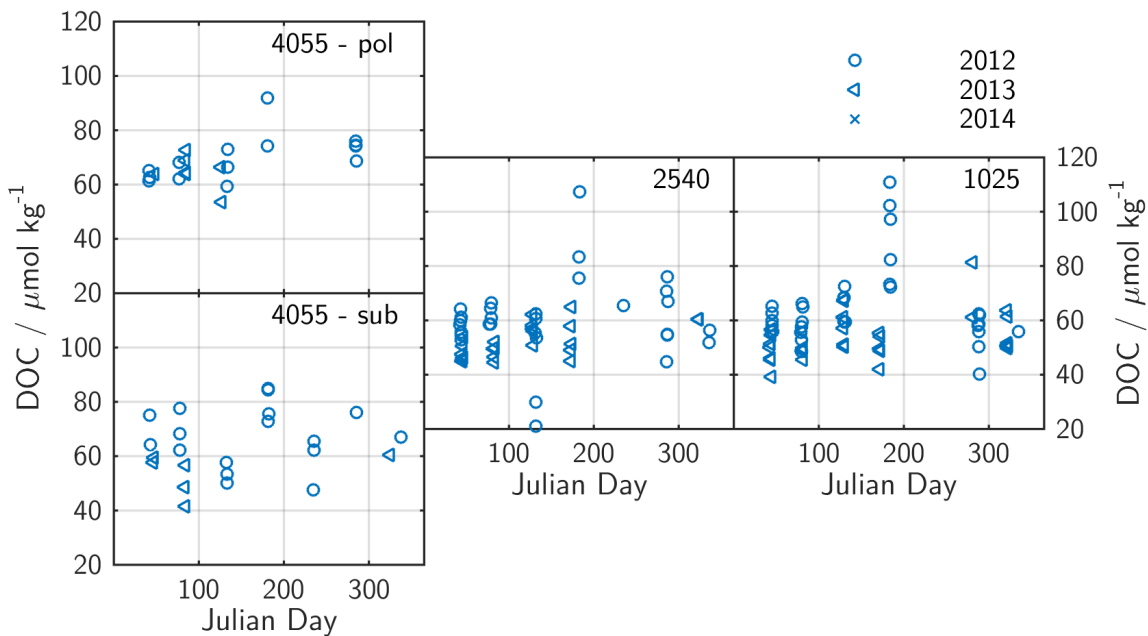


Figure 7.17: Seasonal variation of DOC in the four regional domains (2012: circle, 2013: triangle, 2014: cross).

7.5 Synthesis

In summary, it can be said, that the eastern part of the sampling region is dominated by biology, i.e., net production during spring and the upwelling of products from biomass remineralization during mixed layer deepening. Spring bloom draws down nutrients and DIC with a preferential uptake of the lighter carbon isotope, increasing the $\delta^{13}\text{C}(\text{DIC})$, accordingly. The $f\text{CO}_2$ is continuously undersaturated with a minimum during summer, while its isotopic composition shows a maximum during summer. The Chl a concentration shows a bimodal pattern with a large maximum in spring and a smaller peak in fall. POC concentrations are elevated during the entire productive season and have a minimum during winter. Towards the west, additional processes come into play and the subtropical influence is increasing. The seasonal amplitudes of physical and carbon system parameters increase while those of the nutrients tend to decrease. The decrease in nutrient amplitudes is in agreement with decreasing maximal mixed layer depths towards the western part of the basin. The reduced nutrient concentrations during winter lead to a longer duration of nutrient depletion in summer. The large amplitude of DIC is caused by mixing in late summer which is also causing an increased abundance of the heavier isotopomer. The $f\text{CO}_2$ shows a steep decrease during spring bloom, but almost reaches equilibrium with the atmosphere in late summer, when temperature effects become the dominant driver of $f\text{CO}_2$. The delayed onset of a net entrainment flux during convective mixing in fall and winter as well as the fall peak in Chl a , which has the same size as the spring peak, points to a westward increase of bloom activity during fall.

8 Stoichiometry of biomass production and upwelling of nutrients

For predicting and interpreting the changes in surface ocean $f\text{CO}_2$, not only the physical but also the biological drivers have to be considered. The biological carbon pump is of great importance for transporting carbon into deeper layers of the ocean, and, thus, removing it from the air-sea interface for a time scale of months or longer. For reliable estimates of the ocean carbon sink and the way it is changing on intra- to interannual timescales, the main controls of the biological carbon pump have to be understood. A time series like the one presented in this study is capable of revealing new insights into the mechanisms that regulate the strength and the timing of the biological carbon pump by relating different parameter over the entire seasonal cycle.

The stoichiometric ratio of nutrient uptake and biomass produced has been studied for a long time now with the classical Redfield C:N:P ratio of 106 : 16 : 1 ratio being a prominent example (Redfield, 1958). Anderson and Sarmiento (1994) reported a slightly higher amount of carbon 117 ± 14 : 16 ± 1 : 1 but both estimates are not in a statistically significant way different. Since then, many studies have been conducted revealing varying elemental ratios depending on many different factors such as the sampling region, nutrient availability, season or species (Takahashi et al., 1993; Körtzinger et al., 2001; Koeve, 2006; Geider and Roche, 2002). Also, different methods for the determination of the elemental ratio can influence the reported value. Measured carbon to nitrogen ratios from sampling the produced biomass (CN_{POM}) usually report the C:N ratio of organic carbon, while C:N ratios estimated from nutrient consumption integrate all carbon and nitrogen that has been removed from the dissolved inorganic pool. When the sampled bloom contains a high amount of calcifiers, a significantly higher C:N ratio has been observed (Robertson et al., 1994). This fact has been used as an explanation for the

relatively high differences between the various studies.

This chapter focuses on the stoichiometric characteristics of the production of phytoplankton in the subpolar North Atlantic. The C:N ratio of suspended particulate organic matter will be studied with respect to the location and the time of year and then compared with the CN ratio of particulate matter (PM). From this comparison the fraction of inorganic carbon in the surface layer will be calculated. Moreover, the consumption and entrainment ratios received from gas exchange corrected DIC, nitrate, phosphate and silicate concentrations will be presented and compared to the data of the suspended POM. All data is separated into four boxes of comparable water mass properties as described in Section 3.3.5. The western part was broken into two boxes reducing the data coverage in comparison to the eastern boxes. The seasonal distributions of the nutrients can be found in Section 7. The sample handling and measuring methods are described in Section 3.3. The sampling positions of the data shown in this chapter is shown in Figure 3.4. An overview of which samples were taken during which crossing is given in the Supplement.

8.1 C:N ratios of suspended particulate matter and the influence of calcification

The C:N ratio of suspended particulate matter (PM) and particulate organic matter (POM) (CN_{PM} , CN_{POM}) with its seasonal variability is shown in Figure 8.1. While CN_{POM} was measured during all three years, CN_{PM} was only measured in 2014. The standard deviation of data varies strongly between the respective crossings (between 0.2 and 2, in exceptional cases up to 6). Generally, it can be seen that the scatter is increasing with increasing average CN ratio, while it is quite small at C:N ratios close to the Redfield ratio. Due to the amount of particulate inorganic carbon in particulate matter, the CN_{PM} is systematically higher than the CN_{POM} . Apart from small variations, the shape of CN_{PM} is following that of CN_{POM} . In the eastern region, high CN_{POM} was observed during winter time, while the maximum in CN_{POM} in the subtropical region was found during the summer. Especially after the onset of summer oligotrophy around Julian day 120, elevated carbon fractions in POM were observed. This can be explained by the growth of cyanobacteria such as *Prochlorococcus* or *Synechococcus*, which are known to show an increase in their CN_{POM} under P-limited conditions (Bertilsson et al.,

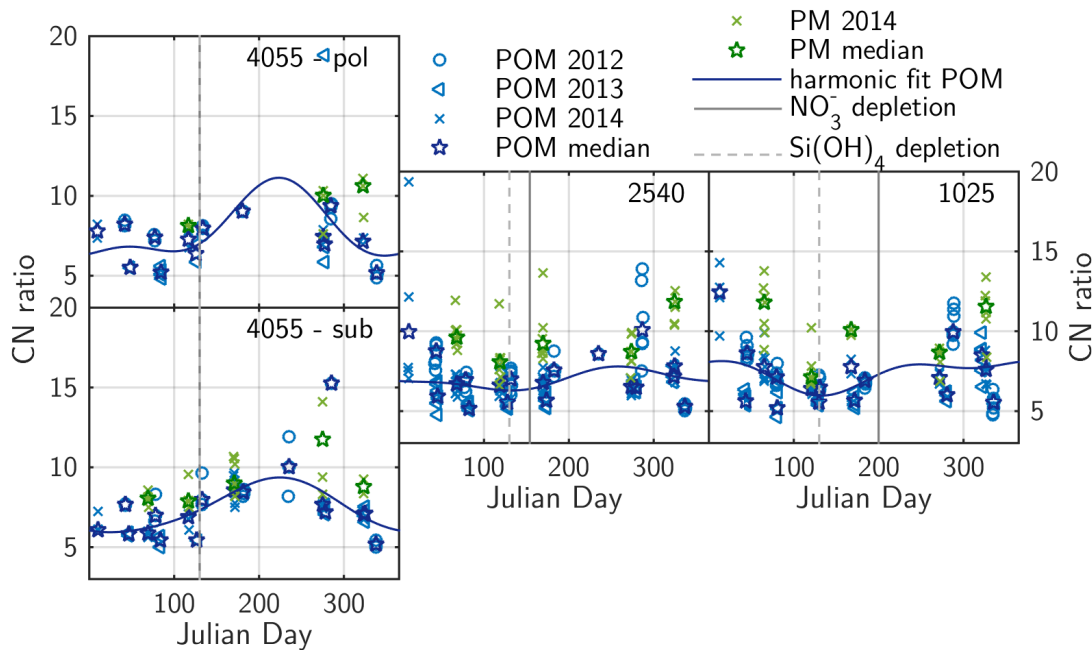


Figure 8.1: The seasonal variation of the C:N ratio of POM (blue) and PM (green) for the four different boxes. Data from different years is denoted with different symbols (2012: circle, 2013: triangle, 2014: cross) and the respective cruise medians are shown as stars. The gray lines indicate the time at which nitrate and silicate start being depleted.

2003). Since the influence of cyanobacteria is only significant in the subtropical region of our study area, the boxes 1025 and 2540 do not show this pattern. Another reason for increasing CN_{POM} during a bloom period can be carbon overconsumption as nitrate becomes more and more depleted (Körtzinger et al., 2001; Koeve, 2004; Jiang et al., 2013). In contrast to other studies, the data shown here do not support the theory of the formation of carbon-rich particulate matter during the bloom phase and more nitrogen-rich particulate matter before and after the bloom. Unfortunately, there is no data between Julian day 180 and 260 for the eastern box so that no statement can be made for the behavior of the CN_{POM} right at the end of the spring bloom (around Julian day 250).

Since the amount of particulate nitrogen is not altered by the acidification of the POM samples prior to measurement, the relative proportion of particulate inorganic carbon (PIC) in suspended particulate carbon (PC) can be calculated from the difference

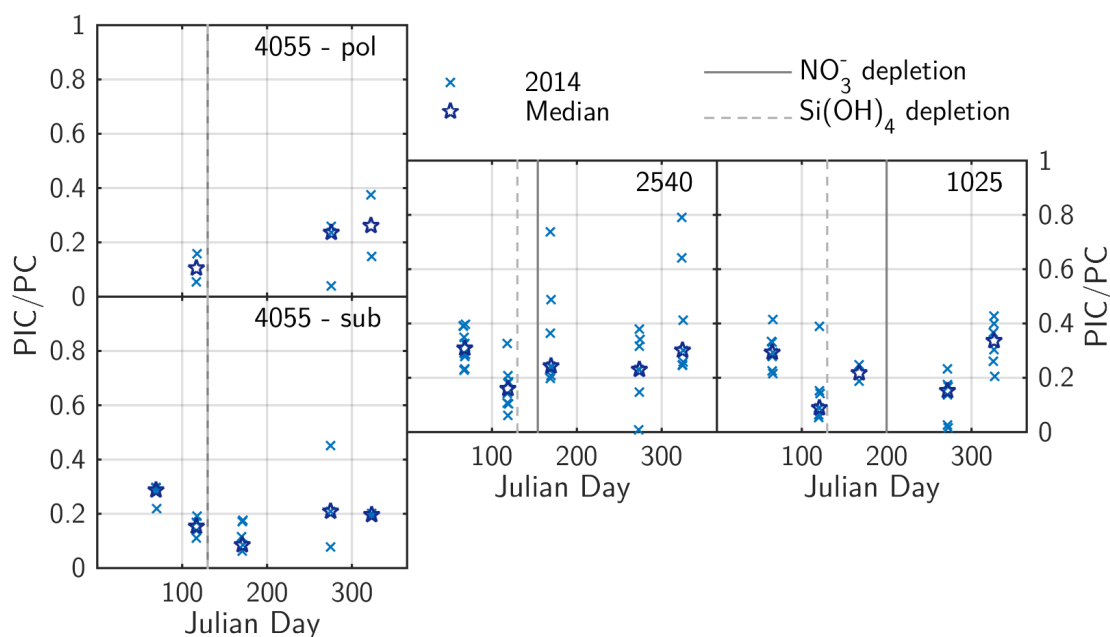


Figure 8.2: The amount of inorganic carbon in particulate matter for the year 2014 (crosses, Median: stars). The gray lines indicate the time at which nitrate and silicate start being depleted.

between CN_{PM} and CN_{POM} according to:

$$\frac{PIC}{PC} = 1 - \frac{CN_{POM}}{CN_{PM}} \quad (8.1)$$

Figure 8.2 shows the fraction of particulate inorganic carbon (PIC/PC) and its variation during 2014. On average, the eastern and central region show a higher fraction of PIC than the western regions. The PIC/PC reaches its maximum in all boxes during winter when slowly growing coccolithophores can develop. The faster growing diatoms can outcompete the coccolithophores in the spring bloom and just by the higher amount of biomass the fraction of PIC is decreasing. After silicate depletion in the boxes 1025 and 2540, we can observe an increase in inorganic carbon which is pointing to a development of a coccolithophore-dominated bloom after the fade-out of the diatoms until the nitrate is also depleted. In the subtropical region, where silicate and nitrate depletion occurs at the same time, such an increase in PIC fraction cannot be seen.

Table 8.1: Time range (Julian day) used for the nutrient correlation plots.

	C:N	C:P	N:P	C:Si	N:Si	Si:P
Bloom						
1025	60-250	60-250	60-250	60-150	60-150	60-150
2540	60-200	60-180	60-180	60-200	60-150	60-150
4055-sub	60-120	60-120	60-120	60-120	60-150	60-120
4055-pol	0-150	0-150	0-150	0-150	0-150	0-150
Entrainment						
1025	280-80	280-80	280-80	280-80	280-80	280-80
2540	280-80	300-80	280-80	280-80	280-80	280-80
4055-sub	300-80	300-80	300-80	300-80	300-80	300-80
4055-pol	300-80	300-80	300-80	300-80	300-80	300-80

8.2 Stoichiometry of nutrient consumption and convective mixing

In this section, the integrated stoichiometric ratios of spring bloom nutrient consumption as well as of the entrainment of nutrients due convective mixing during winter will be presented for the six combinations of DIC, nitrate, phosphate and silicate. The DIC data ($n\text{DIC}_{\text{ASE}}$) were normalized to salinity as described in Section 3.3.5 and corrected for air-sea gas flux by using the mean DIC concentration change due to gas exchange. For the first part of the year (Julian day 0-250), the mean DIC change due to air-sea gas flux until the sampling day was summed up and subtracted from the DIC concentration. For the entrainment (Julian day 250-365), the air-sea gas flux from the sampling day until the end of the year was added to the fall and early winter data. The time range that was used for the respective plots is given in Table 8.1. The mean nutrient ratio was derived from a linear model II regression of the temporal changes of the respective nutrients. The stoichiometric ratios determined by this method are integrating over the entire bloom and entrainment season with fluxes from mixing, primary production and respiration.

The derived C:N uptake ratio during the bloom phase is increasing from east to west, lying slightly above the ratio reported by Redfield (1958) ($\text{CN}_{\text{Redf}} = 6.6$) and Anderson

and Sarmiento (1994) ($CN_{\text{And}} = 7.1$) and well above those in the western boxes (see Figure 8.3 and Table 8.3). The entrainment fluxes, however, are depleted in carbon compared to the drawdown. The variability of the data cannot be fully described by a linear fit as can be seen in box 2540. After the nitrate concentration falls below $5 \mu\text{mol kg}^{-1}$ the slope of the $n\text{DIC}_{\text{ASE}}$ vs NO_3^- plot flattens. This pattern can also be observed in the C:P plot (Figure 8.4). Since this is the time when silicate starts to become limiting a community shift can be hypothesized to be the responsible for this. Also, uncertainties in the air-sea gas flux correction can have an influence on the data, which increases with decreasing mixed layer depth (due to the relative importance of the gas exchange term). Average C:N values from the POM samples reveal near-Redfield composition for all boxes and a CN_{PM} between 8 and 10 (see Table 8.2). The C:N ratios of nutrient consumption are in good agreement with those observed for the PM samples. The production of inorganic carbon can be calculated assuming a mean CN_{POM} as reported by Anderson and Sarmiento (1994). For the boxes 1025 and 2540, a fraction of 20-30 % inorganic carbon is estimated which agrees well with the amount of inorganic carbon estimated from comparing CN_{POM} and CN_{PM} samples while this method overestimates the inorganic carbon that is produced in the western part of the sampling area. Here, N_2 fixation, which can also cause high C:N uptake rates, may be the main reason. N_2 fixation can be inferred in all boxes except the polar one (see Section 9). While the impact of newly fixed nitrogen in the eastern part of the sampling area is negligible for nutrient concentrations, it is reported that a significant amount of nitrogen fixation occurs in subtropical waters (Hansell et al., 2004; Singh et al., 2013). The release of carbon rich DOM is not likely to cause the elevated C:N uptake ratios in the west. Though the DOC concentration is slightly higher ($60 - 70 \mu\text{mol kg}^{-1}$, compared to $50 - 60 \mu\text{mol kg}^{-1}$ in the east) it stays constant during the nutrient drawdown and starts to increase after nutrient depletion. The reduced carbon content in the entrainment flux compared to the bloom period could be explained by preferential remineralization organic carbon compared to inorganic carbon or the addition of newly fixed nitrogen to the produced biomass by nitrogen fixation. According to the appearance of both processes during the bloom phase, the sinking of carbon rich inorganic material beneath the maximal mixed layer depth is the dominant process in the east, while newly fixed nitrogen is accountable for a significant enrichment in upwelled nitrate in the subtropical region.

The carbon to phosphate uptake and entrainment ratio is shown in Figure 8.4. The

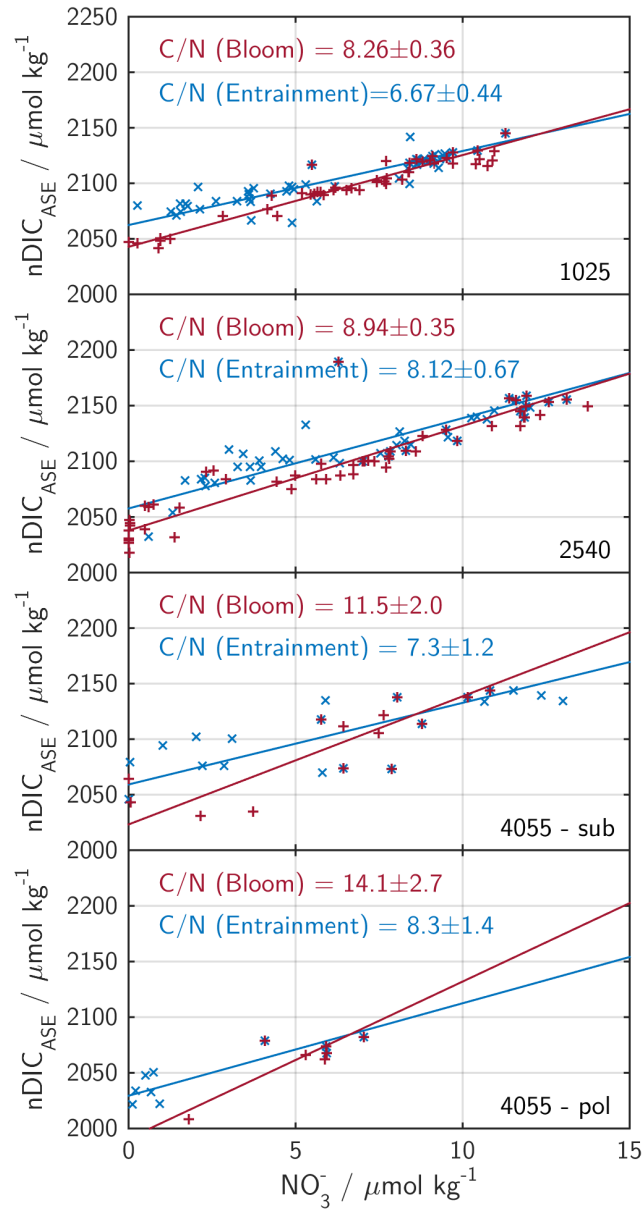


Figure 8.3: DIC to nitrate ratios derived from nutrient consumption during spring bloom (red symbols and fit) and entrainment due to convective mixing in winter (blue symbols and fit).

Table 8.2: Mean C:N_{POM} and C:N_{PM} during the bloom period.

region	C:N _{POM}	C:N _{PM}
1025	6.60 ± 0.97	9.6 ± 2.2
2540	6.48 ± 0.84	9.9 ± 3.5
4055-sub	6.60 ± 0.96	8.12 ± 0.67
4055-pol	7.0 ± 1.2	8.12 ± 0.14

C:P ratio observed during the bloom period is increasing from east to west, with the two eastern and the polar boxes showing C:P ratios only slightly above the Redfield ratio, while the subtropical box has a C:P ratio of 213 ± 27 . The entrainment C:P ratios are lower than those of the bloom period for all boxes and are all close to the average composition of organic matter in the ocean, closer in fact to the value reported by Anderson and Sarmiento (1994) than to the 'original' Redfield ratio. The longitudinal distribution of C:P uptake ratios resembles the findings from the C:N ratios. In the eastern region the production of inorganic carbon leads to an increased amount of carbon consumed per fixed nitrogen. Elevated C:P ratios during primary production up to several times the Redfield ratio are known for colonies of N₂ fixing phytoplankton or cyanobacteria (Nuester et al., 2012; Bertilsson et al., 2003). This can explain the high C:P ratio in the subtropical region. The reduced carbon content in the entrainment flux in the C:N and the C:P ratio compared to the bloom period is probably caused by an enhanced sinking flux of inorganic carbon and its remineralization in deeper water masses than the organic compounds.

The nitrate to phosphate correlation is shown in Figure 8.5. It is often used for estimating the influence of N₂ fixation on a bloom. The intercept of the nitrate vs phosphate plot indicates, whether nitrogen fixation or denitrification is the dominant process in the nitrogen cycle and whether a bloom runs into nitrogen or phosphorous limitation (Deutsch and Weber, 2012). All fits shown in this study have negative intercepts pointing to the possible occurrence of nitrogen fixation. Two boxes show NP ratios close to 16, whereas the eastern and the subtropical box have elevated N:P ratios. For the subtropical box this can be explained by N₂ fixation, while it is unlikely that this process can also explain the high value in the eastern box. In contrast to the C:N and C:P ratios, the N:P ratio during entrainment is slightly smaller, but statistically

Table 8.3: Stoichiometric ratios derived from nutrient concentration changes.

	C:N	C:P	N:P	C:Si	N:Si	Si:P
Bloom						
1025	8.26 ± 0.36	140 ± 12	19.19 ± 0.73	10.8 ± 1.3	1.53 ± 0.14	11.9 ± 1.0
2540	8.94 ± 0.35	151.4 ± 7.2	15.95 ± 0.51	12.80 ± 0.91	1.510 ± 0.090	10.42 ± 0.46
4055-sub	11.5 ± 2.0	213 ± 27	18.6 ± 1.4	22.7 ± 2.1	1.99 ± 0.18	9.2 ± 0.74
4055-pol	14.1 ± 2.7	223 ± 43	15.2 ± 1.2	19.4 ± 2.3	1.33 ± 0.12	11.43 ± 0.98
Entrainment						
1025	6.67 ± 0.44	124.8 ± 9.0	18.4 ± 0.83	15.4 ± 1.0	2.47 ± 0.11	7.22 ± 0.34
2540	8.12 ± 0.67	120.7 ± 8.6	15.42 ± 0.62	15.3 ± 1.3	2.045 ± 0.072	7.62 ± 0.32
4055-sub	7.3 ± 1.2	129 ± 20	17.83 ± 0.75	16.6 ± 2.3	2.24 ± 0.17	7.90 ± 0.47
4055-pol	8.3 ± 1.4	104 ± 18	14.15 ± 0.90	10.4 ± 2.3	1.45 ± 0.13	9.75 ± 0.64
Redfield (1958)	6.6	106	16			
Anderson and Sarmiento (1994)	7.3	117	16			
Brzezinski (1985)			7.7 ± 1.8		0.95 ± 0.33	

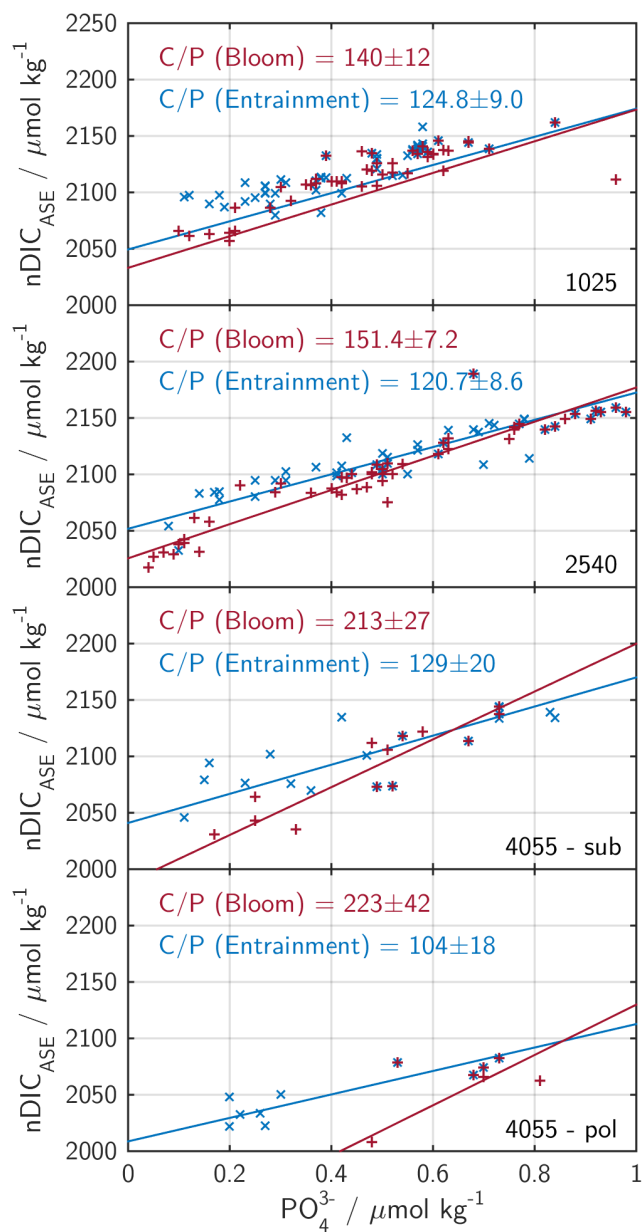


Figure 8.4: Carbon to Phosphate ratios derived from nutrient consumption during spring bloom (red symbols and fit) and entrainment due to convective mixing in winter (blue symbols and fit).

Table 8.4: Fraction of total nutrients fixed by diatoms from the relative consumption of silicate, carbon and nitrate.

Region	$C_{\text{diatom}}/C_{\text{total}}$ from C/Si / %	$N_{\text{diatom}}/N_{\text{total}}$ from N/Si / %
1025	71.2 ± 6.0	63.7 ± 5.7
2540	60.1 ± 4.3	63.1 ± 3.8
4055-sub	33.9 ± 3.2	47.9 ± 4.3
4055-pol	39.7 ± 4.7	71.6 ± 6.6

not distinguishable from that during the bloom period. The linear trend of the relative entrainment of nitrate and phosphate indicates that both nutrients are remineralized at the same depth.

The Figures 8.6 to 8.8 show the relative variations of silicate with respect to DIC, nitrate and phosphate concentrations for the bloom period and the entrainment (C:Si, N:Si and Si:P ratios). For all three correlations it can be seen that the subtropical box differs from the other, while the interpretation of the polar box is limited by the scarce data coverage. In the eastern boxes, the bloom data show higher silicate fractions than the entrainment fluxes while the entrainment flux in the subtropical water is depleted in silicate. This is explicable when keeping in mind that the silicate depletion in the surface water occurs prior to nitrate depletion in the boxes 1025 and 2540. Using a mean elemental ratio of a diatom community ($C/Si = 7.69 \pm 1.8$ and $N/Si = 0.95 \pm 0.33$ (Brzezinski, 1985)), the average fraction of nutrients fixed by diatom growth during the bloom period ($C_{\text{diatom}}/C_{\text{total}}$ and $N_{\text{diatom}}/N_{\text{total}}$) can be calculated (Table 8.4). Although the relative consumption of silicate and carbon or nitrogen can also be influenced by other factors such as growth rate, nutrient limitation or grazing pressure, the shown averages give an idea of the relative importance of diatoms, integrated over the bloom period until silicate depletion. It can be seen that the bloom in the eastern boxes is influenced more strongly by diatom growth than that in the subtropical region, which is in good agreement with higher abundances of the rather big diatoms in subpolar water and their reduced importance for blooms in subtropical areas. The difference between the estimates from C:Si and N:Si reflects the variations in carbon to nitrate uptake and can be distorted by processes like N_2 fixation. The respective elemental ratios of the

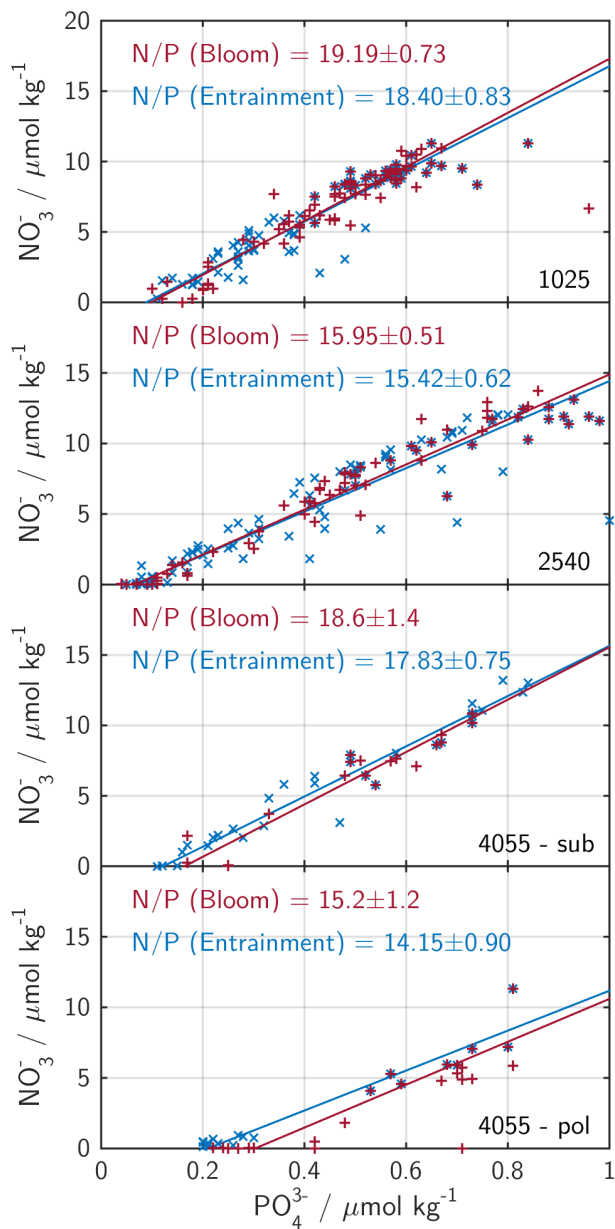


Figure 8.5: Nitrate to Phosphate ratios derived from nutrient consumption during spring bloom (red symbols and fit) and entrainment due to convective mixing in winter (blue symbols and fit).

entrainment fluxes are rather similar for all boxes. In the boxes 1025 and 2540, nitrate and silicate do not show a linear relationship (indicated by the blue logarithmic fits in Figure 8.7). This decoupling can also be observed in the Si:P ratio of the entrainment, though less pronounced due to the higher scatter in the phosphate data. The decoupled entrainment shows a relatively high N:Si ratio at the beginning of the convective mixing and a lower N:Si ratio when the mixed layer depth reaches its maximum. During the sinking of particles carbon, nitrogen and phosphate are remineralized at a shallower depth than silicate. This relative enrichment in silicate with depth can also be seen when studying depth profiles of silicate and is known to have a greater extent in the subpolar region compared to the subtropics (Ragueneau et al., 2006). The much shallower maximal mixed layer depth in the subtropics can be another explanation for the absence of this phenomenon.

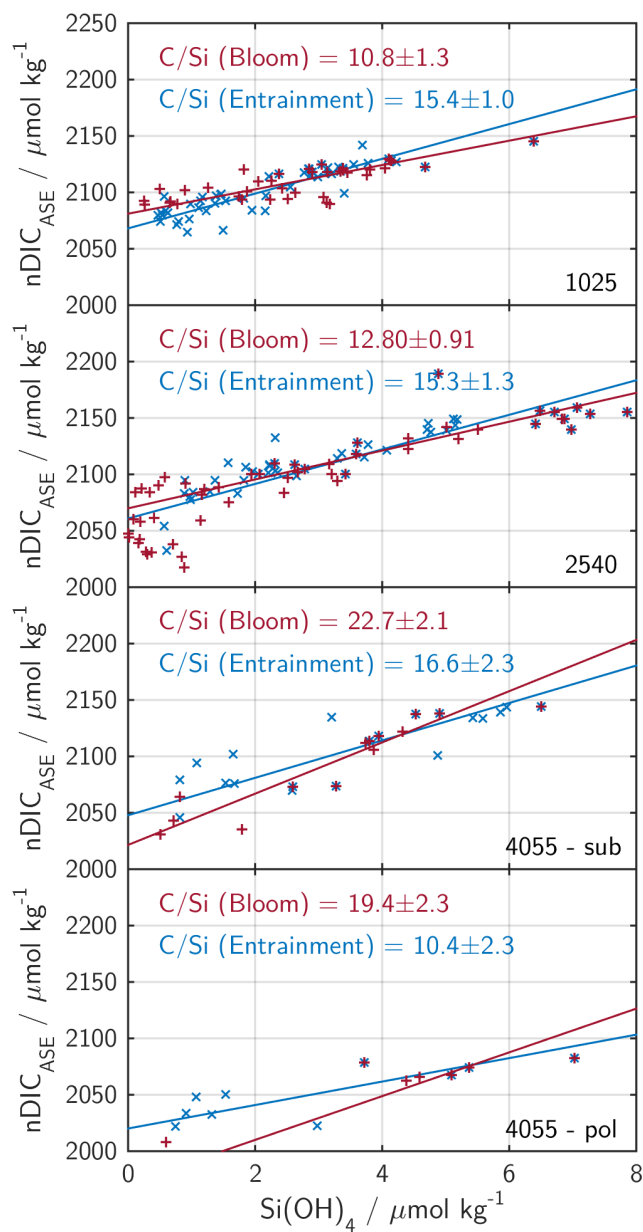


Figure 8.6: Carbon to silicate ratios derived from nutrient consumption during spring bloom (red symbols and fit) and entrainment due to convective mixing in winter (blue symbols and fit).

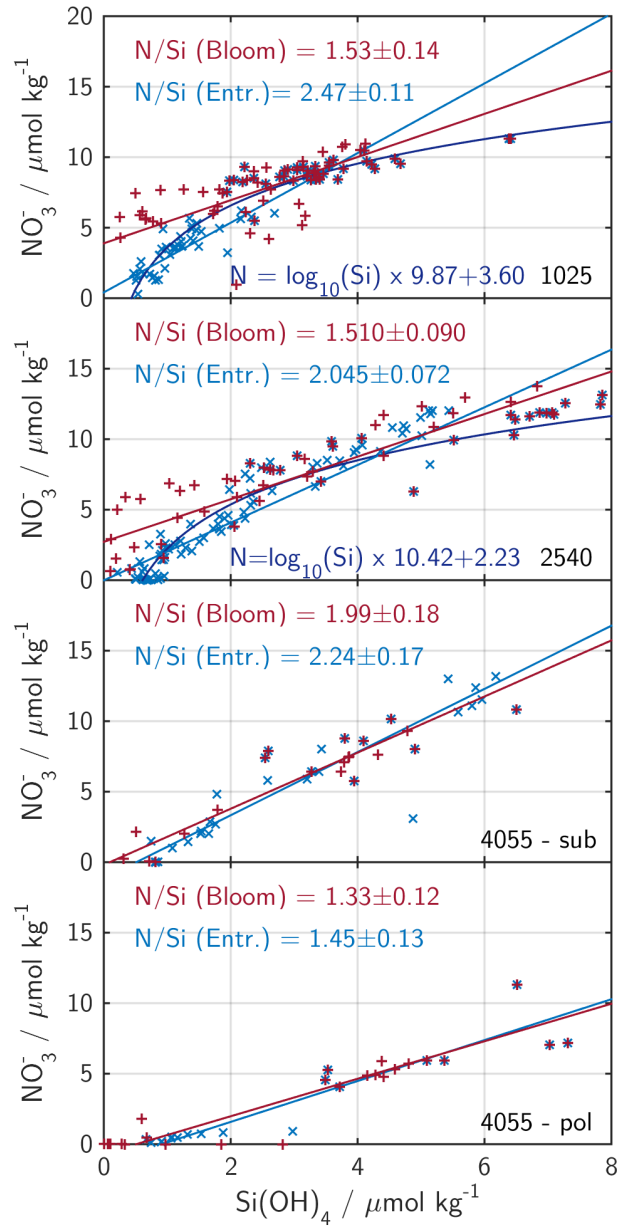


Figure 8.7: Nitrate to silicate ratios derived from nutrient consumption during spring bloom (red symbols and fit) and entrainment due to convective mixing in winter (blue symbols and fit).

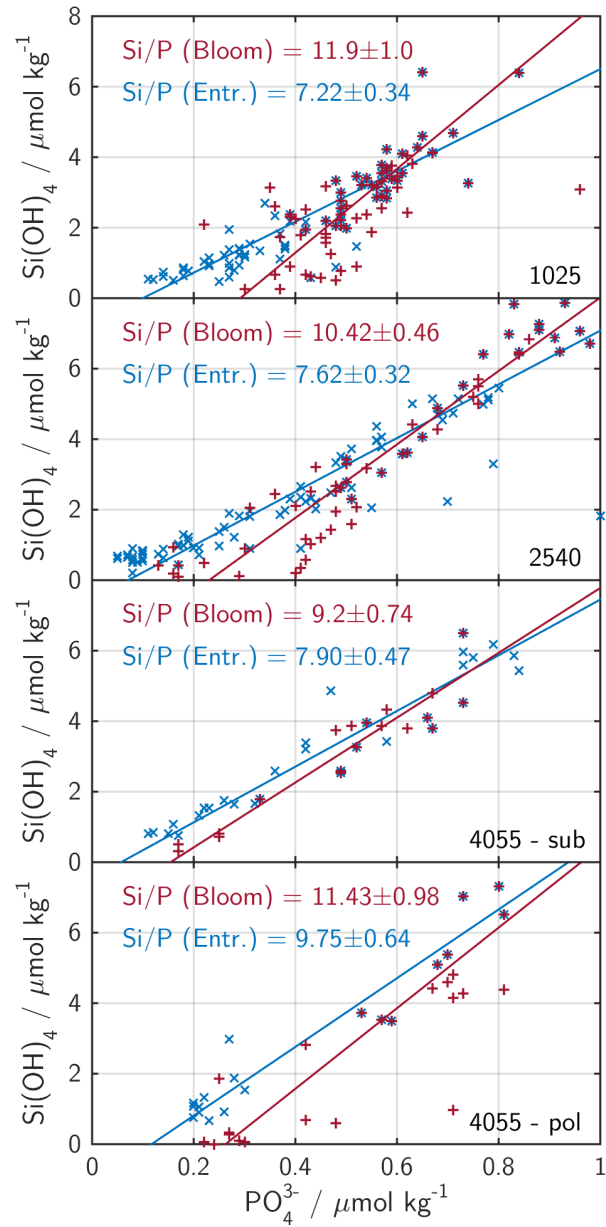


Figure 8.8: Silicate to phosphate ratios derived from nutrient consumption during spring bloom (red symbols and fit) and entrainment due to convective mixing in winter (blue symbols and fit).

9 Measurements of stable isotope signatures of particulate organic matter

In this section I will present the seasonal variations in $\delta^{13}\text{C}(\text{POC})$ and $\delta^{15}\text{N}(\text{PON})$ derived from five transects between March and November 2014. In combination with the underway $\delta^{13}\text{C}(\text{CO}_2)$ data, the fractionation factor ϵ_p between particulate organic carbon and CO_2 will be also shown in its spatial and temporal variability. Finally, a parametrization of ϵ_p depending on the salinity-normalized DIC concentration (nDIC_{35}) will be derived. This equation will be compared with other available parametrizations and the measurements. The sampling locations of the $\delta^{13}\text{C}(\text{POC})$ and DIC samples used in this section are shown in Figure 9.1. The respective sea surface temperatures (SST, left panel) and sea surface salinities (SSS, right panel) are color-coded. For the $\delta^{13}\text{C}(\text{CO}_2)$ data, the underway data were averaged for ≈ 12 min around each sampling time. For studying the differences in the seasonal cycles across the Atlantic, the data was divided into four boxes as described in Chapter 3.3.5.

The first crossing in March was shifted towards the north, especially between 20°W and 35°W . In this longitudinal range significantly lower temperatures were measured during this trip ($6\text{--}8^\circ\text{C}$) compared to the other ($12\text{--}17^\circ\text{C}$) and lower salinities indicated more polar influenced water masses. In the western part the comparability between the crossings is more difficult due the different proportions of cold, fresh water from the Labrador Current and warm and salty water from the Gulf Stream. Here, the ship tracks were shifted southwards during spring and summer, leading to increased SST and SSS along the ship track. During the crossing in June, which was the southernmost crossing, very high SST ($>18^\circ\text{C}$) and SSS (>36 psu) were measured in this area.

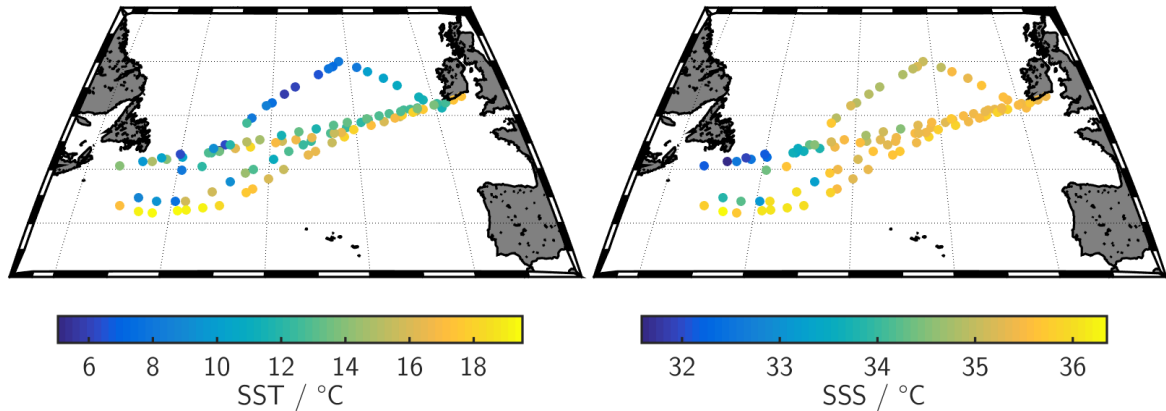


Figure 9.1: Sampling locations of $\delta^{13}\text{C}(\text{POC})$ and $\delta^{15}\text{N}(\text{PON})$ samples and the respective sea surface temperature (left hand plot) and sea surface salinity (right hand plot).

9.1 Seasonality of $\delta^{13}\text{C}(\text{POC})$ and $\delta^{15}\text{N}(\text{PON})$

The seasonal variation of $\delta^{13}\text{C}(\text{POC})$, divided into four boxes, is shown in Figure 9.2. In all boxes, a seasonal variation with heavier POC during the summer season and lighter POC in winter can be clearly seen. The eastern box ($10\text{-}25^\circ\text{W}$) and the adjacent central box ($25\text{-}40^\circ\text{W}$) which are both characterized by water of the North Atlantic Drift Current show a quite similar behavior. In both boxes the lightest values were observed in March (Julian days 60-70). This decrease in $\delta^{13}\text{C}$ is rather attributed to the season than to the slight northward shift of the ship track in winter since the subtropical box also shows light POC values in this month. In this box, the ship track in March overlaps with those in September and November (Julian days 270-280, 320-330). In May (Julian days 110-120), after the bloom developed across the two eastern boxes with high concentrations of *Chl a* (see Figure 7.14) and increased POC concentrations (see Figure 7.16) the particulate organic carbon pool became much heavier, before it started to lighten again in November at the end of the productive season. This progression is in agreement with the observed changes in POC concentrations. The subtropical box in the western part of the basin ($40\text{-}55^\circ\text{W}$) shows a slightly different behavior. Here, the particulate organic carbon pool is continuously becoming heavier from the minimum

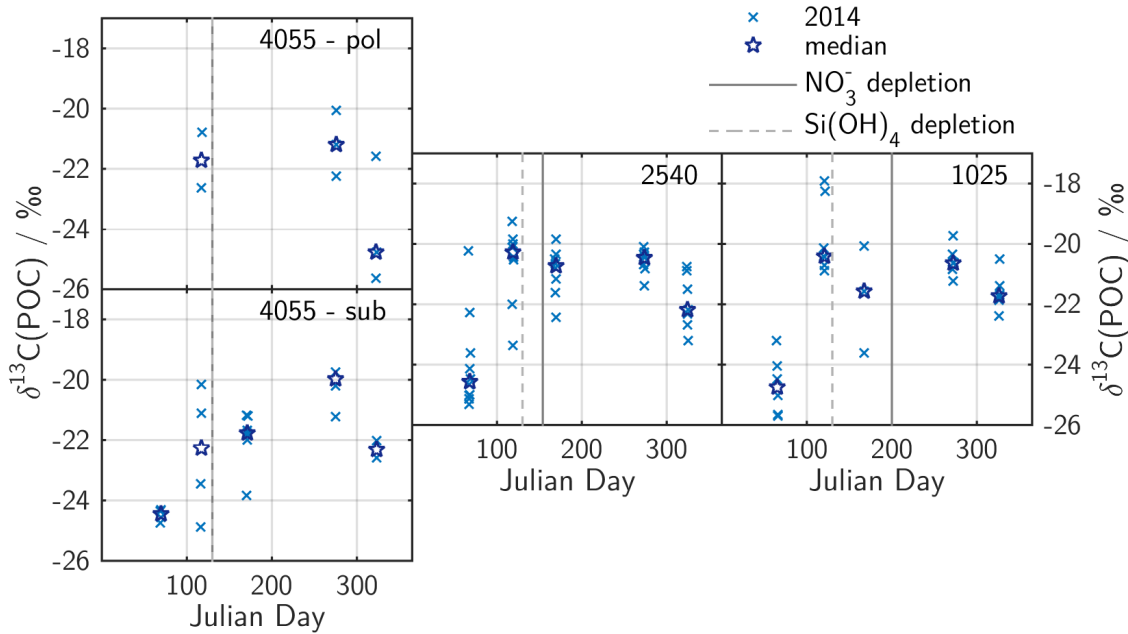


Figure 9.2: Seasonal variations of $\delta^{13}\text{C}(\text{POC})$ in the four regional domains. The gray lines indicate the time at which nitrate and silicate start being depleted.

in March to a maximum in September and after that, lightening again. Unfortunately, samples were not always taken in polar waters, so that this box contains only data from three crossings. However, a trend with heavier POC during the summer and lighter POC during the winter period can be observed, too.

The $\delta^{13}\text{C}(\text{POC})$ follows roughly the shape of the $\delta^{13}\text{C}(\text{CO}_2)$ variations. However, the rapid increase in $\delta^{13}\text{C}(\text{POC})$ during the spring bloom is not seen in the CO_2 isotope ratio and the amplitude of the seasonal variability in $\delta^{13}\text{C}(\text{POC})$ is twice as high as in $\delta^{13}\text{C}(\text{CO}_2)$. Mechanisms which can account for these differences will be discussed in section 9.2. The magnitude of the $\delta^{13}\text{C}(\text{POC})$ data presented here is in good agreement with available $\delta^{13}\text{C}(\text{POC})$ compilations (Goericke and Fry, 1994; Young et al., 2013). Admittedly, these compilations consist of data from 1965-2010 and do not provide information about seasonal variability. During the spring bloom 1989 (April-May) Rau et al. (1992) found $\delta^{13}\text{C}(\text{POC})$ between -22.9‰ and -18.1‰ at 47°N , 20°W which covers the same range as our measurements in May.

For the stable nitrogen isotope ratio of particulate organic nitrogen one would expect increasing values from 0‰ at the start of the bloom to higher values with ongoing de-

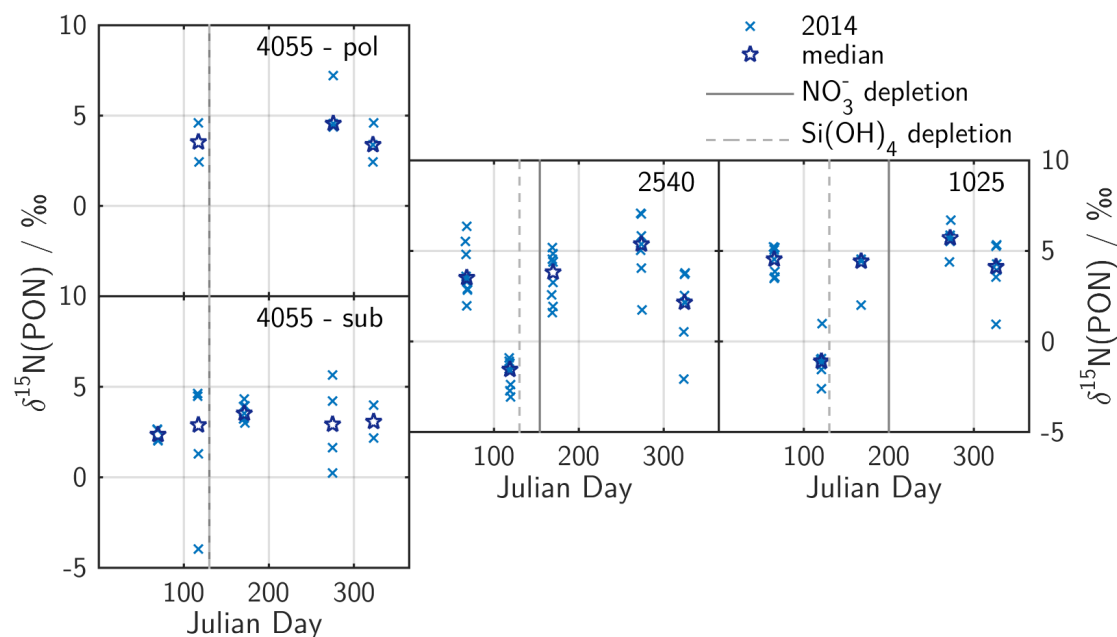


Figure 9.3: Seasonality of $\delta^{15}\text{N}(\text{PON})$ for four different regions across the North Atlantic.

The gray lines indicate the time at which nitrate and silicate start being depleted.

pletion in nitrate concentrations. Organic nitrogen that was introduced by N_2 -fixation should have a negative $\delta^{15}\text{N}(\text{PON})$ of about -2 ‰ (see Chapter 2.3). However, the picture isn't that clear in our data (see Figure 9.3). In all boxes, most samples showed a $\delta^{15}\text{N}(\text{PON})$ of about 5 ‰ , slightly increasing towards September and then decreasing again. This is not consistent with nitrate depletion during the summer months and the respective fractionation changes expected for a Rayleigh process (see Figures 7.4 and 2.3). The duration of this nitrate depletion during summer is increasing from east to west. Moreover, the changes in $\delta^{15}\text{N}$ could not be related to any other measured parameter. In May, the light $\delta^{15}\text{N}(\text{PON})$ indicated the occurrence of nitrogen fixation over almost the entire basin (from $11\text{-}46^\circ\text{W}$). It has been shown, that cyanobacteria such as *Trichodesmium* but also communities of other diazotrophs or diatoms can have such an isotopic signature (Carpenter et al., 1997; Reynolds et al., 2007). The occurrence of this relative depletion is not correlated to a lack of nitrate in the surface water, however. For a more detailed analysis of the processes behind the changes in the stable nitrogen signature of particulate nitrogen more measurements of $\delta^{15}\text{N}(\text{PON})$ are necessary, but

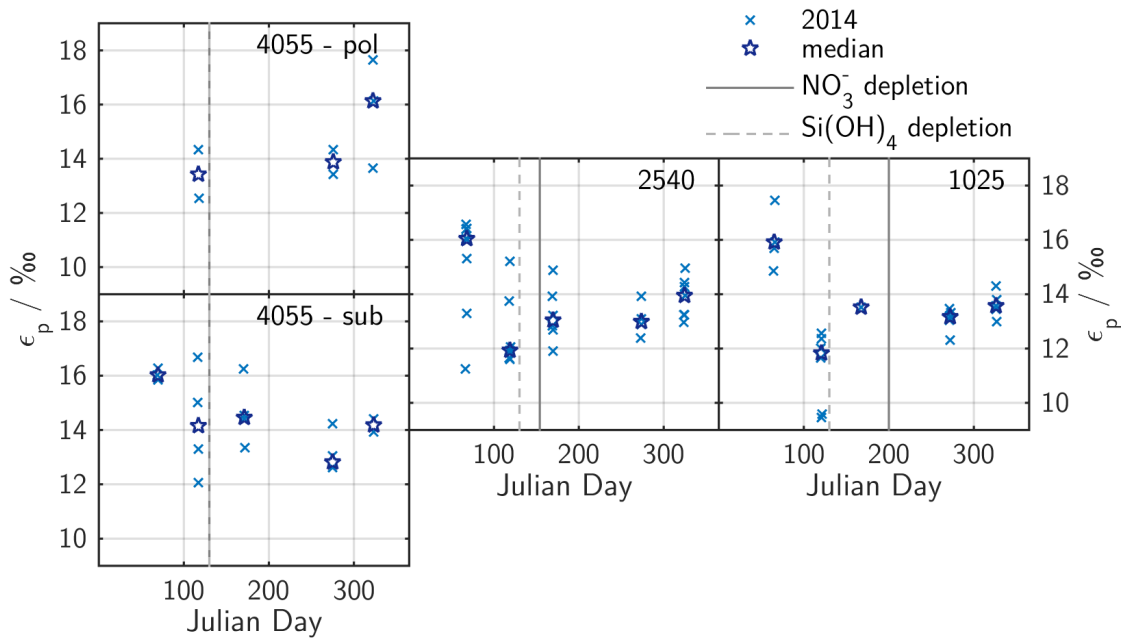


Figure 9.4: The seasonality of fractionation between dissolved CO_2 and POC, ϵ_p . The gray lines indicate the time at which nitrate and silicate start being depleted.

also measurements of additional parameter can help to understand the underlying processes, e.g. trying to close the inorganic part of the nitrogen budget by measuring $\delta^{15}\text{N}$ of nitrate, nitrite and NH_4^+ , the distinction of the isotopic signature of zooplankton and phytoplankton (Hauss et al., 2013), investigating the variability of $\delta^{15}\text{N}(\text{PON})$ with the size of the organisms (Benner et al., 1997) and the analysis of the sampled community structure.

9.2 The fractionation between dissolved CO_2 and POC

The fractionation factor between dissolved CO_2 and particulate organic carbon, ϵ_p , was calculated from $\delta^{13}\text{C}(\text{POC})$ and $\delta^{13}\text{C}(\text{CO}_2)$ according to Equation 2.15. Its seasonal variation, shown in Figure 9.4, reflects mainly the seasonality of $\delta^{13}\text{C}(\text{POC})$ with an increased fractionation during winter and smaller values during summer. This decrease occurs on shorter timescales in the eastern part of the basin with a rapid change towards a minimum in May, whereas in the western, subtropical box, ϵ_p declines slower towards

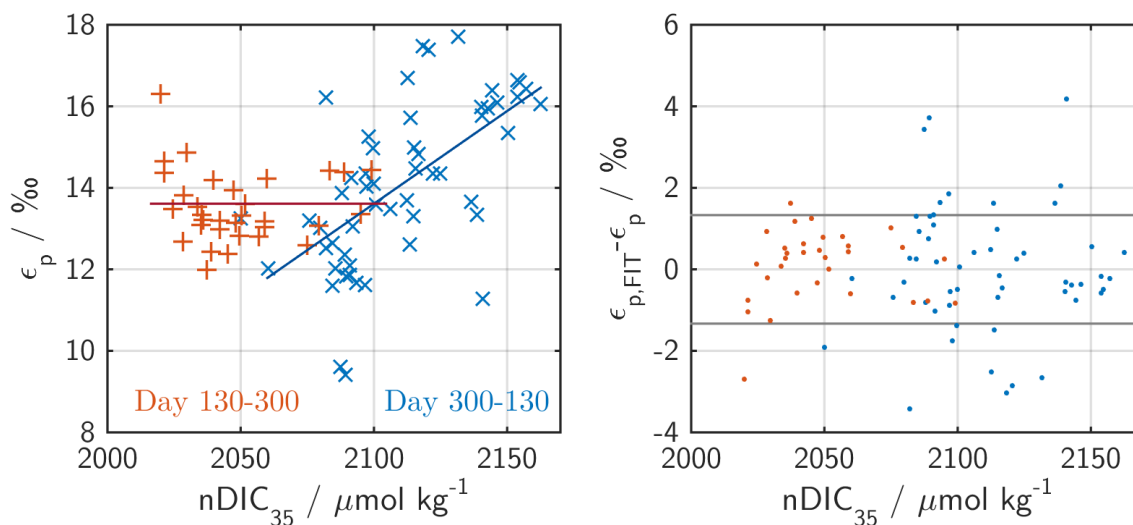


Figure 9.5: Parametrization of ϵ_p based on salinity normalized DIC concentration, $nDIC_{35}$ (left hand plot). The crosses refer to the measured ϵ_p during the periods Julian day 130-300 and 300-130. The lines are the respective fits. The right hand plot shows the deviation between ϵ_p calculated from the parametrization and measured ϵ_p . The gray lines indicate its standard deviation.

a minimum in September. The central box shows signatures that fit to both adjacent boxes, with rapid decrease during spring bloom and a slight decrease from March to September. The data from each month, especially during bloom conditions, show a large scatter in the dimension of the entire seasonal amplitude, showing that there is a high spatial variability and that it is very important for the fractionation during carbon fixation whether the sample was taken in a bloom patch or not. Especially during May very high and variable concentrations of Chl *a* ($0.26 - 5.30 \mu\text{g kg}^{-1}$) and POC ($11 - 60 \mu\text{mol kg}^{-1}$) were measured. The large variability in ϵ_p could be caused by changes that can occur within intense bloom patches, such as a switch in the carbon transport mechanism into the cell from diffusive transport of carbon dioxide to active transport of bicarbonate or by an increased influence of fractionation introduced by this transport process on the overall fractionation.

Several efforts have been made to estimate the fractionation factor with which carbon is fixed by marine primary producers. Goericke and Fry (1994) correlated ϵ_p to the concentration of dissolved CO_2 as well as SST. Young et al. (2013) introduced an estimate

of ϵ_p based on a combination of day of year, SST and nitrate concentration. However, all of these parametrizations underestimate the fractionation shown in this work. The dependence of ϵ_p on DIC, normalized to a salinity of 35, $nDIC_{35}$, is shown in Figure 9.5. Please note, that this relationship could not be improved by using concentrations of dissolved CO_2 instead. The data show a weak correlation of ϵ_p and $nDIC_{35}$ during the winter season ($R^2 = 0.38$), but this correlation breaks down during the productive season. The data from Rau et al. (1992), which were all taken at the same location, shows a strong relationship between ϵ_p and the CO_2 concentration. The fact, that our data do not show such a strong relationship between both parameters, points to the assumption that this direct correlation holds only when the same water mass or bloom event is observed over a certain time, but fails when slightly different water masses or bloom events are sampled.

Based on our observations, we developed two linear parametrizations for different times of the year:

$$\begin{aligned}\epsilon_{p,300-130}/\text{‰} &= (0.05 \pm 0.25) \times nDIC_{35} - (81.9 \pm 2.4) \\ \epsilon_{p,130-300}/\text{‰} &= (13.61 \pm 0.91)\end{aligned}\tag{9.1}$$

Other parameters such as nitrate concentration in the surface water did not show a significant correlation with ϵ_p for the data presented here. Also the isotope signature of dissolved inorganic carbon did not show a significant influence on the fractionation.

Figure 9.6 shows ϵ_p calculated from available parametrizations with respect to seawater properties between $10^\circ W$ and $25^\circ W$. Please note that none of the cited parametrizations claim to correctly reproduce the seasonal variability. There were relative large deviations between the individual parametrizations and none of them could reliably reproduce the observed seasonal changes of ϵ_p . The data calculated from the work of Rau et al. (1992) which was measured in the same area as our data overestimates the amplitude, giving too large fractionations in winter and too small ones in summer time. The parametrization of Popp et al. (1989) which is based on measurements in lakes in New Zealand can reproduce the amplitude, but shows an offset of about 1-2 ‰. The two other parametrizations show a too small amplitude, but the work of Goericke and Fry (1994) captures the summer data, whereas the work of Young et al. (2013) is in agreement with our winter measurements. For estimating the seasonal variations of $\delta^{13}C(DIC)$ from the variability of DIC concentration, it did not make a significant difference which equation was used.

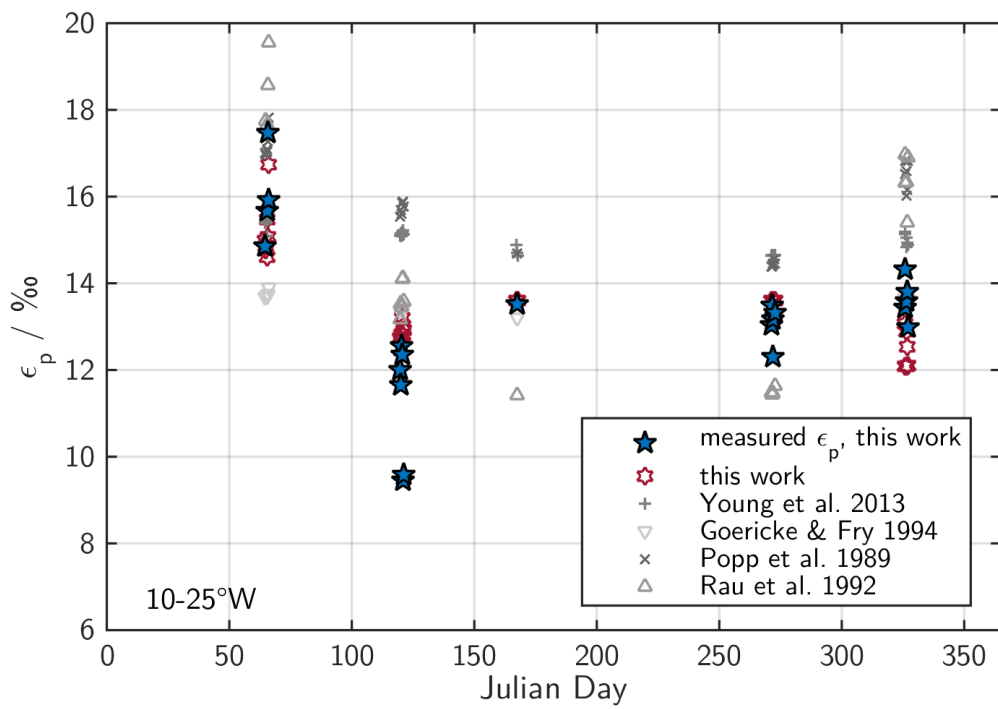


Figure 9.6: Comparison of different parametrizations which relate ϵ_p to carbon system parameter or nitrate concentrations.

However, none of these parametrizations could resolve the strong variability during the spring bloom, implying that the concentrations of CO_2 or NO_3^- in surrounding seawater are not determining the fractionation during primary production under relative intense bloom conditions. For the interpretation of $\delta^{13}\text{C}$ of sedimented POC, however, it is more important to correctly capture the spring/summer fractionation since during this season most of the carbon export takes place.

As already introduced in Section 2.3, the final fractionation factor is a result of the fractionation caused by two main processes during carbon fixation, the transport of inorganic carbon into the cell and the carboxylation reaction of the enzyme *RubisCO*. A smaller fractionation points to an increased influence of the transport process to the overall reaction rate. Based on this theory, it was shown that there is a correlation between the growth rate μ or μ/CO_2 and ϵ_p (Ohkouchi et al., 2015; Rickaby et al., 2010; Baird et al., 2001; Popp et al., 1999; Laws et al., 1995). Correlations were also found for parameter closely related to the growth rate, such as colony size, light intensity (Tchernov and Lipschultz, 2008), nutrient availability (Eek et al., 1999) and the species distribution (Falkowski, 1991).

The data shown in this work lead to the conclusion that the seawater carbon and nutrient concentrations have only a small influence on ϵ_p and can only be the dominant factor during winter time or oligotroph conditions, whereas processes at the cell water interface or within the cell can have a much larger influence and easily determine the overall ϵ_p during bloom periods.

10 Conclusions and outlook

The objectives of this thesis were to establish $\delta^{13}\text{C}(\text{CO}_2)$ -CRDS measurements on a voluntary observing ship and to use the obtained data to draw a picture of processes that drive carbonate and nutrient dynamics in the upper North Atlantic Ocean. Another task of this work was showing the potential that such a diverse time series dataset for the North Atlantic dataset holds for separating important processes. Moreover, the use of stable carbon isotope data as an additional parameter for the carbon system and for calculating the net community production should be explored. So, what can we learn about the North Atlantic from the data presented in this thesis?

The three years of $f\text{CO}_2$ and $\delta^{13}\text{C}(\text{CO}_2)$ data in the North Atlantic that were obtained during this work provide a good insight on the variations of both parameters on seasonal and interannual timescales. In response to increased wind velocities and increased maximal mixed layer depths during years with a positive winter NAO-index, the $f\text{CO}_2$ decrease and the simultaneous $\delta^{13}\text{C}(\text{CO}_2)$ increase due to primary production in spring and summer was more distinct than during the year with negative winter NAO index. This could be a consequence of a higher nutrient supply through the deeper winter mixed layer depth. However, our discrete sampling interval of about seven weeks was too large to resolve these variations in the nutrient data and to verify this assumption.

When interpreting the different regions that were studied in detail across the basin it can be stated, that the variability in all parameters is increasing towards the west. The amplitude of the seasonal cycles also increases towards the west for physical and carbon system parameters, while the amplitude of the nutrient cycles is decreasing in the same direction. This is in agreement with the westwards decreasing maximal winter mixed layer depth. In all regions, the flux associated with net community production for carbon and nutrients becomes positive well before the onset of summer stratification, sometimes even before reaching the maximal mixed layer depth. This leads to the conclusion that a major fraction of the primary production in the mixed layer takes

place between February and May under conditions of a relatively deep mixed layer, i.e. before the establishment of the strongly stratified summer system.

The eastern part of the basin (box 1025 (between 10 °W and 25 °W) and box 2540 (between 25 °W and 40 °W)), the seasonal cycle of carbon is determined by the interplay of primary production in spring and summer and the entrainment of carbon-rich water during convective mixing in fall and winter. The $f\text{CO}_2$ is continuously undersaturated with a disequilibrium of typically $50 \mu\text{atm}$ from April to October and only a small disequilibrium during winter of $< 10 \mu\text{atm}$. The carbon flux due to air-sea gas exchange was calculated to be $(2.22 \pm 0.47) \text{ mol C m}^{-2}\text{yr}^{-1}$ (box 1025) and $(2.54 \pm 0.54) \text{ mol C m}^{-2}\text{yr}^{-1}$ (box 2540).

In both boxes, spring bloom reduces the DIC by about $80 \mu\text{mol kg}^{-1}$ until it is terminated by nitrate depletion. The corresponding $\delta^{13}\text{C}(\text{DIC})$ increases towards a maximum in summer. This increase is caused by the preferred uptake of the lighter isotopomer by primary producers. The entrainment of light, remineralized DIC during convective mixing lightens the DIC pool again.

During bloom period, biomass is produced with a C:N ratio of 8-9 which is slightly higher than during entrainment and the average Redfield ratio but is in agreement with the C:N ratio of suspended particulate matter during the spring period. Based on the different C:N ratios of suspended PM and suspended POM, the fraction of produced inorganic carbon was determined to be between 20 – 30 % with a slightly higher PIC content during winter. During spring bloom, the fraction of PIC in PM is reduced due to a dominating diatom bloom. The reduced carbon content in the entrainment flux suggests that more inorganic carbon is remineralized in deeper water than the organic matter and also deeper than the maximal mixed layer depth.

The silicate is consumed by the diatom bloom until May and, after a species shift away from diatoms, the bloom continues until July. During convective mixing, the entrainment of silicate is decoupled from that of nitrate and phosphate. This decoupling leads to the assumption that the remineralization of biomass silicate is also occurring in deeper water than that of the organic carbon, nitrogen and phosphorus compounds.

The amounts of fixed carbon and nutrients during the bloom were calculated to be $(11.3 \pm 1.9) \text{ mol C m}^{-2}$, $(1.06 \pm 0.14) \text{ mol N m}^{-2}$, $(44.0 \pm 5.6) \text{ mmol P m}^{-2}$ and $(576 \pm 73) \text{ mol Si m}^{-2}$ in box 1025 and $(7.3 \pm 1.1) \text{ mol C m}^{-2}$, $(1.13 \pm 0.11) \text{ mol N m}^{-2}$, $(50.3 \pm 7.2) \text{ mmol P m}^{-2}$ and $(602 \pm 48) \text{ mol Si m}^{-2}$ in box 2540.

Some parameters, such as the concentration of Chl *a*, suggest the appearance of a nutrient-triggered fall bloom. For box 2540, a NCP of about 30 % of the spring bloom was calculated during the fall and winter period. For box 1025, the uncertainty of the entrainment flux did not allow a significant estimate of the fall bloom intensity. However, since silicate and nitrate run into depletion during summer, a small bloom activity in fall is likely, too.

In the western region (boxes 4055 - sub and 4055 - pol (both between 40°W and 55°W)), the picture is slightly more diverse. Two water masses with different characteristics mix; the cold and fresh water of the Labrador Current and the warm and saline Gulf Stream water.

The $f\text{CO}_2$ in both boxes shows a steep minimum caused by the spring bloom and a temperature driven maximum in late summer. This maximum can change the sign of the air-sea disequilibrium for a short time, but during the rest of the year the seawater is undersaturated in CO_2 , as well. This undersaturation can reach values of $\Delta f\text{CO}_2 = -150 \mu\text{atm}$ during spring bloom. The carbon flux due to air sea gas exchange was calculated to be $(3.20 \pm 0.54) \text{ mol C m}^{-2}\text{yr}^{-1}$ (box 4055 - sub) and $(2.11 \pm 1.05) \text{ mol C m}^{-2}\text{yr}^{-1}$ (box 4055 - pol).

The DIC concentration decreases until day 150 and then stays more or less constant for a while. This decrease is associated with an increase in the abundance of the heavier isotope and a rapid decrease of all nutrient abundancies. Around Julian day 120, all nutrients have reached their minimum concentration. Nitrate and silicate concentrations are below the detection limit. The relative consumption of the different nutrients indicates the prevalence of nitrogen fixation in box 4055 - sub.

The fixed carbon and nutrients during the spring bloom period were determined as $(10.7 \pm 1.2) \text{ mol C m}^{-2}$, $(1.02 \pm 0.13) \text{ mol N m}^{-2}$, $(62 \pm 75) \text{ mmol P m}^{-2}$ and $(418 \pm 52) \text{ mol Si m}^{-2}$ in box 4055 - sub and $(3.23 \pm 0.43) \text{ mol C m}^{-2}$, $(0.224 \pm 0.026) \text{ mol N m}^{-2}$, $(14.5 \pm 1.7) \text{ mmol P m}^{-2}$ and $(152 \pm 18) \text{ mol Si m}^{-2}$ in box 4055 - pol.

After spring bloom, the DIC concentration continues to decrease towards a minimum in late summer. This decrease is correlated with a decrease in salinity and is most likely caused by mixing. However, a simultaneous increase in $\delta^{13}\text{C}(\text{DIC})$ indicates that this admixed water mass has a strong biological background. Whether this biological signal stems from a nutrient-triggered fall bloom or an upwelled subsurface bloom could not be distinguished, but both scenarios are possible explanations.

During convective mixing in winter, carbon and nutrient rich waters are mixed to the surface. For the box 4055 - sub, a fall bloom could be observed which fixes about 1/3 of carbon fixed during the spring bloom.

One year of data of stable carbon and nitrogen isotopes of suspended particulate matter gave a hint at their seasonal and spatial variability. The stable carbon isotope ratio of POM was lowest in winter and had a maximum during summer. The fractionation between POM and CO₂ during carbon fixation, ϵ_p , was related to the salinity-normalized DIC concentration. However, the variability in this fractionation during bloom periods could not be resolved by a parametrization based on bulk parameters such as the seawater DIC or CO₂ concentration. Processes occurring within the cell or at the cell wall have a larger influence and determine the supply of carbon to the cell. The $\delta^{15}\text{N}(\text{PON})$ revealed the occurrence of nitrogen fixation all across the basin.

The use of stable carbon isotopes alone to quantitatively distinguish biological influences from mixing fluxes could not be performed. The isotope ratio estimated for a flux caused by lateral transport was too close to that of a flux due to primary production. The propagation of uncertainties associated with the calculation of the input variables, such as measurements uncertainties and the spatial and temporal variability of the data, were too large to yield a reliable output.

For a consistent overview of seasonal and spatial variations in $\delta^{13}\text{C}(\text{DIC})$, also within the water column, publicly available $\delta^{13}\text{C}(\text{DIC})$ data from research cruises between 1981 and 2012 was collected and combined with unpublished data from six additional cruises. This compilation was quality controlled by conducting a crossover study and published at CDIAC (doi:10.3334/CDIAC/OTG.NAC13v1), so that it can be used for future estimates of integrated anthropogenic carbon.

This work demonstrates, that measuring full seasonal cycles of carbon parameter and nutrient concentrations holds a large potential for getting a consistent picture of upper ocean carbon dynamics. However, to some extent, the interpretation and the budget calculation is still limited by the sampling interval and the latitudinal shifts of the vessel track between different crossings. Increasing the sampling rate and the spatial coverage, by operating more $p\text{CO}_2$ systems with sampling program on commercial vessels, or decreasing the interval between crossings with discrete sampling program, could further

improve the calculations and the entire dataset. There is a restriction concerning time and missing financial resources, though. Therefore, a more promising approach would be to develop and install more autonomous instruments for various parameters such as TA, nutrients or organic carbon. Developing system components, which could be installed on a new VOS with less effort than an entire $p\text{CO}_2$ system, and coupling them with small, low maintenance and easy to handle sensors could also be useful. The network that was developed in a whole series of European projects, such as CarboOcean, CarboChange and ICOS, for the coordination and quality control of $f\text{CO}_2$ measurements during the last years should be kept up and expanded to include other parameters or combined with already existing networks.

However, if we aim at gaining a better understanding of such a large, complex and important system as the North Atlantic and enable an improvement of the reliability of forecasting routines for future changes, a strong new attempt should be made. A VOS can provide an excellent, cost-efficient platform for sampling various parameters. By combining our systematic chemical measurement program with a systematic sampling of, for example, biological parameter such as community structure or gene analysis our understanding could be significantly improved. Besides, expanding our sampling program to other disciplines, the cooperation with already existing sampling programs such as the Continuous Plankton Recorder Survey, should be established.

11 Supplement

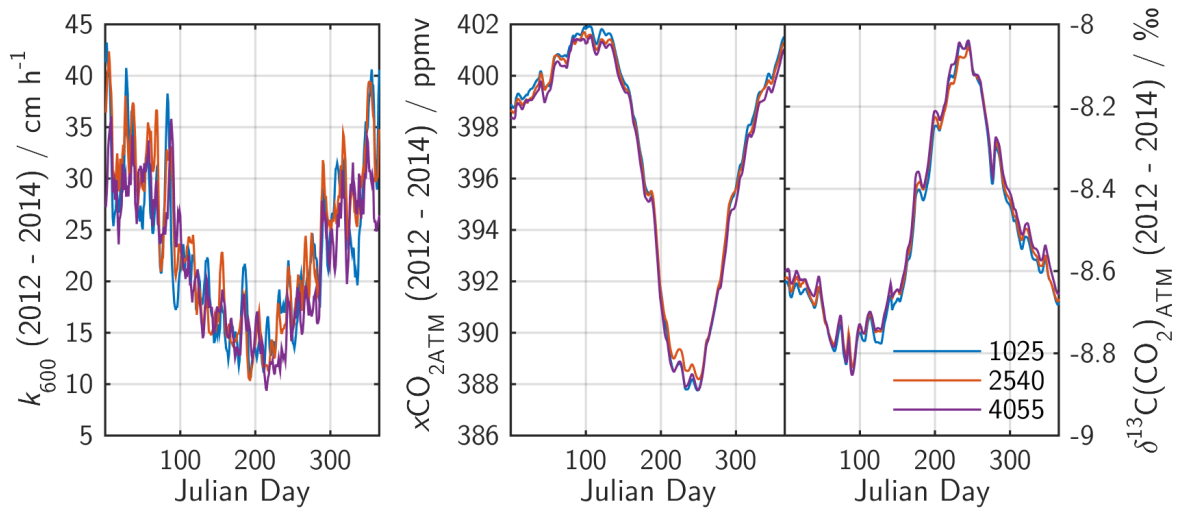


Figure 11.1: Wind speed (left panel), $f\text{CO}_{2,\text{ATM}}$ (central panel) and $\delta^{13}\text{C}(\text{CO}_2)_{\text{ATM}}$ (right panel) that were used in the model calculations. (blue: box 1025, red: box 2540, purple: box 4055).

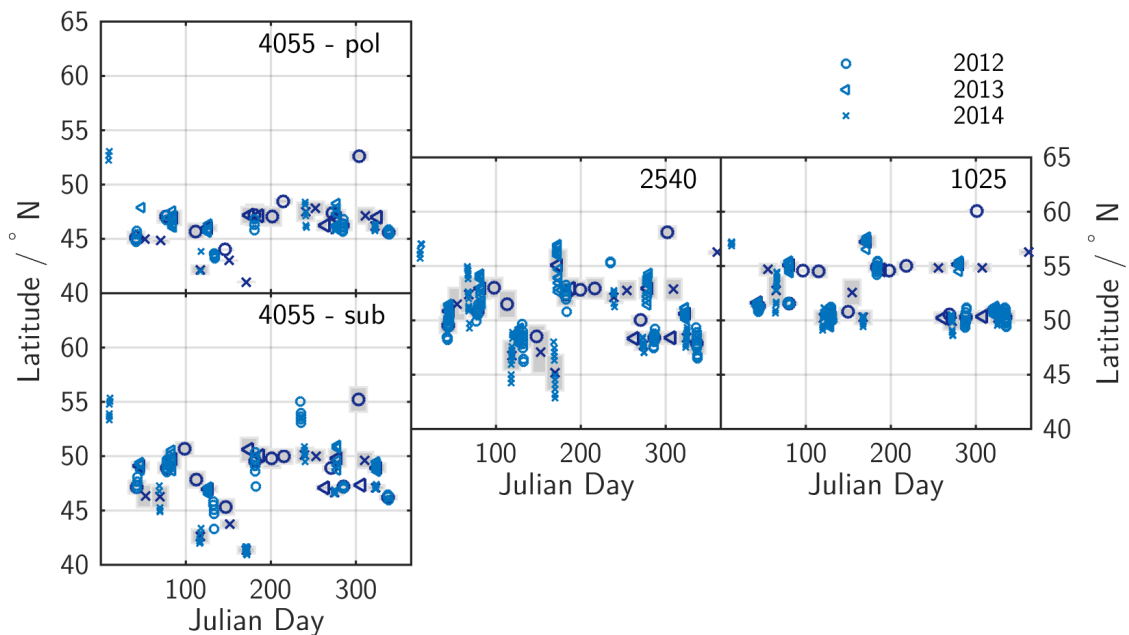


Figure 11.2: Variations in the latitudinal distribution of the data in each regional box (2012: circle, 2013: triangle, 2014: cross; dark blue: box means of underway data, gray bar: box mean \pm standard deviation of underway data, light blue: SST at sampling position).

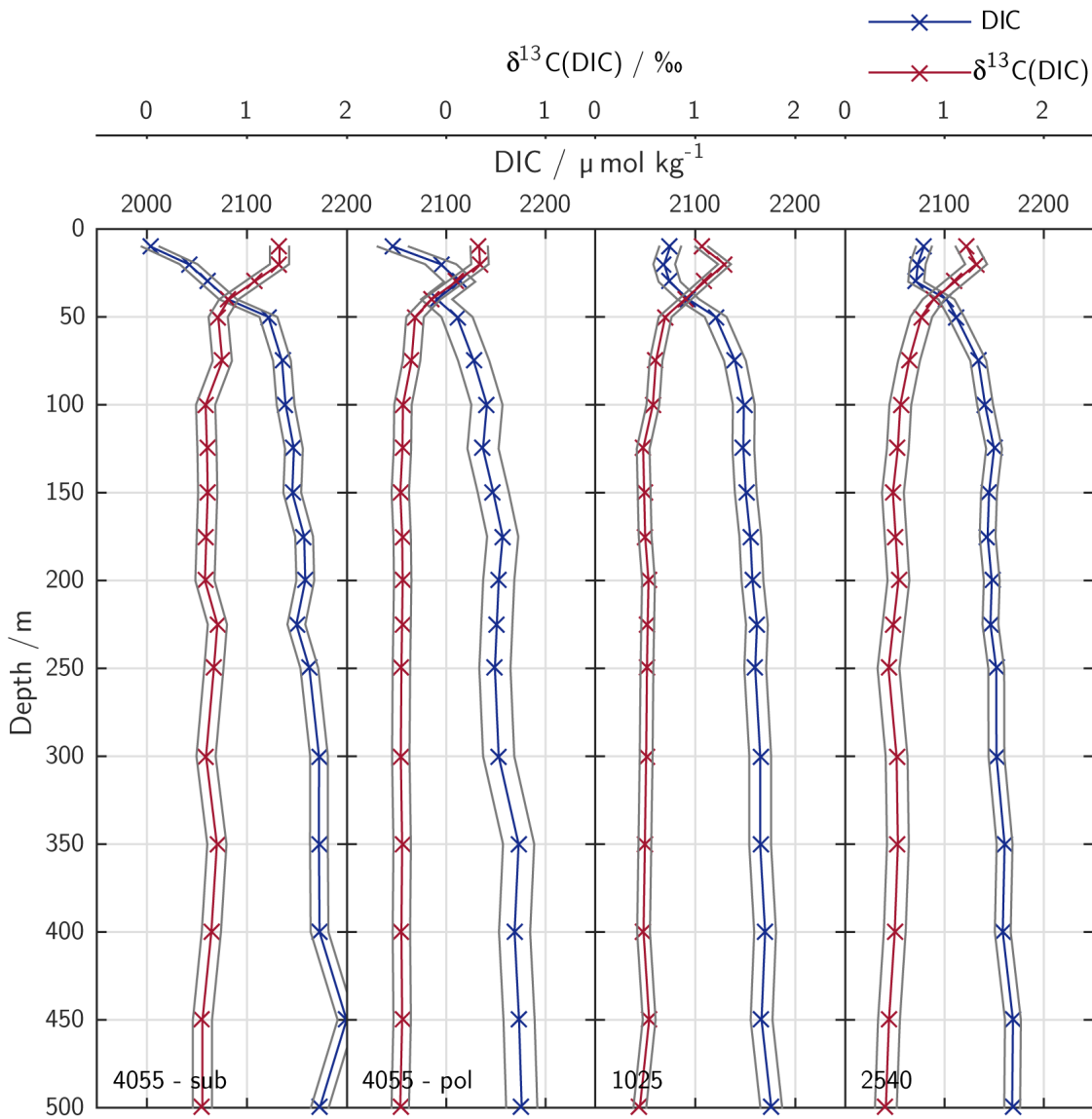


Figure 11.3: Average summer profiles of DIC (blue) and $\delta^{13}\text{C}(\text{DIC})$ (red) for each regional box. The respective mean standard deviation is shown in gray. The DIC data were taken from GLODAP v2 (Olsen et al., 2016) and the $\delta^{13}\text{C}(\text{DIC})$ data from NAC13v1 (Becker et al., 2016).

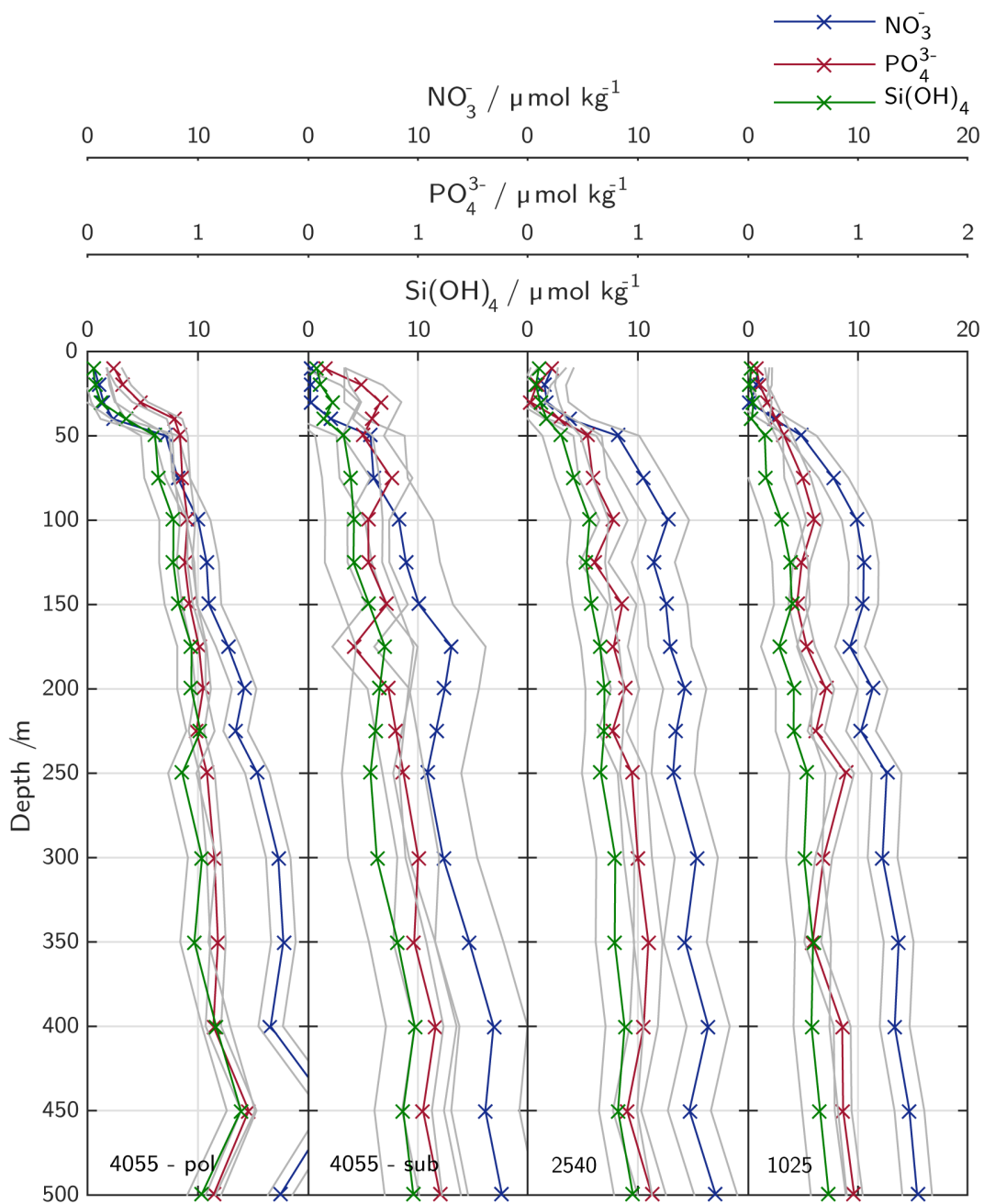


Figure 11.4: Average summer profiles of nitrate (blue), phosphate (red) and silicate (green) for each regional box. The respective mean standard deviation is shown in gray. The data were taken from GLODAP v2 (Olsen et al., 2016).

Table 11.1: Overview of all measurements performed during the crossings.

cruise ID	Month	NDIR	CRDS	sampling				
		data	data	TA/DIC	nutrients	CN	$\delta^{13}\text{C}(\text{DIC})$	i-POM
COM 12-03	Feb	yes		yes	yes	yes		
COM 12-05	Mar	yes		yes	yes	yes		
COM 12-06	Apr	yes						
COM 12-07	Apr	yes						
COM 12-08	May	yes	yes	yes	yes	yes		
COM 12-09	May	yes	yes					
COM 12-11	Jun	yes	yes	yes	yes	yes		
COM 12-12	Jul	yes	yes					
COM 12-13	Jul	yes	yes					
COM 12-15	Sep	yes						
COM 12-16	Sep	yes						
COM 12-17	Oct	yes		yes	yes	yes		
COM 12-18	Nov	yes						
COM 12-20	Dec	yes	yes	yes	yes	yes		
COM 12-21	Dec	yes	yes					
COM 13-03	Feb	yes	yes	yes	yes	yes		
COM 13-05	Mar	yes	yes	yes	yes	yes		
COM 13-08	May	yes	yes	yes	yes	yes		
COM 13-11	Jun		yes		yes	yes		
COM 13-12	Jul		yes					
COM 13-15	Sep	yes						
COM 13-16	Oct	yes		yes	yes	yes	yes	
COM 13-18	Nov	yes						
COM 13-19	Nov	yes		yes	yes	yes		
COM 14-01	Jan			yes	yes	yes	yes	
COM 14-03	Feb	yes						
COM 14-04	Mar		yes	yes	yes	yes	yes	yes
COM 14-05	Mar		yes					

continued on next page

continued from previous page

cruise ID	Month	NDIR data	CRDS data	sampling				
				TA/DIC	nutrients	CN	$\delta^{13}\text{C}(\text{DIC})$	i-POM
COM 14-06	Apr	yes	yes					
COM 14-07	Apr	yes	yes	yes	yes	yes	yes	yes
COM 14-08	May	yes	yes					
COM 14-09	Jun	yes	yes					
COM 14-10	Jun	yes	yes		yes	yes		yes
COM 14-14	Aug	yes	yes					
COM 14-15	Sep	yes	yes					
COM 14-16	Sep	yes	yes		yes	yes		yes
COM 14-18	Nov	yes	yes					
COM 14-19	Nov	yes	yes	yes	yes	yes		yes
COM 14-21	Dec	yes	yes					

Bibliography

Alkire, M. B., D'Asaro, E., Lee, C., Perry, M. J., Gray, A., Cetinic, I., Briggs, N., Rehm, E., Kallin, E., Kaiser, J., and González-Posada, A.: Estimates of net community production and export using high-resolution, Lagrangian measurements of O_2 , NO_3^- , and POC through the evolution of a spring diatom bloom in the North Atlantic, *Deep-Sea Res. Pt I*, 64, 157 – 174, doi:10.1016/j.dsr.2012.01.012, 2012.

Alkire, M. B., Lee, C., D'Asaro, E., Perry, M. J., Briggs, N., Cetinic, I., and Gray, A.: Net community production and export from Seaglider measurements in the North Atlantic after the spring bloom, *J. Geophys. Res. Oceans*, 119, 6121–6139, doi:10.1002/2014JC010105, 2014.

Anderson, L. A. and Sarmiento, J. L.: Redfield ratios of remineralization determined by nutrient data analysis, *Global Biogeochem. Cycles*, 8, 65–80, doi:10.1029/93GB03318, 1994.

Auer, S. J.: Five-year climatological survey of the Gulf Stream system and its associated rings, *J. Geophys. Res. Oceans*, 92, 11 709–11 726, doi:10.1029/JC092iC11p11709, 1987.

Baird, M. E., Emsley, S. M., and Mcglade, J. M.: Using a phytoplankton growth model to predict the fractionation of stable carbon isotopes, *J. Plankton Res.*, 23, 841–848, 2001.

Bakker, D. C. E., Pfeil, B., Smith, K., Hankin, S., Olsen, A., Alin, S. R., Cosca, C., Hara-sawa, S., Kozyr, A., Nojiri, Y., O'Brien, K. M., Schuster, U., Telszewski, M., Tilbrook, B., Wada, C., Akl, J., Barbero, L., Bates, N. R., Boutin, J., Bozec, Y., Cai, W.-J., Castle, R. D., Chavez, F. P., Chen, L., Chierici, M., Currie, K., de Baar, H. J. W., Evans, W., Feely, R. A., Fransson, A., Gao, Z., Hales, B., Hardman-Mountford, N. J., Hoppema, M., Huang, W.-J., Hunt, C. W., Huss, B., Ichikawa, T., Johannessen, T.,

- Jones, E. M., Jones, S. D., Jutterström, S., Kitidis, V., Körtzinger, A., Landschützer, P., Lauvset, S. K., Lefèvre, N., Manke, A. B., Mathis, J. T., Merlivat, L., Metzl, N., Murata, A., Newberger, T., Omar, A. M., Ono, T., Park, G.-H., Paterson, K., Pierrot, D., Ríos, A. F., Sabine, C. L., Saito, S., Salisbury, J., Sarma, V. V. S. S., Schlitzer, R., Sieger, R., Skjelvan, I., Steinhoff, T., Sullivan, K. F., Sun, H., Sutton, A. J., Suzuki, T., Sweeney, C., Takahashi, T., Tjiputra, J., Tsurushima, N., van Heuven, S. M. A. C., Vandemark, D., Vlahos, P., Wallace, D. W. R., Wanninkhof, R., and Watson, A. J.: An update to the Surface Ocean CO₂ Atlas (SOCAT version 2), *Earth Syst. Sci. Data*, 6, 69–90, doi:10.5194/essd-6-69-2014, 2014.
- Becker, M., Andersen, N., Fiedler, B., Fietzek, P., Körtzinger, A., Steinhoff, T., and Friedrichs, G.: Using cavity ringdown spectroscopy for continuous monitoring of $\delta^{13}\text{C}(\text{CO}_2)$ and $f\text{CO}_2$ in the surface ocean, *Limnol. Oceanogr.: Methods*, 10, 752–766, doi:10.4319/lom.2012.10.752, 2012.
- Becker, M., Andersen, N., Erlenkeuser, H., Humphreys, M., Tanhua, T., and Körtzinger, A.: An Internally Consistent Dataset of $\delta^{13}\text{C}$ -DIC in the North Atlantic Ocean - NAC13v1, *Earth Syst. Sci. Data Dis.*, 2016, 1–18, doi:10.5194/essd-2016-7, 2016.
- Benner, R., Biddanda, B., Black, B., and McCarthy, M.: Abundance, size distribution, and stable carbon and nitrogen isotopic compositions of marine organic matter isolated by tangential-flow ultrafiltration, *Mar. Chem.*, 57, 243 – 263, doi: [http://dx.doi.org/10.1016/S0304-4203\(97\)00013-3](http://dx.doi.org/10.1016/S0304-4203(97)00013-3), 1997.
- Bertilsson, S., Berglund, O., Karl, D. M., and Chisholm, S. W.: Elemental composition of marine *Prochlorococcus* and *Synechococcus*: Implications for the ecological stoichiometry of the sea, *Limnol. Oceanogr.*, 48, 1721–1731, doi:10.4319/lo.2003.48.5.1721, 2003.
- Bigg, G. R., Dye, S. R., and Wadley, M. R.: Interannual variability in the 1990s in the northern Atlantic and Nordic Seas, *J. Atmos. Oc. Sci.*, 10, 123–143, doi: 10.1080/17417530500282873, 2005.
- Bonjean, F. and Lagerloef, G. S. E.: Diagnostic Model and Analysis of the Surface Currents in the Tropical Pacific Ocean, *J. Phys. Oceanogr.*, 32, 2938–2954, doi: 10.1175/1520-0485(2002)032<2938:DMAAOT>2.0.CO;2, 2002.

- Borkman, D. G. and Smayda, T. J.: Gulf Stream position and winter NAO as drivers of long-term variations in the bloom phenology of the diatom *Skeletonema costatum* 'species-complex' in Narragansett Bay, RI, USA, *J. Plankton Res.*, doi:10.1093/plankt/fbp072, 2009.
- Brzezinski, M. A.: The Si:C:N ratio of marine diatoms: interspecific variability and the effect of some environmental variables, *J. Phycol.*, 21, 347–357, doi:10.1111/j.0022-3646.1985.00347.x, 1985.
- Carlson, C. A., Hansell, D. A., Nelson, N. B., Siegel, D. A., Smethie, W. M., Khatiwala, S., Meyers, M. M., and Halewood, E.: Dissolved organic carbon export and subsequent remineralization in the mesopelagic and bathypelagic realms of the North Atlantic basin, *Deep-Sea Res. Pt II*, 57, 1433 – 1445, doi:10.1016/j.dsr2.2010.02.013, *ecological and Biogeochemical Interactions in the Dark Ocean*, 2010.
- Carpenter, E. J., Harvey, H., Fry, B., and Capone, D. G.: Biogeochemical tracers of the marine cyanobacterium *Trichodesmium*, *Deep-Sea Res. Pt I*, 44, 27 – 38, doi:10.1016/S0967-0637(96)00091-X, 1997.
- Chikaraishi, Y.: $^{13}\text{C}/^{12}\text{C}$ signatures in plants and algae, in: *Treatise on geochemistry*, edited by Freeman, K. H., Elsevier, Amsterdam, 2 edn., 2014.
- Chipman, D. W., Marra, J., and Takahashi, T.: Primary production at 47°N and 20°W in the North Atlantic Ocean: a comparison between the ^{14}C incubation method and the mixed layer carbon budget, *Deep-Sea Res. Pt II*, 40, 151 – 169, doi:10.1016/0967-0645(93)90011-B, 1993.
- Chiswell, S. M., Calil, P. H., and Boyd, P. W.: Spring blooms and annual cycles of phytoplankton: a unified perspective, *J. Plankton Res.*, doi:10.1093/plankt/fbv021, 2015.
- Ciais, P., Sabine, C., Bala, G., Bopp, L., Brovkin, V., Canadell, J., Chabra, A., DeFries, R., Galloway, J., Heimann, M., Jones, C., LeQuere, C., Myneni, R., Piao, S., and Thornton, P.: Carbon and Other Biogeochemical Cycles, in: *Climate Change 2013: The Physical Science Basis. Contribution of Working Group I to the Fifth Assessment Report of the Intergovernmental Panel on Climate Change*, edited by Stocker, T., Qin, D., Plattner, D.-K., Tignor, M., Allen, S., Boschung, J., Nauels, A., Xia, Y., Bex,

- V., and Midgley, P., pp. 465–570, Cambridge University Press, Cambridge, United Kingdom and New York, NY, USA, doi:10.1017/CBO9781107415324.015, 2013.
- Colebrook, J.: Continuous plankton records: seasonal variations in the distribution and abundance of plankton in the North Atlantic Ocean and the North Sea, *J. Plankton Res.*, 4, 435–462, doi:10.1093/plankt/4.3.435, 1982.
- Colebrook, J. M.: Continuous Plankton Records: Seasonal cycles of phytoplankton and copepods in the North Atlantic ocean and the North Sea, *Mar. Biol.*, 51, 23–32, doi: 10.1007/BF00389027, 1979.
- "Cooperative Global Atmospheric Data Integration Project": Multi-laboratory compilation of atmospheric carbon dioxide data for the period 1968-2014, obspack_co2_1_GLOBALVIEWplus_v1.0_2015-07-30, NOAA Earth System Research Laboratory, Global Monitoring Division, doi:10.15138/G3RP42, compiled by NOAA Global Monitoring Division: Boulder, Colorado, U.S.A, 2015.
- Craig, H.: Isotopic standards for carbon and oxygen and correction factors for mass-spectrometric analysis of carbon dioxide, *Geochim. Cosmochim. Acta*, 12, 133–149, 1957.
- Cullen, J. J.: The Deep Chlorophyll Maximum: Comparing Vertical Profiles of Chlorophyll a, *Can. J. Fish. Aquat. Sci.*, 39, 791–803, doi:10.1139/f82-108, 1982.
- Deutsch, C. and Weber, T.: Nutrient Ratios as a Tracer and Driver of Ocean Biogeochemistry, *Ann. Rev. Mar. Sci.*, 4, 113–141, doi:10.1146/annurev-marine-120709-142821, 2012.
- Dickson, A. and Millero, F.: A comparison of the equilibrium constants for the dissociation of carbonic acid in seawater media, *Deep-Sea Res. Pt I*, 34, 1733 – 1743, doi:10.1016/0198-0149(87)90021-5, 1987.
- Dickson, A., Sabine, C., and Christian, J., eds.: Guide to Best Practices for Ocean CO₂ measurements, PICES Special Publication 3, 2007.
- Dickson, A. G.: The development of the alkalinity concept in marine chemistry, *Mar. Chem.*, 40, 49–63, 1992.

- Dlugokencky, E. and Tans, P. P.: Recent CO₂, NOAA, ESRS, URL www.esrl.noaa.gov/gmd/ccgg/trends/global.html, 2016.
- Eek, M. K., Whiticar, M. J., Bishop, J. K. B., and Wong, C. S.: Influence of nutrients on carbon isotope fractionation by natural populations of Prymnesiophyte algae in NE Pacific, *Deep-Sea Res. Pt II*, 46, 2863–2876, 1999.
- Falkowski, P. G.: Species variability in the fractionation of ¹³C and ¹²C by marine phytoplankton, *J. Plankton Res.*, 13, 21–28, 1991.
- Ferrari, R., Merrifield, S. T., and Taylor, J. R.: Shutdown of convection triggers increase of surface chlorophyll, *J. Marine Syst.*, 147, 116 – 122, doi:10.1016/j.jmarsys.2014.02.009, 2015.
- Frankignoul, C., de Coëtlogon, G., Joyce, T. M., and Dong, S.: Gulf Stream Variability and Ocean-Atmosphere Interactions, *J. Phys. Oceanogr.*, 31, 3516–3529, doi:10.1175/1520-0485(2002)031<3516:GSVAOA>2.0.CO;2, 2001.
- Friedrichs, G., Bock, J., Temps, F., Fietzek, P., Körtzinger, A., and Wallace, D. W. R.: Toward Continuous Monitoring of Seawater ¹³CO₂/¹²CO₂ Isotope ratio and pCO₂: Performance of Cavity Ringdown Spectroscopy and Linewidth Effects, *Limnol. Oceanogr.: Methods*, 8, 523–551, doi:10.4319/lom.2010.8.539., 2010.
- Friis, K., Körtzinger, A., and Wallace, D. W. R.: The salinity normalization of marine inorganic carbon chemistry data, *Geophys. Res. Lett.*, 30, doi:10.1029/2002GL015898, 1085, 2003.
- Geider, R. and Roche, J. L.: Redfield revisited: variability of C:N:P in marine microalgae and its biochemical basis, *Eur. J. Phycol.*, 37, 1–17, doi:10.1017/S0967026201003456, 2002.
- Goericke, R. and Fry, B.: Variations of marine plankton δ¹³C with latitude, temperature, and dissolved CO₂ in the world ocean, *Global Biogeochem. Cycles*, 8, 85–90, doi:10.1029/93GB03272, 1994.
- Gruber, N. and Deutsch, C. A.: Redfield’s evolving legacy, *Nature Geosci.*, 7, 853–855, doi:10.1038/ngeo2308, 2014.

- Gruber, N., Keeling, C. D., Bacastow, R. B., Guenther, P. R., Lueker, T. J., Wahlen, M., Meijer, H. A. J., Mook, W. G., and Stocker, T. F.: Spatiotemporal patterns of carbon-13 in the global surface oceans and the oceanic suess effect, *Global Biogeochem. Cycles*, 13, 307–335, doi:10.1029/1999GB900019, 1999.
- Guggenheim, E. A.: *Thermodynamics - An advanced Treatment for Chemists and Physics*, North-Holland Publishing Company, 1950.
- Hansell, D. A., Bates, N. R., and Olson, D. B.: Excess nitrate and nitrogen fixation in the North Atlantic Ocean, *Mar. Chem.*, 84, 243 – 265, doi:10.1016/j.marchem.2003.08.004, 2004.
- Hansen, H. and Koroleff, F.: Determination of nutrients., in: *Methods of seawater analysis*, edited by Grasshoff, K., Kremling, K., and Erhardt, M., pp. 159–228, Verlag Chemie, Weinheim, Germany, 1999.
- Hansen, T., Burmeister, A., and Sommer, U.: Simultaneous $\delta^{15}\text{N}$, $\delta^{13}\text{C}$ and $\delta^{34}\text{S}$ measurements of low-biomass samples using a technically advanced high sensitivity elemental analyzer connected to an isotope ratio mass spectrometer, *Rapid Commun. Mass Spectrom.*, 23, 3387–3393, doi:10.1002/rcm.4267, 2009.
- Hauss, H., Franz, J. M., Hansen, T., Struck, U., and Sommer, U.: Relative inputs of upwelled and atmospheric nitrogen to the eastern tropical North Atlantic food web: Spatial distribution of $\delta^{15}\text{N}$ in mesozooplankton and relation to dissolved nutrient dynamics, *Deep-Sea Res. Pt I*, 75, 135 – 145, doi:10.1016/j.dsr.2013.01.010, 2013.
- Hays, G., Carr, M., and Taylor, A.: The relationship between Gulf Stream position and copepod abundance derived from the Continuous Plankton Recorder Survey: separating biological signal from sampling noise, *J. Plankton Res.*, 15, 1359–1373, doi:10.1093/plankt/15.12.1359, 1993.
- Henson, S. A., Dunne, J. P., and Sarmiento, J. L.: Decadal variability in North Atlantic phytoplankton blooms, *J. Geophys. Res. Oceans*, 114, doi:10.1029/2008JC005139, c04013, 2009a.
- Henson, S. A., Sarmiento, J. L., Dunne, J. P., Bopp, L., Lima, I., Doney, S. C., John, J., and Beaulieu, C.: Is global warming already changing ocean productivity?, *Biogeosciences Dis.*, 6, 10 311–10 354, 2009b.

- Hoering, T. C. and Ford, H. T.: The Isotope Effect in the Fixation of Nitrogen by Azotobacter, *J. Am. Chem. Soc.*, 82, 376–378, doi:10.1021/ja01487a031, 1960.
- Hogg, N. G. and Johns, W. E.: Western boundary currents, *Rev. Geophys.*, 33, 1311–1334, 1995.
- Jähne, B., Heinz, G., and Dietrich, W.: Measurement of the diffusion coefficients of sparingly soluble gases in water, *J. Geophys. Res.*, 92, 10 767–10 776, 1987.
- Jiang, Z.-P., Hydes, D. J., Tyrrell, T., Hartman, S. E., Hartman, M. C., Dumousseaud, C., Padin, X. A., Skjelvan, I., and González-Pola, C.: Key controls on the seasonal and interannual variations of the carbonate system and air-sea CO₂ flux in the Northeast Atlantic (Bay of Biscay), *J. Geophys. Res. Oceans*, 118, 785–800, doi:10.1002/jgrc.20087, 2013.
- Johnson, K., Wills, K., Butler, D., Johnson, W., and Wong, C.: Coulometric total carbon dioxide analysis for marine studies: maximizing the performance of an automated gas extraction system and coulometric detector, *Mar. Chem.*, 44, 167 – 187, doi:10.1016/0304-4203(93)90201-X, *marine Physical Chemistry - in memory of the contributions made to the field by Dr. Ricardo Pytkowicz*, 1993.
- Johnson, K. M., Dickson, A. G., Eiseid, G., Goyet, C., Guenther, P., Key, R. M., Millero, F. J., Purkerson, D., Sabine, C. L., Schottle, R. G., Wallace, D. W., Wilke, R. J., and Winn, C. D.: Coulometric total carbon dioxide analysis for marine studies: assessment of the quality of total inorganic carbon measurements made during the US Indian Ocean CO₂ Survey 1994-1996, *Mar. Chem.*, 63, 21 – 37, doi:10.1016/S0304-4203(98)00048-6, 1998.
- Keeling, C. D.: The Concentration and Isotopic Abundances of Carbon Dioxide in the Atmosphere, *Tellus*, 12, 200–203, doi:10.1111/j.2153-3490.1960.tb01300.x, 1960.
- Keeling, C. D.: The Suess effect: ¹³Carbon-¹⁴Carbon interrelations, *Environment International*, 2, 229 – 300, doi:http://dx.doi.org/10.1016/0160-4120(79)90005-9, 1979.
- Keeling, C. D., Whorf, T. P., Wahlen, M., and van der Plichtt, J.: Interannual extremes in the rate of rise of atmospheric carbon dioxide, *Nature*, 375, 666–670, 1995.

- Koeve, W.: Spring bloom carbon to nitrogen ratio of net community production in the temperate N. Atlantic, *Deep-Sea Res. Pt I*, 51, 1579 – 1600, doi:10.1016/j.dsr.2004.07.002, 2004.
- Koeve, W.: C:N stoichiometry of the biological pump in the North Atlantic: Constraints from climatological data, *Global Biogeochem. Cycles*, 20, doi:10.1029/2004GB002407, gB3018, 2006.
- Körtzinger, A., Koeve, W., Kähler, P., and Mintrop, L.: C : N ratios in the mixed layer during the productive season in the northeast Atlantic Ocean, *Deep-Sea Res. Pt I*, 48, 661 – 688, doi:10.1016/S0967-0637(00)00051-0, 2001.
- Körtzinger, A., Quay, P. D., and Sonnerup, R. E.: Relationship between anthropogenic CO₂ and the ¹³C Suess effect in the North Atlantic Ocean, *Global Biogeochem. Cycles*, 17, 5–1–5–20, doi:10.1029/2001GB001427, 1005, 2003.
- Körtzinger, A., Send, U., Lampitt, R. S., Hartman, S., Wallace, D. W. R., Karstensen, J., Villagarica, M. G., Llinás, O., and DeGrandpre, M. D.: The seasonal *p*CO₂ cycle at 49°N/16.5°W in the northeastern Atlantic Ocean and what it tells us about biological productivity, *J. Geophys. Res. Oceans*, 113, doi:10.1029/2007JC004347, c04020, 2008.
- Krauss, W., Fahrbach, E., Aitsam, A., Elken, J., and Koske, P.: The North Atlantic current and its associated eddy field southeast of Flemish Cap, *Deep-Sea Res. Pt I*, 34, 1163 – 1185, doi:10.1016/0198-0149(87)90070-7, 1987.
- Landschützer, P., Gruber, N., Bakker, D. C. E., and Schuster, U.: Recent variability of the global ocean carbon sink, *Global Biogeochem. Cycles*, 28, 927–949, doi:10.1002/2014GB004853, 2014.
- Laws, E. A., Popp, B. N., Bidigare, R. R., Kennicutt, M. C., and Macko, S. A.: Dependence of phytoplankton carbon isotopic composition on growth rate and [CO₂]_{aq}: Theoretical considerations and experimental results, *Geochim. Cosmochim. Acta*, 59, 1131 – 1138, 1995.
- Le Quéré, C., Moriarty, R., Andrew, R. M., Canadell, J. G., Sitch, S., Korsbakken, J. I., Friedlingstein, P., Peters, G. P., Andres, R. J., Boden, T. A., Houghton, R. A., House, J. I., Keeling, R. F., Tans, P., Arneeth, A., Bakker, D. C. E., Barbero, L., Bopp, L., Chang, J., Chevallier, F., Chini, L. P., Ciais, P., Fader, M., Feely, R. A., Gkritzalis,

- T., Harris, I., Hauck, J., Ilyina, T., Jain, A. K., Kato, E., Kitidis, V., Klein Goldewijk, K., Koven, C., Landschützer, P., Lauvset, S. K., Lefèvre, N., Lenton, A., Lima, I. D., Metzl, N., Millero, F., Munro, D. R., Murata, A., Nabel, J. E. M. S., Nakaoka, S., Nojiri, Y., O'Brien, K., Olsen, A., Ono, T., Pérez, F. F., Pfeil, B., Pierrot, D., Poulter, B., Rehder, G., Rödenbeck, C., Saito, S., Schuster, U., Schwinger, J., Séférian, R., Steinhoff, T., Stocker, B. D., Sutton, A. J., Takahashi, T., Tilbrook, B., van der Laan-Luijkx, I. T., van der Werf, G. R., van Heuven, S., Vandemark, D., Viovy, N., Wiltshire, A., Zaehle, S., and Zeng, N.: Global Carbon Budget 2015, *Earth Syst. Sci. Data*, 7, 349–396, doi:10.5194/essd-7-349-2015, 2015.
- Lipschultz, F.: A time-series assessment of the nitrogen cycle at BATS, *Deep-Sea Res. Pt II*, 48, 1897 – 1924, doi:10.1016/S0967-0645(00)00168-5, 2001.
- Lochte, K., Ducklow, H., Fasham, M., and Stienen, C.: Plankton succession and carbon cycling at 47°N 20°W during the JGOFS North Atlantic Bloom Experiment, *Deep-Sea Res. Pt II*, 40, 91 – 114, doi:10.1016/0967-0645(93)90008-B, 1993.
- Longhurst, A. R.: *Ecological Geography of the sea*, Academic Press, Boston, 2nd edition edn., 2007.
- Lueker, T. J., Dickson, A. G., and Keeling, C. D.: Ocean $p\text{CO}_2$ calculated from dissolved inorganic carbon, alkalinity, and equations for K_1 and K_2 : validation based on laboratory measurements of CO_2 in gas and seawater at equilibrium, *Mar. Chem.*, 70, 105 – 119, 2000.
- Lüger, H., Wallace, D. W. R., Körtzinger, A., and Nojiri, Y.: The $p\text{CO}_2$ variability in the midlatitude North Atlantic Ocean during a full annual cycle, *Global Biogeochem. Cycles*, 18, doi:10.1029/2003GB002200, gB3023, 2004.
- Lüger, H., Wanninkhof, R., Wallace, D. W. R., and Körtzinger, A.: CO_2 fluxes in the subtropical and subarctic North Atlantic based on measurements from a volunteer observing ship, *J. Geophys. Res. Oceans*, 111, doi:10.1029/2005JC003101, c06024, 2006.
- Mehrbach, C., Culberson, C., Hawley, J., and Pytkowicz, R.: Measurement of the apparent dissociation constants of carbonic acid in seawater at atmospheric pressure, *Limnol. Oceanogr.*, 18, 897–907, 1973.

- Millero, F. J., Pierrot, D., Lee, K., Wanninkhof, R., Feely, R., Sabine, C. L., Key, R. M., and Takahashi, T.: Dissociation constants for carbonic acid determined from field measurements, *Deep-Sea Res. Pt I*, 49, 1705 – 1723, doi:10.1016/S0967-0637(02)00093-6, 2002.
- Minagawa, M. and Wada, E.: Nitrogen isotope ratios of red tide organisms in the East China Sea: A characterization of biological nitrogen fixation, *Mar. Chem.*, 19, 245 – 259, doi:10.1016/0304-4203(86)90026-5, 1986.
- Mintrop, L., Pérez, F. F., González-Dávila, M., Santana-Casiano, M., and Körtzinger, A.: Alkalinity determination by potentiometry: Intercalibration using three different methods, *Ciencias Marinas*, 2000.
- Newton, R., Schlosser, P., Mortlock, R., Swift, J., and MacDonald, R.: Canadian Basin freshwater sources and changes: Results from the 2005 Arctic Ocean Section, *J. Geophys. Res. Oceans*, 118, 2133–2154, doi:10.1002/jgrc.20101, 2013.
- Nightingale, P. D., Malin, G., Law, C. S., Watson, A. J., Liss, P. S., Liddicoat, M. I., Boutin, J., and Upstill-Goddard, R. C.: In situ evaluation of air-sea gas exchange parameterizations using novel conservative and volatile tracers, *Global Biogeochem. Cycles*, 14, 373–387, 2000.
- Nuester, J., Vogt, S., Newville, M., Kustka, A. B., and Twining, B. S.: The unique biogeochemical signature of the marine diazotroph *Trichodesmium*, *Frontiers in Microbiology*, 3, doi:10.3389/fmicb.2012.00150, 2012.
- Ohkouchi, N., Ogawa, N. O., Chikaraishi, Y., Tanaka, H., and Wada, E.: Biochemical and physiological bases for the use of carbon and nitrogen isotopes in environmental and ecological studies, *Prog. Earth Plan.*, 2, 1–17, doi:10.1186/s40645-015-0032-y, 2015.
- O’Leary, M. H.: Measurement of the isotope fractionation associated with diffusion of carbon dioxide in aqueous solution, *J. Phys. Chem.*, 88, 823–825, doi:10.1021/j150648a041, 1984.
- Olsen, A., Key, R. M., van Heuven, S., Lauvset, S. K., Velo, A., Lin, X., Schirnick, C., Kozyr, A., Tanhua, T., Hoppema, M., Jutterström, S., Steinfeldt, R., Jeansson, E., Ishii, M., Pérez, F. F., and Suzuki, T.: An internally consistent data product for the

- world ocean: the Global Ocean Data Analysis Project, version 2 (GLODAPv2), *Earth Syst. Sci. Data Dis.*, 2016, 1–78, doi:10.5194/essd-2015-42, 2016.
- Ostle, C., Johnson, M., Landschützer, P., Schuster, U., Hartman, S., Hull, T., and Robinson, C.: Net community production in the North Atlantic Ocean derived from Volunteer Observing Ship data, *Global Biogeochem. Cycles*, 29, 80–95, doi:10.1002/2014GB004868, 2014GB004868, 2015.
- "Picarro Inc.": WS-CRDS - A Universal Instrument for Precision Measurement of GHGs, URL http://www.picarro.com/sites/default/files/GHG_whitepaper.pdf.
- Pierrot, D., Neill, C., Sullivan, K., Castle, R., Wanninkhof, R., Lüger, H., Johannessen, T., Olsen, A., Feely, R. A., and Cosca, C. E.: Recommendations for autonomous underway $p\text{CO}_2$ measuring systems and data-reduction routines, *Deep-Sea Res. Pt II*, 56, 512–522, doi:10.1016/j.dsr2.2008.12.005, 2009.
- Popp, B. N., Takigiku, R., Hayes, J., Louda, J., and Baker, E.: The post-Paleozoic chronology and mechanism of ^{13}C depletion in primary marine organic matter, *Am. J. Sci.*, 289, 436–454, 1989.
- Popp, B. N., Trull, T., Kenig, F., Wakeham, S. G., Rust, T. M., Tilbrook, B., Griffiths, B., Wright, S. W., Marchant, H. J., Bidigare, R. R., and Laws, E. A.: Controls on the carbon isotopic composition of southern ocean phytoplankton, *Global Biogeochem. Cycles*, 13, 827–843, doi:10.1029/1999GB900041, 1999.
- Quay, P., Stutsman, J., and Steinhoff, T.: Primary production and carbon export rates across the subpolar N. Atlantic Ocean basin based on triple oxygen isotope and dissolved O_2 and Ar gas measurements, *Global Biogeochem. Cycles*, 26, doi:10.1029/2010GB004003, gB2003, 2012.
- Quay, P. D., Sonnerup, R., Westby, T., Stutsman, J., and McNichol, A.: Changes in the $^{13}\text{C}/^{12}\text{C}$ of dissolved inorganic carbon in the ocean as a tracer of anthropogenic CO_2 uptake, *Global Biogeochem. Cycles*, 17, 1–20, doi:10.1029/2001GB001817, 2003.
- Quay, P. D., Stutsman, J., Feely, R. A., and Juranek, L. W.: Net community production rates across the subtropical and equatorial Pacific Ocean estimated from air-sea $\delta^{13}\text{C}$

- disequilibrium, *Global Biogeochem. Cycles*, 23, 1–15, doi:10.1029/2008GB003193, 2009.
- Racapé, V., Metzl, N., Pierre, C., Reverdin, G., Quay, P. D., and Olafsdottir, S. R.: The seasonal cycle of $\delta^{13}\text{C}_{\text{DIC}}$ in the North Atlantic subpolar gyre, *Biogeosciences*, 11, 1683–1692, doi:10.5194/bg-11-1683-2014, 2014.
- Ragueneau, O., Schultes, S., Bidle, K., Claquin, P., and Moriceau, B.: Si and C interactions in the world ocean: Importance of ecological processes and implications for the role of diatoms in the biological pump, *Global Biogeochem. Cycles*, 20, doi:10.1029/2006GB002688, gB4S02, 2006.
- Rau, G. H., Takahashi, T., Des, Marais, D. J., Repeta, D. J., and Martin, J. H.: The relationship between carbon-13 of organic matter and $[\text{CO}_{2\text{aq}}]$ in ocean surface water: Data from a JGOFS site in the northeast Atlantic Ocean and a model, *Geochim. Cosmochim. Acta*, 56, 1413–9, 1992.
- Redfield, A. C.: The biological control of chemical factors in the environment, *Am. Sci.*, 46, 230A–221, 1958.
- Reid, P., Colebrook, J., Matthews, J., and Aiken, J.: The Continuous Plankton Recorder: concepts and history, from Plankton Indicator to undulating recorders, *Prog. Oceanogr.*, 58, 117 – 173, doi:10.1016/j.pocean.2003.08.002, 2003.
- Reynolds, S. E., Mather, R. L., Wolff, G. A., Williams, R. G., Landolfi, A., Sanders, R., and Woodward, E. M. S.: How widespread and important is N_2 fixation in the North Atlantic Ocean?, *Global Biogeochem. Cycles*, 21, doi:10.1029/2006GB002886, gB4015, 2007.
- Rickaby, R. E. M., Henderiks, J., and Young, J. N.: Perturbing phytoplankton: response and isotopic fractionation with changing carbonate chemistry in two coccolithophore species, *Climate of the Past*, 6, 771–785, doi:10.5194/cp-6-771-2010, 2010.
- Robertson, J., Robinson, C., Turner, D., Holligan, P., Watson, A., Boyd, P., Fernandez, E., and Finch, M.: The impact of a coccolithophore bloom on oceanic carbon uptake in the northeast Atlantic during summer 1991, *Deep-Sea Res. Pt I*, 41, 297–314, 1994.

- Sambrotto, R. N., Savidge, G., Robinson, C., Boyd, P., Takahashi, T., Karl, D. M., Langdon, C., Chipman, D., Marra, J., and Codispoti, L.: Elevated consumption of carbon relative to nitrogen in the surface ocean, *Nature*, 363, 248–250, doi:10.1038/363248a0, 1993.
- Sieracki, M. E., Verity, P. G., and Stoecker, D. K.: Plankton community response to sequential silicate and nitrate depletion during the 1989 North Atlantic spring bloom, *Deep-Sea Res. Pt II*, 40, 213 – 225, doi:10.1016/0967-0645(93)90014-E, 1993.
- Sigman, D., Karsh, K., and Casciotti, K.: Nitrogen Isotopes in the Ocean, in: *Encyclopedia of Ocean Sciences (Second Edition)*, edited by Steele, J. H., pp. 40 – 54, Academic Press, Oxford, second edition edn., doi:10.1016/B978-012374473-9.00632-9, 2009.
- Singh, A., Lomas, M., and Bates, N.: Revisiting N₂ fixation in the North Atlantic Ocean: Significance of deviations from the Redfield Ratio, atmospheric deposition and climate variability, *Deep-Sea Res. Pt I*, 93, 148 – 158, doi:10.1016/j.dsr2.2013.04.008, 2013.
- Steinhoff, T.: Carbon and nutrient fluxes in the North Atlantic Ocean, Ph.D. thesis, Christian-Albrechts-Universität zu Kiel, 2010.
- Steinhoff, T., Friedrich, T., Hartman, S., Oschlies, A., Wallace, D. W., and Körtzinger, A.: Estimating mixed layer nitrate in the North Atlantic Ocean, *Biogeosciences*, 7, 795–807, 2010.
- Tagliabue, A. and Bopp, L.: Towards understanding global variability in ocean carbon-13, *Global Biogeochem. Cycles*, 22, 2008.
- Takahashi, T., Olafsson, J., Goddard, J., Chipman, D., and Sutherland, S.: Seasonal variation of CO₂ and nutrients in the high-latitude surface oceans: a comparative study, *Global Biogeochem. Cycles*, 7, 843–878, 1993.
- Takahashi, T., Sutherland, S. C., Wanninkhof, R., Sweeney, C., Feely, R. A., Chipman, D. W., Hales, B., Friederich, G., Chavez, F., Sabine, C., Watson, A., Bakker, D. C., Schuster, U., Metzl, N., Yoshikawa-Inoue, H., Ishii, M., Midorikawa, T., Nojiri, Y., Körtzinger, A., Steinhoff, T., Hoppema, M., Olafsson, J., Arnarson, T. S., Tilbrook, B., Johannessen, T., Olsen, A., Bellerby, R., Wong, C., Delille, B., Bates, N., and

- de Baar, H. J.: Climatological mean and decadal change in surface ocean $p\text{CO}_2$, and net sea-air CO_2 flux over the global oceans, *Deep-Sea Res. Pt II*, 56, 554–577, 2009.
- Tchernov, D. and Lipschultz, F.: Carbon isotopic composition of *Trichodesmium* spp. colonies off Bermuda: effects of colony mass and season, *J. Plankton Res.*, 30, 21–31, doi:10.1093/plankt/fbm085, 2008.
- Thomas, H., Friederike Prowe, A. E., Lima, I. D., Doney, S. C., Wanninkhof, R., Greatbatch, R. J., Schuster, U., and Corbiere, A.: Changes in the North Atlantic Oscillation influence CO_2 uptake in the North Atlantic over the past 2 decades, *Global Biogeochem. Cycles*, 22, doi:10.1029/2007GB003167, gB4027, 2008.
- van Heuven, S., Pierrot, D., Lewis, E., and Wallace, D.: MATLAB Program Developed for CO_2 System Calculations. ORNL/CDIAC-105b., 2009.
- van Pelt, A.: Real-Time Atmospheric Monitoring of Stable Isotopes and Trace Greenhouse Gases, Tech. rep., Picarro Inc., 2008.
- Wada, E. and Hattori, A.: Nitrogen isotope effects in the assimilation of inorganic nitrogenous compounds by marine diatoms, *Geomicrobiol. J.*, 1, 85–101, doi:10.1080/01490457809377725, 1978.
- Wanninkhof, R.: Relationship between wind speed and gas exchange over the ocean, *J. Geophys. Res. Oceans*, 97, 7373–7382, doi:10.1029/92JC00188, 1992.
- Wanninkhof, R., Asher, W. E., Ho, D. T., Sweeney, C., and McGillis, W. R.: Advances in Quantifying Air-Sea Gas Exchange and Environmental Forcing, *Ann. Rev. Mar. Sci.*, 1, 213–244, doi:10.1146/annurev.marine.010908.163742, pMID: 21141036, 2009.
- Watson, A. J., Schuster, U., Bakker, D. C. E., Bates, N. R., Corbiere, A., Gonzalez-Davila, M., Friedrich, T., Hauck, J., Heinze, C., Johannessen, T., Kortzinger, A., Metzl, N., Olafsson, J., Olsen, A., Oschlies, A., Padin, X. A., Pfeil, B., Santana-Casiano, J. M., Steinhoff, T., Telszewski, M., Rios, A. F., Wallace, D. W. R., and Wanninkhof, R.: Tracking the Variable North Atlantic Sink for Atmospheric CO_2 , *Science*, 326, 1391–1393, 2009.
- Weiss, R. F.: Carbon dioxide in water and seawater: The solubility of a non-ideal gas, *Mar. Chem.*, 2, 203–215, 1974.

- White, J., Vaughn, B. H., and Michel, S.: Stable Isotopic Composition of Atmospheric Carbon Dioxide (^{13}C and ^{18}O) from the NOAA ESRL Carbon Cycle Cooperative Global Air Sampling Network, 1990-2014, Version: 2015-10-26, University of Colorado, Institute of Arctic and Alpine Research (INSTAAR), URL ftp://aftp.cmdl.noaa.gov/data/trace_gases/co2c13/flask/, 2015.
- Wolf-Gladrow, D. A., Zeebe, R. E., Klaas, C., Körtzinger, A., and Dickson, A. G.: Total alkalinity: The explicit conservative expression and its application to biogeochemical processes, *Mar. Chem.*, 106, 287–300, 2007.
- Young, J. N., Bruggeman, J., Rickaby, R. E. M., Erez, J., and Conte, M.: Evidence for changes in carbon isotopic fractionation by phytoplankton between 1960 and 2010, *Global Biogeochem. Cycles*, 27, 505–515, doi:10.1002/gbc.20045, 2013.
- Zeebe, R. E. and Wolf-Gladrow, D.: *CO₂ in Seawater: Equilibrium, Kinetics, Isotopes*, ELSEVIER, 2005.
- Zehr, J. and Ward, B.: Nitrogen Cycling in the Ocean: New Perspectives on Processes and Paradigms, *Appl. Environ. Microbiol.*, 68, 1015–1024, 2002.
- Zeng, J., Nojiri, Y., Murphy, P. P., Wong, C., and Fujinuma, Y.: A comparison of $\Delta p\text{CO}_2$ distributions in the northern North Pacific using results from a commercial vessel in 1995 - 1999, *Deep-Sea Res. Pt II*, 49, 5303 – 5315, doi:10.1016/S0967-0645(02)00192-3, 2002.
- Zhang, J., Quay, P. D., and Wilbur, D. O.: Carbon isotope fractionation during gas-water exchange and dissolution of CO_2 , *Geochim. Cosmochim. Acta*, 59, 107–114, doi:10.1016/0016-7037(95)91550-D, 1995.
- Zlotnicki, V.: Sea Level Differences across the Gulf Stream and Kuroshio Extension, *J. Phys. Oceanogr.*, 21, 599–609, doi:10.1175/1520-0485(1991)021<0599:SLDATG>2.0.CO;2, 1991.

Curriculum Vitae

Meike Becker

Personal Information

Date of birth: 7 May 1986
Nationality: German
Address: Eckernförder Str. 26, 24103 Kiel, Germany
Phone: 0176/20325693
E-mail: mbecker@geomar.de

Work experience

2/2012 to 3/2016: Research scientist, PhD student, GEOMAR Helmholtz Centre for Ocean Research, Kiel
1/2011 to 1/2012: Research scientist, Institute of Physical Chemistry, Christian-Albrechts-Universität zu Kiel
2008 to 2010: Several jobs as student assistant: Analysis of CFC-samples in the laboratory and at sea (GEOMAR), supervision of lab courses and seminars (Institute of Physical Chemistry)

Education

2007 to 2010: Graduate program, Christian-Albrechts-Universität zu Kiel, Chemistry (Diploma) with a major in Marine Chemistry
Diploma: *CRDS Based Field Measurements of Surface Water $p\text{CO}_2$ and $\delta^{13}\text{C}(\text{CO}_2)$* , Advisors: Prof. G. Friedrichs, Prof. A. Körtzinger
2005 to 2007: Undergraduate program, Humboldt-Universität zu Berlin, Chemistry (Diploma)
Intermediate Diploma
1996 to 2005: Secondary school: Hammonense Gymnasium, Hamm, Germany, Qualification: Abitur

Awards

2010: Otto-Diels diploma prize of the Faculty of Chemistry
2005: DPG book prize for high-school graduates

Proposals

2012: PhD proposal, Future Ocean Cluster, "Field Measurements of Surface Water $p\text{CO}_2$ and $\delta^{13}\text{C}(\text{CO}_2)$ in the North Atlantic using Cavity Ringdown Spectroscopy and a Voluntary Observing Ship", Becker, M., Friedrichs, G., Körtzinger, A.

Talks

'The seasonality of $\delta^{13}\text{C}(\text{CO}_2)$ in the North Atlantic as derived from underway measurements onboard a Voluntary Observing Ship (VOS)' at Workshop "Cavity Enhanced Optical Detection Schemes", Kiel, Germany, April 2015.
'Field Measurements of CO_2 Partial Pressure and $\delta^{13}\text{C}(\text{CO}_2)$ using Cavity Ringdown Spectroscopy' at "Dissertations Symposium in Chemical Oceanography (DISCO) XXIV", Lihue, Kaua'i, Hawai'i, October 2014.
'Field Measurements of CO_2 Partial Pressure and $\delta^{13}\text{C}(\text{CO}_2)$ using Cavity Ringdown Spectroscopy', Bornö Summer School "An Introduction to the Earth-Life system", Niels Bohr Institute, University of Copenhagen, Denmark, July 2014.
'Field Measurements of CO_2 Partial Pressure and $\delta^{13}\text{C}(\text{CO}_2)$ using Cavity Ringdown Spectroscopy' at, Dalhousie University, Halifax, CA, May 2013.

Teaching

Exercises in Physical Chemistry

Supervision of students in Physical Chemistry during their lab work and seminar preparation

Supervision of students in Marine Chemistry

Workshops and Summer Schools

- 04/2015 Workshop "Cavity Enhanced Optical Detection Schemes", Kiel, Germany.
- 10/2014 "Dissertations Symposium in Chemical Oceanography XXIV (DISCO XXIV)", Lihue, Kaua'i, Hawai'i.
- 09/2014 Summer Field Course "Cutting Edge Observational Technology in Marine Biogeochemistry", Sven Lovén Centre Tjärnö, Sweden.
- 07/2014 Bornö Summer School "An Introduction to the Earth-Life system", Niels Bohr Institute, University of Copenhagen, Denmark.
- 2012-2015 Courses of the Integrated School of Oceans Science (ISOS) at the University of Kiel:
- "Stepping Stones and Stumbling Blocks"
 - "Getting Started with the PhD"
 - "Basics in Physical Oceanography"
 - "LabView Programming"
 - "Using Ocean Data View"

Scientific Cruises

- M/V Atlantic Cartier Summer 2015, several 3-day-trips in Europe (Liverpool-Antwerp or Hamburg-Gothenburg); installation of pCO₂ system.
- M/V Atlantic Companion Between May 2012 – May 2015, 9 sampling trips (about 7 days each, Liverpool/UK - Halifax/Canada or Halifax/Canada - Liverpool/UK); collection of discrete samples of several carbon system parameters
- M/V Atlantic Companion 2013 - 2015, several 3-day-trips in Europe (Antwerp - Hamburg - Gothenburg); maintenance of pCO₂ system
- R/V Polarstern 07.04.2010 - 17.05.2010, Punta Arenas/Chile - Bremerhaven/Germany, PI: A. Körtzinger, pCO₂ and $\delta^{13}\text{C}(\text{CO}_2)$ measurements with a CRDS
- ANT XXXVI/4
- R/V Maria S. Merian 10/1 01.11.2008 - 06.12.2008, Ponta Delgada/Azores - Mindelo/Cape Verde, PI: M. Visbeck; CFC measurements

Additional Skills

Language

- German mother tongue
- English fluent in written and spoken
- Swedish basic knowledge (B1)

Computer Skills TeX, MATLAB, Labview, Origin, Office, ODV

Hobbies Sailing, Gardening

First Aid personnel training at GEOMAR

Kiel, 02.04.2016



Acknowledgment

First, I would like to thank my supervisor Prof. Dr. Arne Körtzinger who always offered me advice and support. Thanks for having an open ear for all the smaller and bigger issues that came up during the last years. Thanks for giving me the opportunity to pursue my passion for the ocean, gain unique experiences, see the world and get to know so many nice people.

I also want to thank Prof. Dr. Gernot Friedrichs for additional support and knowledge during the ISOS meetings. Thanks to Prof. Dr. Christa Marandino for being my second referee.

This work would not have been possible without the vessel, its captains and crew. Thanks to ACL for providing the vessel and giving us the possibility to join the vessel for sampling. Thanks a lot to all the people I've met on board. Thanks for becoming friends and making me a part of the crew. Thanks for all your help and support during the years. I learned a lot about pumps and how they can break down. Thanks for plenty nice days with playing volleyball and badminton, watching movies and singing karaoke and hanging out in the bubble pool or in the bar. Och tack för att ni lärt mig svenska.

Thank you so much - Tack så mycket - maraming salamat

This work was funded by the Future Ocean Excellence Cluster Project CP1140 and supported through CarboChange and ICOS.

Special thanks to Tobi for spending plenty long, long nights in Hamburg and on our Europe trips with me, always with enough coffee and cookie supply. Thanks, for keeping up the motivation in the middle of the night and for all the helpful input. I would also like to thank the (C)O₂ group, Basti, Björn, Henry, Peer, tobi, and Anna, and the entire chemistry department. It was always fun to work with you and I will miss all the tasty birthday cakes.

For all the help with sampling and sample measurements, I would like to thank Sebastian Fessler, Martina Lohmann, Frank Malin, Kerstin Nachtigall, Thomas Hansen, Damian Arevalo Martinez, Mirja Dunker, Ann-Katrin Baumann, Bodil Klärman, Ryan Barkhouse and Lisa Hoffmann. Thanks to Doug Wallace and Claire Normandeau for the support on the other side of the North Atlantic.

Special thanks to the girls I probably spent most of my awake time with, at least during the last weeks. Thank you, Helmke, Sinikka, Alina, Cathleen, Annette and Kathrin. Thanks for all discussions about Matlab issues, family planning, women in science, society itself and the Friday afternoon beer...

I would like to thank my friends here in Kiel. Thanks for cooking every Wednesday (it was good to come home after busy days and finding dinner and a cold beer in the fridge), sunny days in the garden and all the evenings playing board games.

Thanks to my parents, my sisters and my grandparents. Now, I become the first Doctor in the family. :-)

And finally, Maren, thanks for being the reason why I came to Kiel and thanks for all your support during the years, although you maybe didn't always understand what and why I was doing it. Thank you for always believing in me.

And last, but not least, thanks to the North Atlantic. For full circle rainbows, gorgeous nights with a supermoon at port side and midnight sunset/sunrise at starboard, beautiful sunny and wavy days, plenty dolphins passing by and lots of storm experience.

Eidesstattliche Erklärung

Hiermit erkläre ich, dass die von mir vorgelegte Dissertation - abgesehen von der Beratung durch meine Betreuer - selbstständig und ohne Zuhilfenahme unerlaubter Hilfsmittel angefertigt habe. Alle benutzten Quellen und Hilfsmittel habe ich vollständig angegeben und die Zusammenarbeit mit Dritten habe ich kenntlich gemacht. Ich versichere, dass diese Arbeit unter Einhaltung der Regeln guter wissenschaftlicher Praxis der Deutschen Forschungsgemeinschaft verfasst wurde, und dass sie nach Form und Inhalt meine eigene Arbeit ist. Weder diese noch eine ähnliche Arbeit wurden an einer anderen Abteilung oder Hochschule im Rahmen eines Prüfungsverfahrens vorgelegt, veröffentlicht oder zur Veröffentlichung vorgelegt.

Kiel, den 30. März 2016

Meike Becker